Condition Monitoring and Fault Detection of Inverter-fed Rotating Machinery

Prepared by:

Andrew Ipurale

IPRAND001

Department of Electrical Engineering
University of Cape Town

Prepared for:

A/Prof Paul Barendse

Department of Electrical Engineering
University of Cape Town

May, 2017

Submitted to the Department of Electrical Engineering at the University of Cape Town in partial fulfilment of the academic requirements for a Master of Science degree in Electrical Engineering.

Key Words: Condition Monitoring, Fault Detection, Induction Motors, Gearboxes, Reciprocating Compressors, Fourier Transform, Wavelet Transform

Declaration

I know the meaning of plagiarism and declare that all the work in the document, save for that which is properly acknowledged, is my own. This dissertation has been submitted to the Turnitin module (or equivalent similarity and originality checking software) and I confirm that my supervisor has seen my report and any concerns revealed by such have been resolved with my supervisor.

Name: Andrew Matthew Ipurale

Signature: Signed by candidate **Date:** 30th May, 2017

Acknowledgements

I would first like to thank A/Prof Paul Barendse for always having his door open whenever I ran into a problem with my research or writing. He consistently allowed this document to be my own work, but steered me in the right direction whenever he thought I needed it. I would also like to thank A/Prof Azeem Khan for his support and guidance throughout this thesis.

I would also like to thank Mr. Chris Wozniak and Mr. Phillip Titus for their vital support in Machines lab, and were indispensable in the technical aspect of this work.

Thanks to the administration staff of the Department of Electrical Engineering for their kindness and assistance during this project.

I would like to thank my mum, dad and my sisters for their endless support and encouragement prior to and during this project.

Many thanks to Alfred, Jona, Emma, Tumi, Victor and the UCT-AMES Group who were not only colleagues but also friends.

Executive Summary

Condition monitoring of rotating machinery is crucial in industry. It can prevent long term outages that can prove costly, prevent injury to machine operators, and lower product quality. Induction motors, often described as the workhorse of industry, are popular in industry because of their robustness, efficiency and the need for low maintenance. They are, however, prone to faults when used improperly or under strenuous conditions. Gearboxes are also an important component in industry, used to transmit motion and force by means of successively engaging teeth. They too are prone to damage and can disrupt industrial processes if failure is unplanned for. Reciprocating compressors are widely used in the petroleum and the petrochemical industry. Their complex structure, and operation under poor conditions makes them prone to faults, making condition monitoring necessary to prevent accidents, and for maintenance decision-making and cost minimization [1].

Various techniques have been extensively investigated and found to be reliable tools for the identification of faults in these machines. This thesis, however, sets out to establish a single non-invasive tool that can be used to identify the faults on all these machines. Literature on condition monitoring of induction motors, gearboxes, and reciprocating compressors is extensively reviewed. The time, frequency, and time-frequency domain techniques that are used in this thesis are also discussed. Statistical indicators were used in the time domain, the Fourier Transform in the frequency domain, and Wavelet Transforms in the time-frequency domain. Vibration and current, which are two of the most popular parameters for fault detection, were considered. The test rig equipment that is used to carry to the experiments, which comprised a modified Machine Fault Simulator -Magnum (MFS-MG), is presented and discussed.

The fault detection strategies rely on the presence of a fault signature. The test rig that was used allows for the simulation of individual or multiple concurrent faults to the test machinery. The experiments were carried out under steady-state and transient conditions with the faults in the machines isolated, and then with multiple faults implemented concurrently.

The results of the fault detection strategies are analysed, and conclusions are drawn based on the performances of these tools in the detection of the faults in the machinery.

Table of Contents

Condition Monitoring and Fault Detection of Inverter-fed Rotating Machinery **1**
Prepared by: **1**
Department of Electrical Engineering **1**
Prepared for: **1**
Key Words: Condition Monitoring, Fault Detection, Induction Motors, Gearboxes, Reciprocating Compressors, Fourier Transform, Wavelet Transform **1**
Declaration ..... **i**
Acknowledgements ..... **ii**
Executive Summary ..... **iii**
Table of Contents ..... **iv**
List of Figures ..... **viii**
1. Introduction **1**
1.1 Background to the Study 1
1.2 Motivation for Research 2
1.3 Objectives of this Study 2
1.3.1 Problems to be investigated 3
1.4 Scope and Limitations 3
1.5 Plan of Development 3
2. Literature Review **5**
2.1 Introduction 5
2.2 Induction Motors 5
2.2.1 Common types of faults associated with induction motors 6
2.3 Gears 10
2.4 Reciprocating Compressors 11
2.5 Maintenance of Equipment 12
2.5.1 Reactive Maintenance 12
2.5.2 Preventive Maintenance 12
2.5.3 Predictive /Condition-based maintenance 13
2.6 Importance of Condition Monitoring 13
2.7 Condition Monitoring Techniques 13
2.7.1 Vibration monitoring 13
2.7.2 Stator Current Monitoring 14
2.7.3 Thermal monitoring 14
2.7.4 Magnetic Flux Monitoring 14
2.7.5 Stator Voltage Monitoring 15
2.7.6 Partial Discharge 15
2.7.7 Air-Gap Torque 15
2.7.8 Acoustic Noise 15
2.7.9 Artificial Intelligence 15
3. Signal Processing Techniques for Condition Monitoring of Rotating Machinery **16**
3.1 Introduction 16
3.2 Signal Classification 16
3.3 Fault Diagnosis Techniques 16
3.4 Time-domain Analysis 17
3.4.1 Peak Value (PV) 17
3.4.2 Root Mean Square (RMS) 17

3.4.3 Crest Factor (CF) ... 17
3.4.4 Kurtosis ... 18
3.5 Frequency Domain Analysis ... 18
3.5.1 Fourier Transform ... 18
3.6 Frequency-time Domain Analysis ... 19
3.6.1 Wavelets and Wavelet Transforms ... 19
3.7 Hilbert Transform ... 23
3.7.1 Analytic signal of the Current in a Healthy Machine ... 23
4. Motor Current Signature Analysis (MCSA) and Vibration Monitoring in Condition Monitoring 25
4.1 Introduction ... 25
4.2 Motor Current Signature Analysis (MCSA) ... 25
4.3 Vibration Monitoring ... 26
4.3.2 Vibration in Induction Motors ... 27
4.4 Fault Signatures in Induction Motors ... 28
4.4.1 Eccentricity ... 28
4.4.2 Broken rotor bars ... 30
4.4.3 Stator inter-turn faults ... 31
4.4.4 Bearing faults ... 31
4.5 Fault Signatures in Gearboxes and Reciprocating Compressors ... 33
4.5.1 Gears ... 33
4.5.2 Reciprocating Compressor ... 34
4.6 Fault Signatures of Mechanical Loads in Motor Current ... 38
5. Experimental Setup ... 39
5.1 Introduction ... 39
5.2 The MFS-MG Test-rig ... 39
5.2.1 The General Setup ... 39
5.2.2 Vibration Sensor ... 40
5.2.3 Current and Voltage Transducers ... 41
5.2.4 Signal Conditioning and Data Acquisition Hardware devices ... 41
5.2.5 DAQ Hardware and Interfacing Software ... 44
5.3 The Test Motors ... 44
5.4 The Test Loads ... 44
5.4.1 The Gearbox ... 44
5.4.2 The Reciprocating Compressor ... 46
6. Results and Discussions using Frequency Domain Techniques ... 48
6.1 Introduction ... 48
6.2 Induction Motor Faults ... 48
6.2.1 Stator Inter-turn Fault ... 48
6.2.2 Broken Rotor Bar Fault ... 51
6.2.3 Bowed Rotor Fault ... 53
6.2.4 Bearing Fault ... 56
6.2.5 Concluding remarks ... 58
6.3 Gearbox faults ... 59
6.3.1 Healthy Gearbox ... 59
6.3.2 Chipped Tooth Gearbox ... 61
6.3.3 Missing Tooth Gearbox ... 63
6.3.4 Worn-out Gearbox ... 65
6.3.5 Concluding Remarks ... 66

6.4 Reciprocating Compressor faults 68
6.4.1 Healthy Compressor 68
6.4.2 Partially Blocked Discharge Fault 71
6.4.3 Blocked Suction Fault 74
6.4.4 Concluding Remarks 77
7. Results and Discussion for Start-up Conditions 78
7.1 Introduction 78
7.2 Induction Motors 78
7.2.1 Stator Inter-turn Fault 79
7.2.2 Broken Rotor Bar Fault 80
7.2.3 Bearing Fault 82
7.2.4 Bowed Rotor Fault 83
7.2.5 Concluding Remarks 84
7.3 Gearboxes 85
7.3.1 Introduction 85
7.3.2 Chipped Tooth Gearbox 86
7.3.3 Missing Tooth Gearbox 88
7.3.4 Worn-out Gearbox 90
7.3.5 Concluding Remarks 91
8. Detection of Individual Faults within Multiple Faulty Equipment 92
8.1 Introduction 92
8.2 Healthy Motor, Healthy Gearbox, and Healthy Compressor 92
8.2.1 Motor in Steady-state 92
8.2.2 Motor during Start-up 93
8.2.3 Gearbox in Steady-state 94
8.2.4 Reciprocating Compressor in Steady-state 95
8.3 Motor with Broken Rotor Bars, Gearbox with Missing Tooth Pinion and Compressor with Blocked Suction 95
8.3.1 Motor in Steady-state 95
8.3.2 Motor during Start-up 96
8.3.3 Gearbox in Steady-state 96
8.3.4 Reciprocating Compressor in Steady-state 98
8.3.5 Concluding Remarks 98
8.4 Motor with Shorted Stator Inter-turns, Gearbox with a Missing Tooth Pinion and Compressor with a Partially Blocked Discharge 98
8.4.1 Motor in Steady-state 98
8.4.2 Motor during Start-up 99
8.4.3 Gearbox in Steady-state 100
8.4.4 Reciprocating Compressor in Steady-state 101
8.4.5 Concluding Remarks 101
9. Conclusions and Recommendations 102
9.1 Conclusions 102
9.1.1 Time Domain Analysis 102
9.1.2 Frequency Domain Analysis 102
9.1.3 Time-frequency Domain Analysis 103
9.2 Recommendations 103
10. List of References 105
11. Appendices 114
11.1 Appendix A – Gearbox 114

11.1.1 Piston Frequencies 114
11.1.2 MCSA of the Worn-out Gearbox 115
11.2 Appendix B – Reciprocating Compressor 116
11.2.1 Partially Blocked Discharge Valve Fault 116
11.2.2 Blocked Suction Fault 116
11.3 Appendix C - Code 117

List of Figures

Figure 2-1 Exploded view of a squirrel cage induction motor showing stator, rotor, end-bells, cooling fan, ball bearings and terminal box [12] 5
Figure 2-2 Schematic representation of possible failure modes [19] 7
Figure 2-3 Schematic equivalent of the environment of slot discharge [20] 7
Figure 2-4 Illustration of the broken rotor bar fault [14] 8
Figure 2-5 Various types of bearing faults 9
Figure 2-6 Gear system 10
Figure 2-7 Types of gears [27] 10
Figure 2-8 Types of gear failure [27] 11
Figure 2-9 Parts of a reciprocating compressor [29] 12
Figure 3-1 The Daubechies wavelet [121] 19
Figure 3-2 [122] 20
Figure 3-3 (a) Two-level Discrete Wavelet Transform of a discrete signal and (b) The two-level Wavelet Packet Transform of a discrete signal [122] 22
Figure 4-1 Current spectrum showing experimental healthy (---) and faulty (two broken rotor bars) stator current spectrum around fundamental [125] 25
Figure 4-2 The Trending of Measured Characteristic [27] 26
Figure 4-3 Vibration generated by an induction motor with a broken rotor bar 27
Figure 4-4 Air-gap eccentricity in induction motors [124] 28
Figure 4-5 Vibration frequencies for a motor with stator eccentricity [107] 29
Figure 4-6 Vibration frequencies for a motor with rotor eccentricity [107] 30
Figure 4-7 Vibration frequency spectrum of broken rotor bar [107] 31
Figure 4-8 Four types of rolling-element bearing misalignment [41] 32
Figure 4-9 Ball bearing dimensions [41] 33
Figure 4-10 Fault frequencies of a discrete gear tooth irregularity [130] 34
Figure 4-11 Time waveform of a gearbox with a discrete gear tooth irregularity [130] 34
Figure 4-12 Pressure-time trace (pressure angle) with vibration and ultrasonic traces imposed of a healthy reciprocating compressor [131] 35
Figure 4-13 One compression cycle of a reciprocating compressor [63] 36
Figure 4-14 Pressure-time trace with vibration and ultrasonic traces imposed of a reciprocating compressor with springs in the discharge valve too heavy [131] 36
Figure 4-15 Pressure-time trace with vibration and ultrasonic traces imposed of a reciprocating compressor with a (a) leaking suction valve (b) leaking discharge valve [131] 37
Figure 5-1 The Machinery Fault Simulator Magnum (MFS-MG) [136] 39
Figure 5-2 Schematic of the test rig 40
Figure 5-3 Circuit diagram of the anti-aliasing analogue RC filter [137] 41
Figure 5-4 NI 9215 module [139] 42
Figure 5-5 Connecting a floating differential voltage signal to the NI 9215 [140] 42
Figure 5-6 NI 9234 module [141] 43
Figure 5-7 Connecting a floating signal source in NI 9234 module [142] 43
Figure 5-8 Gearbox load 45
Figure 5-9 Faulty gearbox pinions 45
Figure 5-10 Reciprocating compressor discharge valves 46
Figure 5-11 Reciprocating compressor with blocked suction valve 47
Figure 5-12 MFS-MG Test rig set up with the reciprocating compressor and air tank installed 47

Figure 6-1 FFT of the motor current of the motor at 50% and 100% load showing the stator fault frequency 48
Figure 6-2 Vibration spectrum of the motor with shorted stator windings showing the 1X Rotational frequency 49
Figure 6-3 Vibration spectrum of the motor with shorted stator windings showing the 2X Rotational frequency and the 2X Line frequency 50
Figure 6-4 Current spectrum of the healthy motor and the motor with broken rotor bars showing the sidebands of the fundamental frequency 51
Figure 6-5 Vibration spectrum of the motor with the with broken rotor bars showing the 1X rotational frequency 52
Figure 6-6 Current spectrum showing the fault components of the motor with the bowed rotor at 0%, 50%, and 100% load 53
Figure 6-7 Vibration spectrum of the healthy motor and the motor with a bowed rotor at 100% load, 50% load and 0% load showing the 1X frequency 54
Figure 6-8 Vibration spectrum of the healthy motor and the motor with a bowed rotor at 0%, 50%, and 100% load showing the $\boldsymbol{2fs + fr}$ frequency 55
Figure 6-9 Vibration spectrum showing the BPFI of the healthy motor and the motor with faulty bearings at 100%, 50% and 0% load 56
Figure 6-10 BPFO of the healthy motor and the motor with faulty bearings at 0%, 50%, and 100% load 57
Figure 6-11 Raw data captured from the vibration of the healthy gearbox 59
Figure 6-12 Vibration spectrum of the healthy gearbox in steady state 60
Figure 6-13 Motor current spectrum showing $\boldsymbol{fs + fm}$ of the healthy gearbox 61
Figure 6-14 Motor current spectrum showing $\boldsymbol{fs + fp}$ and $\boldsymbol{fs - fp}$ of the healthy gearbox 61
Figure 6-15 Raw data captured from the vibration of the chipped tooth gearbox 61
Figure 6-16 Vibration spectrum of the chipped tooth gearbox in steady state showing the mesh frequency and the corresponding sidebands 62
Figure 6-17 Motor current spectrum showing $\boldsymbol{fs + fm}$ of the healthy gearbox and the gearbox with a chipped tooth 63
Figure 6-18 Motor current spectrum showing $\boldsymbol{fs + fp}$ and $\boldsymbol{fs - fp}$ of the healthy gearbox and the gearbox with the chipped tooth 63
Figure 6-19 Raw vibration data of the gearbox with a missing tooth pinion 63
Figure 6-20 Vibration spectrum of the missing tooth gearbox in steady state showing the mesh frequency and the corresponding sidebands 64
Figure 6-21 Motor current spectrum showing $\boldsymbol{fs + fm}$ of the healthy gearbox and the gearbox with a missing tooth pinion 65
Figure 6-22 Motor current spectrum showing $\boldsymbol{fs + fp}$ and $\boldsymbol{fs - fp}$ of the healthy gearbox and the gearbox with the missing tooth pinion 65
Figure 6-23 Raw data captured from the vibration of the gearbox with the worn-out teeth 65
Figure 6-24 Vibration spectrum of the worn-out tooth gearbox in steady state showing the mesh frequency and the corresponding sidebands 66
Figure 6-25 One cycle of raw vibration data of the compressor with the normal sized rod at 70 psi and 0 psi 68
Figure 6-26 Vibration spectrum of healthy compressor at 70 psi and 0 psi using the compressor accelerometer data 69
Figure 6-27 Vibration spectrum of the motor showing the piston frequency of the reciprocating compressor and its harmonics 70
Figure 6-28 Current spectrum of the motor showing the $\boldsymbol{fs \pm nfr}$ frequencies for $\boldsymbol{n = 1, 2}$ with and without a healthy compressor connected as a load 70

Figure 6-29 One cycle of raw vibration data of the healthy compressor with the normal sized rod at 70 psi and 0 psi 71
Figure 6-30 FFT of vibrations from the compressor accelerometer showing the 1X and 2X piston frequencies of the healthy compressor and the compressor with a partially blocked discharge valve at 70 psi and 0 psi 72
Figure 6-31 FFT of vibrations from the motor accelerometer showing the 1X and 2X piston frequencies of the healthy compressor and the compressor with a partially blocked discharge valve at 70 psi and 0 psi 73
Figure 6-32 Current Spectrum of the healthy compressor and the compressor with a partially blocked discharge valve under steady state conditions showing the $\boldsymbol{fs \pm fr}$ frequencies with air-tank pressure of 70 psi and 0 psi 74
Figure 6-33 One cycle of raw vibration data of the blocked suction compressor with the normal sized rod at 0 psi 75
Figure 6-34 Vibration spectrum from the compressor accelerometer of the blocked suction compressor with the normal sized rod at 0 psi 75
Figure 6-35 Vibration spectrum from the motor accelerometer of the blocked suction compressor with the normal sized rod at 0 psi 76
Figure 6-36 Current Spectrum of the motor current under steady state conditions showing the $\boldsymbol{fs \pm nfr}$ frequencies $\boldsymbol{n = 1, 2}$ with the healthy compressor connected and with the compressor with the blocked suction connected 76
Figure 7-1 Raw data of the current and vibration signals of the healthy motor during start-up 78
Figure 7-2 Progression of the fault frequency components during start-up 79
Figure 7-3 Raw current data of the motor with shorted stator turns during start-up 79
Figure 7-4 DWT of the motor current with shorted stator turns showing the progression of the stator fault frequency 80
Figure 7-5 DWT of the motor vibrations with shorted stator turns showing the progression of the 2X rotational and 2X line frequencies 80
Figure 7-6 Raw current data of the healthy motor and the motor with 3 broken rotor bars in the time domain 80
Figure 7-7 DWT of the start-up current signals of the healthy motor and the motor with 3 broken rotor bars showing the progression of the $(\boldsymbol{1 \pm 2s})\boldsymbol{f}$ frequencies 81
Figure 7-8 Raw vibration data of the healthy motor and the motor with 3 broken rotor bars 81
Figure 7-9 DWT of the start-up vibration signals of the healthy motor and the motor with 3 broken rotor bars showing the progression of the 1X and 2X rotational frequencies 82
Figure 7-10 Raw vibration data of the healthy motor and the motor with faulty bearings during start-up 82
Figure 7-11 DWT's showing the BPFI and BPFO frequencies from the motor vibrations during start-up 83
Figure 7-12 Raw vibration data of the healthy motor and the motor with the bowed rotor 83
Figure 7-13 DWT's showing the $\boldsymbol{2fs + fr}$ and 2X rotational frequencies from the motor vibrations during start-up 84
Figure 7-14 Raw vibration data from the healthy gearbox during start-up 85
Figure 7-15 Theoretical evolution of the gearbox mesh frequency and the shaft frequency sidebands 85
Figure 7-16 Evolution of the frequency components during start-up 86
Figure 7-17 Raw vibration data of the healthy gearbox and the chipped tooth gearbox 86
Figure 7-18 Raw motor current data of with the motor loaded with a healthy gearbox and the chipped tooth gearbox 86
Figure 7-19 DWT of the Healthy gearbox vs Chipped tooth gearbox (66.67 Hz to 533.33 Hz) [1] showing the progression of the mesh frequency and the pinion sidebands 87

Figure 7-20 Hilbert DWT of motor current showing the evolution of the pinion frequency 88
Figure 7-21 Raw vibration data of the healthy gearbox and the missing tooth gearbox 88
Figure 7-22 Raw motor current data of with the motor loaded with a healthy gearbox and the missing tooth gearbox 89
Figure 7-23 DWT of the vibration data of the healthy gearbox vs the missing tooth gearbox [1] 89
Figure 7-24 Hilbert DWT of the motor current showing the evolution of the pinion frequency 90
Figure 7-25 Raw vibration data of the healthy gearbox and the gearbox with a worn-out pinion 90
Figure 7-26 DWT of the vibration data of the healthy gearbox vs the gearbox with a worn-out pinion 91
Figure 8-1 Raw data of the healthy motor current under steady state conditions 92
Figure 8-2 Current spectrum of the healthy motor 93
Figure 8-3 Raw data of the healthy motor current under transient conditions 93
Figure 8-4 Progression of the fault frequencies during start-up 93
Figure 8-5 Motor current spectrum showing the $\boldsymbol{fs + fm}$ and $\boldsymbol{fs \pm fp}$ frequencies 94
Figure 8-6 Motor current spectrum showing the $\boldsymbol{fs \pm fr}$ frequencies with the healthy motor loaded with the healthy compressor 95
Figure 8-7 Spectra of the motor current under steady state conditions for the healthy motor and the motor with broken rotor bars 95
Figure 8-8 DWT of the motor current during start-up 96
Figure 8-9 Motor current spectrum showing the $\boldsymbol{fs + fm}$ and $\boldsymbol{fs \pm fp}$ frequencies 97
Figure 8-10 Motor current spectrum showing the $\boldsymbol{fs \pm fr}$ frequencies for the healthy compressor and the compressor with a blocked suction 98
Figure 8-12 Spectra of the motor current under steady state conditions for the healthy motor and the motor with shorted stator turns 99
Figure 8-13 DWT of the current of the healthy motor and the motor with shorted stator turns showing the progression of the fault frequency 99
Figure 8-14 Motor current spectrum showing the $\boldsymbol{fs + fm}$ and $\boldsymbol{fs \pm fp}$ frequencies 100
Figure 8-15 Motor current spectrum showing the $\boldsymbol{fs \pm fr}$ frequencies for the healthy compressor and the compressor with a partially blocked discharge valve 101
Figure 11-1 Piston frequencies of the various gearboxes at no load 114
Figure 11-2 Motor current spectrum showing $\boldsymbol{fs + fm}$, $\boldsymbol{fs + fp}$ and $\boldsymbol{fs - fp}$ of the healthy gearbox and the gearbox with the worn-out teeth 115
Figure 11-3 FFT of the healthy compressor and the compressor with a partially blocked discharge at 70 psi and 0 psi air tank pressure 116
Figure 11-4 FFT of the healthy compressor and the compressor with a blocked suction at 0 psi air tank pressure 116

List of Tables

Table 1-1 Fault occurrence possibility in induction motors [2], [3] 1
Table 1-2 Quantitative assessment of the damage histories of reciprocating compressors over 10 years [7] 1
Table 5-1 The IEPE accelerometer details [137] 40
Table 5-2 Gearbox Data 46
Table 6-1 Amplitude and frequency of the fault frequencies at 0%, 50%, and 100% load 49
Table 6-2 Amplitudes and frequencies of the 1X Rotational frequency of the motor with shorted stator turns 49

Table 6-3 Amplitudes and frequencies of the 2X Line frequency of the motor with shorted stator turns 50
Table 6-4 Amplitudes and frequencies of the 2X Rotational frequency of the motor with shorted stator turns 50
Table 6-5 Calculated $(\mathbf{1} \pm \mathbf{2}\boldsymbol{s})\boldsymbol{f}$ frequencies 51
Table 6-6 $(\mathbf{1} \pm \mathbf{2}\boldsymbol{s})\boldsymbol{f}$ frequencies and amplitudes from the current spectrum 52
Table 6-7 Other sidebands frequencies 52
Table 6-8 Amplitudes and frequencies of the 1X rotational frequency 53
Table 6-9 Estimated fault frequencies for the bowed rotor fault under different loads 53
Table 6-10 Estimated and actual fault frequencies of the motor with the bowed rotor in the current spectrum 54
Table 6-11 1X Rotational frequency of the healthy motor and the motor with a bowed rotor at varying loads 54
Table 6-12 Calculated $\mathbf{2}\boldsymbol{fs} + \boldsymbol{fr}$ frequencies at 0%, 50%, and 100% load 55
Table 6-13 $\mathbf{2}\boldsymbol{fs} + \boldsymbol{fr}$ frequencies from PSD 55
Table 6-14 Calculated BPFI frequencies 56
Table 6-15 BPFI frequencies from the PSD 57
Table 6-16 Calculated BPFO frequencies 57
Table 6-17 BPFO frequencies from the PSD 58
Table 6-18 Estimated fault components frequencies of the healthy gearbox 59
Table 6-19 Statistical indicators of the healthy gearbox vibration data 60
Table 6-20 Fault components frequencies and amplitudes of the healthy gearbox 60
Table 6-21 Fault component and the estimated frequencies 61
Table 6-22 Frequencies and amplitudes of the $\boldsymbol{fs} + \boldsymbol{fm}$, $\boldsymbol{fs} + \boldsymbol{fp}$ and $\boldsymbol{fs} - \boldsymbol{fp}$ frequency components in the motor current spectrum for the healthy gearbox 61
Table 6-23 Statistical indicators of the chipped tooth gearbox vibration data 62
Table 6-24 Fault components frequencies and amplitudes of the chipped tooth gearbox 62
Table 6-25 Frequencies and amplitudes of the $\boldsymbol{fs} + \boldsymbol{fm}$, $\boldsymbol{fs} + \boldsymbol{fp}$ and $\boldsymbol{fs} - \boldsymbol{fp}$ frequency components in the motor current spectrum for the gearbox with the chipped tooth 63
Table 6-26 Statistical indicators of the vibration data of the gearbox with a missing tooth pinion 64
Table 6-27 Fault component frequencies and amplitudes of the missing tooth gearbox 64
Table 6-28 Frequencies and amplitudes of the $\boldsymbol{fs} + \boldsymbol{fm}$, $\boldsymbol{fs} + \boldsymbol{fp}$ and $\boldsymbol{fs} - \boldsymbol{fp}$ frequency components in the motor current spectrum for the gearbox with the missing tooth pinion 65
Table 6-29 Statistical indicators of the vibration data of the gearbox with worn-out teeth 66
Table 6-30 Fault components frequencies and amplitudes of the worn-out tooth gearbox 66
Table 6-31 Statistical indicators of the healthy compressor vibration data 68
Table 6-32 Amplitudes and vibrations of the piston frequencies and their harmonics for the healthy compressor using the compressor accelerometer data 69
Table 6-33 Amplitudes and frequencies of the 1X and 2X piston frequencies of the healthy compressor vibrations from the motor's accelerometer 70
Table 6-34 Amplitudes and frequencies of the $\boldsymbol{fs} \pm \boldsymbol{nfr}$ frequencies for $\boldsymbol{n} = \mathbf{1}, \mathbf{2}$ of the healthy motor with the healthy compressor connected as a load 71
Table 6-35 Statistical indicators of the vibration data of the compressor with a partially blocked discharge 71
Table 6-36 Variations in the statistical indicators of the vibration data of the compressor with a partially blocked discharge 72
Table 6-37 Amplitudes and vibrations of the piston frequencies and their harmonics for the compressor with a partially blocked discharge valve from the compressor accelerometer 72

Table 6-38 Amplitudes and vibrations of the piston frequencies and their harmonics for the compressor with a partially blocked discharge valve from the motor's accelerometer 73
Table 6-39 Amplitudes and frequencies of the $\boldsymbol{fs \pm nfr}$ frequencies for $\boldsymbol{n = 1, 2}$ with the air-tank pressure at 70 psi and 0 psi 74
Table 6-40 Statistical indicators of the vibration data of the compressor with a blocked suction 75
Table 6-41 Amplitudes and vibrations of the piston frequencies and their harmonics for the compressor with a blocked suction observed from the compressor accelerometer 75
Table 6-42 Amplitudes and vibrations of the piston frequencies and their harmonics for the compressor with a blocked suction observed from the motor accelerometer 76
Table 6-43 Amplitudes and frequencies of $\boldsymbol{fs \pm nfr}$ frequencies $\boldsymbol{n = 1, 2}$ of the healthy motor current with the healthy compressor connected and with the blocked suction connected 76
Table 7-1 DWT Decomposition levels 78
Table 8-1 Mesh frequencies and corresponding pinion sidebands of the healthy gearbox and gearbox with a missing tooth 94
Table 8-2 Amplitudes and frequencies of the $\boldsymbol{fs + fm}$ and $\boldsymbol{fs \pm fp}$ frequencies of the motor current spectrum for the healthy gearbox 94
Table 8-3 Amplitudes and frequencies of the $\boldsymbol{fs \pm fr}$ frequencies of the healthy motor current spectrum 95
Table 8-4 Amplitudes and frequencies of the $\boldsymbol{fs + fm}$ and $\boldsymbol{fs \pm fp}$ frequencies of the motor current spectrum with the healthy gearbox and missing tooth gearbox connected 97
Table 8-5 Amplitudes and frequencies of the $\boldsymbol{fs + fm}$ and $\boldsymbol{fs \pm fp}$ frequencies of the motor current spectrum with the healthy gearbox and missing tooth gearbox connected 100
Table 11-1 Piston frequencies of the gearboxes at no load 114
Table 11-2 Energy in the various frequency bands of the test gearboxes 114
Table 11-3 Frequencies and amplitudes of the $\boldsymbol{fs + fm}$, $\boldsymbol{fs + fp}$ and $\boldsymbol{fs - fp}$ frequency components in the motor current spectrum for the gearbox with the worn-out teeth 115
Table 11-4 Energy in the various frequency bands of the DWT's of the healthy compressor and the compressor with a partially blocked discharge valve at 0 psi 116

1. Introduction

1.1 Background to the Study

Induction motors, gearboxes, and reciprocating compressors are important devices used widely in industry. Induction motors are used in pumps, conveyors, presses, packaging equipment, and machine tools. Induction motors are favoured because of their durability, robustness, efficiency and low maintenance. Many of these motors are operated using inverter drives which enables variation of the motor voltage amplitude and frequency. Common faults in induction motors include the broken rotor bar fault, bearing faults, stator winding faults and the bowed rotor faults. Statistical studies on the occurrence of these faults in machines were done by [2], [3]. The findings of the surveys are summarised in Table 1-1 below. The Motor Reliability Working Group of the IEEE-IAS (IEEE) and the Electric Power Research Institute (EPRI) surveyed 1141 and 6312 motors, respectively.

Table 1-1 Fault occurrence possibility in induction motors [2], [3]

Studied by	Bearing fault (%)	Stator fault (%)	Rotor fault (%)	Others (%)
IEEE	42	28	8	22
EPRI	41	36	9	14

Gearboxes are also an important component in industry, used to transmit motion and force by means of successively engaging teeth. They are ubiquitous in rotating machinery including heavy-duty industrial machinery, automobiles, and conveyor systems. They too are prone to damage and can disrupt industrial processes if failure is unplanned for. Some typical faults in gearboxes include misalignment, cracked teeth, worn teeth, pitting, chipped and missing teeth [4]. A survey by [5] showed that almost two thirds of gear faults are localised faults such chipped, missing, or fatigue induced fractures.

Reciprocating compressors are an important tool in refineries and chemical plants. They prevent bottlenecks and increase production which is crucial in the current environment of global competition and cost reduction [6]. Compressors are also susceptible for faults resulting from wear over time, and from strenuous operation of the equipment. A survey by PROGNOST Systems in 2010 of 542 failure events in 192 compressors from 62 different companies and in 80 different plants established valve faults in compressors to be the most common failure mode [7]. Further details from the survey are presented Table 1-2 below.

Table 1-2 Quantitative assessment of the damage histories of reciprocating compressors over 10 years [7]

Component	Occurrence (%)
Valves	29%
Piston rod	7%
Sensors	6%
Crosshead	5%
HydroCOM	4%
Piston rings	3%
Plunger	3%

Regardless of regular maintenance of each component, a certain level of wear cannot be avoided. This wear mostly cannot be monitored with the naked eye over a long period which can lead to failures, unexpected outages, injury and unanticipated financial losses. Potential costs for lost productivity

increase with the criticality of the fault on the component making it crucial to identify faults in their early stages. Fortunately, most types of failures can be prevented by condition monitoring which reduces downtime, increases productivity, and improves operational safety. This makes it important to monitor the condition of each component throughout the operation.

Condition monitoring can be grouped into five different techniques, namely:

- **Route-based monitoring:** This involves intermittent recording of data with a handheld instrument, and then trending this data to determine whether further analysis is required.
- **Portable Machine Diagnostics:** This involves the use of portable equipment to monitor healthy of machinery using sensors that are usually permanently attached to machine, and portable data acquisition equipment to read the data.
- **Factory Assurance Test:** This involves testing a finished product to see that it meets the design specifications, and also to determine possible failure modes of the equipment.
- **Online Machine Monitoring:** This is the process of monitoring equipment during operation. Data is acquired using embedded equipment and data analysis is performed externally to determine maintenance scheduling.
- **Online Machine Protection:** This also involves the monitoring of equipment as it runs. However, the data is captured and monitored using embedded equipment. Settings can be applied to enable switching off of machinery when critical faults are detected.

1.2 Motivation for Research

There has been a lot of work done to determine reliable tools for fault detection in inverter-fed machinery. These include analysis of oil analysis, temperature, acoustics, current, and vibration, which is the most popular today [8]. Vibration analysis is common because of its proven ability to detect faults early and its ability to determine over 60% of faults [9]. Both vibration analysis and MCSA are based on frequency and time-frequency domain techniques.

Although vibrations are a reliable tool for condition monitoring of rotating machinery, it is sometimes impractical to measure vibrations directly at the source. Motor Current Signature Analysis (MCSA) provides an easily accessible parameter for analysis in the motor current which can provide a solution to situations where vibrations cannot be measured on the motor, gearbox or loads that are connected to the system. Current monitoring is non-invasive and allows for the implementation of both online machine monitoring and online machine protection.

The focus of this study is to validate MCSA as a tool for detecting various faults on motorised systems by considering the components separately before studying them as a system. Steady-state and transient conditions are considered.

1.3 Objectives of this Study

The research presented in this thesis focuses on the detection of electrical and mechanical faults in low voltage induction motors, and mechanical faults in gearboxes and reciprocating compressors. The parameters used are current and vibration.

In this regard, the following questions have been formulated:

1.3.1 Problems to be investigated

i. If a fault is imposed on an inverter-fed induction machine in isolation, can conventional techniques be used to the fault in steady-state and transient conditions?
ii. If a fault is imposed on a gearbox connected to an inverter-fed motor, can the fault be identified in both steady-state and transient conditions?
iii. If a fault is imposed on a reciprocating compressor connected to an inverted-fed motor, can the fault be identified under steady-state conditions?
iv. Which tool performs better between the vibration analysis and current analysis for each of these faults?
v. If faults are imposed on the inverter-fed motor, gearbox and reciprocating compressor concurrently, can they each be identified under steady-state and transient conditions?
vi. Can MCSA reliably identify each of the faults imposed on the inverter-fed motor, gearbox and reciprocating compressor concurrently?

1.4 Scope and Limitations

This study is limited to the investigation of the broken rotor bar fault, stator inter-turn fault, bowed rotor bar, and bearing fault in inverter-fed induction motors. In the gearboxes, only the chipped-tooth fault, missing tooth fault, and worn teeth faults have been considered. Lastly, the faults considered for the reciprocating compressor are the blocked suction fault and the partially discharge valve fault. The faults in the induction motor and gearbox are investigated under steady-state conditions and during start-up. The faults in the reciprocating compressor are investigated under steady-state conditions. The effect of load variation of the gearbox is not discussed. The effect of voltage supply unbalance is also not considered, and efforts are made to use a balanced supply.

1.5 Plan of Development

The remainder of this thesis is structured as follows:

Chapter 2 presents a literature review on the condition monitoring of induction motors, gearboxes, and reciprocating compressors.

Chapter 3 presents signal processing techniques that can be used to identify faults in machines. Specifically, time domain, frequency domain and time-frequency domain analysis is investigated.

Chapter 4 presents the use of vibration and MCSA to detect and identify faults in induction motors, gearboxes, and reciprocating compressors.

Chapter 5 presents the equipment and experimental set-up that were used in the following chapters.

Chapter 6 presents the experimental results and analysis of the induction machine, gearbox and reciprocating compressor faults under steady-state conditions, and in isolation.

Chapter 7 presents the experimental results and analysis of the induction machine, and gearbox faults under start-up conditions, and in isolation.

Chapter 8 presents the experimental results and analysis of the induction machine, gearbox and reciprocating compressor faults when faults are imposed on the equipment concurrently.

Chapter 9 finally draws conclusions based on the results obtained in the previous chapters.

2. Literature Review

2.1 Introduction

This chapter starts by giving an introduction on induction motors, gearboxes, and reciprocating compressors and how they work. It proceeds to describe the common faults associated with induction motors, gearboxes, and reciprocating compressors. Then, it discusses the importance of condition monitoring, and the previous works that have been done in condition monitoring.

2.2 Induction Motors

The induction motor is a motor that carries alternating currents in both the stator and the rotor; the current that flows in the stator is supplied directly while that of the rotor is induced from the alternating stator currents. The induction motor is the most popular motor in industry because of its robust, simple and inexpensive nature [10]. They operate at roughly constant speed but this speed can be varied by supplying power to the motor via an inverter. The stator windings run through evenly spaced slots punched in the inner circumference of a hollow cylindrical core made up of stacked laminations as shown in Figure 2-1.

The rotor windings of an induction motor are of two types, namely; the wound rotor and the squirrel cage rotor. The wound cage rotor also comprises hollow laminations with uniformly distributed 3-phase windings. The terminals are connected to slip rings which turn the rotor. The squirrel-cage rotor, on the other hand, comprises copper rods that are fitted into the holes in the lamination. The copper rods are slightly longer than the rotor, and their ends are linked to two copper end rings. Squirrel cage induction motors are the most popular in industries. [11]

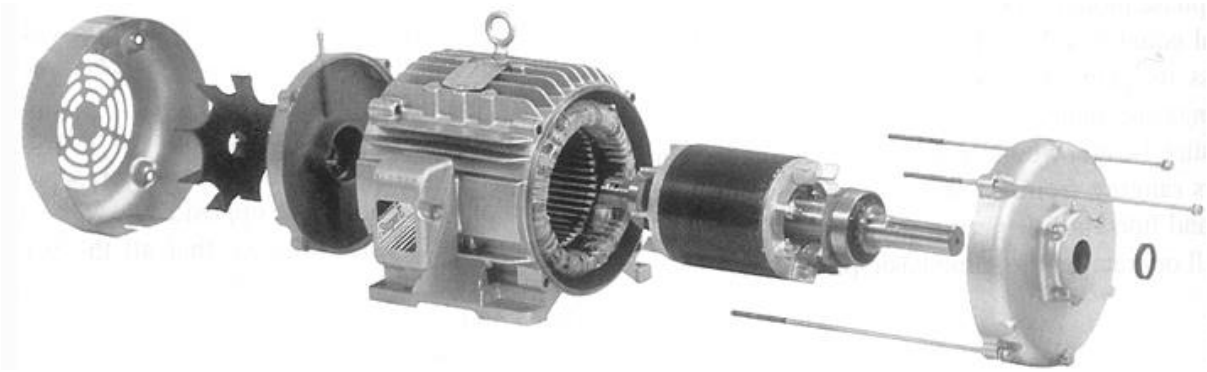

Figure 2-1 Exploded view of a squirrel cage induction motor showing stator, rotor, end-bells, cooling fan, ball bearings and terminal box [12]

A 3-phase induction motor uses Faraday's law of induction and Lorentz force as a basis for operation. Faraday's law of induction states that a conductor placed in a changing magnetic flux will experience an induced electromotive force. Therefore, the rotor bars that comprise electrical conductors, are placed in a rotating magnetic field. The rotating magnetic field is generated by the 3-phase voltage supplied to the stator windings which rotates at synchronous speed n_s where

$$n_s = \frac{120f}{p},$$

where,

$$n_s = synchronous\ speed\ [r/min]$$
$$f = frequency\ of\ the\ source\ [Hz]$$
$$p = number\ of\ poles$$

The speed of rotation of the rotor is always less than synchronous speed. This is because when the rotor is rotating at synchronous speed, the flux does not cut the rotor bars and thus the induced voltage and current will drop to zero. This causes the force acting on the rotor bars to reduce to zero which in turn results in Lorentz force dropping to zero. The speed of the rotor bars would then slow down due to friction and windage [12].

2.2.1 Common types of faults associated with induction motors

Induction motors, though reliable, are prone to undesirable stress which results in various types of failures. These stresses include electrical stress, mechanical stress and environmental stresses/contamination [13]. Many of these occur when the machines of a wrong specification are used for a particular application.

Electrical stresses may result from the variety of transients at the supply to the machine including slow fluctuations in the supply voltage or unbalance between the three phases. For example, the machine may not have the thermal capacity to cope with the overheating resulting from voltage unbalance. Winding insulation can also be affected by rapid transients in the supply voltage since the electrical load is not uniformly distributed throughout the length of the winding. Transients at start-up have also been known to contribute to overheating, loosening of windings, movement of electrical connections and overstressing of terminal boxes [14].

Mechanical stresses may result from laborious duty cycles, overloading the machine, and periods of intermittent running that include frequent restarts. Mechanical stresses can lead to loosening of windings, wear of the bearings, and insulation degradation.

Environmental stresses include thermal and contamination problems. Thermal stresses may result from operation of the machine in an inadequate enclosure, cooling problems, or overloading of the machine. Machines in industry are prone to alien contamination such as textile or paper entering the cooling system. Dirt in the main coolant system can lead to contamination of the windings and cause a deterioration in insulation integrity [14].

The stresses mentioned above lead to various faults in the machine. These are discussed in the following sections.

i. Stator faults

Stator insulation failures can be caused by a combination of the stresses discussed above. The main causes include: [15]

- Abrasion of insulation due to vibration of loose coils or abrasive particles.
- Degradation due to repetitive electrical stresses.
- Electrical tracking or chemical degradation due to contamination.
- Delamination or cracking of insulation due to thermal overload.

Stator winding inter-turn faults

Winding faults are usually due to slow and continuous aging of winding insulation [16]. The aged winding can fail due to overheating, vibrations, or overvoltage which results in an inter-turn short-circuit fault. Usually the insulation failure starts with inter-turn short circuit which induces a high current between the shorted turns. The insulation failure eventually leads to *stator-core to ground*

insulation failure, which ultimately damages the stator core [17]. The entire process takes about 20 to 60 seconds for a low-voltage motors [18]. It is imperative that the fault is arrested in its incipient stages to prevent catastrophic failure. Winding faults in the stator can be classified as turn-to-turn, phase-to-phase, or phase-to-ground as illustrated in Figure 2-2 below.

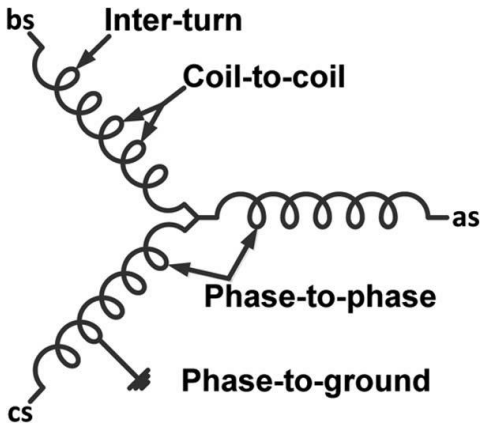

Figure 2-2 Schematic representation of possible failure modes [19]

Stator end winding faults

End windings of induction motors are prone to environmental and mechanical stresses. These include surface contamination, internal voids or delaminations, and mechanical aspects such as long term cyclic fatigue in normal operation and or during transient events causing end-winding distortion [14].

Stator core faults

These are very rare and usually occur in large turbine-driven generators with massive laminated steel cores. They are initiated when the core plates are electrically connected usually due to insulation failure or to foreign bodies physically imposed on them.

Slot discharge

Slot discharge is a type of dielectric barrier discharge that occurs in High-Voltage motors. Dielectric barrier discharge is an electrical discharge that occurs between two electrodes separated by an insulating dielectric barrier. The schematic equivalent of slot discharge is shown in Figure 2-3. It usually results from loss of good electrical contact between the insulated bar or coil surface and the stator core.

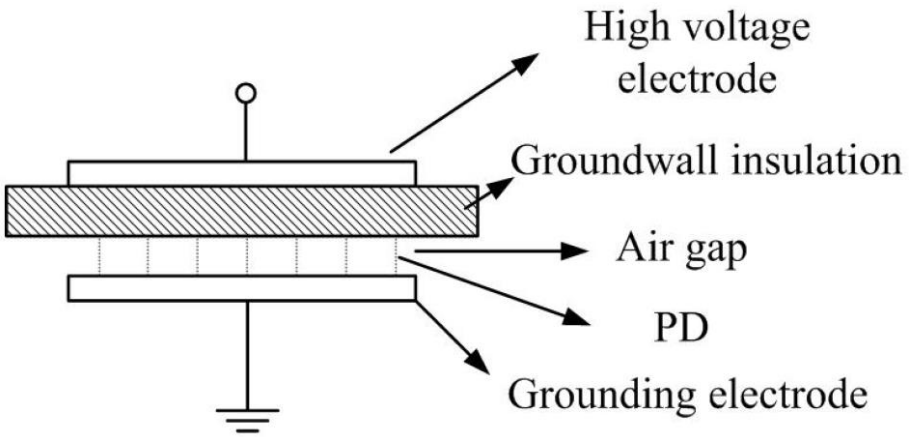

Figure 2-3 Schematic equivalent of the environment of slot discharge [20]

When the airgap is created, the potential difference rises on the inner surface of the ground wall insulation causing an electric field to exist between the ground wall insulation and the stator core which is the equivalent of the ground electrode. Spatial electrons in the air-gap gain energy and collide with the surrounding atoms leading to excitation and ionization. The resulting avalanche leads to a breakdown of the air in the gap when the voltage exceeds the voltage discharge inception voltage. During the breakdown process, the current flowing through the discharge passage is actually the displacement current through the organic insulation, rather than the short circuit current. The current is hence blocked by the ground wall insulation so there is neither arcing nor sparks, as several stable discharge filaments appear across the air-gap [20]. Slot discharge can be prevented by minimising the stator winding and the core [14].

ii. ***Rotor faults***

These are classified as electrical and mechanical faults. Electrical faults include rotor unbalance resulting from broken rotor bars or cracked end-rings, and rotor magnetic faults such as demagnetisation, and rotor magnetic faults such as demagnetisation. Mechanical faults include bearing damage, eccentricity, bent shaft, and misalignment. Broken bar and cracked end-ring faults account for 5%-10% of induction machine faults but it is still crucial that these faults are detected [21].

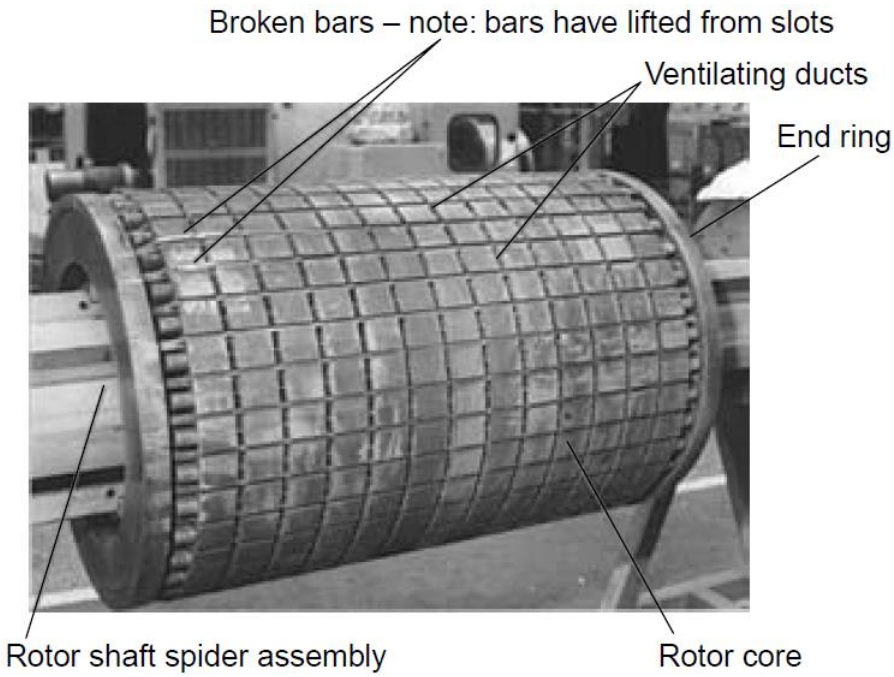

Figure 2-4 Illustration of the broken rotor bar fault [14]

Rotor faults may result from errors in the manufacturing process, defective casing in cast case motors, or poor jointing in the case of brazed or welded end-rings. The high resistance developed causes overheating of the cage which in turn may lead to cracking of the rotor bars at the cage end-rings.
Fluctuating speeds also strain the end rings of the motor since the bars provide the braking and accelerating forces during the speed changes. Broken bar failures in their early stages can be detected by the pulsations in the speed, supply current, and stray leakage flux of the machine.

iii. ***Air-gap eccentricities***

This occurs when the distance between the rotor and the stator in the air-gap is irregular. There are two types of air-gap eccentricity: static and dynamic eccentricity. Static eccentricity occurs when there is

displacement from the axis of rotation where the position of the minimal airgap length is fixed in space. The field distribution in the airgap is not symmetrical since the rotor axis is not aligned with the stator axis. Dynamic eccentricity occurs when the rotor does not rotate about its own axis and also causes a non-uniform airgap. In some cases, static eccentricity has been known to cause dynamic eccentricity [22], [23]. Combined static and dynamic eccentricity is called mixed eccentricity and it occurs when both the rotor and rotation axes are misaligned from the stator axis [24], [25].

iv. ***Bearing faults***

Bearing faults account for 40% of the machine failures [26] . Rolling-element bearings consist of an inner and outer ring between which a set of balls or rollers rotate in raceways. Bearings operating under normal conditions usually experience fatigue failure when small fissures, located below the surfaces of the raceway and rolling-elements, which propagate to the surface generating detectable vibrations and increasing noise levels [26] .

Bearing faults are slow to mature but the can lead to catastrophic failure of the machine. Failure is accompanied by a rising temperature at the bearing surface, in the lubricant and in the bearing housing, which are detectable by temperature sensors. Bearing faults have been known to contribute the air-gap eccentricities [14]. Figure 2-5 below shows the types of bearing faults and their different locations.

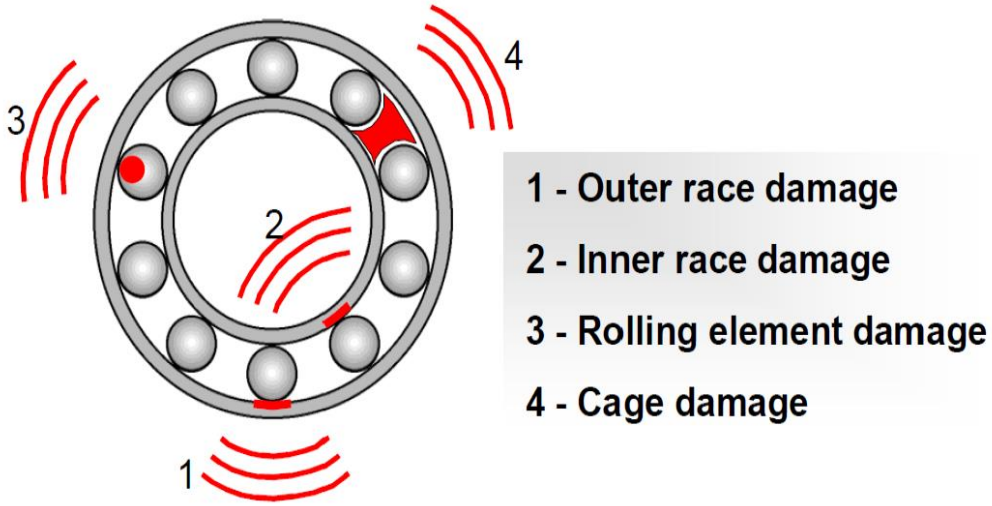

Figure 2-5 Various types of bearing faults

2.3 Gears

Gears are machine elements that transmit motion and force by means of successively engaging teeth. A gear comprises a wheel (gear) and a pinion as shown in Figure 2-6 below.

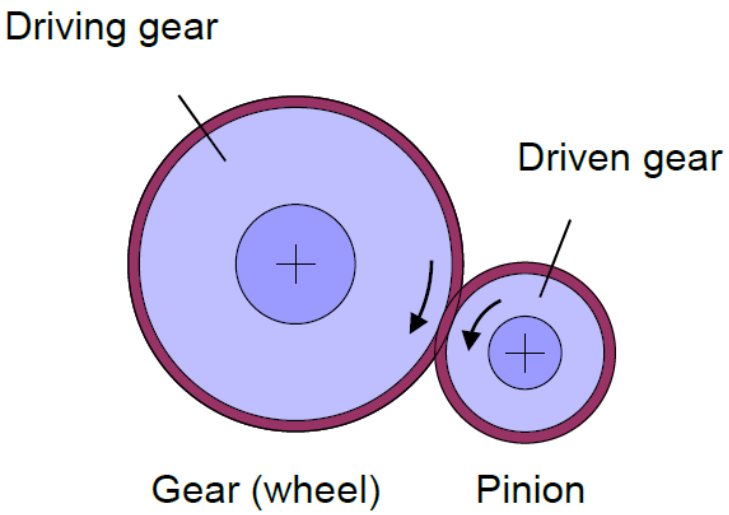

Figure 2-6 Gear system

There are many types of gears which include the spur gear, helical gears, bevel gears, and spiral bevel gears. These are shown in Figure 2-7.

(a) Spur Gear (b) Helical Gears

(c) Bevel Gears (d) Spiral Bevel Gear

Figure 2-7 Types of gears [27]

Gearboxes are prone to faults when operated under high stress conditions [28], various kinds of which can cause a gear to transmit torque inefficiently. A particular type of failure that has its own descriptive

identification is called a mode of gear failure. The most frequent are fatigue failure, and impact and wear. In an analysis of over 1500 studies, tooth bending accounted for 32%, tooth bending impact accounted for 12%, and abrasive tooth wear accounted for 10% [27].

There are four main types of gear failure shown in Figure 2-8 below, namely: pitting, scuffing, wear and root cracking. Pitting occurs due to fatigue from higher Hertzian contact stresses than the surface can stand. A crack is formed on the gear which breaks out and leaves a small smooth bottomed crater. Scuffing occurs when the oil film breaks down thus allowing metal to metal contact. This leads to local welding followed by tearing of the surface as the welds are sheared. Wear involves the gradual removal of metal from the gear flank usually over the whole face. It may look like a lapped surface or surface grooved in the sliding direction. Root cracking which results from stress in the root of the tooth. It occurs when the root cracks under repeated stresses much lower than the ultimate tensile strength.

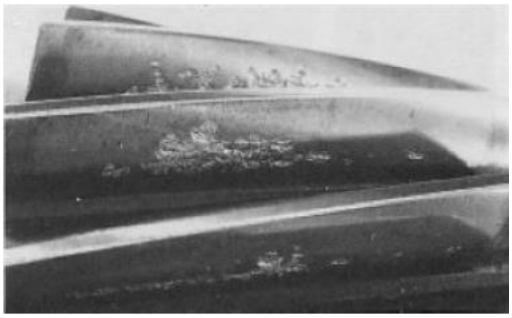

(a) Pitting

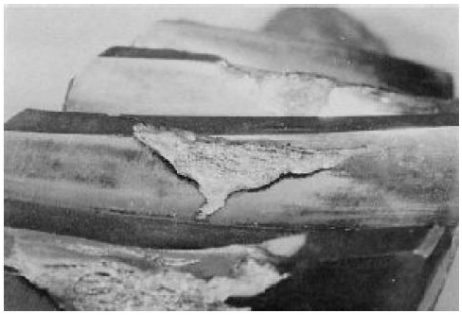

(b) Scuffing

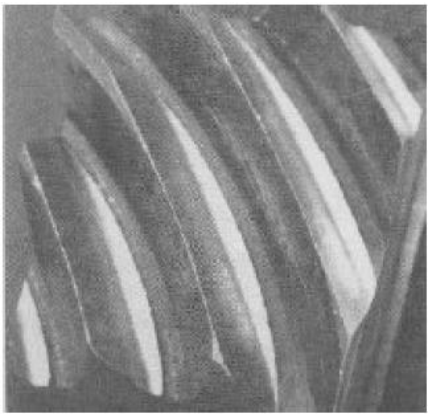

(c) Wear

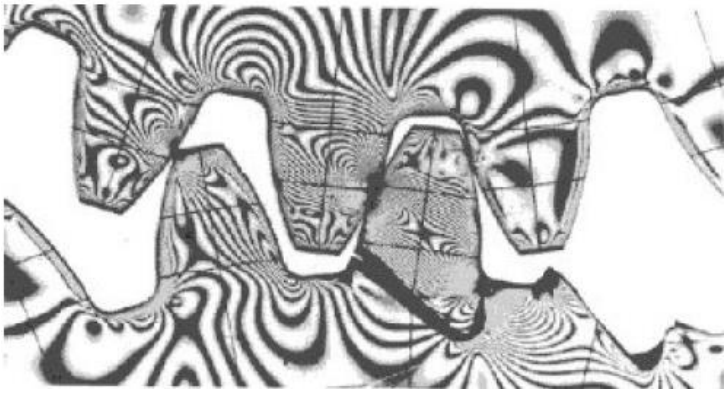

(d) Root crack

Figure 2-8 Types of gear failure [27]

2.4 Reciprocating Compressors

Compressors are devices used to move gas/air from one place to another. A reciprocating compressor comprises a piston which moves up and down in a reciprocating motion. This enables suction and compression of the gas. In larger compressors, piston rings are usually fitted to prevent leakage of gas in the container with the crankshaft. The crankshaft is responsible for the reciprocating motion in the compressor, and is connected to the motor either by a direct coupling or via a belt and pulley arrangement. The crankshaft is connected to the connecting rod such that the rotary motion is translated to a linear up and down movement of the piston. The suction valve is a valve through which air enters the cylinder while the discharge valve is the valve through which air exits the cylinder. The suction valve and discharge valve are never open at the same time.

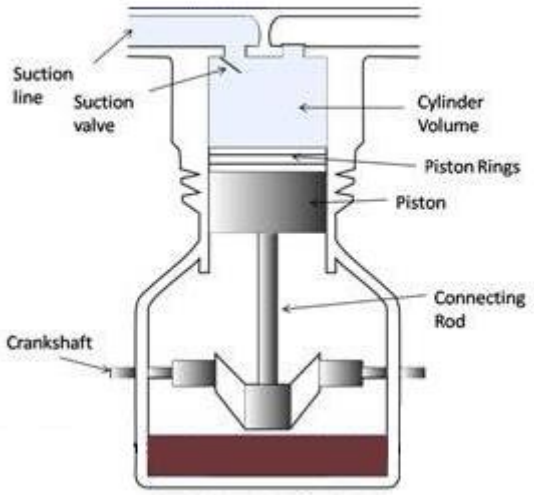

Figure 2-9 Parts of a reciprocating compressor [29]

Faults that commonly occur in reciprocating compressors include valve failures, and loose drive belts [30]. The causes of valve failures include improper installation of valves, wrong selection of valve meters and operation of the compressor outside rated conditions [31].

2.5 Maintenance of Equipment

There has been rapid development of industry automation in recent years which has motivated the need for more intelligent and reliable systems. To minimize the loss due to interruption of production and repair/replacement of expensive machines, it is imperative that reliable on-line condition monitoring systems are in place to provide timely information for maintenance decision-making [32].

Run-to-failure maintenance is mostly shunned in most industrial applications since it is relatively uneconomical. Alternative systems that collect and analyse real-time machine data are widely used due to their ability to provide early detection of faults in machinery. Selecting the most appropriate condition monitoring system is important to maximise the life span of the machinery and to mitigate costs.

There are three common methods of managing maintenance, namely: reactive maintenance, preventive maintenance, and predictive maintenance.

2.5.1 Reactive Maintenance

Reactive maintenance, as known as run-to-failure, involves inaction until the machine has failed. Though it may be viable in some scenarios, reactive maintenance can lead to very costly maintenance and unexpected downtime. It is the most expensive method due to the highest losses in production and it would also require a large inventory of spare parts to minimise downtime [33].

2.5.2 Preventive Maintenance

Preventive/Time-based maintenance is where the parts of a machine are serviced on a regular basis regardless of their condition [34]. This often requires replacement of machine parts periodically. This has the disadvantages of down-time during the replacement of machine parts and the cost of the parts that are being replaced. Preventive maintenance is often used with reactive maintenance to prevent

unexpected catastrophic failures and can provide up to 30% maintenance cost compared to reactive maintenance [34].

2.5.3 Predictive /Condition-based maintenance

Predictive/Condition-based maintenance is a system of maintenance that assesses the condition of the machine, identifies any existing/incipient faults, and allows for planned corrective action to be taken prior to failure of the machine. This system minimises down time, facilitates efficient manpower scheduling, enables other repairs to be carried out during the planned down-time and allows for ordering of replacement parts in advance.

2.6 Importance of Condition Monitoring

Condition monitoring is defined as any activity or set of activities, performed either manually or automatically, intended to determine at pre-determined intervals the characteristics and parameters of the actual state of an item [35]. One of the main applications of condition monitoring is condition-based maintenance.

A consistent evaluation of the health of the rotating machinery is essential during its service life. Faults can be detected in their incipient stages and the necessary steps can be taken to reduce or prevent down-time and save the equipment [36]. This results in minimum down-time and optimum maintenance schedules [37].

Some advantages of conditioning monitoring in industry include: [37]

- Reduction in the cost of maintenance
- Prediction of equipment failure
- Improvement of the equipment and component reliability
- Optimization of the equipment performance
- Improvement of the accuracy in failure prediction

2.7 Condition Monitoring Techniques

There have been significant efforts dedicated to condition monitoring/fault diagnosis in induction motors, gearboxes, and reciprocating compressors in recent decades. A brief review of some of the techniques and condition monitoring parameters that have been investigated are presented below.

2.7.1 Vibration monitoring

Rotating machinery, including new ones, generate some level of vibration. Condition monitoring of rotating machinery via vibration analysis entails identification of abnormalities in the vibrations generated by the machine. There are three types of vibration generated by the machine, namely:

- Stationary vibrations
- Random vibrations
- Noise

During signal processing, noise and random vibration are suppressed via signal processing techniques such as filtering, though sometimes random vibrations are also analysed to identify faults [38]. The analysis of the vibration signals can be in the time domain or in the frequency domain. The latter is preferred because of it provides more detailed information about the condition of the machine.

Vibration monitoring has been used to identify faults in induction motors such as stator and rotor faults in [13], [17], [32], [39]-[47], detecting airgap eccentricity in [48], and the detection of bearing faults in [21], [36], [49]. There has also been plenty of work done investigating the use of vibration signals to detect faults in gearboxes in [50]-[61]. In reciprocating compressors, [6], [62]-[64] investigate the use of vibration signals to detect faults in the valves and cylinder.

2.7.2 Stator Current Monitoring

Stator current is a popular parameter for fault detection and usually entails analysis of the current in the frequency domain to identify mechanical and magnetic asymmetries, broken rotor bars, and shorted turns in the stator windings. This uses Motor Current Signature Analysis (MCSA) to identify and locate faults in induction motor drives. The presence of a fault in the system deviates the line current from that of a healthy system. This current can then be analysed to identify and even locate faults in the system. Stator current monitoring has been investigated as a tool for detection of faults in induction motors including stator faults such as the stator inter-turn fault and degradation of stator insulation in [15], [19], [41], [65]-[72], rotor faults such as broken and cracked rotor bars in [45], [66], [70], [73]-[80], bearing faults [49], [68], [72], [81] and air-gap eccentricity [23], [82]. Stator current has also been investigated for the detection of faults in gearboxes in [33], [83]-[88], and reciprocating compressors in [62], [89]-[92].

2.7.3 Thermal monitoring

Thermal monitoring is achieved by measurement or estimation of the local temperature of the machinery. For instance, in case of shorted stator windings in an induction motor, the current through the stator will increase and produce excessive heat. The thermal model of the motor is used to analyse the machine for faults. Thermal models of the induction motor can be classified into the Finite Element Analysis (FEA) based model and the Lumped Parameter based model. The FEA model is more accurate than the lumped parameter based model but is very highly computational [93]. The lumped parameter based model comprises thermal resistances, capacitances and corresponding power losses. The temperature in the region of the fault rises for an inter-turn fault but the model may not be able to detect the fault before it progresses to a more severe fault [94]. Thermal monitoring has been used for detection of stator faults and bearing faults in induction motors [13], [17], [93]-[95], and gearbox faults [96]. In reciprocating compressors, the inlet and discharge temperatures are important for analysis of the real-time P-V diagram against the ideal P-V diagram.

2.7.4 Magnetic Flux Monitoring

A recent trend in condition monitoring of induction motors has been the analysis of stray flux from the motor as a basis for fault detection [97]. The advantage of flux monitoring is that is non-invasive and is easy to implement. The drawback, however, is the difficulty of modelling the magnetic field which is very dependent on the electromagnetic behaviour of the stator yoke and the motor housing which have important shielding effects [98]. A stator inter-turn short circuit fault causes asymmetry in the air gap flux density and hence in the external magnetic field. The asymmetry produces flux density components that clearly appear in the stray flux. It is also important to note that the sensitivity of the external magnetic field is higher than the line current [98].

Broken rotor bars on the other hand generate a negative sequence on the rotor fundamental air gap flux density, and produce spectral lines in the line current spectrum and the stray flux [97].

Eccentricity also produces components in the stray flux that appear in the axial field but not the radial field or the line current [99].

2.7.5 Stator Voltage Monitoring

Stator voltage monitoring has been used to calculate the instantaneous power, instantaneous torque and the negative sequence impedance to detect faults in induction motors [41], [100]-[104].

2.7.6 Partial Discharge

The partial discharge analyser test developed in 1976 is one of the first techniques to be used during normal machine operation [13]. Various other techniques have been developed using specialized sensors. The partial discharge from a deteriorated winding is approximately 30 times or even higher than that of a winding in a good condition. Partial discharge for condition monitoring of stator windings has been investigated in various literature including [28], [32], [42], [105]-[107].

2.7.7 Air-Gap Torque

The air-gap torque is produced by the flux linkage and the currents of a rotating machine. Zero frequency of the air-gap harmonics shows that the motor is healthy. The air-gap torque is sensitive to unbalance due to defects and can be used to identify faults [97], [108].

2.7.8 Acoustic Noise

Acoustic noise such as air conditioning noise and electromagnetic motive noise has been used to detect winding faults in induction motors [47], [109] and gearboxes [110]. The periodic air pressure distortion caused by the rotational parts affects the air conditioning noise while the electromagnetic motive noise is related to the Maxwell stress in the presence of magnetic field acting on the metal surfaces. The stresses induce vibrations in the structure of the motor causing noise radiation [111].

2.7.9 Artificial Intelligence

Artificial Intelligence is a powerful tool which has grown in popularity in recent years. It has been used to improve the efficiency and effectiveness of fault diagnosis of electrical machines. This includes tools like neural networks, fuzzy logic, fuzzy neural networks and algorithms. Although not yet very popular in industry [98], artificial intelligence has been investigated as a tool to identify faults in induction motor drives, for example using neural networks, to detect stator and rotor faults in induction motors [18], [21], [112]-[115] as well as faults in gearboxes [116] and reciprocating compressors [89].

3. Signal Processing Techniques for Condition Monitoring of Rotating Machinery

3.1 Introduction

In this chapter, classification of signals, and the commonly used signal processing techniques for condition monitoring of rotating machinery are discussed. The signals that are captured include vibrations, current, voltage, magnetic flux and air-gap torque among others. Research is constantly being carried out to develop better and more reliable techniques for condition monitoring and fault diagnosis.

3.2 Signal Classification

Signals can be classified based on various properties. The type of signal and the properties that it possesses are important for the appropriate choice of signal analysis and processing method.
Signals can be classified as deterministic and non-deterministic. Deterministic signals are described by analytical expressions, and can be predicted for arbitrary times and can often be regenerated arbitrarily. Non-deterministic signals comprise random and irregular signals. There is uncertainty about the value of the signal at a specific instant of time. Random signals cannot be described by analytical expressions, though they are statistically or probabilistically describable while irregular signals cannot be represented statistically or stochastically.

3.3 Fault Diagnosis Techniques

The captured signals need to be processed to determine the health of the machinery. It usually entails transforming the signal into a format that allows dominant features to be extracted and analysed for fault detection. These techniques can be classified into 3 groups, namely:

- Standard digital signal processing based techniques
- Advanced digital signal processing techniques
- Artificial intelligence based techniques

Standard digital signal processing techniques are those that are applied to stationary signals. They are applied in the frequency domain for stationary signals and in the time-frequency domain for transient signals. They include the discrete Fourier transform (DFT), fast Fourier transform (FFT), short time Fourier transform (STFT), and the Wigner-Ville distribution.

The advanced digital signal processing techniques include applications of the continuous wavelet transform (CWT), the wavelet packet transform (WPT), and wavelet neural networks (WNN).

Artificial intelligence (AI) is the study of system conditions using computational models. They include expert systems, genetic algorithms, support vector machines, and fuzzy logic.

3.4 Time-domain Analysis

Time-domain analysis is one of the simplest techniques and uses the amplitudes of the signal to distinguish between a healthy signal and a faulty one [117]. However, although time-domain analysis can be used to detect a fault, it is difficult to use time-domain analysis to identify the type of fault. For instance, if a system contains high levels of mechanical vibration, it may be difficult to identify a small, yet consistent and progressive increase in vibration levels making it difficult to detect the existence of a fault in the waveform.

A signal is termed as deterministic if it has a relatively consistent frequency or level content such that it becomes predictable overtime. A fault such as a localised gear fault could result in a signal becoming random or non-deterministic, making it difficult to accurately predict. Statistical parameters can be used to detect fault progression in these scenarios [118]. Commonly used statistical indicators for fault detection based on the time-domain waveform are Peak Value (PV), Root Mean Square (RMS), Kurtosis, and Crest Factor (CF) [60].

3.4.1 Peak Value (PV)

This is the maximum amplitude of the signal.

$$PV = y_{max}(t) \tag{3-1}$$

where y_{max} is the maximum amplitude of the signal.

3.4.2 Root Mean Square (RMS)

The RMS of a signal is related to the energy of the signal and the existence of faults can be directly detected using a variation in the RMS of a signal [119]. The RMS is the normalised second moment of the signal and can be effective in tracking system noise.

The RMS, however, cannot be used solely to identify which fault is developing in most scenarios.

$$RMS = \sqrt{\frac{1}{N} \cdot \sum_{n=1}^{N} (x(n) - \bar{x})^2}$$
$$\bar{x} = \frac{1}{N} \cdot \sum_{n=1}^{N} x(n) \tag{3-2}$$

where N is the number of samples taken in the signal, $x(n)$ is the amplitude of the signal for the nth sample, and $\bar{x}$ is the mean value of the N samples.

3.4.3 Crest Factor (CF)

The CF of a signal is useful in detecting discrete impulses above the background signal which do not occur frequently enough or which do not have sufficient duration to significantly affect the RMS level.

$$CF = \frac{PV}{RMS} \tag{3-3}$$

where PV is the peak value and RMS is the Root Mean Square.

3.4.4 Kurtosis

Kurtosis is used to detect the presence of significant peaks in the time-domain of the signal. It is the fourth order statistical moment of a signal and because it raises the signal to the fourth power, it effectively amplifies the isolated peaks in the signal [120]. The normalised kurtosis for a distribution $x(t)$ given by its sample values $x_i, \dots, x_n$ measured at times $t_i, \dots, t_n$ can be define as:

$$kurtosis = \frac{\frac{1}{N} \cdot \sum_{i=1}^{N} (x_i - \bar{x})^4}{\left[\frac{1}{N} \cdot \sum_{i=1}^{N} (x_i - \bar{x})^2\right]^2} \tag{3-4}$$

where N is the number of samples taken in the signal, $x(n)$ is the amplitude of the signal for the nth sample, and $\bar{x}$ is the mean value of the N samples.
The higher the kurtosis value, the sharper the peak(s) and the longer the tails of the signal. The lower the kurtosis, the more rounded the peak(s). When a signal comprises random noise, then it follows Gaussian (Normal) distribution and it has a kurtosis value of 3.0. Kurtosis is commonly used as a parameter for the detection of gear faults [43].

3.5 Frequency Domain Analysis

3.5.1 Fourier Transform

The Fourier transform is used to analyse periodic and non-periodic continuous time signals in terms of frequency content given by sinusoidal components. The Fourier transform $X(\omega)$ of a continuous time signal $x(t)$ is defined by:

$$X(\omega) = \mathcal{F}\{x(t)\} = \int_{-\infty}^{\infty} x(t) e^{-j\omega t} dt \tag{3-5}$$

Equation (3-5) is known as the analysis or forward transform since it extracts the frequency information from the time domain signal.

$$x(t) = \mathcal{F}^{-1}\{X(\omega)\} = \frac{1}{2\pi} \int_{-\infty}^{\infty} X(\omega) e^{j\omega t} d\omega \tag{3-6}$$

Equation (3-6) is known as the inverse transform since it extracts the time domain information from the frequency spectrum.

Discrete Fourier Transform (DFT)

The Discrete Fourier Transform (DFT) is the equivalent of the Continuous Fourier Transform for signals only known at a discrete number of instances separated by specific time intervals.
A continuous signal $x(t)$ sampled N times with the samples denoted $x[0], x[1], x[2], \dots, x[k], \dots x[N-1]$ has a Discrete Fourier Transform shown below.

$$X(\omega) = \sum_{k=0}^{N-1} x[k] e^{-j\omega kT} \tag{3-7}$$

The corresponding inverse Discrete Fourier Transform of

$$X[n] = \sum_{k=0}^{N-1} x[k] e^{-j\frac{2\pi}{N}nk} \tag{3-8}$$

is

$$x[n] = \frac{1}{N} \sum_{n=0}^{N-1} X[n] e^{j\frac{2\pi}{N}nk} \tag{3-9}$$

The time taken to evaluate a DFT on a digital computer depends principally on the number of multiplications involved. This number is directly related to N^2, where N is the length of the transform. The Fast Fourier Transform (FFT) is an efficient algorithm for calculating the Discrete Fourier Transform. At each stage of the FFT, $\frac{N}{2}$ complex multiplications are required to combine the results of the previous stage. Since there are $\log_2 N$ stages, the number of complex multiplications required to evaluate an N-point DFT with the FFT is approximately $\frac{N}{\log_2 N}$.

3.6 Frequency-time Domain Analysis

3.6.1 Wavelets and Wavelet Transforms

The wavelet transform is a technique that is used to analyse a signal simultaneously in the time and frequency domains. It is very useful in analysing non-stationary, non-periodic, intermittent, and transient signals. Wavelets are waves with a short duration, with finite energy and a quick decay in time. The wavelets have an oscillating feature, which comes along with the location in time and frequency. Orthogonal wavelet functions have a companion function known as a scaling function. The scaling function is used to generate basis functions, which are used during the decomposition and reconstruction of a signal. Figure 3-1 shows the Daubechies scaling function and mother wavelet function.

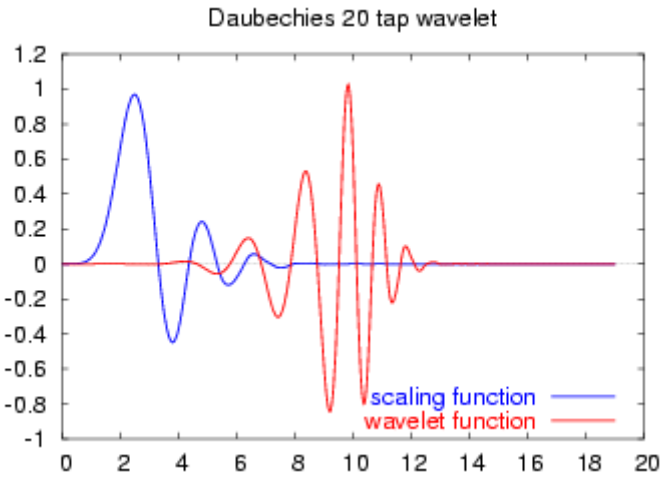

Figure 3-1 The Daubechies wavelet [121]

i. Continuous wavelet function

The wavelet transform of a continuous signal $x(t)$ with respect the wavelet function $\psi(t)$ is defined as

$$T(a,b) = w(a) \int_{-\infty}^{\infty} x(t) \psi^* \left(\frac{t-b}{a} \right) dt \tag{3-10}$$

where $w(a)$ is the weighting function, a and b are the dilation and translation parameters, respectively. The asterisk denotes that the complex conjugate of the wavelet function is used in the transformation. The wavelet transform is a correlation of a signal with a set of wavelets of various widths. $w(a)$ in equation (3-10) can be set to $\frac{1}{\sqrt{a}}$ to ensure that the wavelets at each scale have identical energy. The resulting equation is as shown in equation (3-11).

$$T(a,b) = \frac{1}{\sqrt{a}} \int_{-\infty}^{\infty} x(t)\psi^*\left(\frac{t-b}{a}\right) dt \tag{3-11}$$

Equation (3-11) can be rewritten as equation (3-12) below.

$$T(a,b) = \int_{-\infty}^{\infty} x(t){\psi_{a,b}}^*(t)dt \tag{3-12}$$

Dilation and contraction of the mother wavelet is governed by the dilation parameter a which is the distance between the centre of the wavelet and its crossing on the time axis. The shifting of the wavelet along the time axis is governed by the translation parameter b. Stretching and squeezing of the Mexican hat wavelet is demonstrated in Figure 3-2 below.

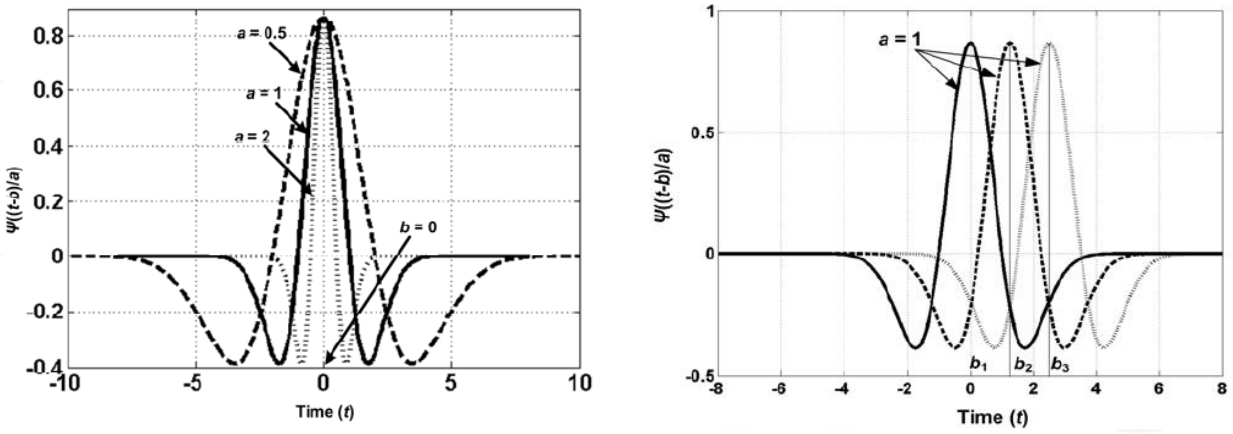

(a) A novel approach for broken-rotor-bar detection in cage induction motors

(b) Translation ($\boldsymbol{b_1}$via $\boldsymbol{b_2}$ to $\boldsymbol{b_3}$) of the Mexican Hat wavelet function

Figure 3-2 [122]

ii. ***Discrete wavelet transform***

The mother wavelet can be dilated and translated discretely by replacing a with ${a_0}^m$ and b with $nb_0{a_0}^m$, where a_0 and b_0 are fixed constants, $a_0 > 1$, $b_0 > 0$, and $m, n \in \mathbb{N}$. The discrete mother wavelet function can hence be defined as

$$\psi_{m,n}(t) = {a_0}^{-m/2}\psi\left(\frac{t - nb_0{a_0}^m}{{a_0}^m}\right) \tag{3-13}$$

And the corresponding discrete wavelet transform (DWT) can be defined as

$$T(m,n) = \int_{-\infty}^{\infty} x(t){\psi_{m,n}}^*(t)dt \tag{3-14}$$

The DWT process begins by passing the discrete signal $x[n]$ through a low pass filter with an impulse response $g[n]$ and a high pass filter with the impulse response $h[n]$. The low pass and high pass filters are scaling and wavelet filters respectively. The low pass filter returns the approximation coefficients of the discrete signal at first level of resolution of the DWT while the high pass filter returns the detail coefficients of the discrete signal at first level resolution of the DWT. The output of these filters are N wavelet coefficients. Thus, the first level of decomposition of the discrete signal can be mathematically expressed as

$$a^p[n] = \sum_{k=0}^{N-1} g[k]x[n-k] \tag{3-15}$$

The decomposition of the discrete signal can be mathematically expressed as

$$d^p[n] = \sum_{k=0}^{N-1} h[k]x[n-k] \tag{3-16}$$

where p is the level of the decomposition. The next level of decomposition uses the approximation coefficients from the previous level as the inputs to the wavelet filters $g[k]$ and $h[k]$. The approximation and detail coefficients generated at a particular level are half the number of those in the previous level. The process is illustrated in Figure 3-3(a).

iii. ***Wavelet Packet Transform***

Wavelet packets can be formed by linear combinations of usual wavelet functions. Similar to wavelet functions, they also possess properties like orthonormality, and time-frequency localization from their corresponding wavelet functions. A wavelet function however also possesses a modulation or oscillation parameter, in addition to the scaling and translation parameters. The wavelet function can be defined as

$$W_{j,k}{}^n(t) = 2^{j/2} W^n(2^j t - k) \tag{3-17}$$

where j is the scaling parameter, k is the translation parameter, and n is the modulation parameter.
The first two wavelet functions are the corresponding scaling function and mother wavelet function, which can be defined by

$$W_{0,0}{}^0(t) = \varphi(t) \tag{3-18}$$

$$W_{0,0}{}^1(t) = \psi(t) \tag{3-19}$$

The wavelet packet functions of the corresponding levels can be computed as

$$W_{0,0}{}^{2n}(t) = \sqrt{2}\sum_k g(k) W_{1,k}{}^n(2t-k) \tag{3-20}$$

$$W_{0,0}{}^{2n-1}(t) = \sqrt{2}\sum_k h(k) W_{1,k}{}^n(2t-k) \tag{3-21}$$

where $g[k]$ and $h[k]$ are quadrature mirror filter associated with the predefined scaling and mother wavelet functions. The inner product of the signal and the particular basis function returns the specific time-frequency information of a signal.

Wavelet Packet Decomposition involves applying both high pass and low pass filters to a discrete signal and then recursively to each intermediate signal. The procedure is illustrated in Figure 3-3 below.

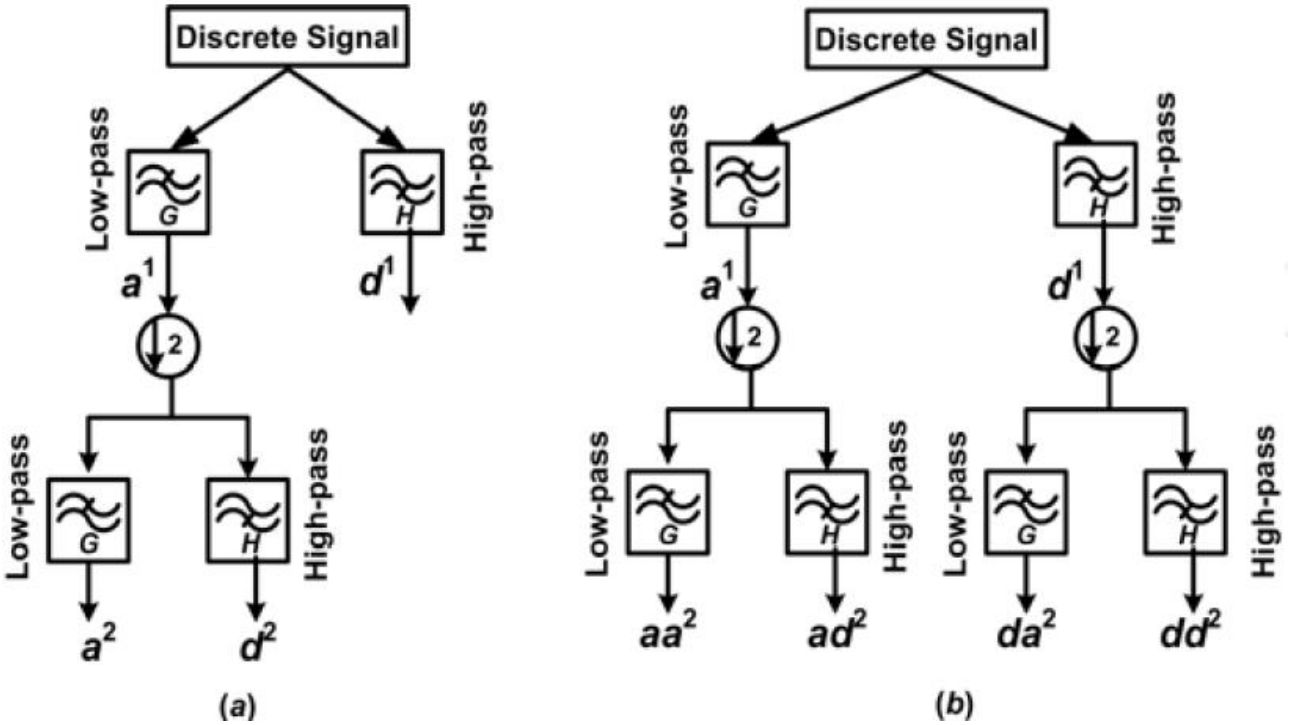

Figure 3-3 (a) Two-level Discrete Wavelet Transform of a discrete signal and (b) The two-level Wavelet Packet Transform of a discrete signal [122]

The first level of decomposition of the signal $x[n]$ of length N generates two frequency sub-bands, which are the approximation coefficients ${a_n}^1 = [{a_0}^1, {a_1}^1, {a_2}^1, \dots, {a_{N-1}}^1]$ and the detail coefficients ${d_n}^1 = [{d_0}^1, {d_1}^1, {d_2}^1, \dots, {d_{N-1}}^1]$. These are defined as

$$aa^2[n] = \sum_{k=0}^{N/2-1} g[k]a^1[2n-k] \tag{3-22}$$

$$ad^2[n] = \sum_{k=0}^{N/2-1} h[k]a^1[2n-k] \tag{3-23}$$

$$da^2[n] = \sum_{k=0}^{N/2-1} g[k]d^1[2n-k] \tag{3-24}$$

$$dd^2[n] = \sum_{k=0}^{N/2-1} h[k]d^1[2n-k] \tag{3-25}$$

where aa^2 is the second level low frequency approximation of the original signal is, ad^2 is the second level low frequency low frequency details of the original signal, da^2 is the second level high frequency approximation of the original signal, and dd^2 is the second level high frequency detail of the original signal.

3.7 Hilbert Transform

The Hilbert transform is a signal analysis method that can be used to emphasize the local properties of a signal. It is defined as a convolution with the function $1/t$, as follows [123]:

$$HT\big(x(t)\big) = y(t) = \frac{1}{\pi t} \times x(t) = \frac{1}{\pi} \int_{-\infty}^{+\infty} \frac{x(\tau)}{t-\tau} d\tau \tag{3-26}$$

The analytical signal $\vec{x}(t)$ of the signal $x(t)$ is defined by coupling $x(t)$ and its Hilbert transform.

$$\vec{x}(t) = x(t) + jy(t) = a(t)e^{j\theta(t)} \tag{3-27}$$

where

$$a(t) = [x^2(t) + y^2(t)]^{1/2}, and\ \theta(t) = \tan^{-1}\left(\frac{x(t)}{y(t)}\right) \tag{3-28}$$

where $a(t)$ is the instantaneous amplitude of $\vec{x}(t)$ and is a reflection on how the energy of $x(t)$ varies with time, and $\theta(t)$ is the instantaneous phase of $\vec{x}(t)$.

Three important properties of the Hilbert transform and the analytic signal are: [80]

1. The Hilbert transform of a trigonometric function is the trigonometric function with a 90° phase shift: sines are transformed to cosines and cosines are transformed to sines. The spectrum of the Hilbert transform of a signal has the same amplitude and frequency content as the original signal, but the phase of the frequency components is shifted by 90°.
2. The analytic signal $\vec{x}(t)$ has a one-sided Fourier transform. It retains the positive frequency content of the original signal and the negative frequencies are annulated. It also doubles the dc component.
3. The low frequencies of the original signal are in the amplitude $a(t)$, and the high frequencies are in the phase $\theta(t)$ of the analytic signal.

3.7.1 Analytic signal of the Current in a Healthy Machine

The phase current $i(t)$ in an ideal healthy machine is

$$i(t) = I_m \cos(\omega t) = I_m \cos(2\pi f t) \tag{3-29}$$

The $\cos(\omega t)$ function can be written as

$$\cos(\omega t) = \left(\frac{e^{j\omega t} + e^{-j\omega t}}{2}\right) \tag{3-30}$$

Combining (3-29) and (3-30)

$$i(t) = I_m \left(\frac{e^{j\omega t} + e^{-j\omega t}}{2}\right) = \frac{I_m}{2} e^{j\omega t} + \frac{I_m}{2} e^{-j\omega t} \tag{3-31}$$

The Fourier transform of $i(t)$ will show distinct components at the frequencies f and $-f$. The Fourier transform, when computed using the Discrete Fourier Transform uses a sequence of N values of the original function sampled at a frequency f_s that meets the Nyquist condition $f_s > 2f$. The frequencies will appear the indices $m(f)$ and $m(-f)$ respectively, which are defined as:

$$m(f) = \frac{f}{f_s}N, \qquad m(-f) = N - m(f), \tag{3-32}$$

The analytic signal $\vec{\imath}(t)$ corresponding to $i(t)$ is

$$\vec{\imath}(t) = i(t) + jHT\big(i(t)\big) = I_m(\cos(\omega t) + jsin(\omega t)) \tag{3-33}$$

The $\sin(\omega t)$ function in terms of complex exponentials is

$$\sin(\omega t) = \left(\frac{e^{j\omega t} - e^{-jwt}}{2j}\right) \tag{3-34}$$

Combining (3-30), (3-31), (3-33) and (3-34) gives

$$\vec{\imath}(t) = I_m e^{j\omega t} \tag{3-35}$$

The Discrete Fourier Transform of (3-35) will show a single spike corresponding to $f = {}^{\omega}/_{2\pi}$ and has a doubled amplitude with respect to the original signal spectrum component [95].

4. Motor Current Signature Analysis (MCSA) and Vibration Monitoring in Condition Monitoring

4.1 Introduction

This section discusses Motor Current Signature Analysis and Vibration Analysis as tools for the detection of faults in induction motors, gearboxes, and reciprocating compressors. The common faults that occur in induction motors, gearboxes and reciprocating compressors, as well as, their associated fault frequencies for the current and vibration spectrum are also deliberated.

4.2 Motor Current Signature Analysis (MCSA)

Motor Current Signature Analysis is the most popular method of fault detection and condition monitoring in induction machines [41], [67]. MCSA can be used a predictive maintenance tool, preventing catastrophic failure, production outages, and extending motor lifetime. It is a very potent tool and can be used in parallel with other techniques such as vibration and thermal monitoring to detect faults in the motor [46].

MCSA involves monitoring of the stator (supply) current. Usually a single phase is monitored. The current is measured using a current sensor and recorded in the time domain. The captured signal data is then fed into an MCSA instrument such as a spectrum analyser for analysis. The MCSA then processes the signal using any of the techniques discussed in Chapter 3.

An ideal motor current is pure sine wave. However, in the practical world, there are harmonics present in the signal. Faults that are present in the motor will further modulate the current signal leading to additional sideband harmonics [124]. Particular faults lead to particular current signatures such as the alteration in the current spectrum of the motor with the broken rotor bar shown in Figure 4-1 below. These can be used to determine the fault and its severity [65].

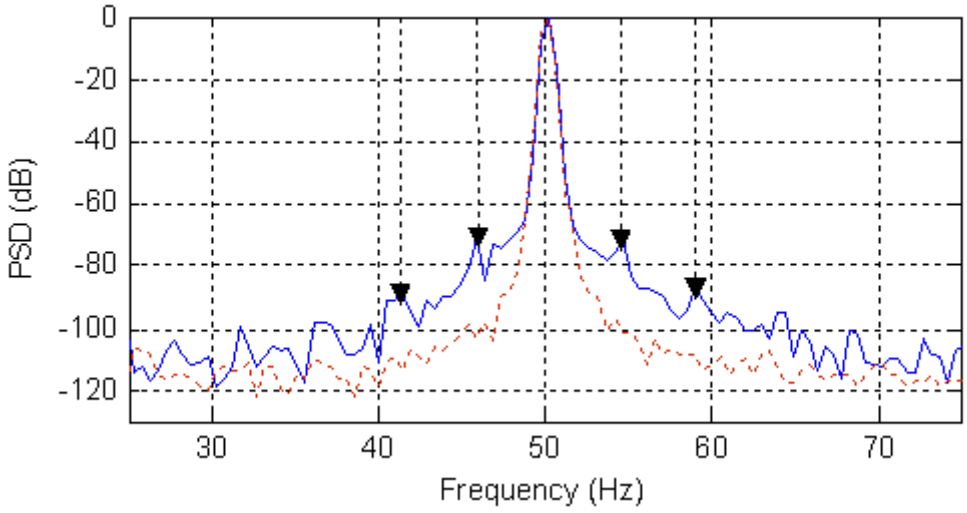

Figure 4-1 Current spectrum showing experimental healthy (---) and faulty (two broken rotor bars) stator current spectrum around fundamental [125]

4.3 Vibration Monitoring

Vibration is the motion of a machine or a part of machine back and forth from its position of rest. Rotating machines exhibit characteristic vibration signatures that are unique to them and these can be measured to obtain information regarding the machine's condition and any mechanical faults. Vibration monitoring entails routine collection of vibration data on the specified machine with the intent to capture relevant vibration frequencies and amplitudes. These are used to establish a trend for each machine over an extended period. Baseline measurements can be obtained for the motor whilst in a healthy state. Alarm limits can be defined at critical frequency ranges to indicate the possibility of a fault in the machine. Presumably there will be enough "lead time" after the alarm, before failure of the machine, which allows for proactive measures to be taken to prevent damage to the machine. This is illustrated in Figure 4-2 below.

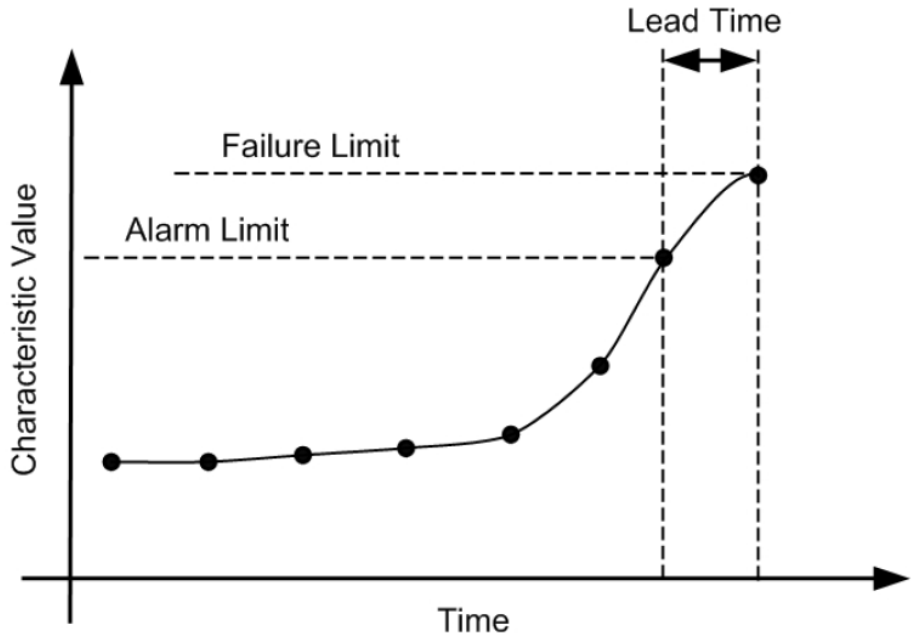

Figure 4-2 The Trending of Measured Characteristic [27]

Theoretically, it is possible to use the slope of the graph to estimate and predict the actual time in hours or weeks before failure, hence preventing an emergency breakdown and allowing production to be adjusted in an organised manner [27].

Vibrations in induction motor drives can be classified into two parts: benign vibration and serious vibration.

i. Benign vibration

These are characteristic of regular operation of the machine in normal conditions. The amplitudes of the vibrations are specific to the machine that is being monitored. Examples of benign vibrations include:

- 120 Hz hum (60 Hz operating frequency) and 100 Hz hum (50 Hz operating frequency).
- Blade passing frequency.
- Broadband turbulence from fluid handling machines e.g. fans and pumps.
- Gear mesh frequencies.
- Pure tones from motors especially those driven by Variable Frequency Drives.

ii. Serious vibration

These are vibrations that lead to accelerated wear and tear of the machine, and/or premature failure. It is imperative that corrective action is taken to reduce or eliminate these vibrations to increase the life span of the machine. Examples of serious vibration include:

- 1X amplitudes above the balance limits.
- Shock pulses.
- Large shaking motion.
- Abnormal noise.

Serious vibrations can also be classified into two types: forced and natural vibrations (resonance). Forced vibrations are caused by faulty or wrong machine parts, imbalance in the drive, and misalignment. Natural vibrations are caused by the structural nature of the drive and its parts.

4.3.2 Vibration in Induction Motors

Vibrations in electrical machinery are caused by mechanical faults such as misalignment, unbalance, and mechanical looseness. Common causes of vibration due to electro-magnetic problems include:

- Rotor not round.
- Eccentric armature journals.
- Rotor and stator misalignment.
- Elliptical stator bore.
- Open or shorted windings.
- Shorted rotor iron.

The vibration frequency from electrical problems is 1X RPM. One can check for vibration resulting from electrical vibration by observing the change in amplitude the instant that the electric motor is disconnected from the machine.
Vibration due to electromagnetic faults is generally associated with the amount of load placed on the motor. As the load changes, the amplitude and frequency readings can show a significant change.

Rotor or armature faults such as broken rotor bars, open or shorted rotor windings, bowed rotor, and eccentric rotor have been known to cause electrical vibration. The pulsating vibration amplitude characteristic of these faults produces a single vibration frequency with an amplitude modulated with time. The vibration is generated from a broken rotor bar fault as illustrated in Figure 4-3 below.

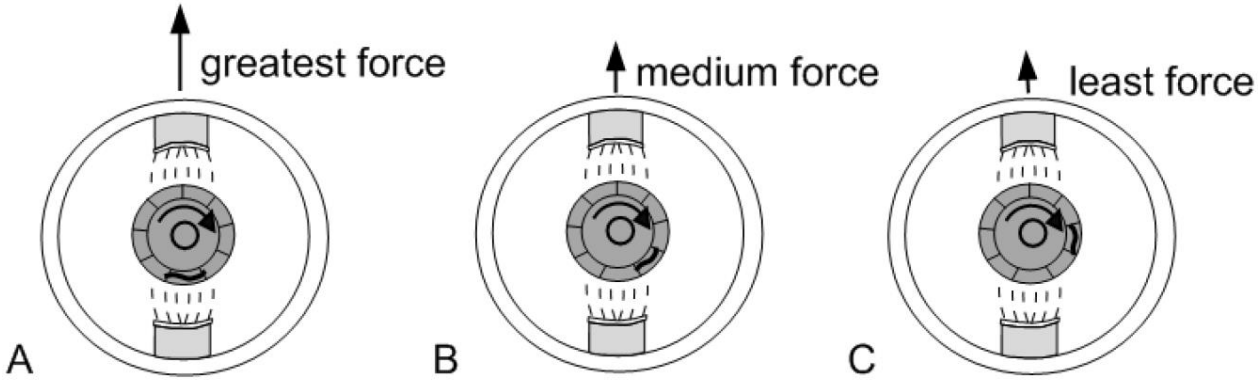

Figure 4-3 Vibration generated by an induction motor with a broken rotor bar

Figure 4-3 shows a two-pole motor with a broken rotor bar. During operation, the broken rotor bar will align with the lower pole when the pole is energised by peak current as shown in Figure 4-3(A). The

polarities of the poles are equal and opposite. However, because of the rotor bars is broken, the magnetic forces between the motor poles and the armature will have a resultant force. When the AC current peaks again in the next revolution (*see Figure 4-3(B)*), the broken rotor bar will not align with the poles like it did initially in Figure 4-3(A), and it will lag by a $^1/_{50}$ of a revolution since the motor armature rotates at a frequency less than that of the stator current. During the next revolution (*see Figure 4-3(C)*), the rotor bar will lag even further with the resultant magnetic force on the rotor dropping even further. This causes a single frequency vibration whose amplitude is modulated at a rate equal to the slip frequency.

Stator related problems can also result in vibration with a pulsating amplitude. The pulsation is the result of a beat between two separate frequencies that are close to one another. This can be observed in the time domain as a steady pulsation in the waveform, or from the frequency domain.

4.4 Fault Signatures in Induction Motors

The following section discusses the faults in induction motors and their corresponding fault frequencies in the current and vibration spectra.

4.4.1 Eccentricity

Eccentricity in induction machines is caused by formation of an unequal airgap between the stator and the rotor. Static eccentricity occurs when the rotor or stator of the motor is incorrectly positioned; the axis of rotation of the motor does not change. Dynamic eccentricity occurs when the axis of rotation of the rotor changes and is caused by bent shafts, unbalance, and cracked rotor bars. As the rotor moves towards and away from the stator magnetic fields, the stator current is altered. The different types of air-gap eccentricity are illustrated in Figure 4-4 below.

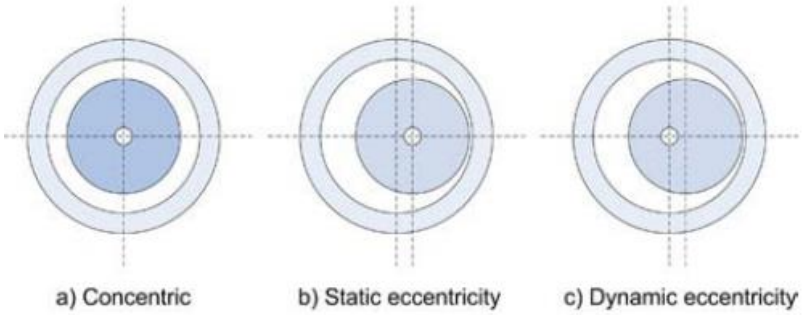

Figure 4-4 Air-gap eccentricity in induction motors [124]

The presence of static or dynamic eccentricity using MCSA can be detected using

$$f_{ecc} = f\left[(kR \pm n_d)\frac{(1-s)}{p} \pm v\right] \tag{4-1}$$

where the eccentricity order $n_d = 0$ in the case of static eccentricity, and $n_d = 1,2,3,\ldots$ in case of dynamic eccentricity, f is the fundamental supply frequency, R is the number of rotor slots, s is the slip, p is the number of pole pairs, k is any integer, and v is the order of the stator time harmonics present in the power supply driving the motor ($v = \pm 1, \pm 3, \pm 5, \ldots$). However, only a particular combination of machine pole pairs and rotor slot number cause a significant rise in only the static or only the dynamic eccentricity-related components. The relationship for a 3-phase integral slot 60° phase belt machine is given by

$$R = 2p[3(m \pm q) \pm r] \pm k \quad (4\text{-}2)$$

where $(m \pm q) = 0,1,2,3, \ldots$ and $r = 0\ or\ 1$, $k = 1\ or\ 2$.

Mixed eccentricity is a combination of both static and dynamic eccentricity and can be detected using

$$f_{ecc} = 2f \pm f_r \quad (4\text{-}3)$$

Machines generating principal slot harmonics (PSHs) will not give rise to the components in equation (4-1). [24]

In the vibration spectrum, stator eccentricity causes an increase in the 1X, 2X rotational frequencies, and twice the line frequency $(2 \cdot f_L)$. Stator eccentricity is caused by loose iron, shorted stator laminations or soft foot. The vibration spectrum of a motor with stator eccentricity is shown in Figure 4-5 below.

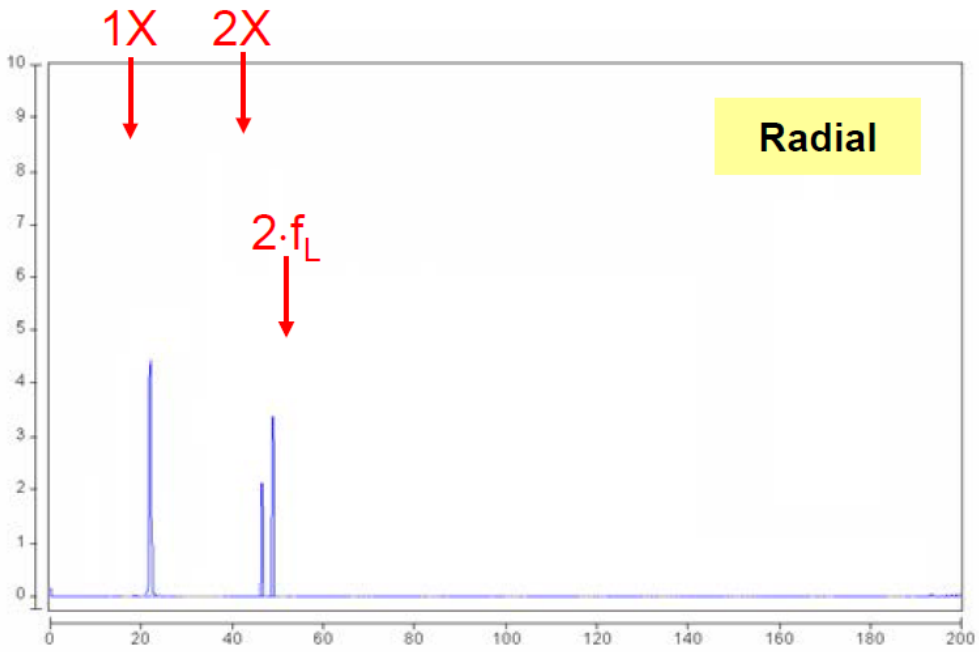

Figure 4-5 Vibration frequencies for a motor with stator eccentricity [107]

Rotor eccentricity causes an increase in the vibration amplitude at the slip frequency, f_p the 1X rotational frequency, and at twice the line frequency, $(2 \cdot f_L)$. Rotor eccentricity can be a result of rotor offset, misalignment and poor base for the motor. The vibration spectrum of a motor with rotor eccentricity is shown in Figure 4-6 below.

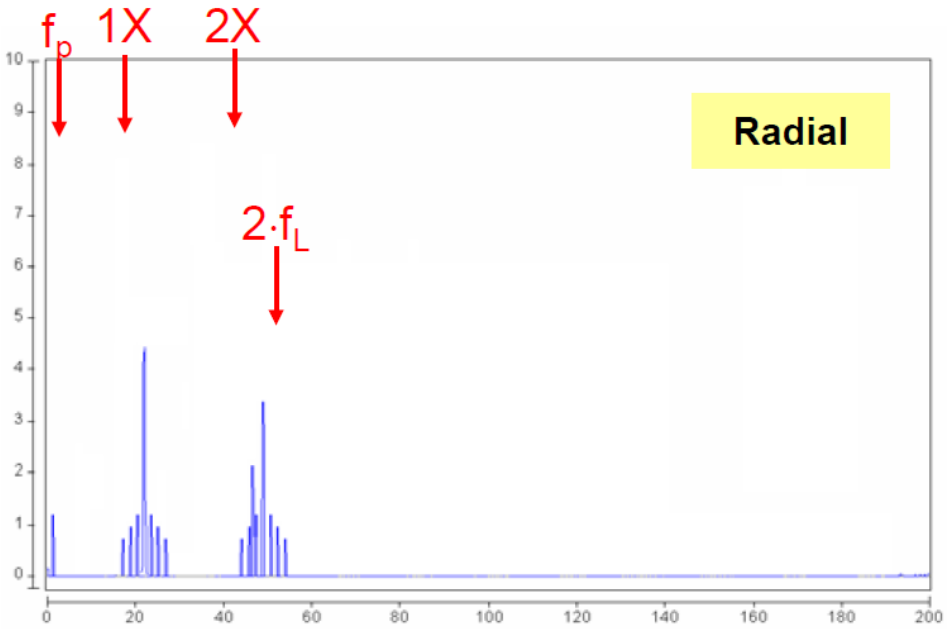

Figure 4-6 Vibration frequencies for a motor with rotor eccentricity [107]

4.4.2 Broken rotor bars

They are usually caused by the strain on the motor during start-up that leads to currents that can be up to five times the rated current of the motor [124]. In a healthy induction motor, the electromagnetic and mechanical forces in the machine are symmetrically distributed. A broken rotor bar results in a reverse rotating magnetic field at pole frequency. The frequency component is in a negative sequence and is reflected on the stator side and produces the frequency component $(1 - 2sf)$. This consequently results in a torque ripple and a speed ripple at $2sf$ which modulates the rotating magnetic flux [45] which causes the left and right side components of the fundamental at $(1 - 2sf)$ and $(1 + 2sf)$ respectively. This in turn leads to series of fault components in the stator current which can be found at the frequencies in equation (4-4) below [75], [76], [127], [128].

$$(1 \pm 2ks)f \tag{4-4}$$

where f is supply frequency, s is the slip, and $k = 1,2,3, \ldots$

Broken rotor bars in induction motors also generate a pulsing vibration causing a significant rise in the vibration amplitude of the 1X and 2X rotational frequencies, and/or higher harmonics. A significant increase in the 2X frequency amplitude indicates a growth of a transverse crack is getting critical. Changes in the 1X or higher harmonic frequencies may also occur. The changes in the amplitude of the 1X frequency and its harmonics is due to the asymmetry that results from the broken rotor bar. The vibration spectrum of the induction motor with the broken rotor bar is shown in Figure 4-7 below.

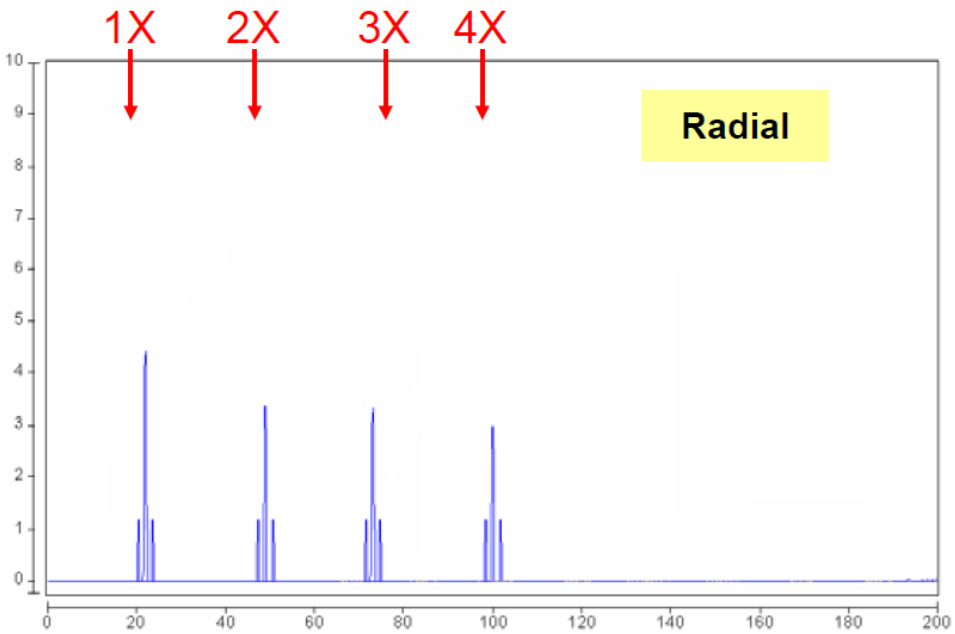

Figure 4-7 Vibration frequency spectrum of broken rotor bar [107]

4.4.3 Stator inter-turn faults

Most stator failures have been linked to stator windings [124]. Shorted turns produce excessive heat and cause current imbalance in the stator coils [126]. Rotating flux waves induce components in the stator current and these components can be identified using MCSA at the frequencies, f_{stator}, in equation (4-5) below.

$$f_{stator} = f_s\left(\frac{n}{p}(1-s) \pm k\right) \tag{4-5}$$

where f_s is the supply frequency, $n = 1,2,3, \ldots$

Inter-turn stator faults result in a vibration spectrum similar to that in Figure 4-5 with an increase in magnitude of the 1X and 2X rotational frequencies, and the 2X line frequency.

4.4.4 Bearing faults

Bearing faults are usually a result of physical damage to the bearings in the form of brinelling or false brinelling of the race ways, and can lead to premature failure. Misalignment of the bearings as shown in Figure 4-8 below may also result from flawed bearing installation.

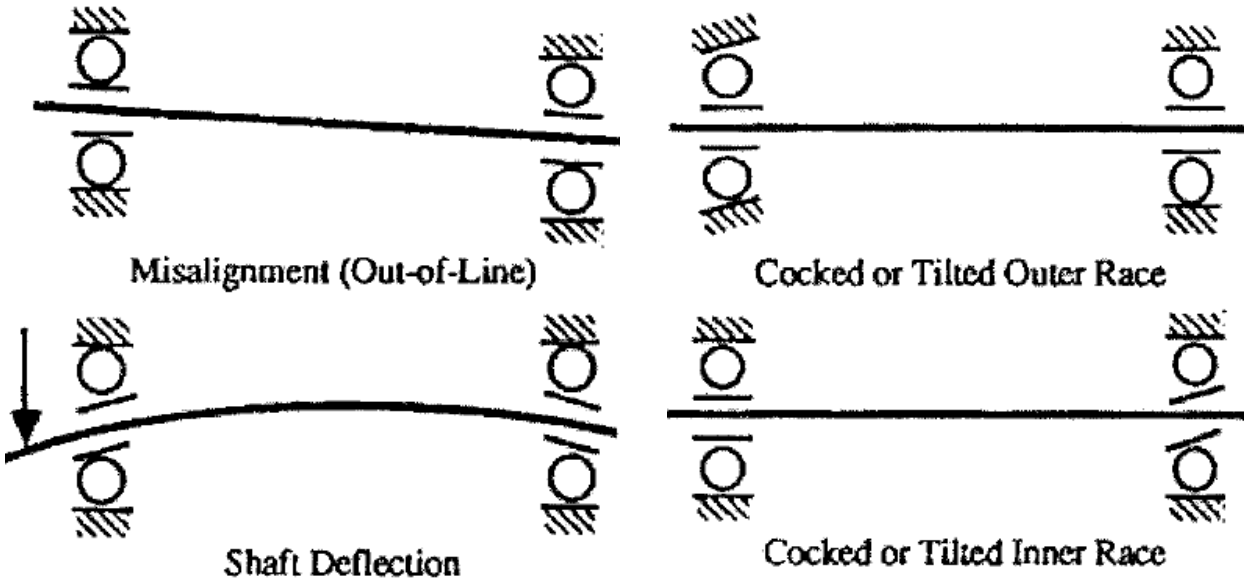

Figure 4-8 Four types of rolling-element bearing misalignment [41]

The ball bearings support the rotor and thus faulty bearings affect the eccentricity of the air-gap which may result in one or more of the frequencies described in 4.4.1. There is no perfect bearing and therefore all rolling element bearings will have defects such as irregularities in the surface of the race, and the roundness of the balls. These faults create periodic frequencies called fundamental defect frequencies, namely:

- Fundamental Train Frequency (FTF): This is the rotational speed of the bearing cage and ball/roller assembly.
- Ball Pass Frequency of the Inner Race (BPFI): This is the frequency created as the balls roll across a fault in the inner race.
- Ball Pass Frequency of the Outer Race (BPFO): This is the frequency created as all the balls roll across a fault in the outer race.
- Ball/Roller Spin Frequency (BSF): This is the circular frequency of each ball/roller as it spins during revolution around the shaft. For a roller bearing, $2 \cdot BSF$ is a more appropriate parameter.

The BPFI and BPFO vibration frequencies, f_i and f_o can be obtained from [26], [129]

$$f_{i,o} = \frac{n}{2} f_r \left[1 \pm \frac{bd}{pd} \cos\beta\right] \tag{4-6}$$

where n is the number of bearing balls, f_r is the mechanical rotor speed in hertz, bd is the ball diameter, pd is the bearing pitch diameter, and β is the contact angle of the balls on the races.
The BPFI and BPFO frequencies can also be estimated using Equations (4-7) and (4-8) below [41] .

$$f_i = 0.6 \cdot n \cdot f_r \tag{4-7}$$
$$f_o = 0.4 \cdot n \cdot f_r \tag{4-8}$$

And the bearing fault frequencies in the current spectrum are located at [129]

$$f_{bearing} = f_s \pm n_b f_{i,o} \tag{4-9}$$

where $f_{bearing}$ is the fault frequency, f_s is the supply frequency, n_b is the number of bearings, and f_i and f_o are the BPFI and BPFO frequencies respectively.

Figure 4-9 below shows the ball bearing dimensions used in the calculation of the bearing fault frequencies of the current and vibration spectra.

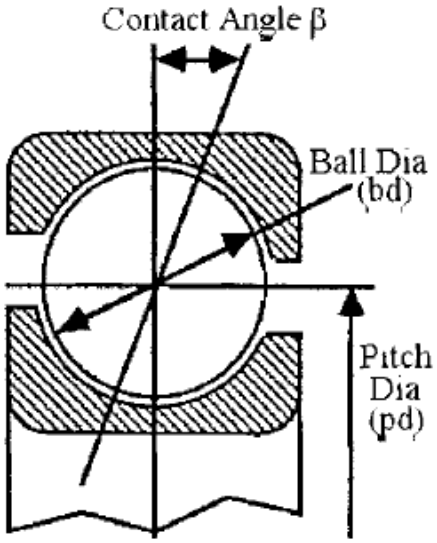

Figure 4-9 Ball bearing dimensions [41]

4.5 Fault Signatures in Gearboxes and Reciprocating Compressors

4.5.1 Gears

There are three fundamental vibration frequencies for fault detection in gears namely:

$$Gear\ rotational\ frequency, f_{rg} = {R_g}/{f_s}\ [Hz] \tag{4-10}$$

$$Pinion\ rotational\ frequency, f_{rp} = {R_p}/{f_s}\ [Hz] \tag{4-11}$$

$$Tooth\ mesh\ frequency, f_m = f_{rp} \cdot N_p\ [Hz] = f_{rg} \cdot N_g\ [Hz] \tag{4-12}$$

where R_g is the gear speed [rpm], f_s is the supply frequency [Hz], R_p is the pinion speed [rpm], N_p is the number of teeth on the pinion, and N_g is the number of teeth on the gear.

A discrete gear tooth irregularity such as a chipped tooth or a broken tooth leads to high noise and vibration levels at the shaft rotational frequency of the faulty component and the associated harmonics. These narrowband peaks are in addition to the various gear meshing frequencies and their harmonics. This is illustrated in Figure 4-10 below.

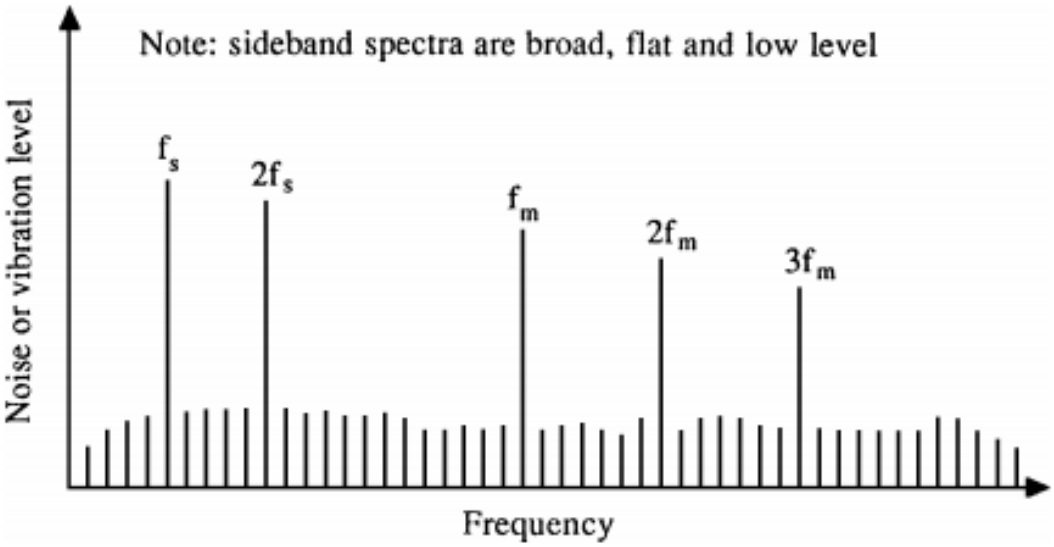

Figure 4-10 Fault frequencies of a discrete gear tooth irregularity [130]

Discrete faults also tend to produce low-level flat sideband spectra at ± the shaft rotational speed and its associated harmonics around the various gear meshing frequency harmonics [44]. A discrete fault is best detected in the time domain which will show a pronounced spike every time between impacts at $^{1}/_{Speed}$ of the gear with the broken tooth. The amplitude of the impact spike in the waveform is often much higher than that of the 1X gear rpm in the time domain as shown in Figure 4-11 below.

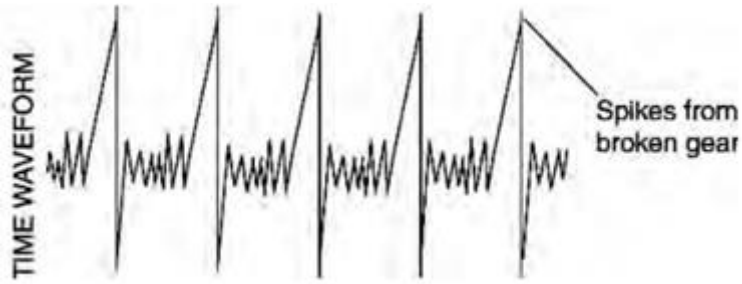

Figure 4-11 Time waveform of a gearbox with a discrete gear tooth irregularity [130]

Gear tooth wear excites the natural frequencies of the gear and the sidebands around them which hare spaced with the running speed of the bad gear. The mesh frequency may or may not change in amplitude though high amplitude sidebands surrounding the gear mesh frequency and its harmonics usually occur when wear is present. Sidebands are a better indicator of wear the gear mesh frequency itself.

4.5.2 Reciprocating Compressor

The time-varying gas pressure pulsations created between inlet and discharge valves is the main source of noise and vibration in the reciprocating compressor. The frequency spectrum of the reciprocating compressor comprises piston frequency, valve natural frequencies, and acoustical and structural resonances. The opening and closing of the suction and discharge valves can be detected using an accelerometer. There is impact from the valve at least once a cycle since it must hit the valve seat during closing.

The accelerometer is attached to the valve cover with a magnetic clamp. The patterns shown in Figure 4-12 are those of a healthy reciprocating compressor.

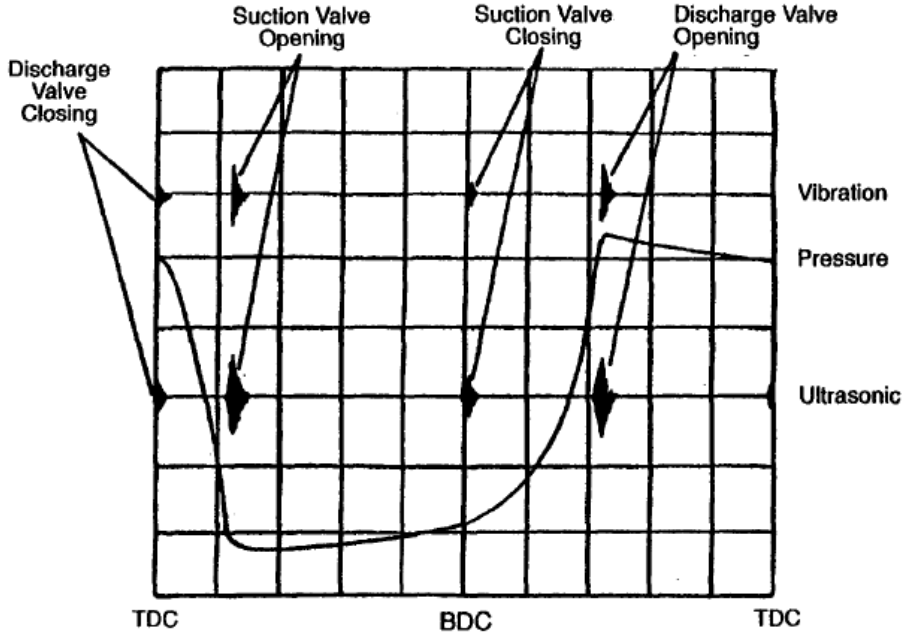

Figure 4-12 Pressure-time trace (pressure angle) with vibration and ultrasonic traces imposed of a healthy reciprocating compressor [131]

[63] analyses the compression cycle of a reciprocating compressor shown in Figure 4-13 below. The signals labelled A to G represent the different actions of the compressor. Signal A corresponds to the piston reaching the top dead center (TDC). At this point, the acceleration of the piston is maximum although the velocity is zero, and the pressure in the compressor cylinder is high. The combination of the high piston acceleration and the high-pressure results in the high acceleration spike on the top of the compressor.

After TDC, the piston moves downwards and the pressure in the compressor reduces till a point at which it is less than that of the tank, at which point the discharge valve closes causing spike B. The piston moves further down until the compressor pressure is less than the atmospheric pressure, and the inlet valve opens causing spike C. When the piston reaches Bottom Dead Center (BDC), a small mechanical impact is produced causing the spike D. The piston has maximum acceleration in the upwards direction but pressure in the compressor cylinder is relatively low, hence the amplitude of D is not as high as that of A. The piston then moves upwards increasing the pressure in the compressor until a point at which it is greater than the atmospheric pressure causing the inlet valve to close, and a corresponding spike at E. The pressure continues to build until it exceeds that of the tank causing the discharge valve to open and a corresponding spike, F. The piston then returns to TDC at spike G, and the process begins all over again.

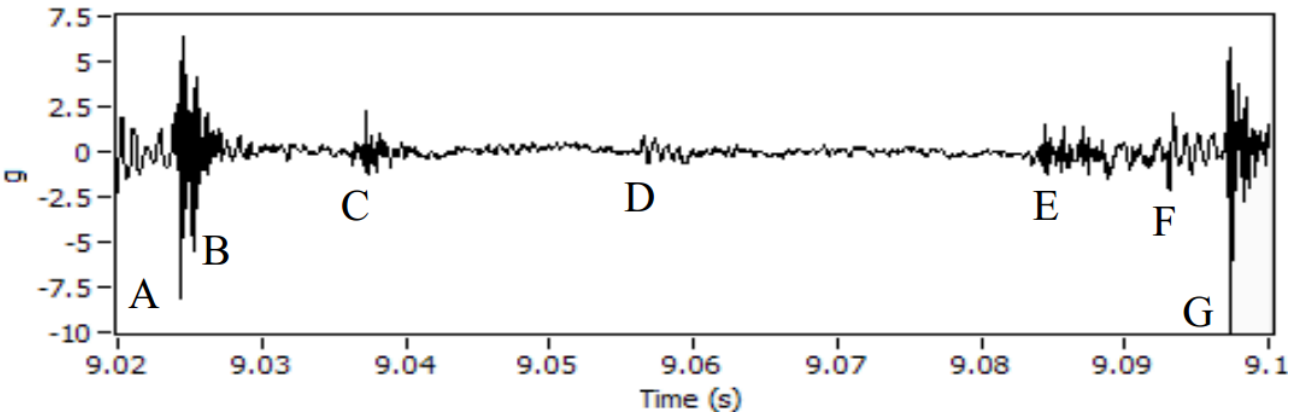

Figure 4-13 One compression cycle of a reciprocating compressor [63]

The spring tension in the valves can be detected by monitoring the vibration patterns. If the spring is too heavy, the valve is likely to close prematurely multiple times as shown in Figure 4-14 below. If the spring is too tight, a late closure of the valve is likely to occur.

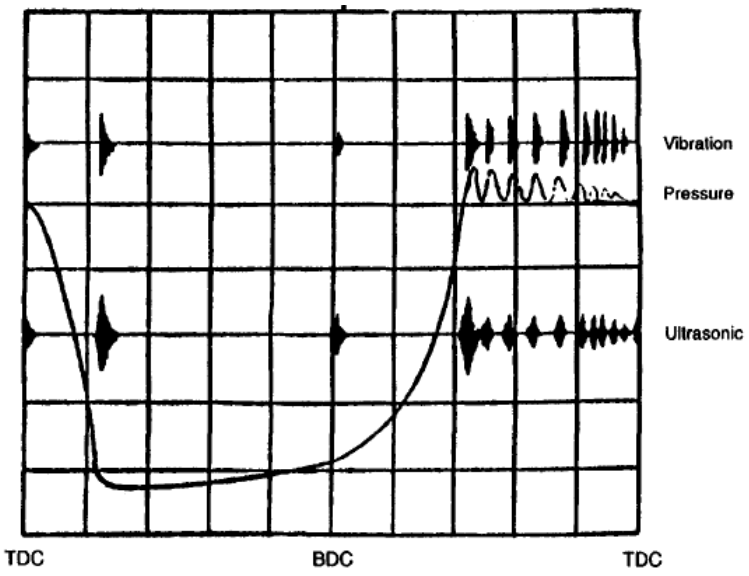

Figure 4-14 Pressure-time trace with vibration and ultrasonic traces imposed of a reciprocating compressor with springs in the discharge valve too heavy [131]

A leaking valve will generate vibrations during the time that the valve is supposed to be closed. Figure 4-15 below shows the vibration patterns for leaking suction valve and discharge valve respectively.

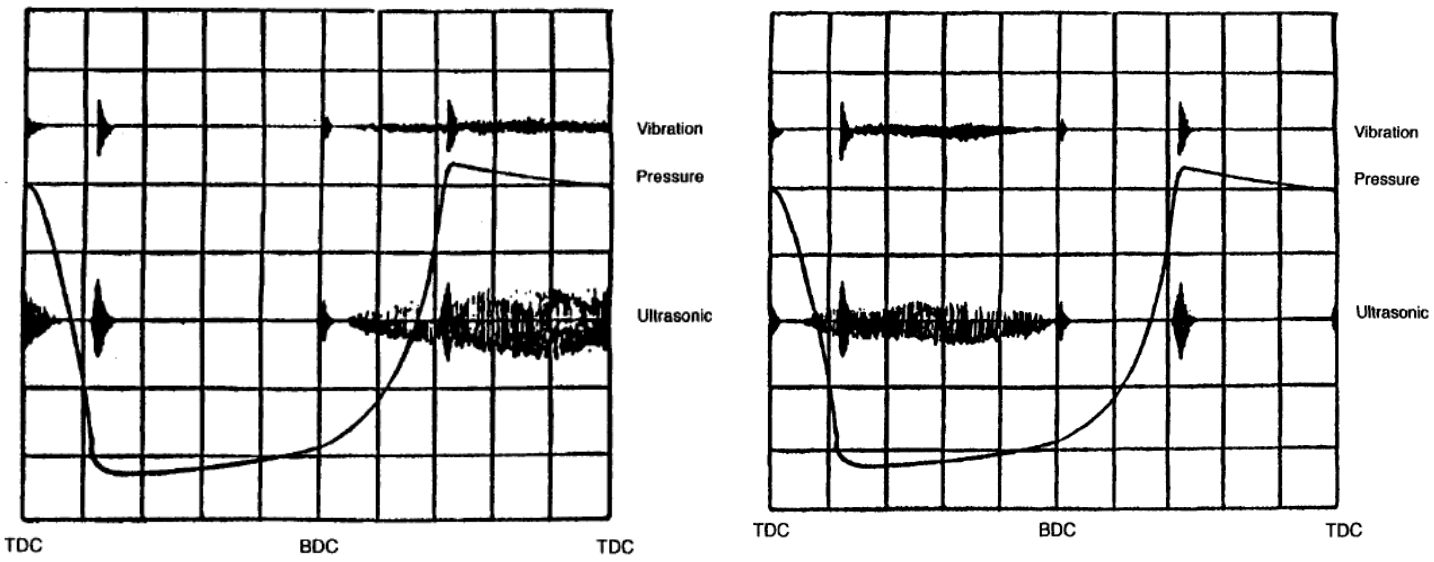

(a) (b)

Figure 4-15 Pressure-time trace with vibration and ultrasonic traces imposed of a reciprocating compressor with a (a) leaking suction valve (b) leaking discharge valve [131]

4.6 Fault Signatures of Mechanical Loads in Motor Current

Although torque oscillations are known to exist in healthy motors due to the space and time harmonics in the airgap field, the mechanical loads result in induced torque oscillations at particular frequencies that are often related to the mechanical speed of the motor and the load [132], [133]. When using the gearboxes as test loads, the sidebands of the mesh, pinion and gear frequencies across the supply frequencies are also observed and can be used to provide information about the state of the gearbox [85], [134], [135]. The frequencies that were observed in the current spectrum as indicators of the gearbox fault are presented below.

$$f_s \pm nf_m \tag{4-13}$$
$$f_s \pm nf_p \tag{4-14}$$

where f_s is the supply frequency, f_m is the mesh frequency, f_p is the pinion sideband frequency, and $n = 1,2,3,...$

Similarly, for the reciprocating compressors, the effect of the piston frequency on the air-gap can be observed in the current spectrum at the following frequencies [90].

$$f_s \pm nf_r \tag{4-15}$$

where f_s is the supply frequency and f_r is the piston frequency, and $n = 1,2,3,...$

5. Experimental Setup

5.1 Introduction

This chapter describes the equipment that was used to carry out the experiments. The MFS-MG rig and the data acquisition equipment that was added to it are detailed in the following sections.

5.2 The MFS-MG Test-rig

5.2.1 The General Setup

The Machinery Fault Simulator Magnum (MFS-MG), shown in Figure 5-1 below, is a tool used to study the signatures of common machinery faults. It has a modular design, and the components that are used are designed for high tolerances to accommodate operation without conflicting vibration. Various faults can be either individually or jointly induced in a controlled environment.

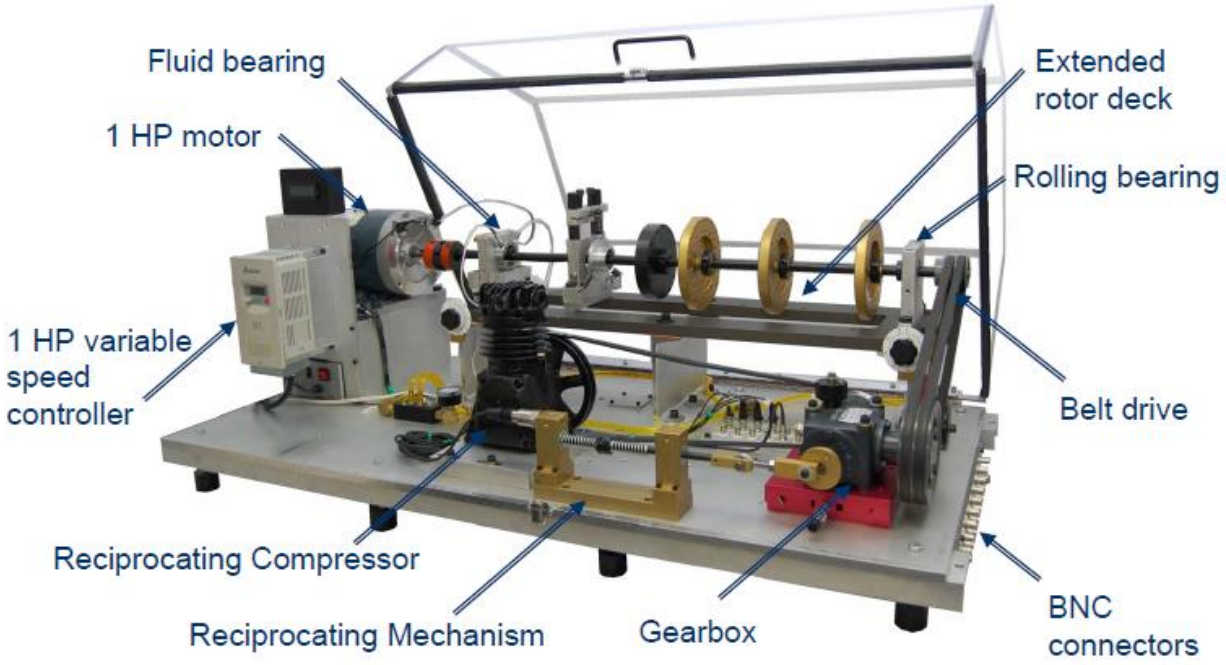

Figure 5-1 The Machinery Fault Simulator Magnum (MFS-MG) [136]

The vibration spectra of different faults can be investigated including:

- Misalignment in all three planes, both angular and parallel.
- Unbalancing in single plane and multiple planes.
- Different types of bearing faults.
- Eccentricity, rotor rubs and bent shaft.
- Mechanical looseness and soft foot.
- Belt tension and gearbox problems.
- Reciprocating mechanism vibration spectra with and without defects.

The rig also comprises six 0.75-hp motors and a healthy 1-hp motor. The faults include rotor unbalance, rotor misalignment, bowed rotor, faulted bearings, broken rotor bars, and stator winding faults and/or voltage unbalance single phasing.

The motors can be loaded with a servo motor, a healthy or faulty centrifugal pump, a healthy or faulty air compressor, a healthy or faulty gearbox loaded with a magnetic clutch mounted on its rear with an adjustable torque setting in the range 0.06 – 1.13 Nm. A magnetic base is attached to each motor and load type to mount a vibration sensor.

A schematic of the test-rig is shown in Figure 5-2 below.

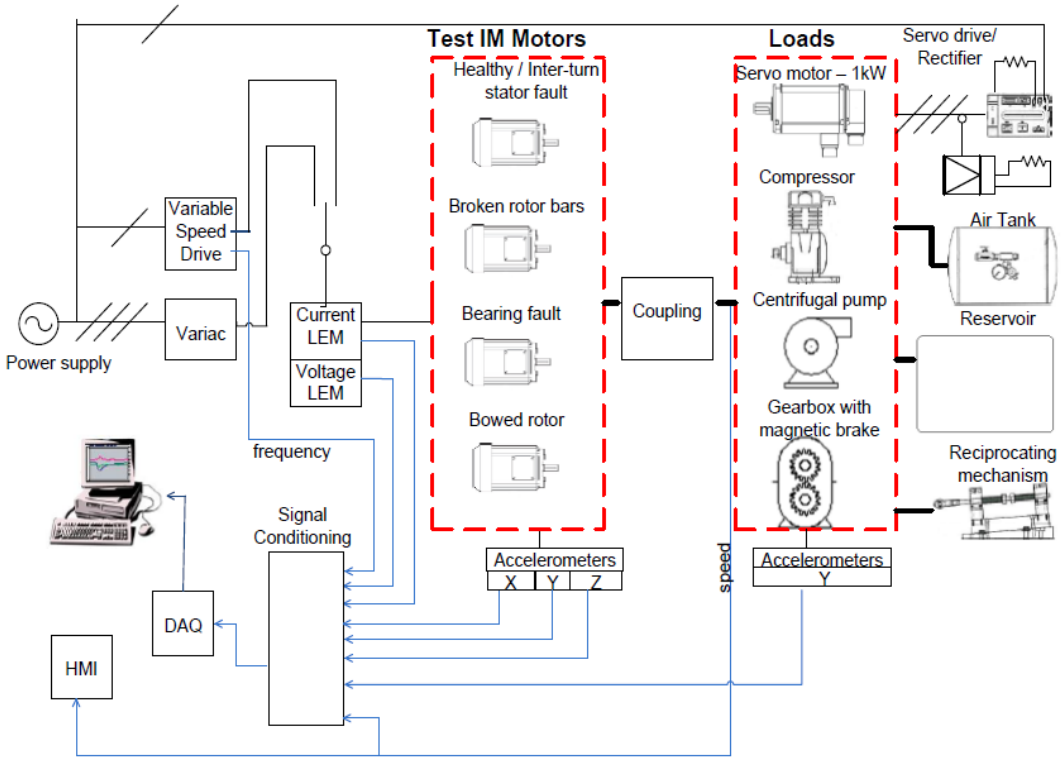

Figure 5-2 Schematic of the test rig

5.2.2 Vibration Sensor

Four general purpose ceramic shear Internal Electronic Piezoelectric (IEPE) accelerometers were used to measure the vibration on the test rig. Three of these were attached to the induction motor in the tangential, radial and axial directions. The fourth accelerometer was attached to the loads in the axial direction.

Table 5-1 The IEPE accelerometer details [137]

Performance parameter	Performance value
Sensitivity (±10%)	10.0 mV/g (1.02 mV/(m/s²))
Measurement Range	±4900 m/s² pk
Frequency Range (±5%)	0.5 to 10,000 Hz
Frequency Range (±10%)	0.3 to 15,000 Hz
Resonant Frequency	≥50 kHz
Broadband Resolution	0.005 m/s² rms

Stud mounting is ideal for measuring high frequency vibrations. However, an adhesive mounting base was added due to the curved and rough surfaces to which the accelerometers were being attached. The

adhesive base is made of hard coated aluminium to provide electrical isolation to eliminate ground loops and to reduce electrical interference that may be propagating from the surface of the test motor [138].

5.2.3 Current and Voltage Transducers

The currents and voltages fed into the motor were measured via LEM modules. The LA 25-NP was used for current measurement while the LV 25-P was used for voltage measurement. Each phase contains a voltage transducer and a current transducer which allows for the measurement of the phase current and the line-to-line voltages.

The LA 25-NP and LV 25-P both provide a good range of linear operation with a linearity error of less than 0.2%, accuracy of ±0.5%, a frequency bandwidth of 0 -150 kHz, high immunity from external interference, and current overload capability. The voltage is measured by connecting a resistor in series with the primary circuit of the transducer and measuring the current on the output of the circuit. The current measured is proportional to the voltage that is being measured. The LV 25-P has of a response time of less than 4 µs while that of the LV 25-NP is 1 µs. The LA 25-NP has a measuring range of 0 to ±36 A and thus can accommodate the high start-up currents in the test motors that can be in the order of 500 – 800% of the rated current. The measuring range of the LV 25-NP is 0 to ±400V and can accommodate the supply voltage of the motors.

The current signals from the LEM sensors are converted to voltage signals via a 200 kΩ shunt variable resistor. The signals are calibrated to output voltages within the ranges ±10V. The outputs from the transducers serve as inputs to the low pass filters. A first stage analogue low pass RC filter shown in Figure 5-3 is used to remove frequencies greater than 12 kHz. This is because the sampling frequency is set to 25.6 kHz and requires a 100 kΩ resistor and an 88 nF capacitor.

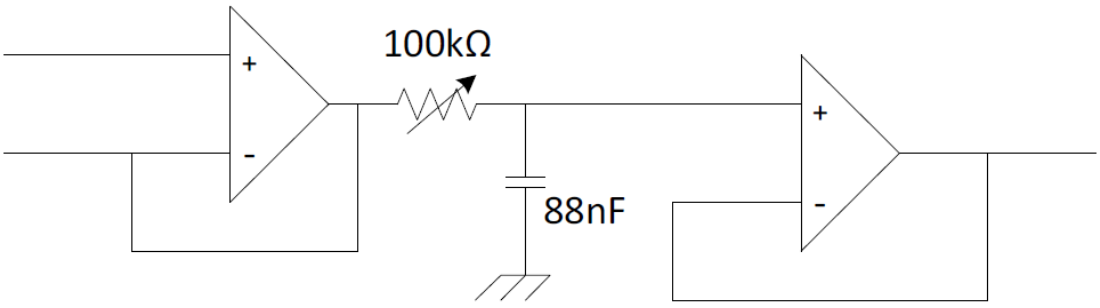

Figure 5-3 Circuit diagram of the anti-aliasing analogue RC filter [137]

5.2.4 Signal Conditioning and Data Acquisition Hardware devices

The voltage signals from the filter are fed into an NI 9215 module while those from the accelerometers are fed into an NI 9234 shown in Figure 5-4 and Figure 5-6 below.

(a) (b)

Figure 5-4 NI 9215 module [139]

The NI 9215 is a four-channel signal acquisition module with 16-bit resolution. The analog inputs have a ±10 V measurement range. The four channels can capture up to 100 kS/s per channel. The module is connected to measure floating differential signals as shown in Figure 5-5 below.

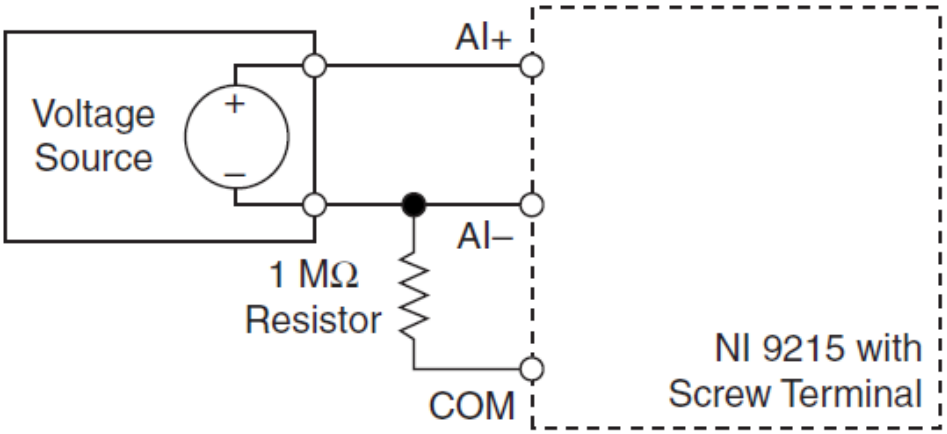

Figure 5-5 Connecting a floating differential voltage signal to the NI 9215 [140]

(a) (b)

Figure 5-6 NI 9234 module [141]

The NI 9234, shown in Figure 5-6 above, is a four-channel signal acquisition module for making measurements from IEPE sensors. The four channels can simultaneously capture signals, via BNC connectors, at rates of 2 – 50 kHz, and contains built-in anti-aliasing filters that automatically adjust to the sampling rate. Each channel contains an AI+ and AI- terminal as shown in Figure 5-6(b). The centre pin of the connector *AI+* provides DC excitation to the IEPE sensor so that the input signal is always positive, while the shell of the connector AI- provides the return path of the DC excitation and the signals' ground reference. A floating-point connection is used as shown in Figure 5-7 below.

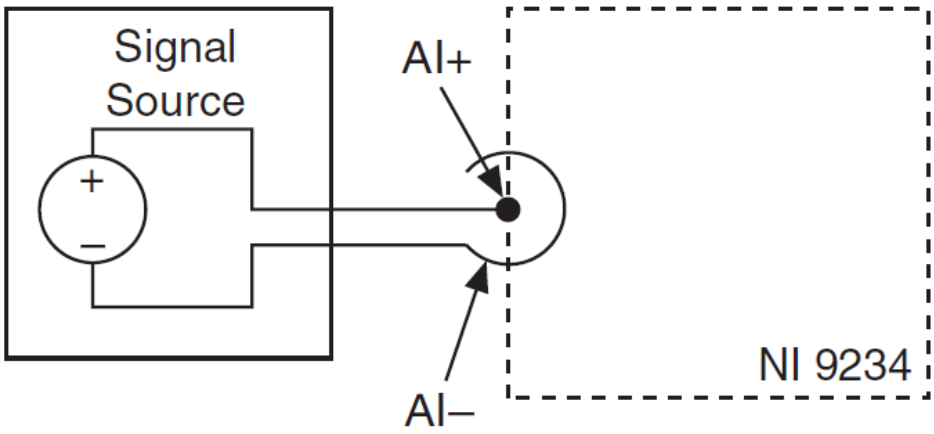

Figure 5-7 Connecting a floating signal source in NI 9234 module [142]

Both digital and analogue filtering techniques are applied in the card to ensure accurate representation of in-band signals while rejecting out-of-band signals. The pass-band of the filters is determined by the sampling rate. The frequency range of the pass-band is about $0.45 \cdot F_s$ and the ADC resolution of the module is 24 bits.

5.2.5 DAQ Hardware and Interfacing Software

The NI 9215 and NI 9234 are connected to an NI CompactDAQ-9178. The cDAQ-9178 has 8 slots and 4 counters, and can perform up to 7 tasks simultaneously. The device requires the NI-DAQmx driver to operate which allows the device to be used in a test system designed in LabVIEW, C/C++, Visual Basic, .NET, and other programming environments.

5.3 The Test Motors

The test rig comprises of 5 test motors; one of which is healthy, and seven with primary defects, namely:

Bowed Rotor

This motor has its rotor intentionally bent at the centre at 12.7 cm to 25.4 cm.

Faulted Bearings

The bearings of the motor are intentionally faulted with an inner race fault, and an outer race fault.

Broken Rotor Bars

This motor is fitted with intentionally broken rotor bars. Enough material has been removed to expose 3 rotor bars.

Stator Winding Faults

The motor has two windings, with a 4 - 5 voltage difference, which have been tapped to enable adding an additional load to the winding via an external control box. A 0 – 4 Ω variable resistor is used to introduce varying amounts of resistance in the turn-to-turn short between the windings; high resistance simulates an insulated winding while low resistance simulates a shorted winding. The motor can be used as a healthy motor when the control box is disconnected.

5.4 The Test Loads

5.4.1 The Gearbox

The test rig comprises a splash lubricated, three-way gearbox with straight cut (spur) bevel gears shown in Figure 5-8 below.

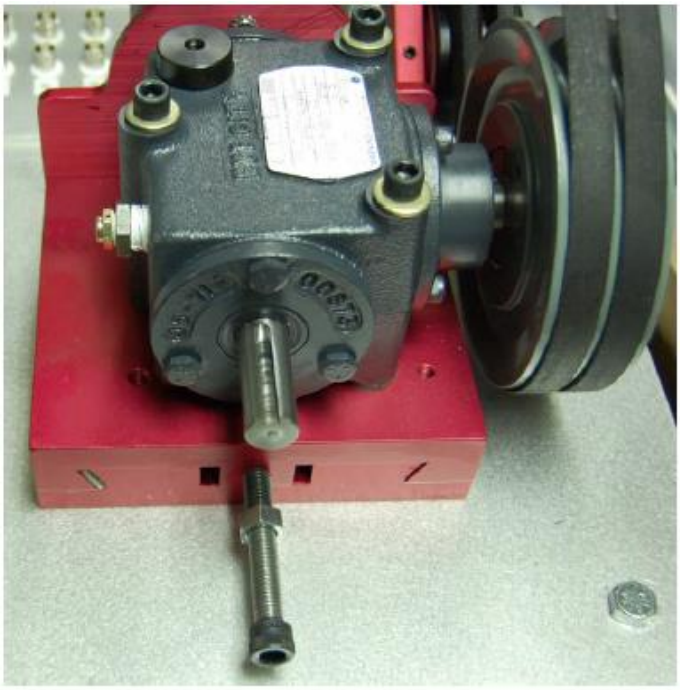

Figure 5-8 Gearbox load

The test gear box uses straight cut gearing as opposed to spiral cut gearing because the former produces distinct peaks by the gear contact while the latter offers a more gradual wiping action which can detract from optimum representation [143].

The pinion can be removed and fitted with a faulty one with a known gear defect. The MFS-MG provides two faulty pinions; one with a chipped tooth and another with a broken tooth, shown in Figure 5-9 below.

(a) Chipped tooth pinion (b) Missing tooth pinion

Figure 5-9 Faulty gearbox pinions

Table 5-2 Gearbox Data

Ratio	1.5:1
Material	Forged steel
Pitch diameter pinion	1.125”
Pitch diameter gear	1.6875”
Number of teeth pinion	18
Number of teeth gear	27

5.4.2 The Reciprocating Compressor

The MFS-MG test rig also comprises two 1-hp compressors; a healthy one and faulty one. The faulty compressor has a leaking suction valve, a blocked suction filter, limited opening discharge valve, and an oversized connecting rod. The kit also comprises a 5-gallon air tank with flow controls, all needed piping and mounting hardware. The partially blocked discharge valve and the healthy discharge are easily swapped between the two compressors as required as per the experiment. The blocked suction filter is also mounted by fitting a cap on the suction end of either compressor as shown in Figure 5-10 below.

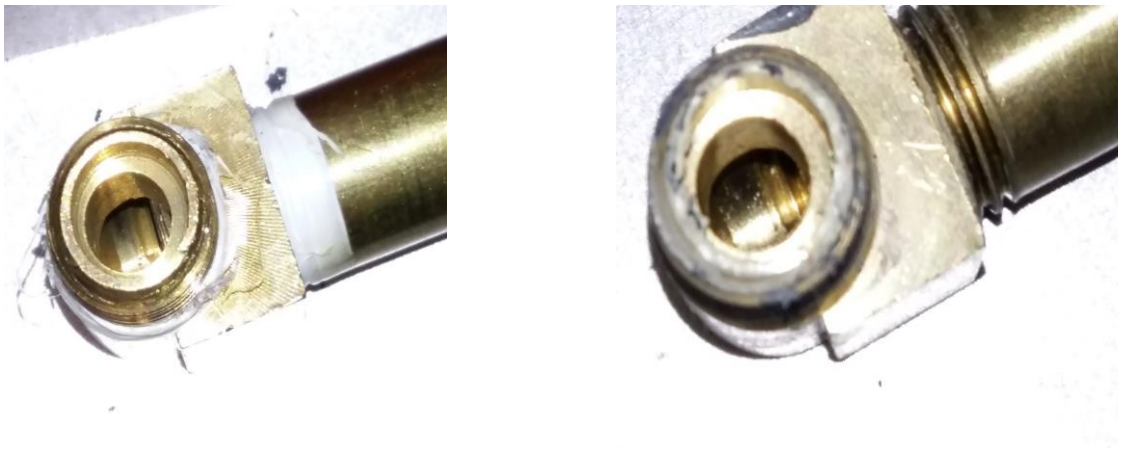

(a) Partially blocked discharge valve (b) Healthy discharge valve

Figure 5-10 Reciprocating compressor discharge valves

The reciprocating compressor with a blocked suction and the test-rig setup with the reciprocating compressor connected as a load are shown in Figure 5-11 and Figure 5-12 respectively.

Figure 5-11 Reciprocating compressor with blocked suction valve

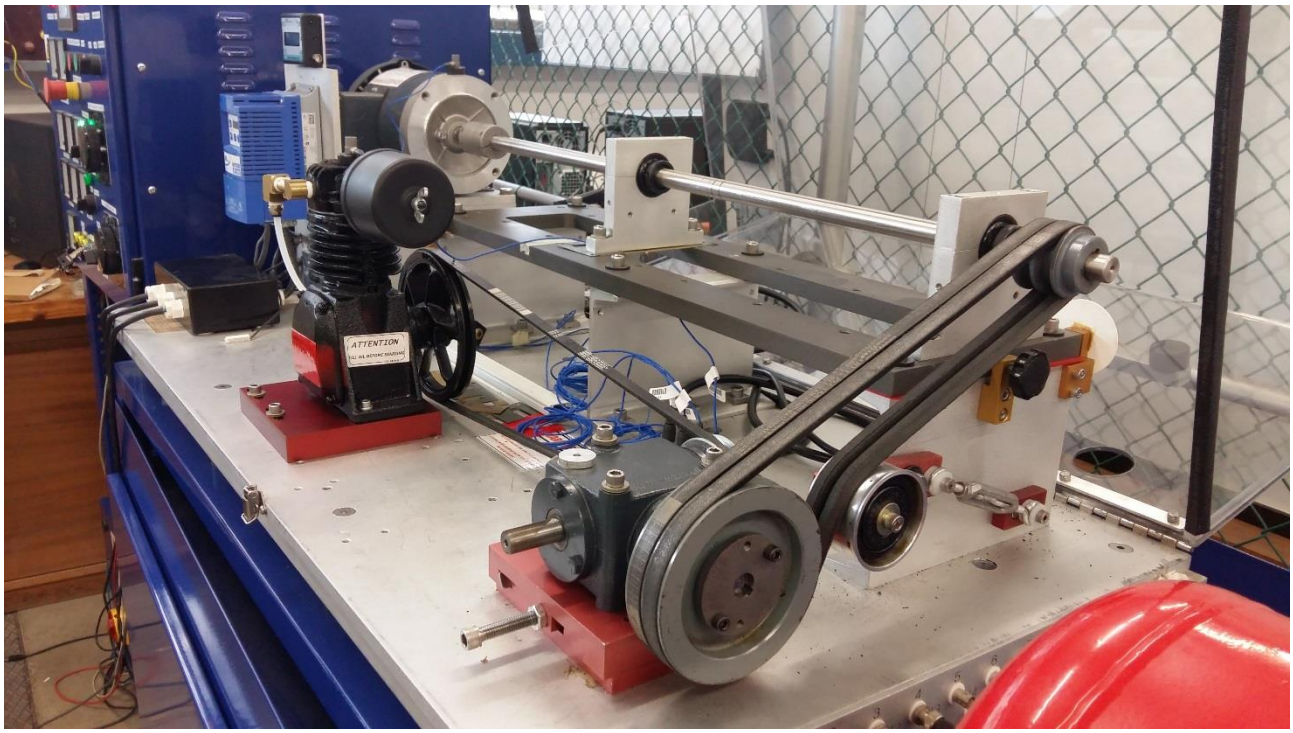

Figure 5-12 MFS-MG Test rig set up with the reciprocating compressor and air tank installed

6. Results and Discussions using Frequency Domain Techniques

6.1 Introduction

The purpose of this chapter is to compare the performance of MCSA and vibration analysis to identify faults in an inverter-fed induction motor, gearbox, and reciprocating compressor under steady state conditions. The stator inter-turn fault, broken rotor bar fault, bearing fault and the bowed rotor fault are investigated.

6.2 Induction Motor Faults

The test motors were directly coupled to a servo motor to serve as a load and they were linearly ramped up to a voltage of 190 Volts and a frequency of 50 Hz. 30 seconds of current and vibration data was captured and the FFT was applied to the data at three different loads which were implemented by varying the opposing torque exerted by the servo motor.

6.2.1 Stator Inter-turn Fault

4 turns of the motor with the stator winding faults were shorted and the motor was directly coupled to the servo motor. The current spectrum was plotted and the stator fault frequency was identified using equation (4-5) with $n = 1$, and $k = 3$. The fault frequencies were calculated to occur at 199.76 Hz, 199.34 Hz, and 198.85 Hz for the 0%, 50%, and 100% loads respectively. The 1X and 2X rotational vibration frequencies are also analysed in the vibration spectrum. The fault frequencies in the current spectrum are shown in Figure 6-1 and Table 6-1 below.

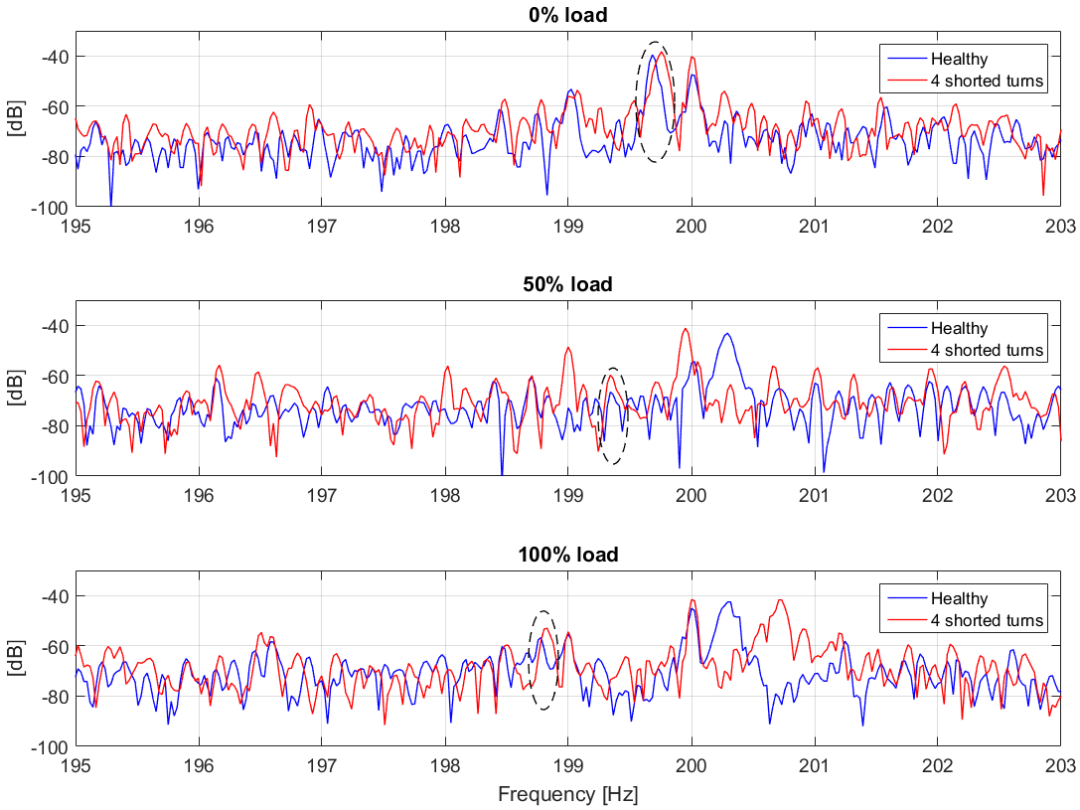

Figure 6-1 FFT of the motor current of the motor at 50% and 100% load showing the stator fault frequency

Table 6-1 Amplitude and frequency of the fault frequencies at 0%, 50%, and 100% load

Load	Amplitude [dB]	Frequency [Hz]
0%	-38.29	199.8
50%	-59.30	199.3
100%	-53.31	198.8

The fault frequencies in the current spectrum were successfully identified at the calculated frequencies though they are not easily noticeable. This can be attributed to the effect of the inverter harmonics which make it difficult to locate the fault frequencies [137].

The vibration spectra of the stator windings with emphasis on the 1X and 2X Rotational and Line frequencies are presented below. Figure 6-2 and Table 6-2 below show the 1X Rotational frequencies.

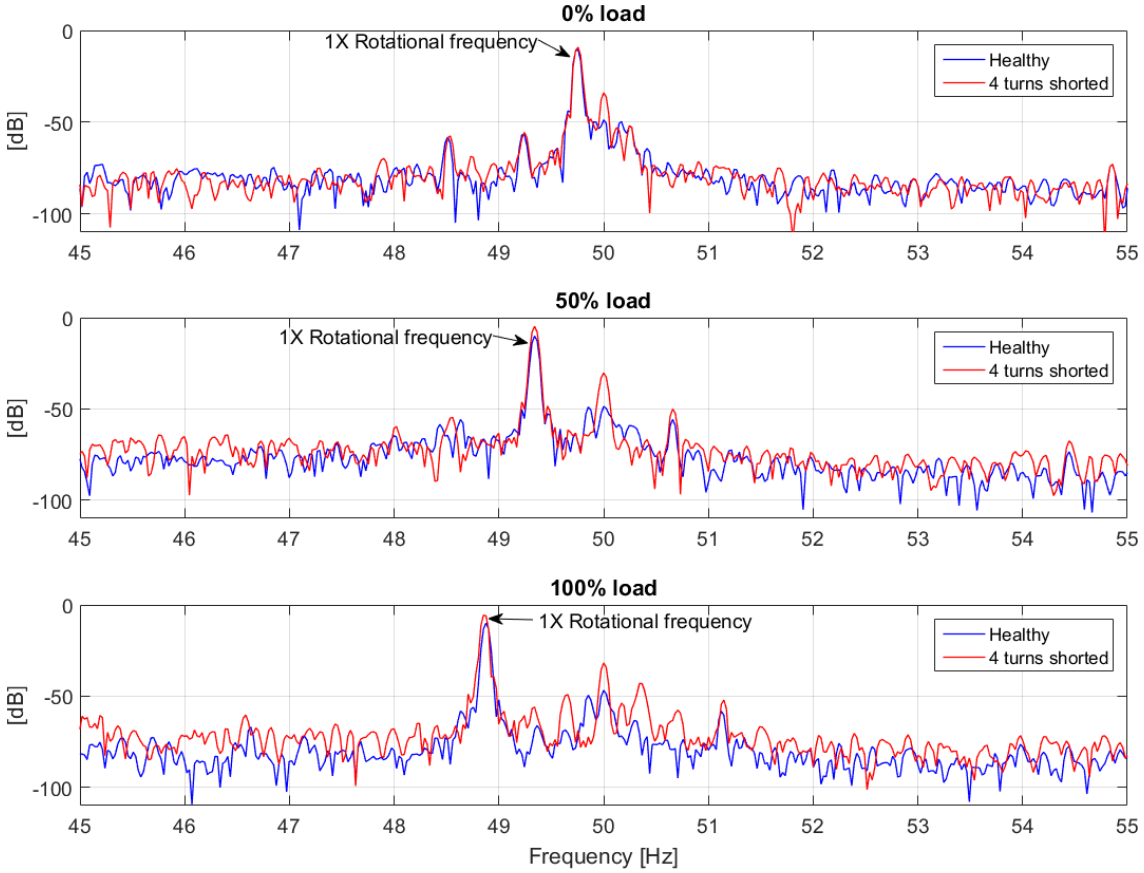

Figure 6-2 Vibration spectrum of the motor with shorted stator windings showing the 1X Rotational frequency

Table 6-2 Amplitudes and frequencies of the 1X Rotational frequency of the motor with shorted stator turns

Load	Healthy Motor		4 turns shorted	
	Amplitude [dB]	Frequency [Hz]	Amplitude [dB]	Frequency [Hz]
0%	-10.52	49.76	-9.16	49.76
50%	-10.07	49.34	-4.76	49.34
100%	-10.00	48.88	-5.50	48.85

There is an increase in the amplitudes of the 1X rotational frequencies by 1.36 dB, 5.24 dB, and 4.5 dB for the 0%, 50% and 100% loads respectively. There is also a reduction in the 1X rotational frequency as the load is increased.

The 2X Rotational and Line frequencies in the vibration spectrum were also analysed and the results are presented in Figure 6-3, Table 6-3, and Table 6-4 below.

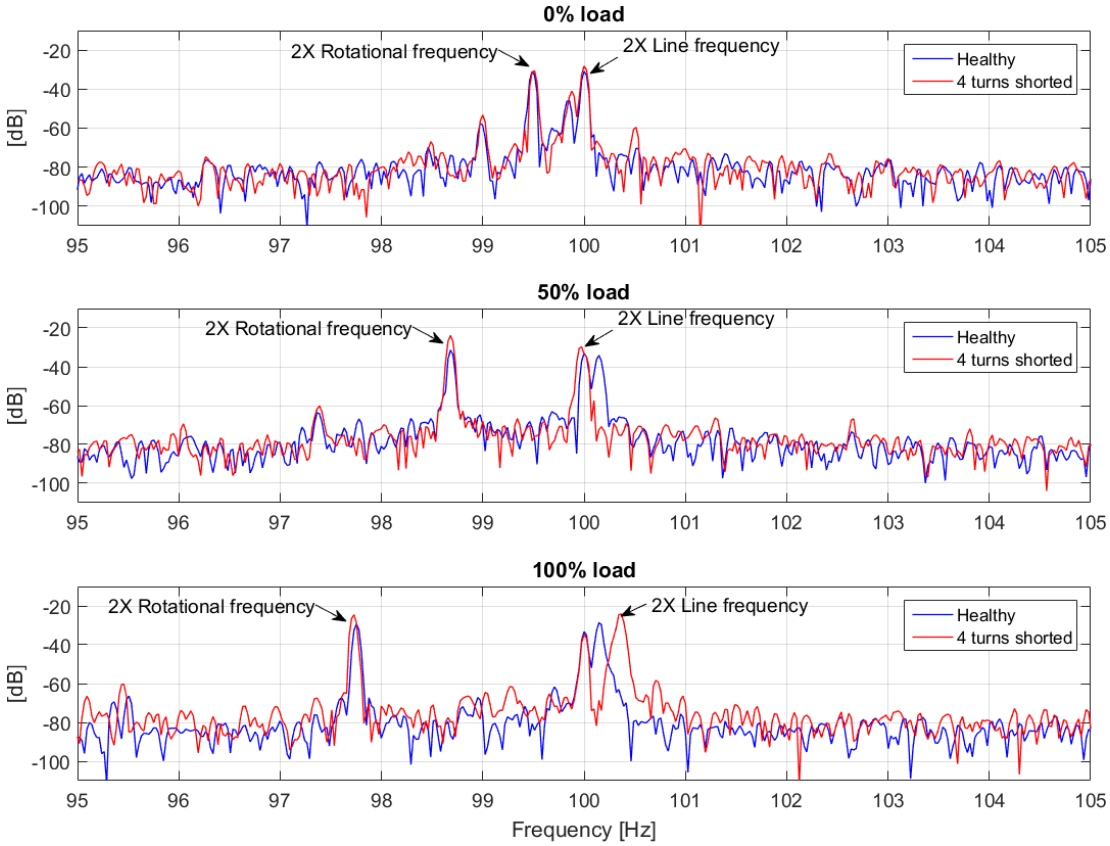

Figure 6-3 Vibration spectrum of the motor with shorted stator windings showing the 2X Rotational frequency and the 2X Line frequency

Table 6-3 Amplitudes and frequencies of the 2X Line frequency of the motor with shorted stator turns

Load	Healthy Motor		4 turns shorted	
	Amplitude [dB]	Frequency [Hz]	Amplitude [dB]	Frequency [Hz]
0%	-30.95	100.0	-28.22	100.0
50%	-33.00	100.0	-30.59	99.95
100%	-28.66	100.1	-24.59	100.3

Table 6-4 Amplitudes and frequencies of the 2X Rotational frequency of the motor with shorted stator turns

Load	Healthy Motor		4 turns shorted	
	Amplitude [dB]	Frequency [Hz]	Amplitude [dB]	Frequency [Hz]
0%	-30.99	99.49	-30.69	99.51
50%	-31.40	98.68	-23.89	98.68
100%	-29.27	97.75	-24.55	97.73

There is also an increase in the amplitude of the 2X Line frequency by 2.73 dB, 2.41 dB, and 4.07 dB, and an increase of 0.3 dB, 7.51 dB, and 4.72 dB in the 2X Rotational frequency for the 0%, 50%, and 100% loads respectively. The 2X Line frequency is not influenced by the load since it is not a function of the load. The 2X Rotational frequency, however, reduces as the load is increased for both the healthy and faulty motors.
The 2X Line frequency performs well as a tool for detection of the inter-turn fault, especially under loaded conditions, because the 2X Line frequency is mainly affected the air-gap dissymmetry [42].

The changes in amplitude can be attributed to the fact that stator frame vibration is a function of inter-turn winding faults, single phasing and supply-voltage unbalance [144].

6.2.2 Broken Rotor Bar Fault

The section discusses the results of the test motor with 3 broken rotor bars. The $(1 \pm 2s)f$ frequencies are analysed in the current spectrum, and the 1X Rotational frequencies are analysed in the vibration spectrum. The 2X Rotational frequency was also analysed in the vibration spectrum and they provided similar results to those observed for the 1X Rotational frequency. The calculated $(1 \pm 2s)f$ frequencies are presented in Table 6-5 below.

Table 6-5 Calculated $(1 \pm 2s)f$ frequencies

Load	1X rotational frequency	$(1-2s)f$	$(1+2s)f$
0%	49.76 Hz	49.52 Hz	50.48 Hz
50%	49.34 Hz	48.68 Hz	51.32 Hz
100%	48.88 Hz	47.76 Hz	52.24 Hz

The current spectra of the healthy motor and the motor with the broken rotor bars are presented in Figure 6-4 and Table 6-6 below.

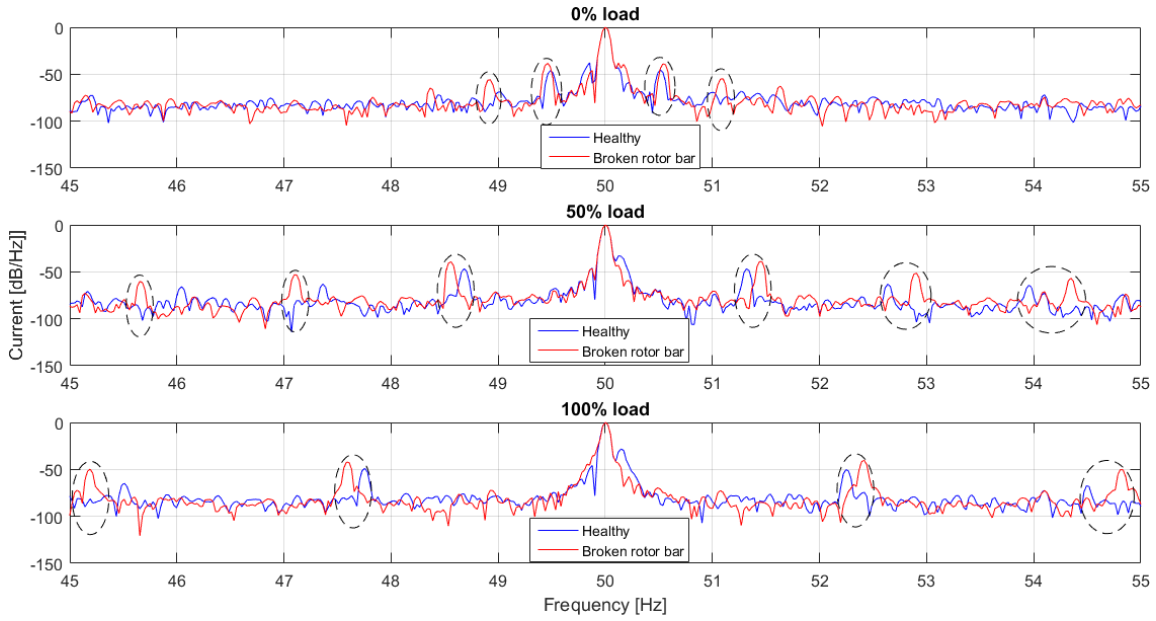

Figure 6-4 Current spectrum of the healthy motor and the motor with broken rotor bars showing the sidebands of the fundamental frequency

Table 6-6 $(1 \pm 2s)f$ frequencies and amplitudes from the current spectrum

Load	Healthy [Hz, dB]		Broken rotor bars [Hz, dB]	
	$(1-2s)f$	$(1+2s)f$	$(1-2s)f$	$(1+2s)f$
0%	49.00, -68.94	50.51, -45.32	48.90, -56.52	50.54, -38.91
50%	47.36, -63.07	51.32, -46.76	47.12, -53.33	51.44, -38.80
100%	45.51, -64.75	52.25, -50.18	45.19, -49.74	52.44, -45.17

There was a notable increase in the $(1 \pm 2s)f$ frequencies of the motor with the broken rotor bars. There were noticeable increments in the other sidebands which have been highlighted in Table 6-7 below.

Table 6-7 Other sidebands frequencies

Load	Healthy [Hz, dB]	Broken rotor bars [Hz, dB]
0%	49.49, -46.14; 50.98, -70.00	49.46, -38.40; 51.07, -55.15
50%	48.68, -46.70; 52.64, -63.12	48.56, -39.19; 52.88, -52.48
100%	47.75, -48.85; 54.49, -67.46	47.58, -42.31; 54.86, -57.94

The $(1 \pm 2s)f$ frequencies and the sidebands move further away from the fundamental as the load is increased. This is because the rotational frequency of the motor reduces with the increased load, which in turn increases the slip.

The vibration spectrum of the motor showing the 1X rotational frequency is presented in Figure 6-5 and Table 6-8 below.

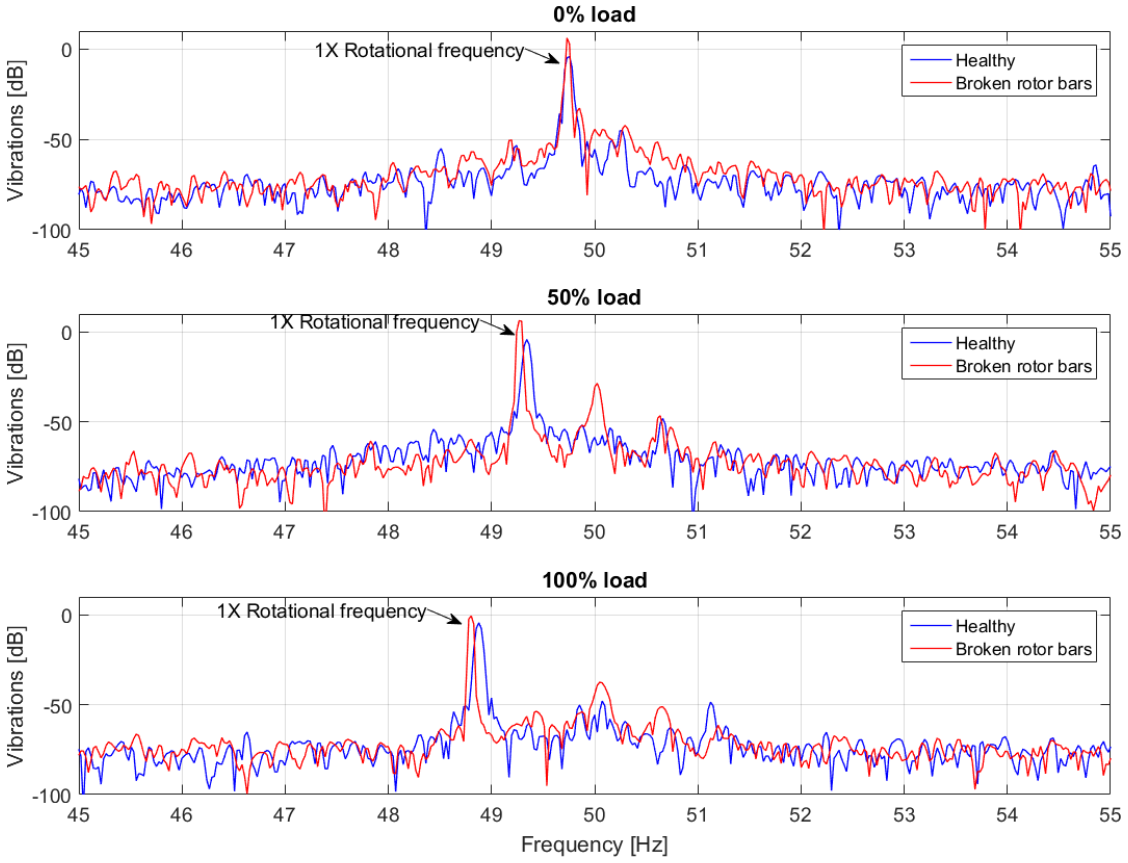

Figure 6-5 Vibration spectrum of the motor with the with broken rotor bars showing the 1X rotational frequency

Table 6-8 Amplitudes and frequencies of the 1X rotational frequency

Load	Healthy Motor		Broken rotor bars	
	Amplitude [dB]	Frequency [Hz]	Amplitude [dB]	Frequency [Hz]
0%	-10.52	49.76	0.18	49.73
50%	-10.07	49.34	0.29	49.27
100%	-10.00	48.88	-0.58	48.80

Analysis of the vibration spectrum of the motor with broken rotor bars showed an increase in the magnitude of the 1X Rotational frequency of 10.7 dB, 10.36 dB, and 9.42 dB at 0%, 50%, and 100% load respectively. There is also a reduction of the 1X Rotational frequency as the load is increased, as the speed of the motor reduces.

6.2.3 Bowed Rotor Fault

The bowed rotor fault results in an unequal airgap in the induction motor which leads to eccentricity. The formulae discussed in section 4.4.1 were used as indicators of eccentricity in the motor. The results are discussed below. The fault frequencies in the current spectrum were calculated using $f\left[(kR \pm n_d)\frac{(1-s)}{p} \pm v\right]$ with $k = 1, R = 34, n_d = 0$, and $v = 0$ and are presented in Table 6-9 below.

Table 6-9 Estimated fault frequencies for the bowed rotor fault under different loads

Load	Estimated frequency
0%	1692.52 Hz
50%	1679.26 Hz
100%	1663.62 Hz

The current spectra of the healthy motor and the motor with the bowed rotor are presented in Figure 6-6 and Table 6-10 below.

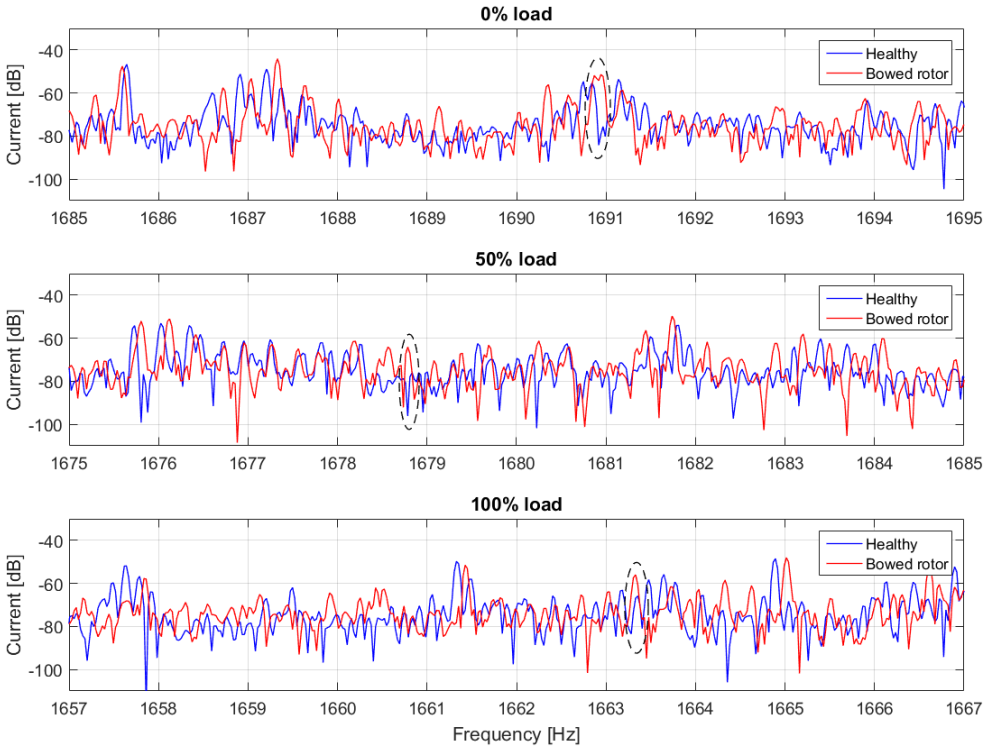

Figure 6-6 Current spectrum showing the fault components of the motor with the bowed rotor at 0%, 50%, and 100% load

Table 6-10 Estimated and actual fault frequencies of the motor with the bowed rotor in the current spectrum

Load	Estimated frequency	Actual frequency	Amplitude
0%	1692.52 Hz	1691 Hz	-51.41 dB
50%	1679.26 Hz	1679 Hz	-64.13 dB
100%	1663.62 Hz	1663 Hz	-56.00 dB

The vibration spectrum of the healthy motor and the motor with the bowed rotor were plotted in Figure 6-7 below and the amplitude of the rotational frequency of the motor was analysed. The results are tabulated in Table 6-11 below.

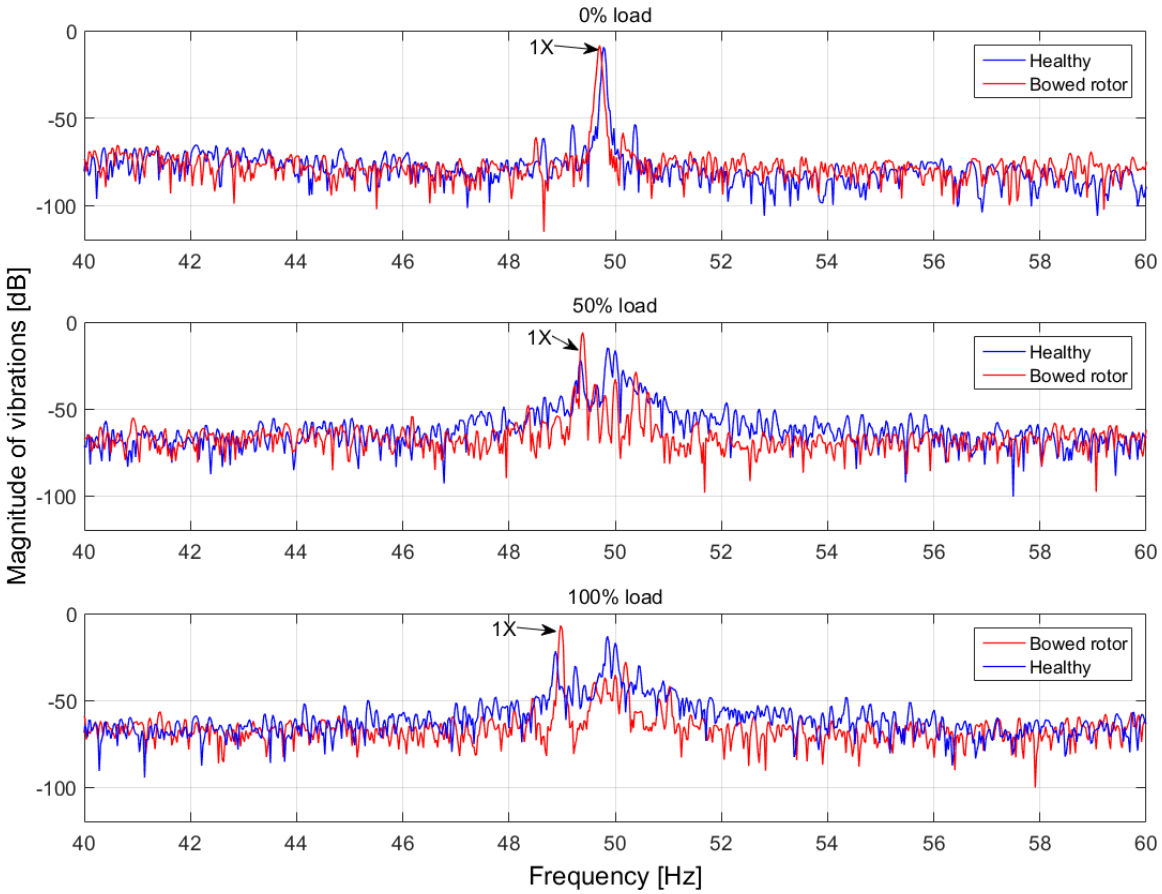

Figure 6-7 Vibration spectrum of the healthy motor and the motor with a bowed rotor at 100% load, 50% load and 0% load showing the 1X frequency

Table 6-11 1X Rotational frequency of the healthy motor and the motor with a bowed rotor at varying loads

Load	Healthy Motor		Motor with a bowed rotor	
	Frequency (Hz)	Amplitude (dB)	Frequency (Hz)	Amplitude (dB)
0%	49.73	-12.40	49.68	-10.5
50%	49.34	-17.62	49.39	-6.00
100%	48.88	-21.67	48.97	-6.87

There is a general increase in the amplitude of the PSD for the motor with the bowed rotor compared to that of the healthy motor. The 1X rotational frequency is directly dependant on the loading of the motor

and increases as the load on the motor is reduced. With the healthy motor, the amplitude of the 1X rotational frequency increases as the load is decreased.

The $2f_s + f_r$ frequencies were also investigated as credible indicators of the bowed rotor fault. The expected values of the $2f_s + f_r$ frequencies were calculated and the results are shown in Table 6-12 below.

Table 6-12 Calculated $2f_s + f_r$ frequencies at 0%, 50%, and 100% load

Load	$2f_s + f_r$
0%	149.71 Hz
50%	149.39 Hz
100%	148.97 Hz

The measured $2f_s + f_r$ frequencies in the vibration spectrum are shown in Figure 6-8 and Table 6-12 below.

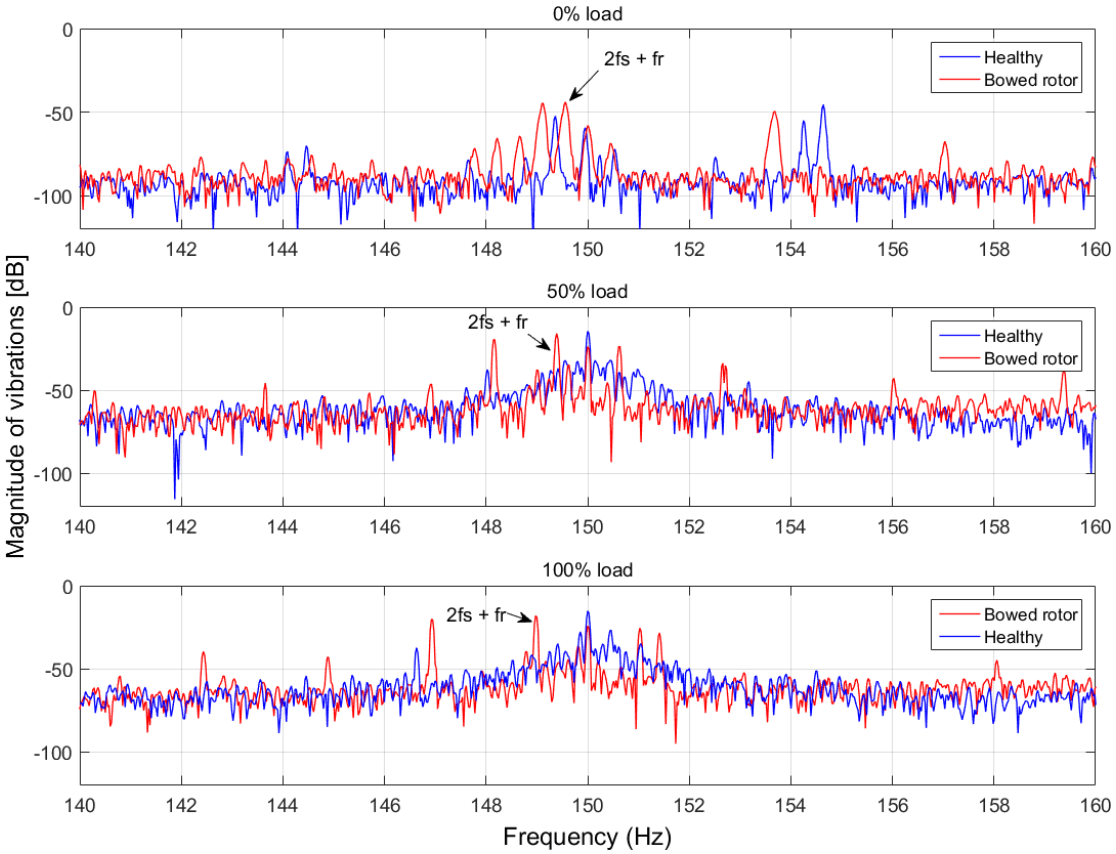

Figure 6-8 Vibration spectrum of the healthy motor and the motor with a bowed rotor at 0%, 50%, and 100% load showing the $2f_s + f_r$ frequency

Table 6-13 $2f_s + f_r$ frequencies from PSD

Load level	Frequency	Amplitude
0%	149.6 Hz	-46.32 dB
50%	149.4 Hz	-15.89 dB
100%	149.0 Hz	-18.05 dB

There is an increase in the $2f_s + f_r$ frequencies as the load is decreased. This is due to the increase in rotor frequency, f_r, as the load is reduced.

6.2.4 Bearing Fault

i. Inner Race Fault

The Ball Pass Frequency of the Inner Race (BPFI) was used to identify inner race fault in the motor. The BPFI was calculated using the formulae described in section 4.4.4. The frequencies at 100% load, 50% load and 0% load were calculated using equations (4-6) and (4-7) and the results are shown in Table 6-14 below.

Table 6-14 Calculated BPFI frequencies

Load level	Equation (4-6)	Equation (4-7)
0%	245.509 Hz	239.520 Hz
50%	242.065 Hz	236.592 Hz
100%	240.589 Hz	235.056 Hz

The vibration spectrum of the motors at 0%, 50% and 100% load were plotted in Figure 6-9 and prominent spikes were seen at the frequencies shown in Table 6-15.

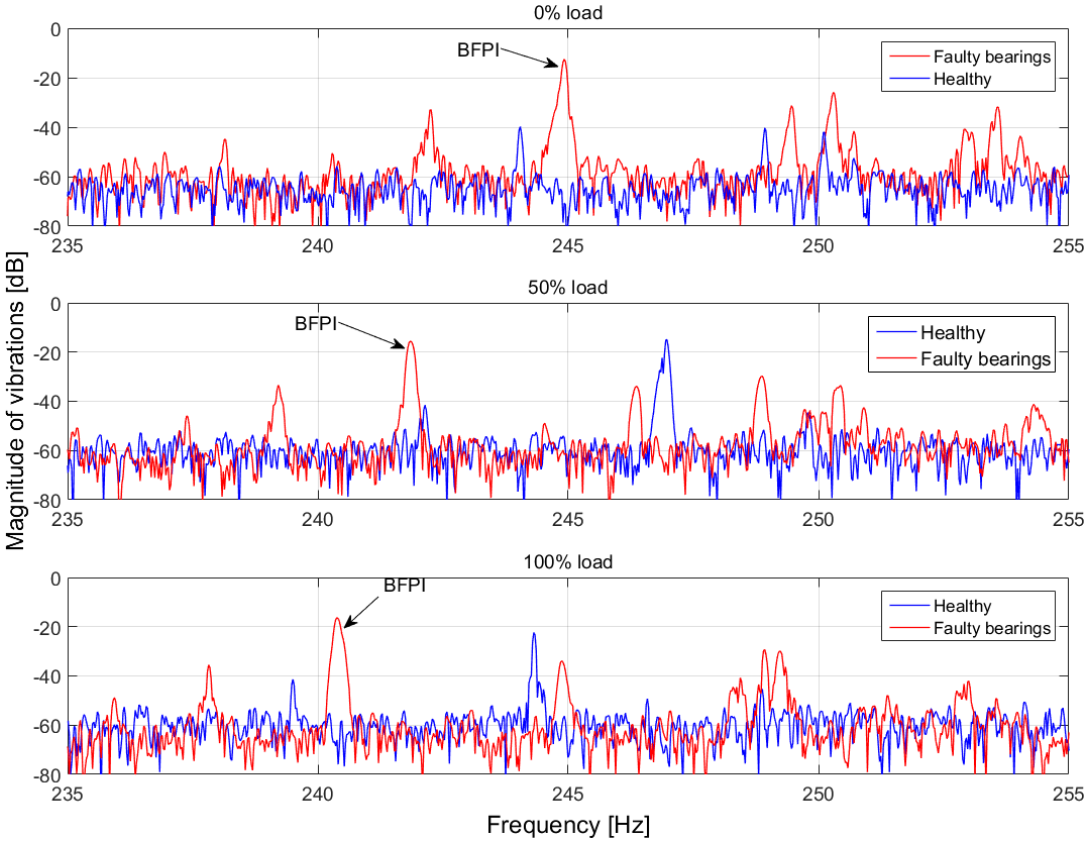

Figure 6-9 Vibration spectrum showing the BPFI of the healthy motor and the motor with faulty bearings at 100%, 50% and 0% load

Table 6-15 BPFI frequencies from the PSD

Load level	Frequency	Amplitude
0%	244.9 Hz	-13.59 dB
50%	241.8 Hz	-15.64 dB
100%	240.4 Hz	-17.10 dB

The BPFI frequency is observed to increase as the load on the motor is reduced and the amplitude of frequency component also increased. The increase in the frequency as the motor load is reduced is because the BPFI frequency is proportional to the speed of the motor which increases as the load on the motor is reduced.

ii. Outer Race fault

The Ball Pass Frequency of the Outer Race (BPFO) was used to identify the outer race faulted bearing. The BPFO was also calculated using the formulae described in section 4.4.4. The frequencies were calculated using equations (4-6) and (4-7) and the results are shown in Table 6-16 below.

Table 6-16 Calculated BPFO frequencies

Load level	Equation (4-6)	Equation (4-7)
0%	153.691 Hz	159.680 Hz
50%	151.750 Hz	157.664 Hz
100%	150.826 Hz	156.704 Hz

The vibration spectrum of the healthy and the faulty motors was plotted for the motors loaded at 0%, 50%, and 100% in Figure 6-10 below and the BFPO frequencies were identified as shown in Table 6-17 below.

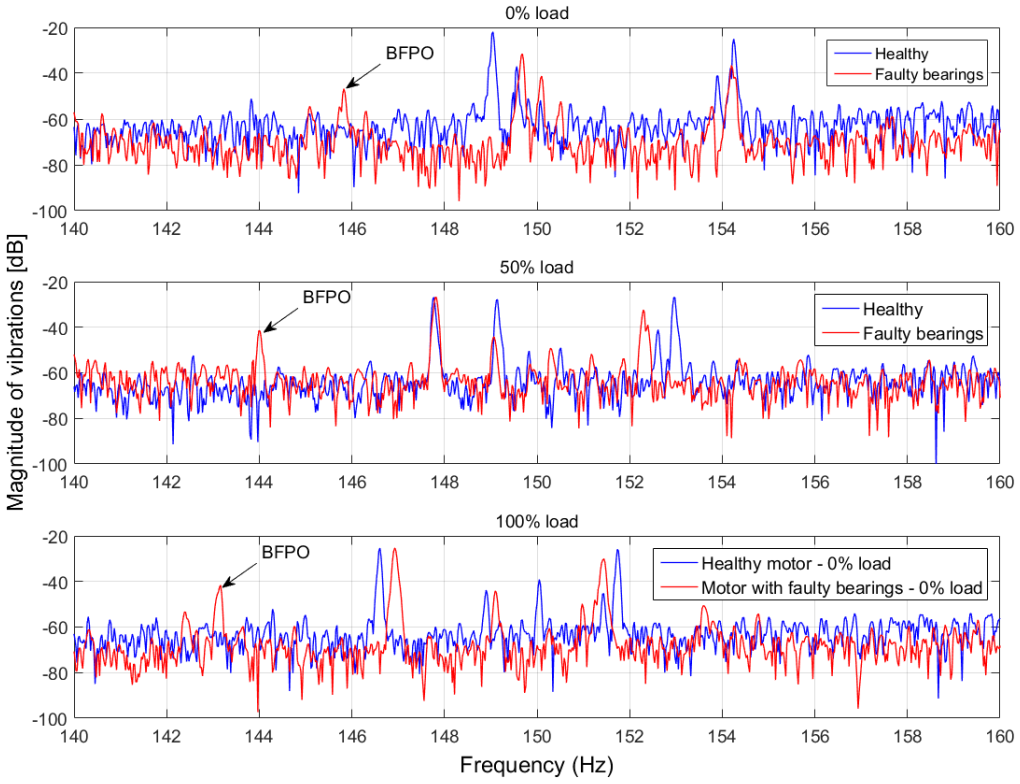

Figure 6-10 BPFO of the healthy motor and the motor with faulty bearings at 0%, 50%, and 100% load

Table 6-17 BPFO frequencies from the PSD

Load level	Frequency	Amplitude
0%	145.8 Hz	-46.80 dB
50%	144.0 Hz	-41.46 dB
100%	143.1 Hz	-42.62 dB

The BPFO is also dependant on the speed of rotation of the rotor which increases as the load on the motor is reduced. There is no particular trend in the amplitude of the BPFO frequency.
The BPFO frequency is not as prominent as the BPFI frequency. This is likely due to the position of the accelerometers on the motor which were not close enough to the bearings to detect the frequency.

6.2.5 Concluding remarks

Overall, the fault frequencies discussed in section 4.4 were investigated and concluded to be viable indicators of faults in the induction motors in steady state conditions.
It was easier to observe the inter-turn fault frequencies in the vibration spectrum compared to the current spectrum. The poor performance of the current spectrum can be attributed to the noise in the current spectrum from the inverter harmonics.
The broken rotor bar fault was evident in both the current and vibration spectra. The fault was, however, easier to identify in the current spectrum, especially due to the sideband harmonics that resulted from the fault.
The bowed rotor fault frequency components were also evident in both the current and vibration spectra. The fault frequencies in the vibration spectrum, however, were easier to identify as they had larger amplitudes than those in the current spectrum.
The bearing faults were visible in both the current and vibration spectra, but the fault frequencies in the vibration spectrum had larger amplitudes and were thus more prominent.

6.3 Gearbox faults

The gearbox faults discussed in this section are the chipped tooth, the missing tooth and the worn-out gearbox. These faults are implemented on the pinion of the gearbox and the vertical vibration data of the gearboxes is captured. The time-domain signal is analysed and the statistical indicators i.e. peak value, RMS, Crest Factor (CF) and kurtosis of the faulty gearboxes are calculated and compared to those of the healthy gearbox which is used as the baseline.
The FFT is the applied to the signal and the mesh frequencies and their corresponding sidebands are compared to those of the healthy gearbox.
The aim is to validate whether the statistical indicators of the vibrations, and the mesh frequencies with their corresponding sidebands can be used to detect and identify the faults in the gearbox. The pinion and gear rotational frequencies in the vibration spectrum were also analysed but the results were inconclusive and are included in the appendix.
In the following experiments, the induction motor is loaded with the gearbox via a pair of V-belt sheaves and is ramped up to a voltage of 190 Volts and a frequency of 50 Hz over a period of 10 seconds. Axial vibration data from the gearbox is captured during start-up and also as the gearbox is run in steady state.

6.3.1 Healthy Gearbox

The vibration signal in the time domain and the corresponding FFT for the healthy gearbox are shown in Figure 6-11 and Figure 6-12 below. This is used to determine the baseline data for the experiments. The mesh frequency is calculated using the information in Table 5-2 and the measured rotational frequency of the motor shaft. The ratio of the diameters of the V-belt sheaves was calculated to be 1.9. The sidebands due to the pinion and gear occur at frequencies ±19.7 Hz and ±13.13 Hz from the mesh frequency, respectively. The estimated fault components are presented in Table 6-18 below.

Table 6-18 Estimated fault components frequencies of the healthy gearbox

Component	Frequency
Mesh frequency	354.6 Hz
Left pinion sideband	334.9 Hz
Right pinion sideband	374.3 Hz
Left gear sideband	341.8 Hz
Right gear sideband	367.7 Hz

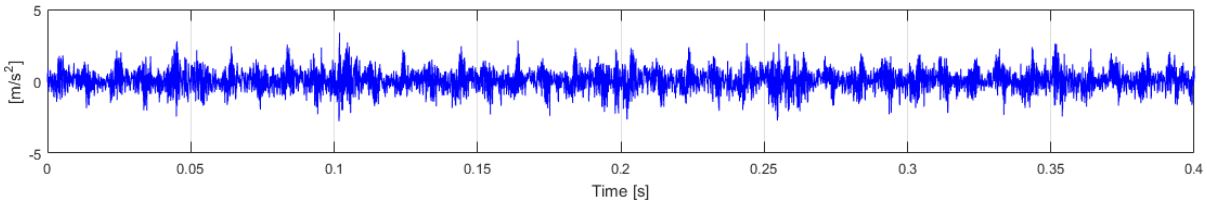

Figure 6-11 Raw data captured from the vibration of the healthy gearbox

The statistical indicators of the healthy gearbox vibration data are presented in Figure 6-19 below.

Table 6-19 Statistical indicators of the healthy gearbox vibration data

Statistical Indicator	Value [m/s²]
Peak value (PV)	4.774
Root Mean Square (RMS)	0.660
Crest Factor (CF)	7.645
Kurtosis	4.115

The kurtosis of a signal comprising random noise, following a Gaussian distribution, has a kurtosis value of 3.0. An ideal healthy gearbox would therefore have kurtosis of approximately 3.0 or less [28]. The kurtosis of the healthy gearbox is observed 1.115 ms^{-2} more than that of an ideal Gaussian signal.

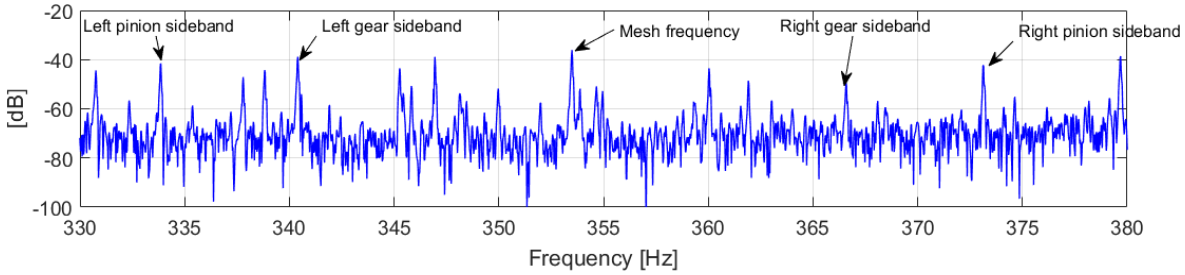

Figure 6-12 Vibration spectrum of the healthy gearbox in steady state

The measured fault frequency components are presented in Table 6-20 below.

Table 6-20 Fault components frequencies and amplitudes of the healthy gearbox

Component	Estimated Frequency [Hz]	Measured	
		Frequency [Hz]	Amplitude [dB]
Mesh frequency	354.6	353.5	-36.14
Left pinion sideband	334.9	333.9	-40.45
Right pinion sideband	374.3	373.1	-42.67
Left gear sideband	341.8	340.4	-40.45
Right gear sideband	367.7	366.6	-49.38

The frequencies observed on the FFT of the steady state vibration signal correspond to those that are estimated in Table 6-18 with a difference of 1.7 Hz for the mesh frequency.

The vibration data of the accelerometer on the motor was also analysed for the mesh frequencies and the corresponding sidebands from the gearbox but these could not be identified.

When using the gearboxes as test loads, the sidebands of the mesh, pinion and gear frequencies across the supply frequencies are also observed and can be used to provide information about the state of the gearbox [85], [134].

The current spectrum of the motor with the gearbox load and without the gearbox load at the frequencies defined by equations (4-13) and (4-14) above was also analysed. For the healthy gearbox scenario, these frequencies are presented below with $n = 1$. The mesh frequency of the healthy gearbox was calculated to be 354.6 Hz and the pinion frequency of the healthy gearbox was calculated to be 19.7 Hz. The corresponding estimated fault frequencies are shown in Table 6-21 below.

Table 6-21 Fault component and the estimated frequencies

Fault component	Frequency [Hz]
$f_s + f_m$	404.6
$f_s + f_p$	69.7
$f_s - f_p$	30.3

The fault frequencies in the current spectra are presented in Figure 6-13, Figure 6-14, and Table 6-22 below.

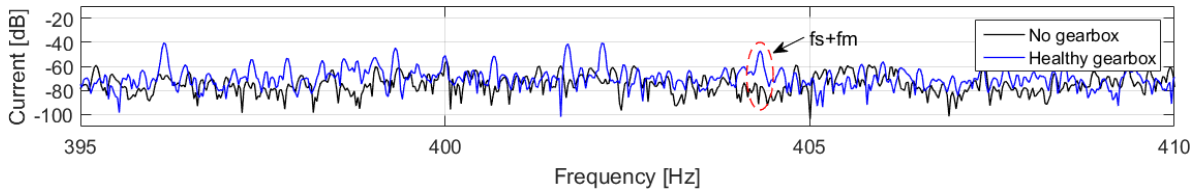

Figure 6-13 Motor current spectrum showing $f_s + f_m$ of the healthy gearbox

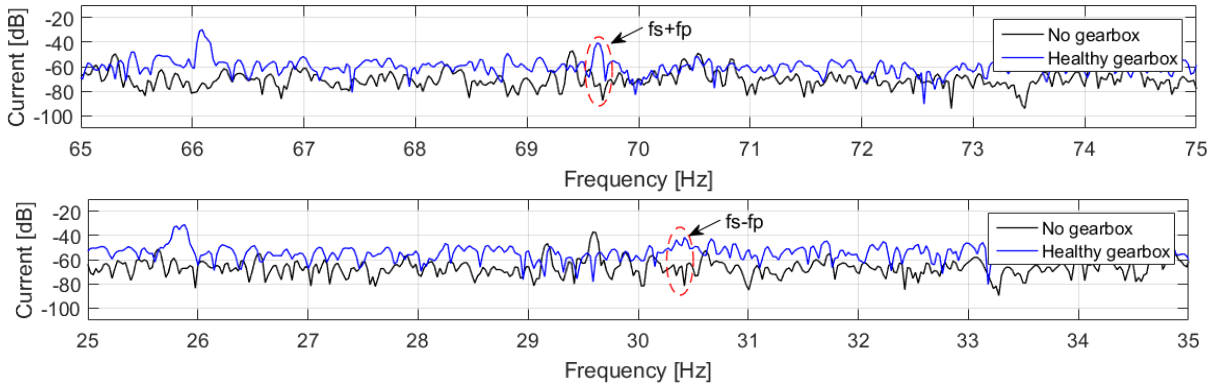

Figure 6-14 Motor current spectrum showing $f_s + f_p$ and $f_s - f_p$ of the healthy gearbox

Table 6-22 Frequencies and amplitudes of the $f_s + f_m$, $f_s + f_p$ and $f_s - f_p$ frequency components in the motor current spectrum for the healthy gearbox

Fault component	Estimated frequency [Hz]	Actual Frequency [Hz]	Amplitude [dB]
$f_s + f_m$	404.6	404.3	-47.11
$f_s + f_p$	69.7	69.63	-40.75
$f_s - f_p$	30.3	30.42	-41.65

6.3.2 Chipped Tooth Gearbox

This section discusses the results of the gearbox with the pinion with a chipped tooth. The gearbox used is identical to the healthy one but for the faulted pinion which has one of its teeth chipped. The vibration signal of the faulty gearbox and its statistical indicators are shown in Figure 6-15 and Table 6-23 below.

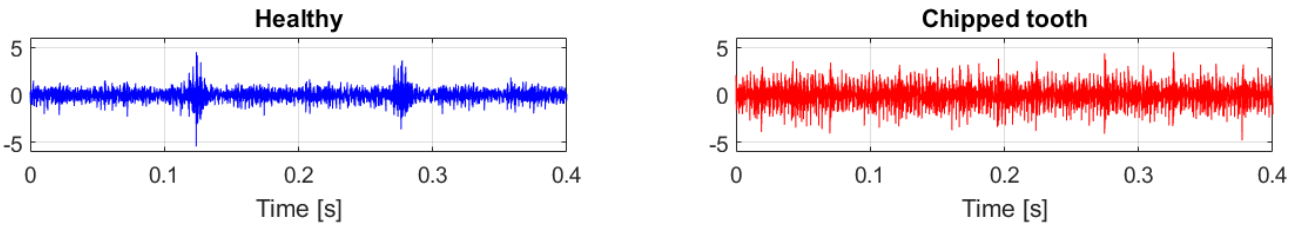

Figure 6-15 Raw data captured from the vibration of the chipped tooth gearbox

Table 6-23 Statistical indicators of the chipped tooth gearbox vibration data

Statistical Indicator	Healthy	Chipped tooth
Peak value (PV)	4.774 ms^{-2}	6.118 ms^{-2}
Root Mean Square (RMS)	0.660 ms^{-2}	0.859 ms^{-2}
Crest Factor (CF)	7.645 ms^{-2}	7.132 ms^{-2}
Kurtosis	4.115 ms^{-2}	4.746 ms^{-2}

The vibrations from the faulty gearbox have more energy than those of the healthy gearbox. Unlike the healthy gearbox, the gearbox with a chipped tooth has periodic spikes in the time domain that are due to the impact/backlash resulting from the extra space between the teeth due to the chip.
There is an increase the peak value, root mean square, and kurtosis by 1.344 m/s^2, 0.199 m/s^2, and 0.631 m/s^2 respectively. The crest factor decreased by 0.513 m/s^2. The increased peak value is due to the impact of the chipped tooth which also increases the RMS and the kurtosis values.

The vibration spectrum was also analysed with emphasis on the mesh frequencies and the corresponding pinion and gear sidebands. The results are presented in Figure 6-16 and Table 6-24 below.

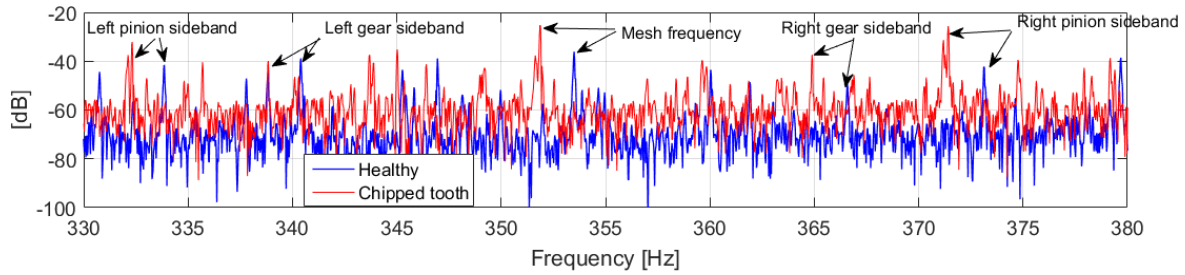

Figure 6-16 Vibration spectrum of the chipped tooth gearbox in steady state showing the mesh frequency and the corresponding sidebands

Table 6-24 Fault components frequencies and amplitudes of the chipped tooth gearbox

Component	Healthy		Chipped tooth	
	Frequency [Hz]	Amplitude [dB]	Frequency [Hz]	Amplitude [dB]
Mesh frequency	353.5	-36.14	351.9	-25.26
Left pinion sideband	333.9	-40.45	332.3	-32.13
Right pinion sideband	373.1	-42.67	371.4	-27.54
Left gear sideband	340.4	-40.45	338.8	-39.90
Right gear sideband	366.6	-49.38	364.9	-37.35

There is an increase in the mesh frequency by 10.88 dB which can be attributed to the backlash from the chipped tooth discussed in section 4.5.1. The left pinion sideband and right pinion sideband frequencies increased by 8.32 dB and 15.13 dB respectively. The left gear sideband and right gear sideband frequencies increased by 0.55 dB and 12.03 dB. The relatively larger increase in the mesh frequencies and the corresponding pinion sideband frequencies with respect to the gear sideband frequencies can be attributed to the fact the chipped tooth is located on the pinion [130].

The motor current was then analysed with emphasis on the $f_s + f_m$ and $f_s \pm f_p$ frequencies, and the results are presented in Figure 6-17, Figure 6-18, and Table 6-25 below.

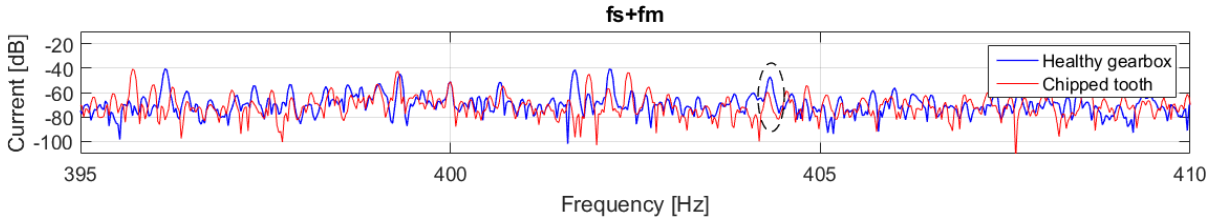

Figure 6-17 Motor current spectrum showing $f_s + f_m$ of the healthy gearbox and the gearbox with a chipped tooth

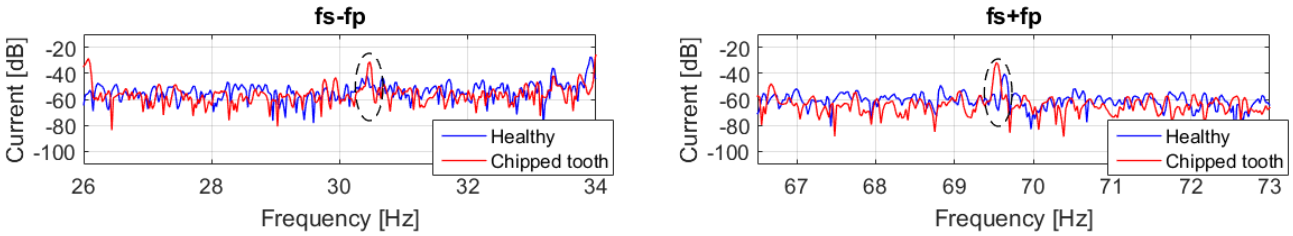

Figure 6-18 Motor current spectrum showing $f_s + f_p$ and $f_s - f_p$ of the healthy gearbox and the gearbox with the chipped tooth

Table 6-25 Frequencies and amplitudes of the $f_s + f_m$, $f_s + f_p$ and $f_s - f_p$ frequency components in the motor current spectrum for the gearbox with the chipped tooth

Fault component	Healthy gearbox		Chipped tooth gearbox	
	Frequency [Hz]	Amplitude [dB]	Frequency [Hz]	Amplitude [dB]
$f_s + f_m$	404.3	-47.11	404.3	-60.09
$f_s + f_p$	69.63	-40.75	69.53	-31.74
$f_s - f_p$	30.42	-41.65	30.47	-31.17

Although there is a decrease in amplitude of the $f_s + f_m$ frequency by 12.98 dB, the amplitudes of the corresponding right and left pinion sidebands, $f_s \pm f_p$, increased by 9.01 dB and 10.68 dB respectively.

6.3.3 Missing Tooth Gearbox

This section discusses the results of the gearbox with a missing tooth on the pinion. The same gearbox that was used in the previous section is also used here but the pinion was swapped for one with missing tooth. The vibration signal in the time domain and its statistical indicators are presented in Figure 6-19 and Table 6-26 below.

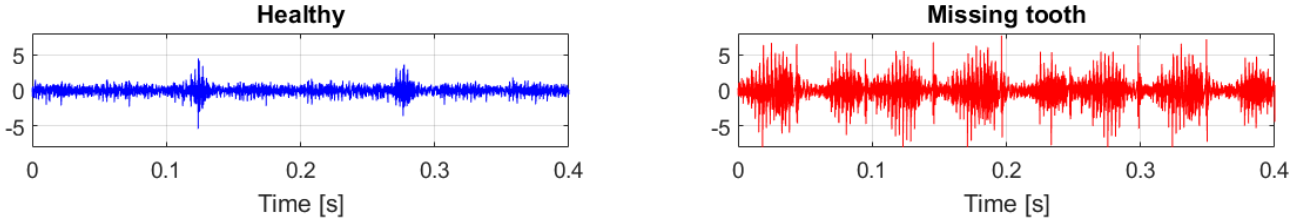

Figure 6-19 Raw vibration data of the gearbox with a missing tooth pinion

Table 6-26 Statistical indicators of the vibration data of the gearbox with a missing tooth pinion

Statistical Indicator	Healthy	Missing tooth
Peak value (PV)	4.774 ms^{-2}	8.149 ms^{-2}
Root Mean Square (RMS)	0.660 ms^{-2}	1.444 ms^{-2}
Crest Factor (CF)	7.645 ms^{-2}	7.191 ms^{-2}
Kurtosis	4.115 ms^{-2}	6.579 ms^{-2}

There is evidently more modulation of the time domain signal compared to that of the healthy gearbox or that of the chipped tooth gearbox. This is because there is more impact/backlash due to the missing tooth compared to the chipped tooth or the healthy gearbox [130].
There is an increase the peak value, root mean square, and kurtosis by 3.375 m/s^2, 0.784 m/s^2, and 2.464 m/s^2. The crest factor decreased by 0.454 m/s^2. The magnitudes of the statistical indicators were higher than those for the gearbox with a chipped tooth as the severity of the fault was increased. There is larger impact/backlash compared to the chipped tooth which results in higher values of PV and RMS.

The results from the analysis of the vibration spectrum of the gearbox are presented in Figure 6-20 and Table 6-27 below.

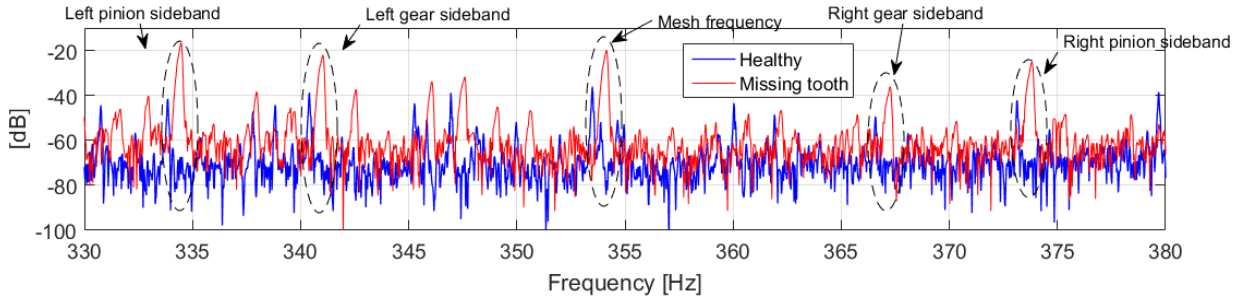

Figure 6-20 Vibration spectrum of the missing tooth gearbox in steady state showing the mesh frequency and the corresponding sidebands

Table 6-27 Fault component frequencies and amplitudes of the missing tooth gearbox

Component	Healthy		Missing tooth	
	Frequency [Hz]	Amplitude [dB]	Frequency [Hz]	Amplitude [dB]
Mesh frequency	353.5	-36.14	354.2	-21.19
Left pinion sideband	333.9	-40.45	334.5	-16.58
Right pinion sideband	373.1	-42.67	373.8	-26.64
Left gear sideband	340.4	-40.45	341.0	-22.23
Right gear sideband	366.6	-49.38	367.3	-37.81

There is an increase in the amplitude of the mesh frequency compared to that of the healthy gearbox by 14.95 dB. The left pinion sideband and right pinion sideband frequencies increase by 23.87 dB and 16.03 dB respectively. The left gear sideband and right gear sideband frequencies increased by 18.22 dB and 11.57 dB respectively.
Similar to the observations in the previous section, the pinion sidebands had a larger increase with respect to the gear sidebands and can be attributed to the fault being located on the pinion. The amplitudes of the mesh frequencies and the corresponding sidebands are also higher than the

corresponding frequencies measured in section 6.3.2. This can be attributed to the increased severity of the fault.

The motor current spectrum was also analysed and the results are presented in Figure 6-21, Figure 6-22, and Table 6-28 below.

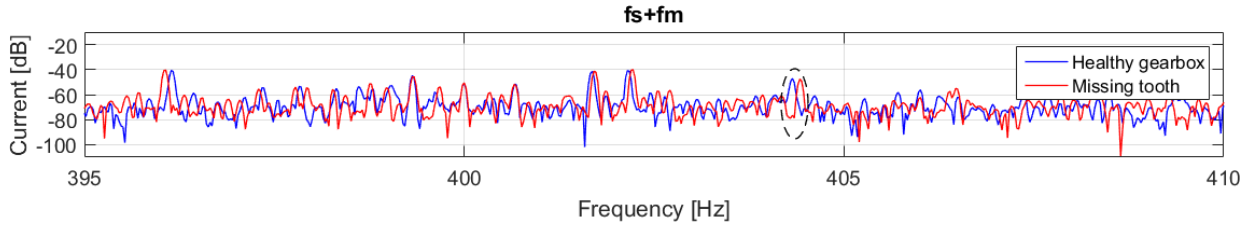

Figure 6-21 Motor current spectrum showing $f_s + f_m$ of the healthy gearbox and the gearbox with a missing tooth pinion

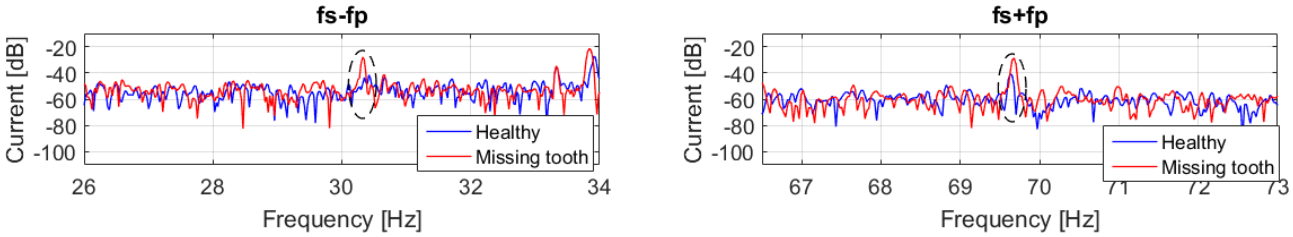

Figure 6-22 Motor current spectrum showing $f_s + f_p$ and $f_s - f_p$ of the healthy gearbox and the gearbox with the missing tooth pinion

Table 6-28 Frequencies and amplitudes of the $f_s + f_m$, $f_s + f_p$ and $f_s - f_p$ frequency components in the motor current spectrum for the gearbox with the missing tooth pinion

Fault component	Healthy gearbox		Missing tooth gearbox	
	Frequency [Hz]	Amplitude [dB]	Frequency [Hz]	Amplitude [dB]
$f_s + f_m$	404.3	-47.11	404.4	-47.61
$f_s + f_p$	69.63	-40.75	69.70	-33.33
$f_s - f_p$	30.42	-41.65	30.32	-28.09

The amplitude of the $f_s + f_m$ frequency decreased by 0.5 dB, while that of the corresponding right and left pinion sideband frequencies, $f_s \pm f_p$, increased by 7.42 dB and 13.56 dB respectively.

6.3.4 Worn-out Gearbox

This section discusses the results from the gearbox with worn-out teeth. The test gearbox was replaced with a gearbox with worn-out teeth. The vibration signal in the time domain and its statistical indicators are shown in Figure 6-23 and Table 6-29 respectively.

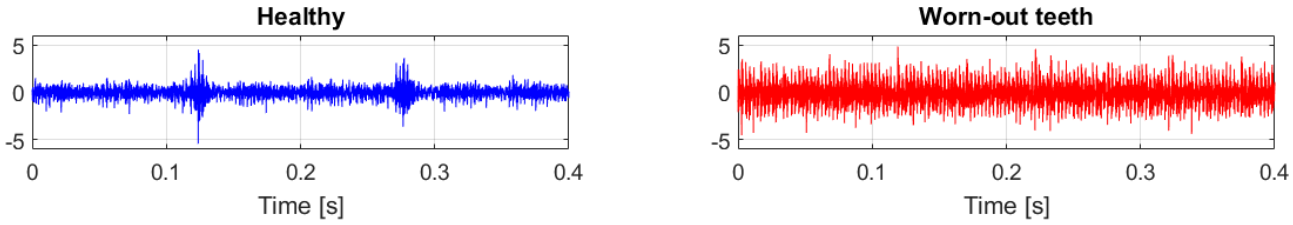

Figure 6-23 Raw data captured from the vibration of the gearbox with the worn-out teeth

Table 6-29 Statistical indicators of the vibration data of the gearbox with worn-out teeth

Statistical Indicator	Healthy	Worn-out teeth
Peak value (PV)	4.774 ms^{-2}	9.358 ms^{-2}
Root Mean Square (RMS)	0.660 ms^{-2}	1.053 ms^{-2}
Crest Factor (CF)	7.645 ms^{-2}	8.887 ms^{-2}
Kurtosis	4.115 ms^{-2}	4.169 ms^{-2}

There is evidently more energy in the vibration signal of the worn-out gearbox compared to the healthy one. This is attributed to the increased backlash within the gearbox teeth as a result of the wear [130]. There is an increase the peak value, root mean square, and kurtosis by 4.584 m/s^2, 0.393 m/s^2, and 0.054 m/s^2. The crest factor also increased by 1.242 m/s^2.

The results and analysis of the vibration spectrum are presented in Figure 6-24 and Table 6-30 below.

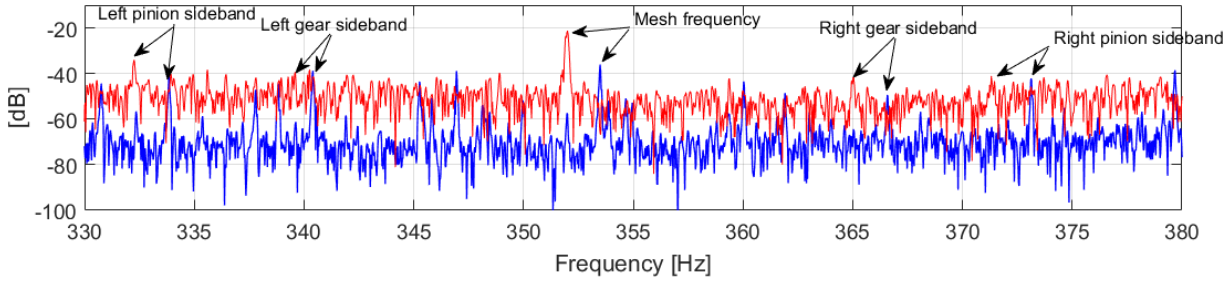

Figure 6-24 Vibration spectrum of the worn-out tooth gearbox in steady state showing the mesh frequency and the corresponding sidebands

Table 6-30 Fault components frequencies and amplitudes of the worn-out tooth gearbox

Component	Healthy		Worn-out teeth	
	Frequency [Hz]	Amplitude [dB]	Frequency [Hz]	Amplitude [dB]
Mesh frequency	353.5	-36.14	352.0	-21.99
Left pinion sideband	333.9	-40.45	332.3	-34.11
Right pinion sideband	373.1	-42.67	371.3	-41.10
Left gear sideband	340.4	-40.45	339.5	-40.90
Right gear sideband	366.6	-49.38	365.0	-43.20

The mesh frequency of the worn-out gearbox compared to the healthy gearbox increased by 14.15 and the left and right pinion sidebands increased by 6.34 dB and 1.57 dB respectively. The left gear sideband decreased by 0.45 dB and the right gear sideband increased by 6.18 dB.

The $f_s + f_m$ frequency of the worn-out gearbox was also investigated but could not be identified in the current spectrum. The results are presented in the appendix.

6.3.5 Concluding Remarks

The peak value, RMS and kurtosis of the faulty gearboxes was always higher than that of the healthy gearbox. The magnitudes of the peak value, RMS and kurtosis of the missing tooth gearbox were higher than that of the chipped tooth gearbox which reflected the increased severity of the fault. The kurtosis increases as the signal becomes less of a Gaussian distribution due to the impulses generated from the faulty gears [43]. Unlike the chipped tooth fault and the missing tooth fault, the crest factor of the worn-out gearbox was less than that of the healthy gearbox.

The peak value of the time signal may present a false positive in case of an isolated spike from a non-fault related source. To improve the credibility of peak value, it could be calculated after shorter time periods and a warning signal only applied in the case of a consistent variation of the peak value. The RMS however is not sensitive to isolated peaks of a short duration. It is a good indication of the overall condition of the gearbox but cannot be used to identify the type of fault. The performance of CF is closely related to that of the PV and the RMS; without reliable values of the PV and the RMS, CF cannot be used. Kurtosis, however, a good indicator of the existence of discrete gearbox fault such as the chipped tooth or the missing tooth. However, proper choice of thresholding parameters is important for the detection of the fault. Kurtosis is not a good indicator for a distributed fault like the worn-out gears.

The mesh frequency increased for the three faults that were investigated. The mesh frequency of the missing tooth gearbox was higher than that of the missing tooth gearbox which could be attributed to the increased severity of the fault. There was also an increase in the pinion sideband frequencies of the missing tooth gearbox compared to the chipped tooth gearbox. The changes in the pinion sideband frequencies can be attributed to the location of the fault on the gearbox pinion[130]. The worn-out gearbox only showed a relatively large increased in the mesh frequency and the left pinion sideband.
The mesh and sideband frequencies are good indicators to distinguish between discrete and distributed faults. The location of the fault can also be predicated by observation of the sideband frequencies. The discrete faults will affect the amplitude particular frequencies in the FFT in a manner similar to the variations of the pinion sideband frequencies observed above. Distributed faults, however, cause a much more significant increase in the mesh frequencies relative to the pinion frequencies. These faults however could not be observed from the vibration spectrum of the motor. This can be attributed to the small amplitudes of the vibrations and the interference from other vibrations on the test rig.

The amplitudes of $f_s + f_m$ frequencies of the faulty gearboxes all decreased while the amplitudes of the $f_s \pm f_p$ frequencies increased for the gearboxes with the discrete faults. MCSA worked very well for the discrete faults especially at the $f_s \pm f_p$ frequencies making this a plausible indicator of the presence of a discrete fault on the gearbox. However, overall, the use of the vibration spectrum of the gearbox vibrations performed better than the current spectrum to identify the faults on the gearbox.

Ultimately, the use of MCSA to identify the faults in the gearbox performed better than using the motor vibration spectrum to identify the faults on the gearbox. But the use of the gearbox vibration spectrum performed better than the MCSA. MCSA can be used to identify the discrete gearbox faults.

6.4 Reciprocating Compressor faults

The following section presents the results from the experiments conducted with the reciprocating compressors as the test loads. The vibrations obtained were from an accelerometer placed on the head of the compressor. The signals captured are essentially a combination of the responses to [30]:

(i) Flow induced vibrations such as those that occur when airflow interacts with valves or other parts of the system to cause periodic oscillations in the flow.

(ii) Vibration due to the valve plate hitting its seat when opening and closing.

Similar to the previous section, the time-domain statistical indicators of the healthy compressor are calculated and used as a baseline data. The FFT is also calculated and the piston frequency and its harmonics are also analysed.

The aim is to investigate the ability of the statistical indicators and the FFT of both the current and vibrations of the motor and reciprocating compressor to detect and identify faults in the compressor during steady state operation. The use of the motor vibrations and motor current to reliably identify the fault is also compared.

6.4.1 Healthy Compressor

The healthy compressor was fitted as the test load and run under steady state conditions for 30 seconds with the air-tank at 70 psi and 0 psi. The time domain signal and its corresponding statistical indicators are presented in Figure 6-25 and Table 6-31 below.

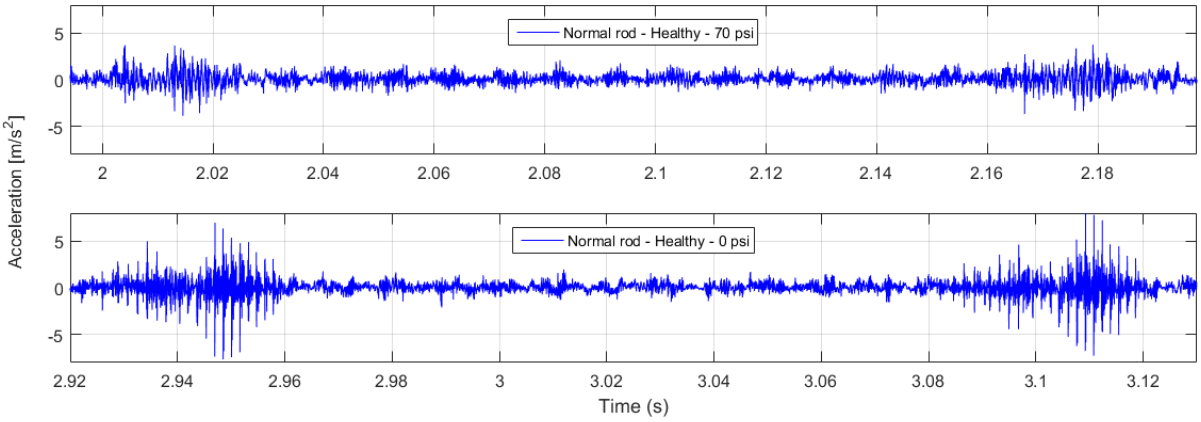

Figure 6-25 One cycle of raw vibration data of the compressor with the normal sized rod at 70 psi and 0 psi

Table 6-31 Statistical indicators of the healthy compressor vibration data

Statistical Indicator	Air-tank at 70 psi [m/s²]	Air-tank at 0 psi [m/s²]
Peak value (PV)	4.740	8.720
Root Mean Square (RMS)	0.627	0.810
Crest Factor (CF)	7.932	11.673
Kurtosis	5.781	16.831

There is a decrease in the statistical indicators of the vibration signals when the pressure in the air-tank is increased. The peak value, RMS and kurtosis all decrease by 3.98 m/s², 0.813 m/s², and 11.05 m/s². This can be attributed to the increased pressure on the air-tank side which leads to less displacement of the valve plate. The kurtosis values of >3 are indicative of the presence of the periodic spikes in the time-domain.

The vibration spectrum of the compressor is also analysed with emphasis on the piston frequency and its harmonics. The vibration data from the compressor accelerometer and that from the motor accelerometer were both analysed. The results and analysis are presented in Figure 6-26 and Table 6-32 below.

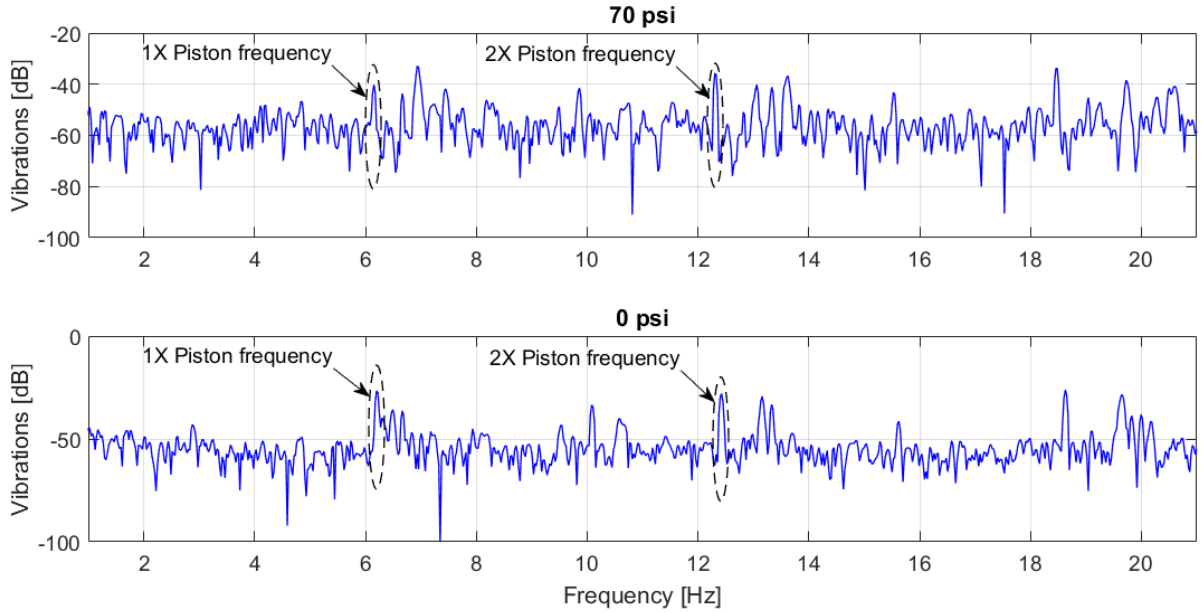

Figure 6-26 Vibration spectrum of healthy compressor at 70 psi and 0 psi using the compressor accelerometer data

Table 6-32 Amplitudes and vibrations of the piston frequencies and their harmonics for the healthy compressor using the compressor accelerometer data

Air-tank pressure	X Piston frequency	Frequency [Hz]	Amplitude [dB]
70 psi	**1X**	6.15	-40.24
	2X	12.30	-35.69
0 psi	**1X**	6.20	-26.65
	2X	12.43	-27.99

There is a reduction of 13.59 dB and 7.7 dB in the amplitudes of the 1X and 2X piston frequency respectively when the pressure in the air-tank was increased from 0 psi to 70 psi. The valves in the compressor open and close periodically (at piston frequency) and the amplitudes of the piston frequency in the FFT reflect the reduction in the displacement of the valves as the pressure in the air-tank is increased.

The vibration spectrum of the motor was also analysed for the piston frequencies of the reciprocating compressor and these are presented in Figure 6-27 and Table 6-33 below.

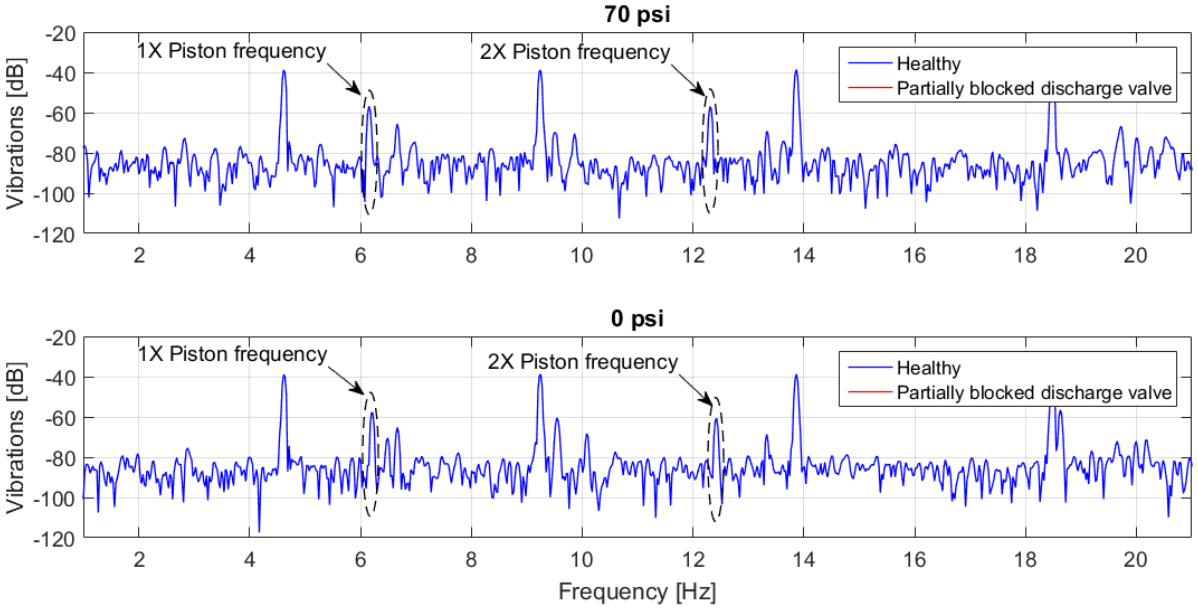

Figure 6-27 Vibration spectrum of the motor showing the piston frequency of the reciprocating compressor and its harmonics

Table 6-33 Amplitudes and frequencies of the 1X and 2X piston frequencies of the healthy compressor vibrations from the motor's accelerometer

Air-tank pressure	X Piston frequency	Frequency [Hz]	Amplitude [dB]
70 psi	1X	6.15	-56.85
	2X	12.30	-57.16
0 psi	1X	6.20	-54.77
	2X	12.43	-56.16

Similar to the observations from the accelerometer on the compressor, the amplitudes of the 1X and 2X piston frequencies decreased when the pressure in the air-tank was increased from 0 psi to 70 psi.

The motor current was also analysed with emphasis on the piston frequency sidebands of the supply frequency, $f_s \pm nf_r$. The results are presented in Figure 6-28 and Table 6-34 below.

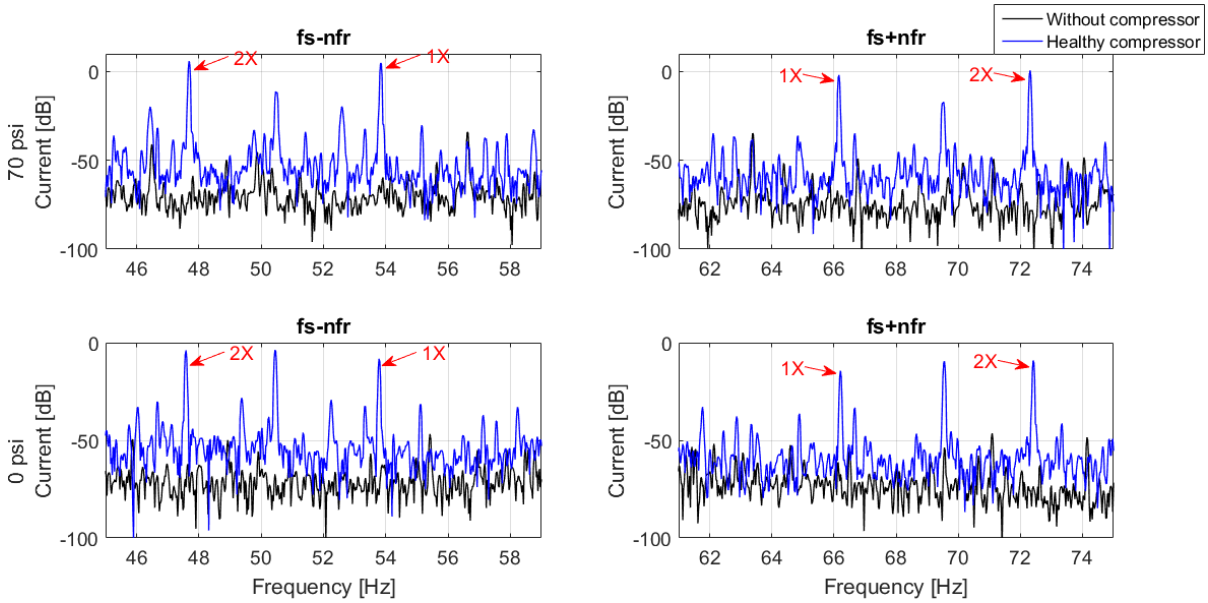

Figure 6-28 Current spectrum of the motor showing the $f_s \pm nf_r$ frequencies for $n = 1, 2$ with and without a healthy compressor connected as a load

Table 6-34 Amplitudes and frequencies of the $f_s \pm nf_r$ frequencies for $n = 1, 2$ of the healthy motor with the healthy compressor connected as a load

Air-tank pressure	Piston frequency	Frequency [Hz]	Amplitude [dB]
70 psi	$f_s - f_r$	53.83	4.88
	$f_s + f_r$	66.16	-1.95
	$f_s - 2 \cdot f_r$	47.68	5.88
	$f_s + 2 \cdot f_r$	72.31	0.63
0 psi	$f_s - f_r$	53.78	-8.25
	$f_s + f_r$	66.21	-14.40
	$f_s - 2 \cdot f_r$	47.56	-5.89
	$f_s + 2 \cdot f_r$	72.44	-10.07

The amplitudes of the 1X and 2X piston frequencies increased when the air-tank pressure was increased from 0 psi to 70 psi.

6.4.2 Partially Blocked Discharge Fault

The healthy compressor was fitted with a partially blocked discharge valve and run under steady state conditions. 30 seconds of vibration data was captured with the pressure in the air-tank at 70 psi and 0 psi. The vibration signals in the time domain and their corresponding statistical indicators are presented in Figure 6-29 and Table 6-35 respectively.

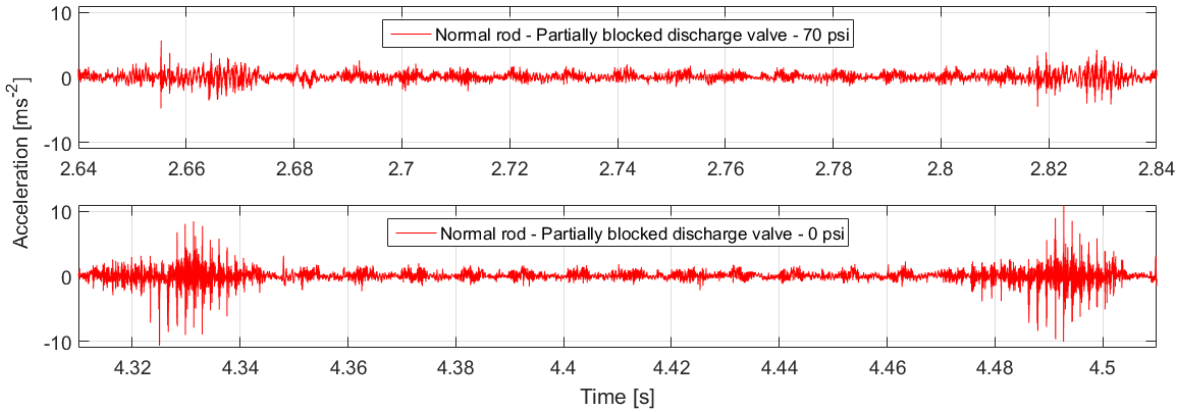

Figure 6-29 One cycle of raw vibration data of the healthy compressor with the normal sized rod at 70 psi and 0 psi

Table 6-35 Statistical indicators of the vibration data of the compressor with a partially blocked discharge

Statistical Indicator	Healthy		Partially blocked discharge	
	70 psi Value [m/s²]	0 psi Value [m/s²]	70 psi Value [m/s²]	0 psi Value [m/s²]
Peak value (PV)	4.740	8.720	6.979	11.293
Root Mean Square (RMS)	0.627	0.810	0.662	0.946
Crest Factor (CF)	7.932	11.673	10.536	15.049
Kurtosis	5.781	16.831	7.184	29.585

The results obtained are similar to those observed in the previous section in that all the statistical indicators of the vibration signals reduced in magnitude when the pressure in the air-tank increased to 70 psi. The peak value, RMS, Crest Factor and kurtosis had a reduction of 4.314 m/s², 0.284 m/s², 4.513 m/s², and 22.401 m/s².

However, the statistical indicators of the vibration signals of the faulty compressor are higher than those of the healthy compressor. This can be attributed to the increased pressure in the cylinder due to the constricted flow of air through the discharge valve which increases the displacement of the valve plate. The increased pressure in the cylinder also results increased mechanical impact at TDC and BDC [63]. The variations in the statistical indicators from the baseline data are shown in Table 6-36 below.

Table 6-36 Variations in the statistical indicators of the vibration data of the compressor with a partially blocked discharge

Statistical Indicator	70 psi Value [m/s²]	0 psi Value [m/s²]
Peak value (PV)	2.239	2.573
Root Mean Square (RMS)	0.035	0.136
Crest Factor (CF)	2.604	3.376
Kurtosis	1.403	12.754

The results from the analysis of the vibration spectrum with the air-tank pressure at 70 psi and at 0 psi are presented in Figure 6-30 and Table 6-37 below.

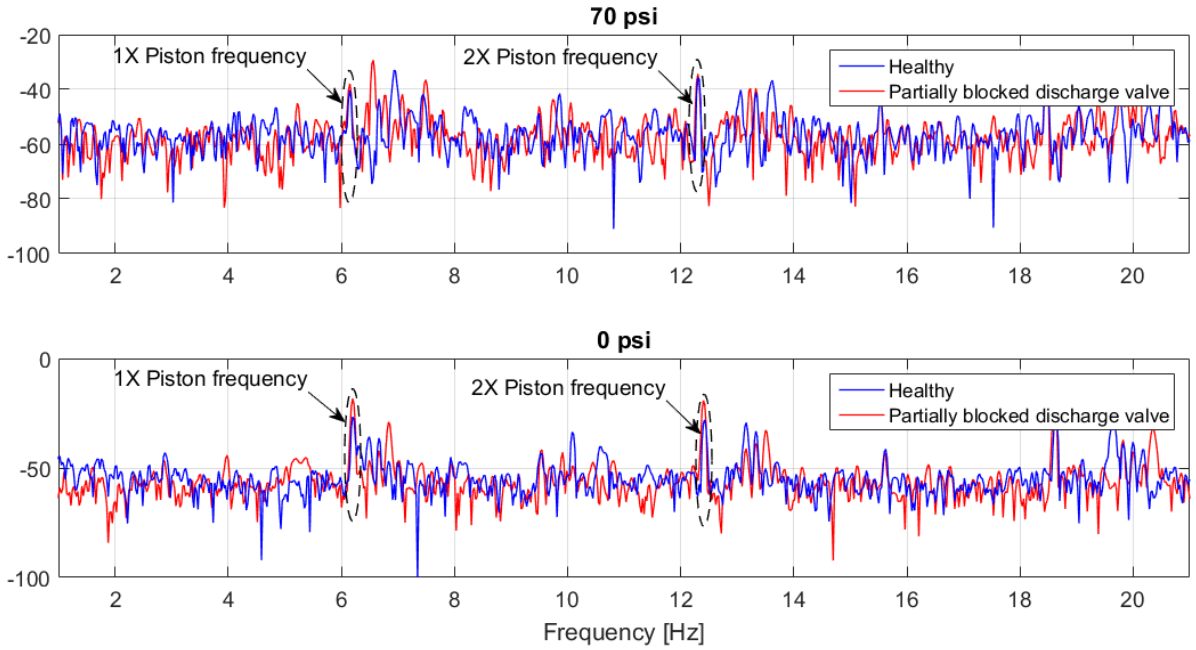

Figure 6-30 FFT of vibrations from the compressor accelerometer showing the 1X and 2X piston frequencies of the healthy compressor and the compressor with a partially blocked discharge valve at 70 psi and 0 psi

Table 6-37 Amplitudes and vibrations of the piston frequencies and their harmonics for the compressor with a partially blocked discharge valve from the compressor accelerometer

Air-tank pressure	Piston frequency	Healthy		Partially blocked discharge		Difference
		Frequency [Hz]	Amplitude [dB]	Frequency [Hz]	Amplitude [dB]	Amplitude [dB]
70 psi	1X	6.15	-40.24	6.15	-37.96	2.28
	2X	12.30	-35.69	12.30	-34.37	1.32
0 psi	1X	6.20	-26.65	6.20	-18.32	8.33
	2X	12.43	-27.99	12.4	-19.22	8.77

With the air-tank pressure at 70 psi, the amplitudes of the 1X and 2X piston frequencies increased for the compressor with the partially blocked discharge valve. However, there was a slight increase in the amplitudes of the 1X and 2X piston frequencies with the air-tank pressure at 70 psi compared to that when the air-tank pressure was at 70 psi. There is also a decrease in the amplitudes of the 1X and 2X piston frequencies as the pressure in the air-tank is increased from 0 psi to 70 psi.

The vibration spectra from the motor's accelerometer are presented in Figure 6-31 and Table 6-38 below.

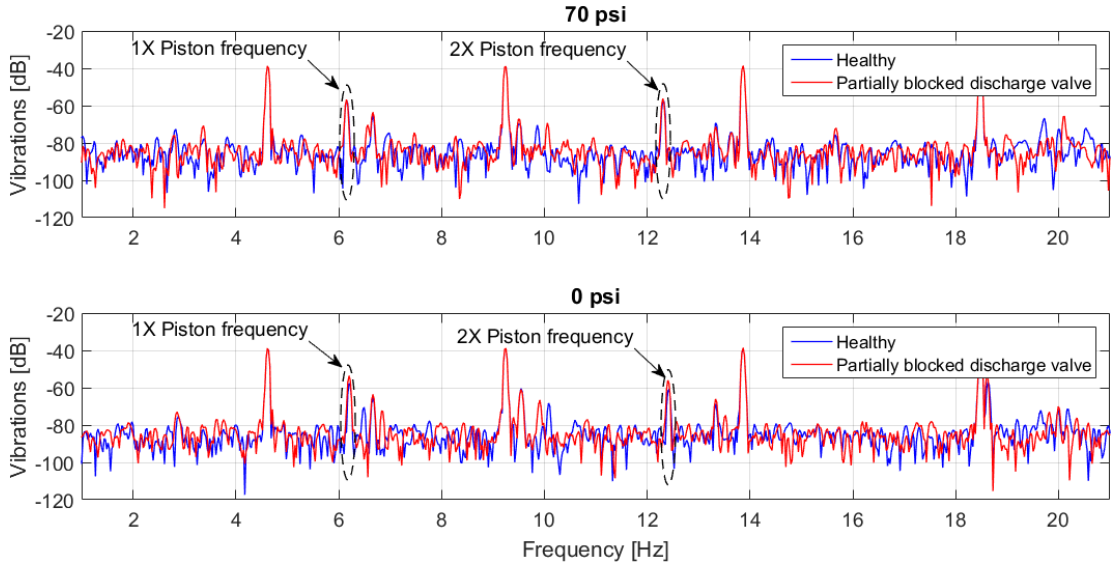

Figure 6-31 FFT of vibrations from the motor accelerometer showing the 1X and 2X piston frequencies of the healthy compressor and the compressor with a partially blocked discharge valve at 70 psi and 0 psi

Table 6-38 Amplitudes and vibrations of the piston frequencies and their harmonics for the compressor with a partially blocked discharge valve from the motor's accelerometer

Air-tank pressure	Frequency	Healthy		Partially blocked discharge		Difference
		Frequency [Hz]	Amplitude [dB]	Frequency [Hz]	Amplitude [dB]	Amplitude [dB]
70 psi	1X	6.15	-56.85	6.15	-56.73	0.12
	2X	12.30	-57.16	12.30	-56.28	0.88
0 psi	1X	6.20	-54.77	6.20	-53.58	1.19
	2X	12.43	-56.16	12.40	-56.04	0.12

Similar to the observations from the accelerometer on the compressor, the 1X and 2X piston frequency amplitudes increased slightly at 70 psi compared to the increases in amplitude with the air-tank pressure at 0 psi.

The results from the analysis of the current spectrum are also presented in Figure 6-32 and Table 6-39 below with emphasis on the $f_s - f_r$, $f_s + f_r$, $f_s - 2 \cdot f_r$ and $f_s + 2 \cdot f_r$ frequencies.

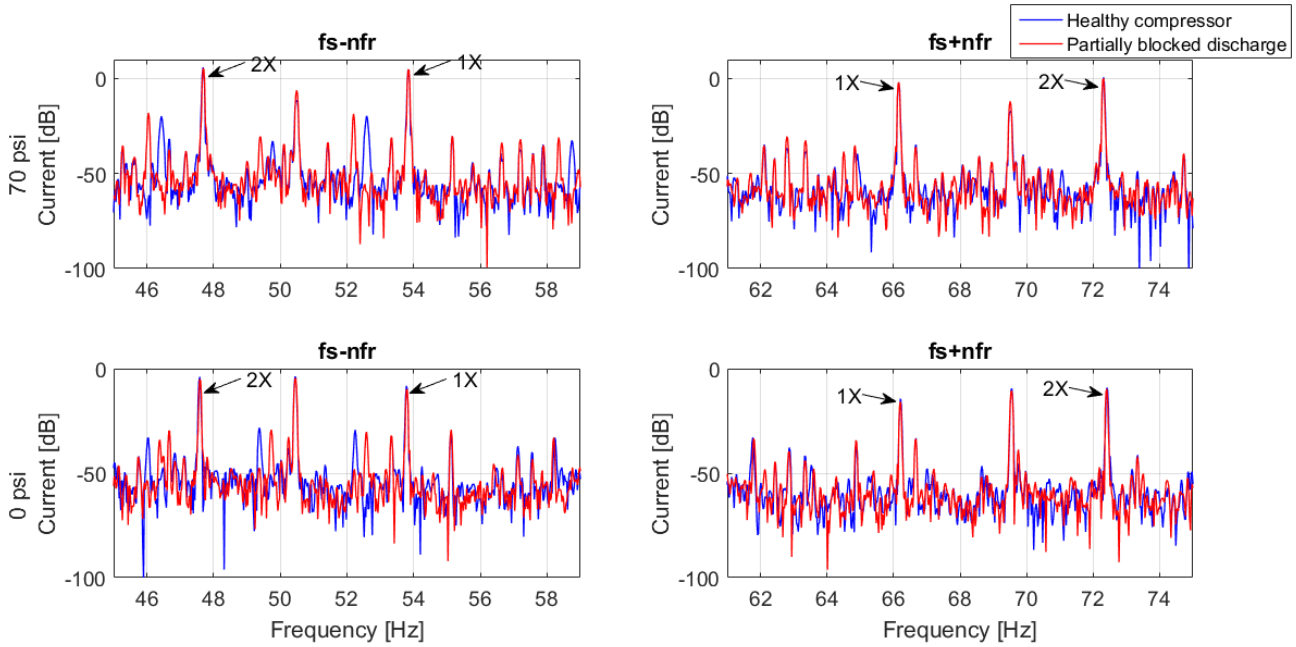

Figure 6-32 Current Spectrum of the healthy compressor and the compressor with a partially blocked discharge valve under steady state conditions showing the $f_s \pm f_r$ frequencies with air-tank pressure of 70 psi and 0 psi

Table 6-39 Amplitudes and frequencies of the $f_s \pm nf_r$ frequencies for $n = 1, 2$ with the air-tank pressure at 70 psi and 0 psi

Air-tank pressure	Frequency	Healthy		Partially blocked discharge		Difference
		Frequency [Hz]	Amplitude [dB]	Frequency [Hz]	Amplitude [dB]	Amplitude [dB]
70 psi	$f_s - f_r$	53.83	4.88	53.86	4.72	- 0.16
	$f_s + f_r$	66.16	-1.95	66.16	-2.12	-0.17
	$f_s - 2 \cdot f_r$	47.68	5.88	47.68	5.10	-0.78
	$f_s + 2 \cdot f_r$	72.31	0.63	72.31	0.10	-0.53
0 psi	$f_s - f_r$	53.78	-8.25	53.81	-10.12	-1.87
	$f_s + f_r$	66.21	-14.40	66.21	-15.84	-1.44
	$f_s - 2 \cdot f_r$	47.56	-5.89	47.58	-5.11	0.78
	$f_s + 2 \cdot f_r$	72.44	-10.07	72.41	-9.77	0.30

The amplitudes of the $f_s \pm f_r$ frequencies for the scenario with the faulty compressor were less than that of the scenario of the healthy compressor. The $f_s \pm 2 \cdot f_r$ frequencies, however, were inconsistent; decreasing for the faulty scenario when the air-tank pressure was 70 psi and increasing for the faulty scenario when the air-tank pressure was 0 psi.

6.4.3 Blocked Suction Fault

The suction of the reciprocating compressor was blocked, as described in section 5.4.2, cutting off air supply to the cylinder. 30 seconds of data was captured and the analysis is presented below. This was only performed with the air-tank pressure at 0 psi as a precautionary measure. The vibration signal in the time domain and its corresponding statistical indicators are shown in Figure 6-33 and Table 6-40 respectively.

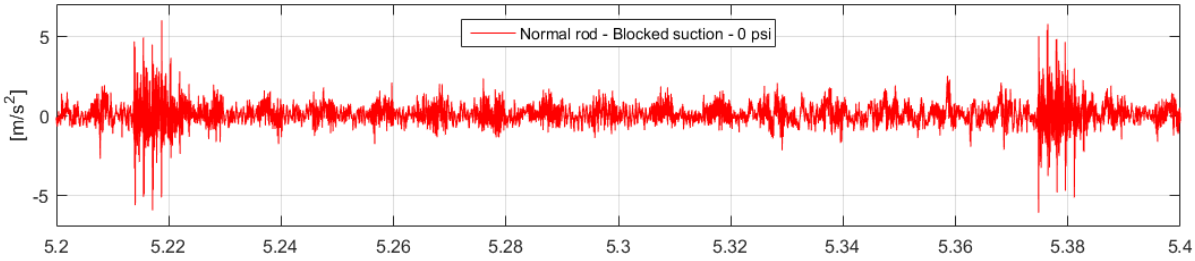

Figure 6-33 One cycle of raw vibration data of the blocked suction compressor with the normal sized rod at 0 psi

Table 6-40 Statistical indicators of the vibration data of the compressor with a blocked suction

Statistical Indicator	Healthy at 0 psi [m/s²]	Blocked suction [m/s²]
Peak value (PV)	8.720	7.302
Root Mean Square (RMS)	0.810	0.681
Crest Factor (CF)	11.673	10.724
Kurtosis	16.831	11.672

The vibration signals observed in the time domain occur in shorter spats compared to those observed for the normal compressor. Unlike the partially blocked discharge fault, the blocked suction fault has a reduction in the statistical indicators of the vibration data. The peak value, RMS, crest factor and kurtosis each decrease by 1.418 m/s², 0.129 m/s², 0.949 m/s², and 5.159 m/s².

The results from the analysis of the vibration spectrum of the compressor using the compressor accelerometer data are presented in Figure 6-34 and Table 6-41 below.

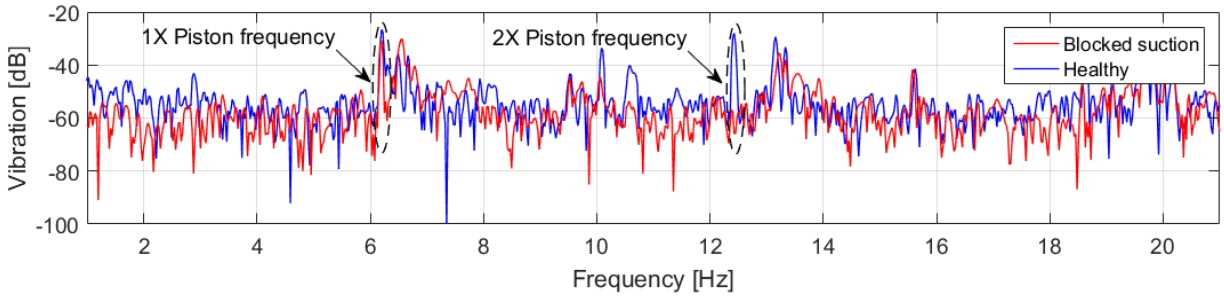

Figure 6-34 Vibration spectrum from the compressor accelerometer of the blocked suction compressor with the normal sized rod at 0 psi

Table 6-41 Amplitudes and vibrations of the piston frequencies and their harmonics for the compressor with a blocked suction observed from the compressor accelerometer

X Piston frequency	Healthy		Blocked suction	
	Frequency [Hz]	Amplitude [dB]	Frequency [Hz]	Amplitude [dB]
1X	6.20	-26.65	6.20	-30.88
2X	12.43	-27.99	12.43	-59.97

The blocked suction fault saw a reduction in the amplitude of the 1X Piston frequency by 4.23 dB while the amplitude of the 2X Piston frequency decreased by 31.98 dB. This is a reflection of the shorter time span of the vibrations observed in the time domain.

The results from the analysis of the vibration spectrum of the compressor using the motor accelerometer data is presented in Figure 6-35 and Table 6-42 below.

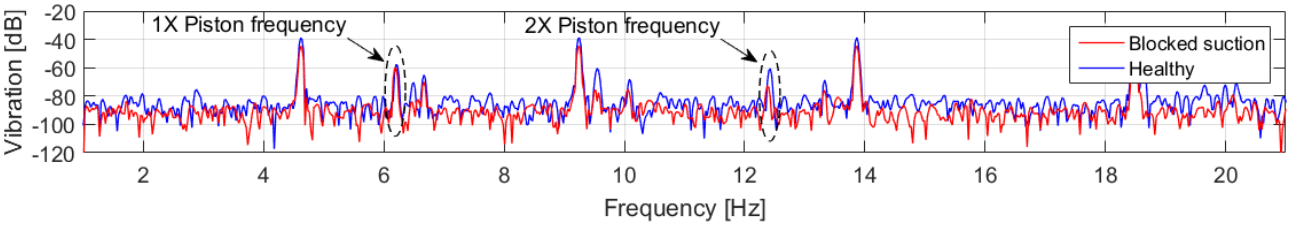

Figure 6-35 Vibration spectrum from the motor accelerometer of the blocked suction compressor with the normal sized rod at 0 psi

Table 6-42 Amplitudes and vibrations of the piston frequencies and their harmonics for the compressor with a blocked suction observed from the motor accelerometer

Piston frequency	Healthy		Blocked suction	
	Frequency [Hz]	Amplitude [dB]	Frequency [Hz]	Amplitude [dB]
1X	6.20	-54.77	6.20	-60.04
2X	12.43	-56.16	12.38	-72.95

For the compressor with a blocked suction, there was a decrease in the amplitude of the 1X piston frequency by 5.27 dB and a reduction of 16.79 dB in the amplitude of the 2X piston frequency.

The current spectrum of the motor was also analysed and the results are presented in Figure 6-36 and Table 6-36 below.

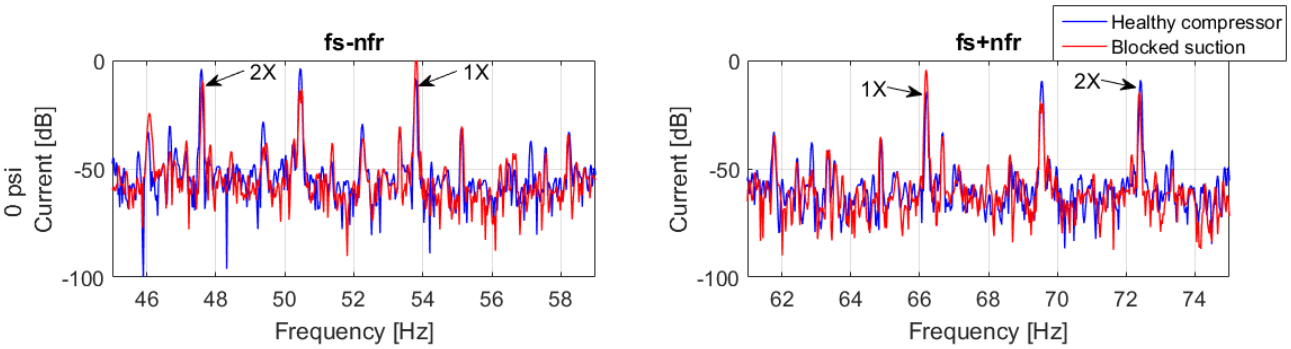

Figure 6-36 Current Spectrum of the motor current under steady state conditions showing the $f_s \pm nf_r$ frequencies $(n = 1, 2)$ with the healthy compressor connected and with the compressor with the blocked suction connected

Table 6-43 Amplitudes and frequencies of $f_s \pm nf_r$ frequencies $(n = 1, 2)$ of the healthy motor current with the healthy compressor connected and with the blocked suction connected

Component	Healthy		Blocked suction	
	Frequency [Hz]	Amplitude [dB]	Frequency [Hz]	Amplitude [dB]
$f_s - f_r$	53.78	-8.25	53.81	-1.60
$f_s + f_r$	66.21	-14.40	66.19	-4.36
$f_s - 2 \cdot f_r$	47.56	-5.89	47.61	-9.58
$f_s + 2 \cdot f_r$	72.44	-10.07	72.39	-14.60

The amplitudes of the $f_s + f_r$ and $f_s - f_r$ frequencies increased by 6.65 dB and 10.04 dB respectively while the amplitudes of the $f_s - 2 \cdot f_r$ and $f_s + 2 \cdot f_r$ frequencies decreased by 3.69 dB and 4.53 dB respectively.

6.4.4 Concluding Remarks

The PV, RMS, and kurtosis of the vibration signals all decreased when the pressure in the air-tank was increased. This is observed in both the healthy compressor and the compressor with the partially blocked discharge valve. This can be attributed to the opening/closing of the discharge valve [63]. However, the PV, RMS, and kurtosis of the vibration signals increased when the discharge of the compressor was partially blocked. This can be attributed to the increased pressure in the cylinder due to the constricted air-flow.
The blocked suction fault, however, led to reduction in the PV, RMS, and kurtosis of the vibration signals. This can be attributed to the reduced pressure in the cylinder which leads to a reduction in the displacement of the discharge valve and the impact of the piston at TDC and BDC [63].

Similar to the observations in 6.3.5, the PV may present a false positive if not carefully evaluated. The RMS value did not change much for either fault and is therefore not a credible indicator of the existence of either of the investigated faults. The lack of the credibility with the PV and RMS makes the CF a poor parameter for detection of the compressor faults. The kurtosis, however, varied significantly with the healthy and faulty compressors. It increased especially with the blocked suction fault because of the shorter durations of the prominent vibration signals. The kurtosis could therefore be used as an indicator of the pressure in the compressor and therefore as an indicator of the existence of a fault. However further analysis of the compressor is still required to identify the fault and careful choice of the thresholding parameters is imperative.

The amplitudes of the 1X and 2X piston frequencies reduced for the compressor with the partially blocked discharge valve increased with the air-tank at 70 psi and 0 psi. However, it increased significantly with the air-tank pressure at 0 psi. The changes in amplitude were less when the vibration data was taken from the motor's accelerometer compared to when it was taken from the compressor's accelerometer. The partially blocked discharge fault showed a consistent reduction in the amplitude of the $f_s \pm f_r$ frequencies, but the changes in amplitude were much less than those of the 1X and 2X piston frequencies observed in the vibration spectrum. The $f_s \pm 2 \cdot f_r$ harmonic frequencies were inconsistent and the results suggest that they should not be used as indicators of the partially blocked discharge fault. The vibration spectrum was a much better option for the identification of the partially blocked discharge valve fault especially under conditions of low air-tank pressure.

The amplitudes of the 1X and 2X piston frequencies of the compressor with the blocked suction both reduced; the decrease in the amplitude of the 2X piston frequency was significantly larger than that of the 1X piston frequency. This was observed in the vibration spectrum of both the data from the accelerometers on the motor and compressor. The blocked suction fault also showed an increase in the amplitudes of the $f_s \pm f_r$ frequencies and an increase in the amplitudes of the $f_s \pm 2 \cdot f_r$ frequencies though the changes in amplitude were not as large as those from the vibration spectrum.

Ultimately, the vibrations from the motor and the motor current both performed well when used for the identification of the faults on the motor.

7. Results and Discussion for Start-up Conditions

7.1 Introduction

This section presents the results from the DWT on the test motors during start up. The sampling frequency is set to 25.6 kHz, but the signal is downsampled by a factor of 3 to 8,533.33 Hz to alter the DWT bands for better observation of the transition of the frequency components. The signal is then decomposed to 10 levels, shown in Table 7-1, after which the transition of the required frequencies is traced based on their expected evolution characteristics like was done in [82].

Table 7-1 DWT Decomposition levels

Level	Frequency band (Hz)
D1	2133.33 – 4266.67
D2	1066.67 – 2133.33
D3	533.33 – 1066.67
D4	266.67 – 533.33
D5	133.33 – 266.67
D6	66.66 – 133.33
D7	33.33 – 66.66
D8	16.66 – 33.33
D9	8.33 – 16.67
D10	4.17 – 8.33
Approximation	0 – 4.17

7.2 Induction Motors

The raw data of the healthy motor current and vibrations are shown in Figure 7-1 below, and the evolution of the signature fault frequencies that will be also investigated in this chapter is shown in Figure 7-2.

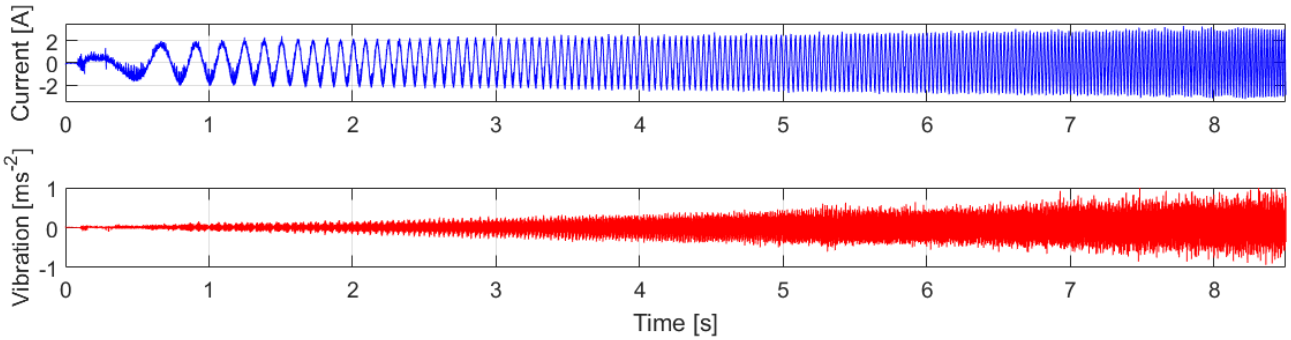

Figure 7-1 Raw data of the current and vibration signals of the healthy motor during start-up

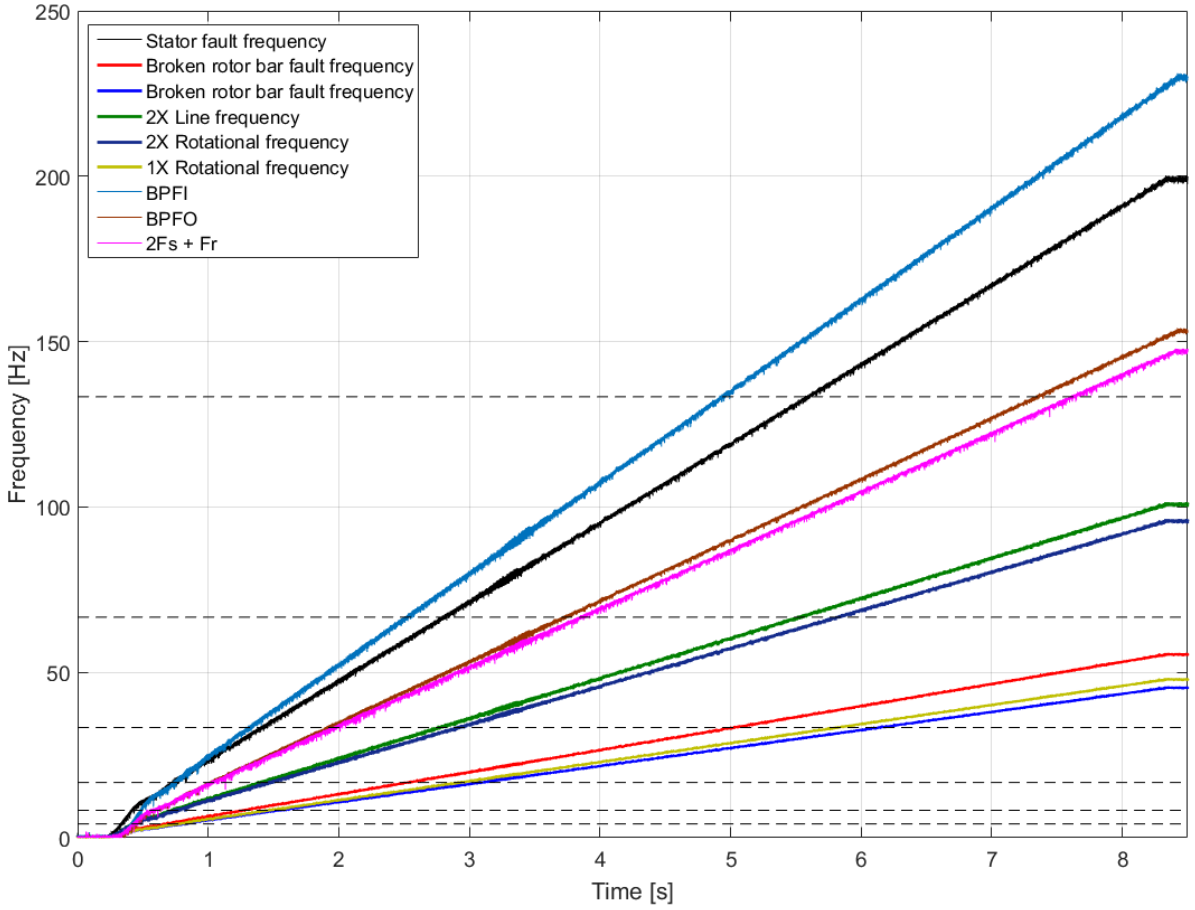

Figure 7-2 Progression of the fault frequency components during start-up

7.2.1 Stator Inter-turn Fault

Four turns of the motor with the inter-turn faults were shorted and the motor was ramped up to a voltage of 190 Volts and a frequency of 50 Hz over a period of 10 seconds. The vibration signal in the time domain is shown in Figure 7-3 below.

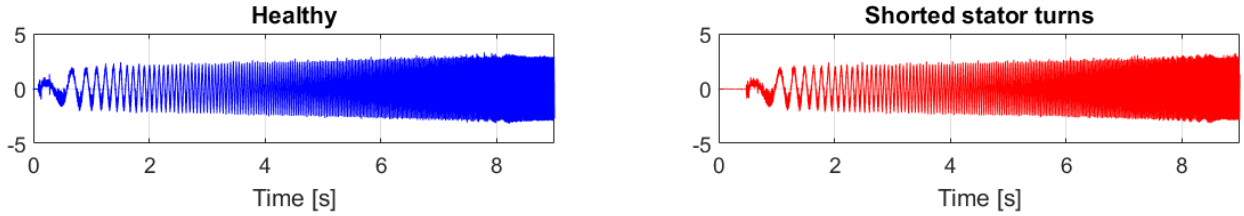

Figure 7-3 Raw current data of the motor with shorted stator turns during start-up

The $f_s\left(\frac{n}{2}(1-s)+k\right)$ frequency component, with $n = 2$ and $k = 3$, was used to identify the shorted stator turn fault in the motor current and the 2X rotational and 2X line frequencies were used to identify the fault in the vibrations. The locations of the signals in the time domain of the DWT are estimated using Figure 7-2. Analysis of the motor under steady-state conditions revealed the fault frequency at 198.85 Hz. The DWT of the motor current showing the progression of the fault through the frequencies 66.67 Hz to 266.67 Hz is shown in Figure 7-4 below.

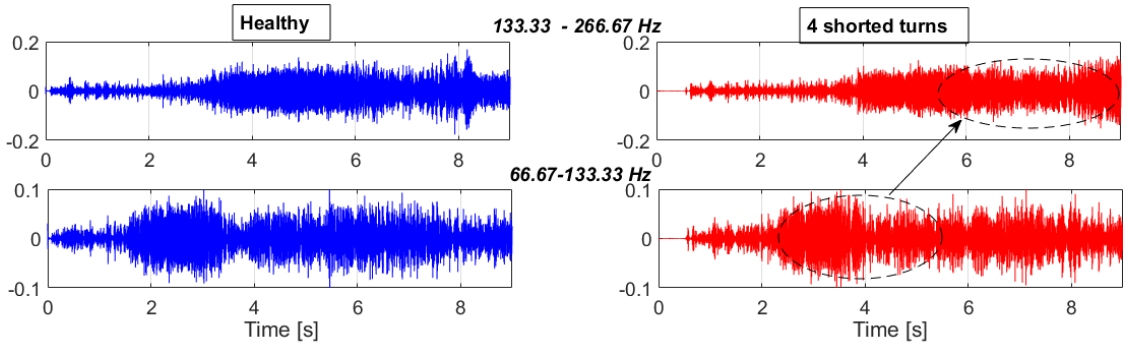

Figure 7-4 DWT of the motor current with shorted stator turns showing the progression of the stator fault frequency

Similar to the observations under steady-state conditions in section 6.2.1, there is no significant change in the energy in the frequency bands through which the fault frequencies traverse.

The DWT of the vibration signal showing the progression of the 2X rotational and 2X line frequencies is also shown in Figure 7-5 below.

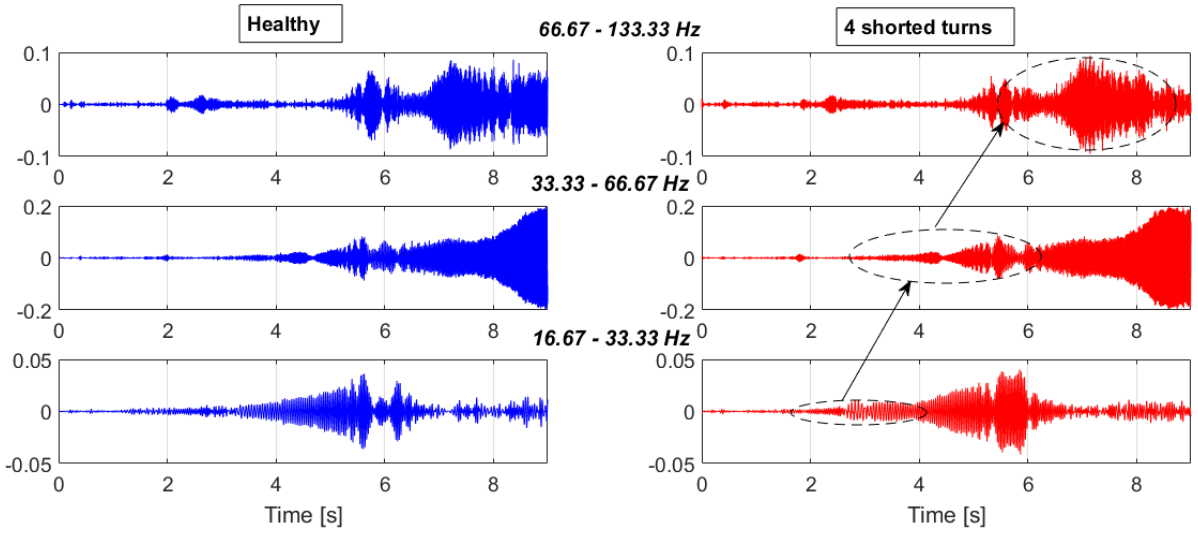

Figure 7-5 DWT of the motor vibrations with shorted stator turns showing the progression of the 2X rotational and 2X line frequencies

The results obtained are also similar to those obtained under steady-state conditions; there is an evident increase the energy in the frequency bands through which the 2X Rotational and 2X Line frequencies traverse for the motor with shorted stator turns.

7.2.2 Broken Rotor Bar Fault

The motor with 3 broken rotor bars was loaded with the servo-motor drive and the load was set to 100%. It was ramped up to a voltage of 190 Volts and a frequency of 50 Hz over a 10 second period and then the DWT was applied to the axial vibration signal. The motor current signal in the time domain is shown in Figure 7-6 below.

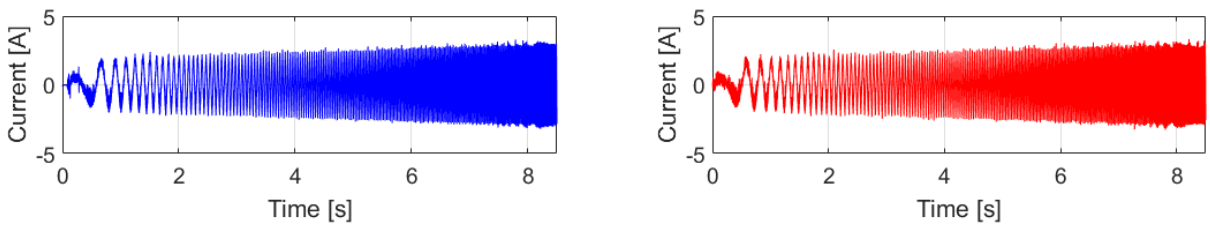

Figure 7-6 Raw current data of the healthy motor and the motor with 3 broken rotor bars in the time domain

The DWT of the current and vibration signals of the motor were analysed for the broken bar fault. The $(1 \pm 2s)f$ frequencies were used identify the fault in the current while the 1X and 2X rotational frequencies were used to identify the faults in the vibration signal. The $(1 - 2s)f$ and $(1 + 2s)f$ frequencies were observed at 45.19 Hz and 52.44 Hz under steady-state conditions.

The DWT of the motor current is presented in Figure 7-7 below.

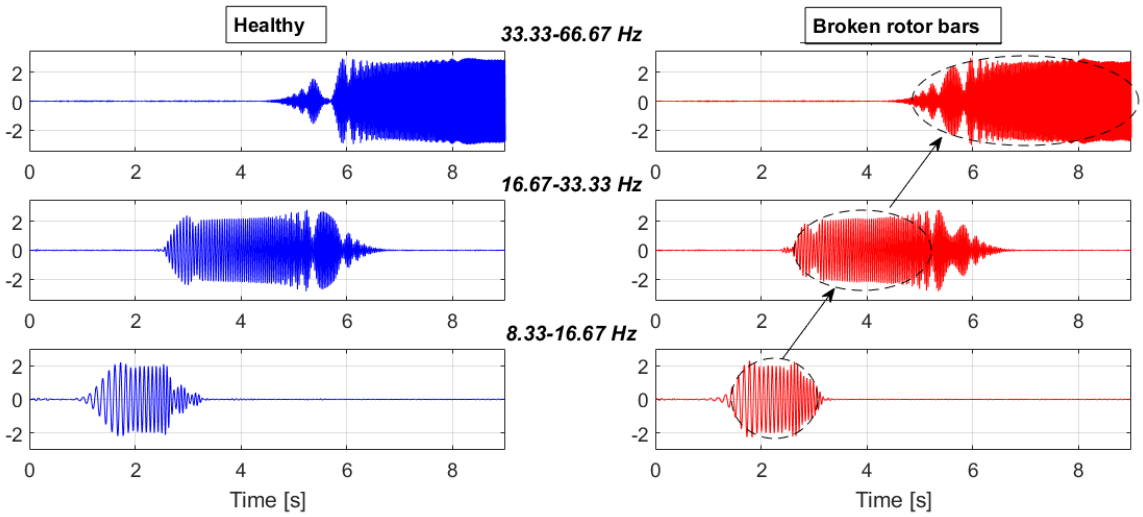

Figure 7-7 DWT of the start-up current signals of the healthy motor and the motor with 3 broken rotor bars showing the progression of the $(1 \pm 2s)f$ frequencies

There is an increase in the energy in the frequency bands of the motor with the broken rotor bars, particularly in the 33.33 – 66.67 Hz frequency band where the sidebands settle.

The vibration data of the motor during the transient conditions was also analysed and the results are presented in Figure 7-8 below.

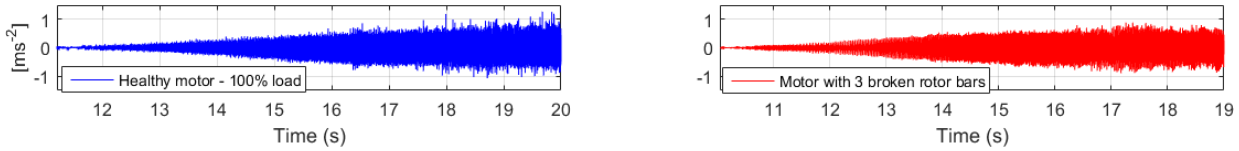

Figure 7-8 Raw vibration data of the healthy motor and the motor with 3 broken rotor bars

The DWT of the motor vibrations showing the progression of the 1X and 2X rotational frequencies is shown in Figure 7-9 below.

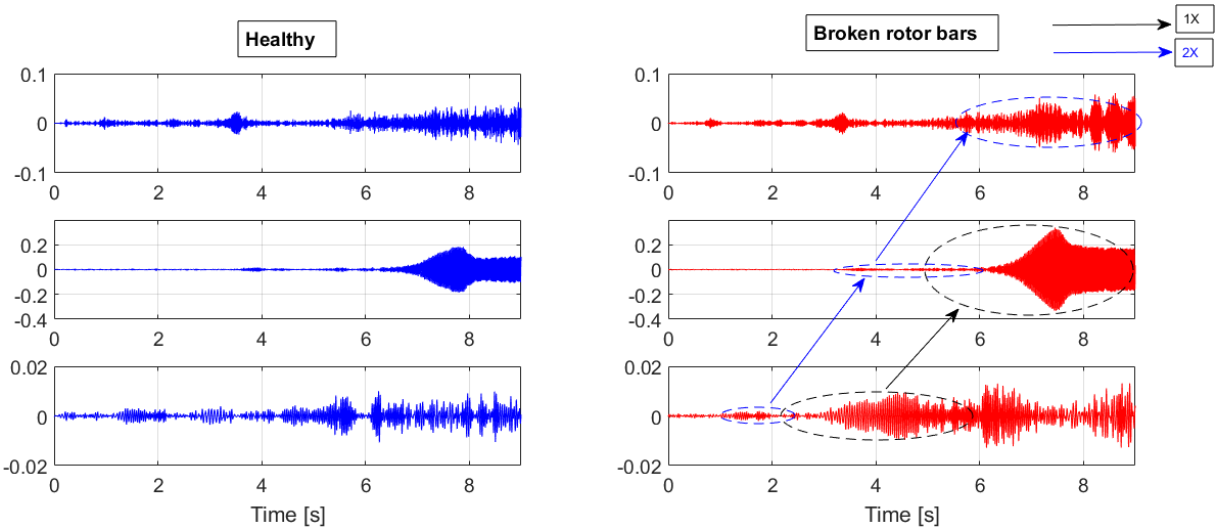

Figure 7-9 DWT of the start-up vibration signals of the healthy motor and the motor with 3 broken rotor bars showing the progression of the 1X and 2X rotational frequencies

Analysis of the DWT of the start-up signal shows increased energy in the frequency bands through which the 1X and 2X rotational frequencies traverse. This is in line with the observations in section 6.2.2 in which it was observed in the FFT of the steady state signals of the healthy motor and the motor with 3 broken bars that the amplitudes at the 1X and 2X rotational frequencies increased in the vibration spectrum and the amplitudes of the $(1 \pm 2s)f$ frequencies increased for the motor with the broken rotor bars.

7.2.3 Bearing Fault

The motor with the bearing faults was loaded with the servo-motor and ramped up to 190 Volts and a frequency of 50 Hz. The progression of the BPFI and BPFO frequencies that was plotted in Figure 7-2. The vibration signals of the healthy and faulty motors during start-up, in the time domain, are shown in Figure 7-10 below.

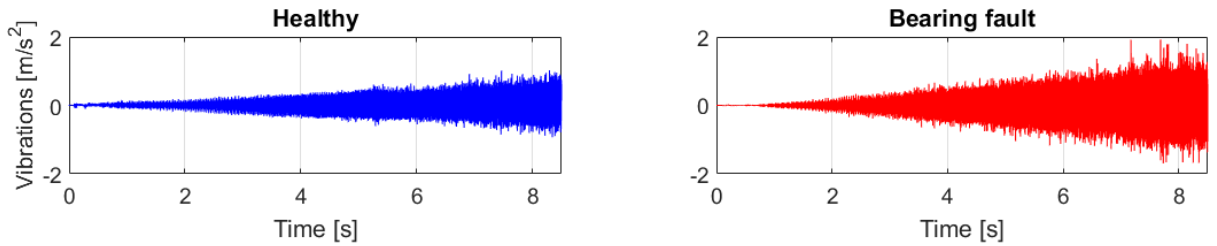

Figure 7-10 Raw vibration data of the healthy motor and the motor with faulty bearings during start-up

Similar to the observations under steady-state conditions, the DWT of the vibration data performed better than that of current and is presented below with the BPFO and BPFI frequencies highlighted. The BPFO and BPFI frequencies were identified at 143.1 Hz and 240.4 Hz respectively under steady state conditions. The DWT of the vibration signals of the healthy and faulty motors showing the progression of the BPFO and BPFI frequencies is shown in Figure 7-11 below.

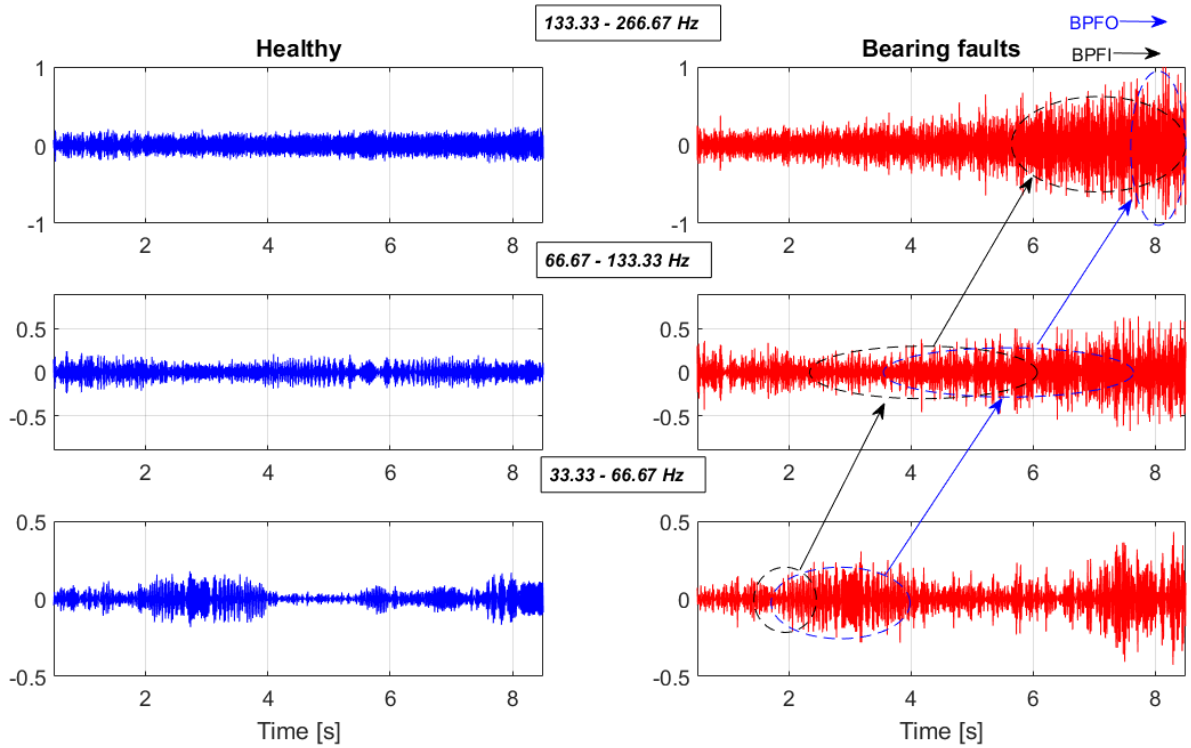

Figure 7-11 DWT's showing the BPFI and BPFO frequencies from the motor vibrations during start-up

For the motor with the faulted bearings, there is an evident increase in the energy in the frequency bands through which the BPFO and BPFI frequencies traverse. The same was observed when the DWT was applied to the motor current, however, there was a more significant increase in the DWT of the vibration.

7.2.4 Bowed Rotor Fault

The healthy motor and the motor with the bowed rotor were loaded with the servo motor and the motors were linearly ramped up to 190 Volts and a frequency of 50 Hz. The vibration signals of the healthy and faulty motors, in the time domain, are shown in Figure 7-12 below.

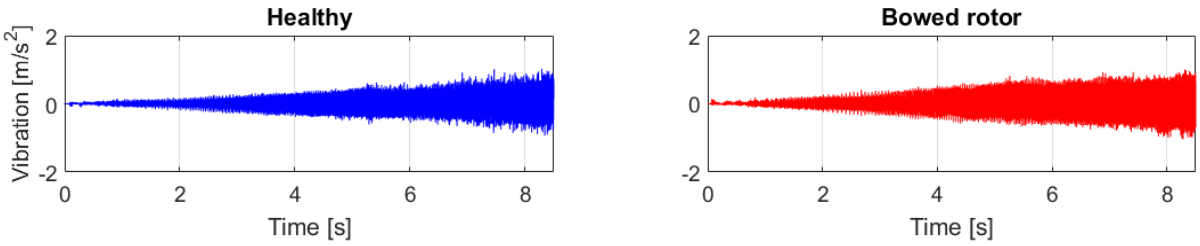

Figure 7-12 Raw vibration data of the healthy motor and the motor with the bowed rotor

The DWT of the vibration data performed better than that of the current data and is plotted in Figure 7-13 below. The progression of the $2f_s + f_r$ and 2X rotational frequencies are shown below. The $2f_s + f_r$ and 2X rotational frequencies were identified at 148.97 Hz and 48.97 Hz respectively under steady-state conditions.

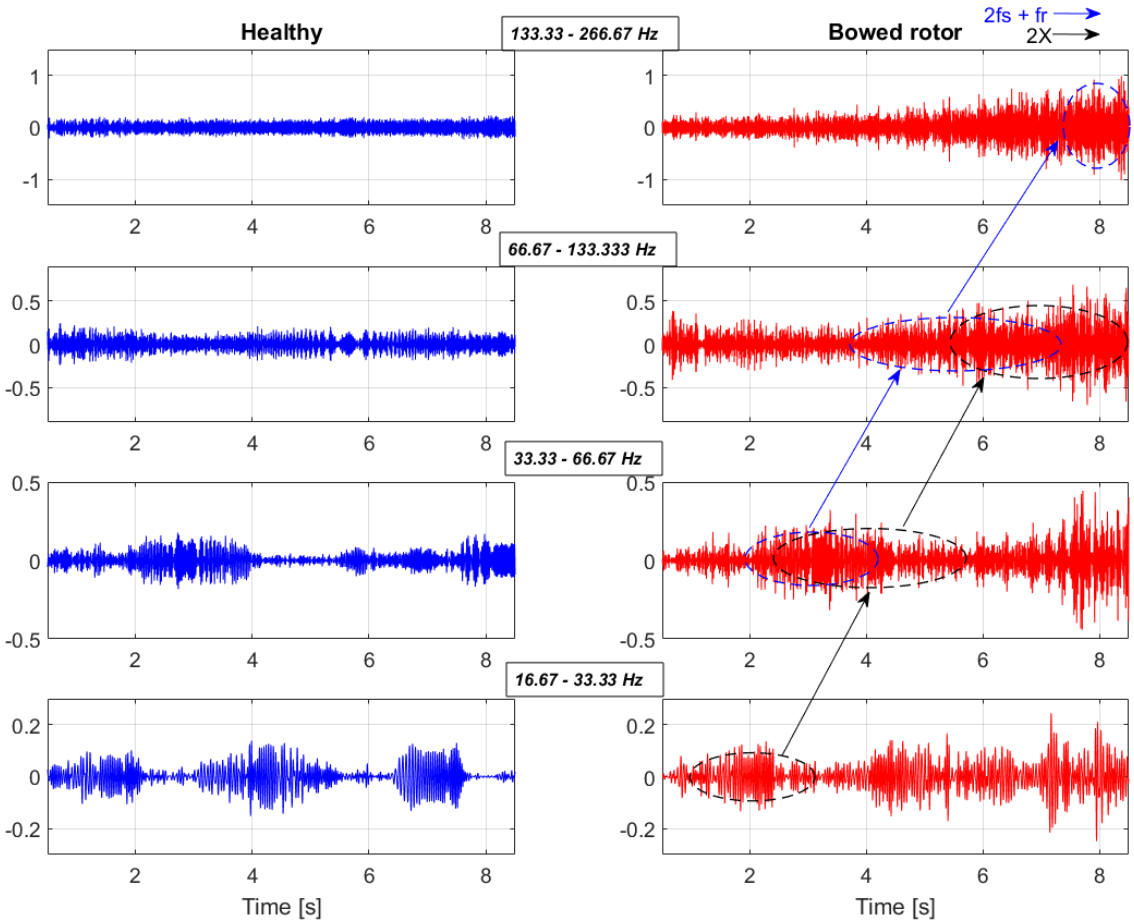

Figure 7-13 DWT's showing the $2f_s + f_r$ and 2X rotational frequencies from the motor vibrations during start-up

For the motor with the bowed rotor, there is an evident increase in the energy in the frequencies through which the $2f_s + f_r$ and 2X rotational frequencies traverse; similar to the observations in section 7.2.4.

7.2.5 Concluding Remarks

The use of the DWT to identify the stator inter-turn, broken rotor bar, bearing and bowed rotor faults was successful. The results obtained were similar to those obtained under steady-state conditions. The DWT of the motor vibrations performed better than that of the motor current for all the faults. This can be attributed to the noise from the inverter harmonics which deteriorates the performance of the DWT of the motor current [137].

The DWT of the motor current, however, was able to identify the faults for the broken rotor bar, both with and without the Hilbert transform, as well as the bearing and bowed rotor faults.

7.3 Gearboxes

7.3.1 Introduction

The vibration signals are captured at a 25.6 kHz during start-up and processed in Matlab 2015b. The drive is configured to ramp up linearly to 50 Hz over a period of 10 seconds with the Volts/Hz ratio kept constant.

The use of the Discrete Wavelet Transform was investigated to identify the gearbox faults during soft start-up using an inverter. The mesh frequency of the gearbox and its associated sidebands from the frequency of the faulty component were identified in section 6.3 as frequency components that can be used to identify the discrete faults in the gearbox. The evolution of the mesh frequency and the pinion frequency sidebands are analysed during the start-up conditions. The vibration signal of the healthy gearbox, in the time domain, during start-up is shown in Figure 7-14 below.

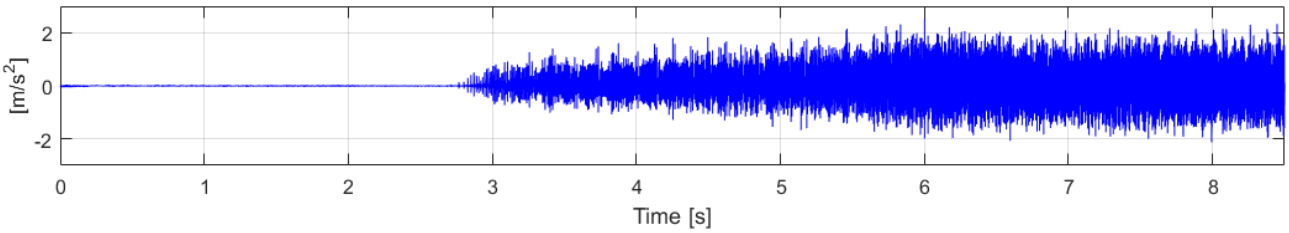

Figure 7-14 Raw vibration data from the healthy gearbox during start-up

During the first 2.7 seconds of start-up, there is very little vibration as the system overcomes inertia. As the rotor starts to rotate after 2.7 seconds the amplitude of the vibrations increases as the voltage and frequency applied to the motor is increased. A similar trend is observed with the faulty gearboxes below.

Figure 7-15 below shows the theoretical evolution of the gearbox mesh frequency and the pinion frequency sidebands of the gearbox mesh frequencies.

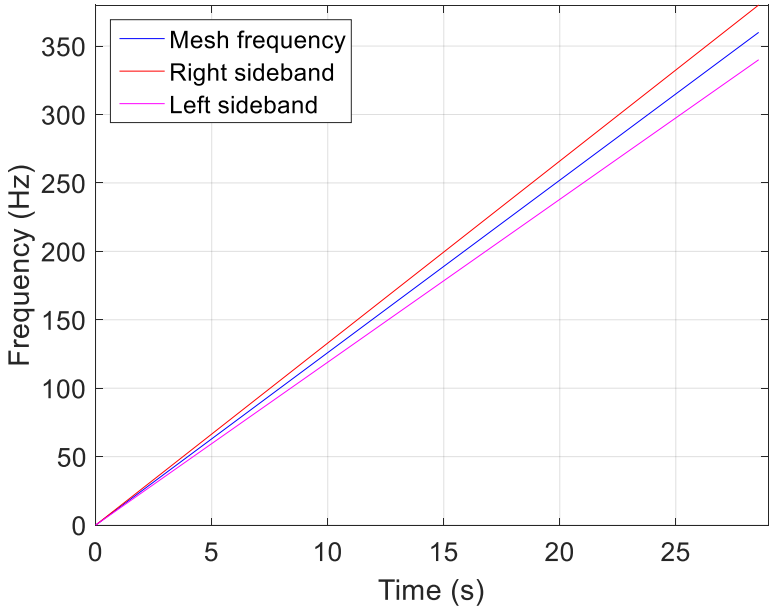

Figure 7-15 Theoretical evolution of the gearbox mesh frequency and the shaft frequency sidebands

The evolution of the mesh frequencies and the corresponding pinion frequency sidebands were estimated using the shaft frequency of the motor during start-up whilst loaded with a servo motor drive and were plotted in Figure 7-16 below.

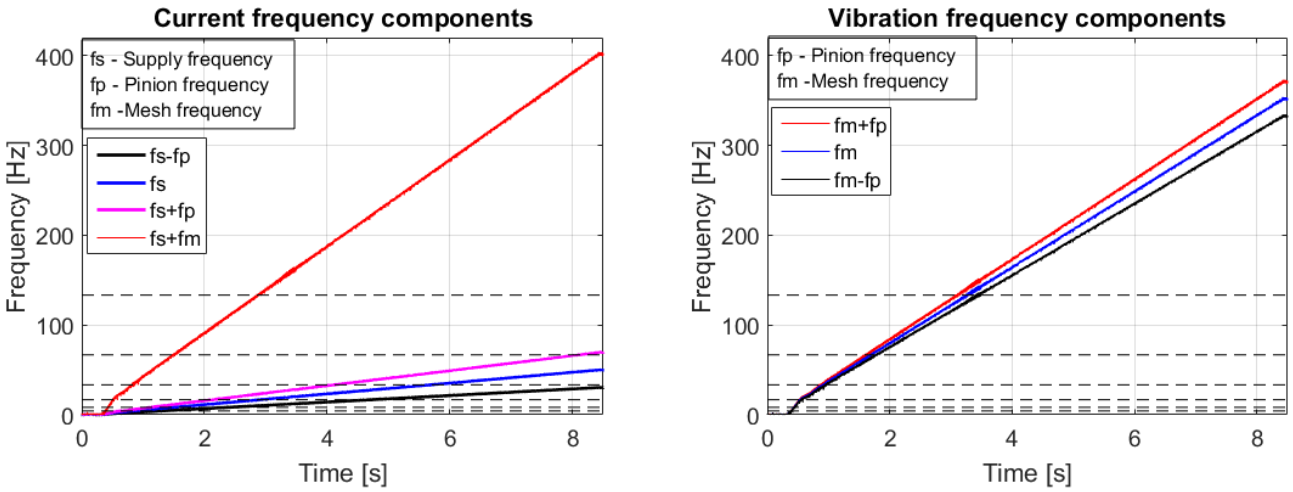

Figure 7-16 Evolution of the frequency components during start-up

The energy of the DWT coefficients was calculated using the equation below. These are listed in the Appendix.

$$Energy = \sum_{n=0}^{N} |C_n|^2 \qquad (7\text{-}1)$$

Where C is the n^{th} coefficient and N is the total number of coefficients.

7.3.2 Chipped Tooth Gearbox

The following section discusses the results obtained from the gearbox fitted with the pinion with chipped tooth during start-up. The pinion with a chipped tooth was fitted on the test gearbox and the motor was ramped up to rated voltage over a period of 10 seconds. The vertical vibrations on the casing of the gearbox and the motor currents were captured for analysis and the results are presented in Figure 7-17 and Figure 7-18 below.

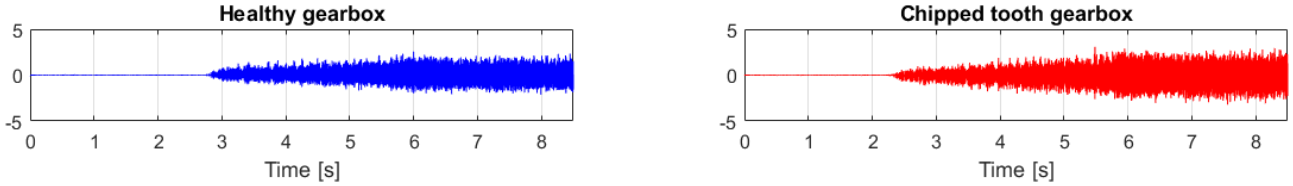

Figure 7-17 Raw vibration data of the healthy gearbox and the chipped tooth gearbox.

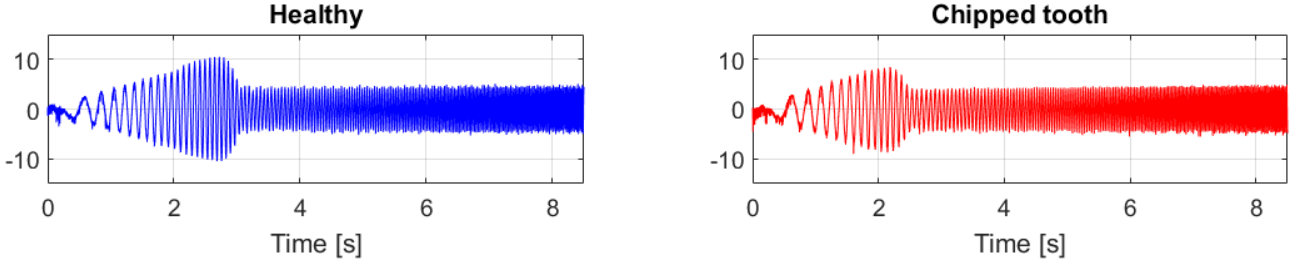

Figure 7-18 Raw motor current data of with the motor loaded with a healthy gearbox and the chipped tooth gearbox

The progression of the mesh frequency and the corresponding sidebands is shown in Figure 7-19 below. The mesh frequency and the left and right pinion sidebands under steady-state conditions were observed at 351.9 Hz, 332.3 Hz and 371.4 Hz respectively.

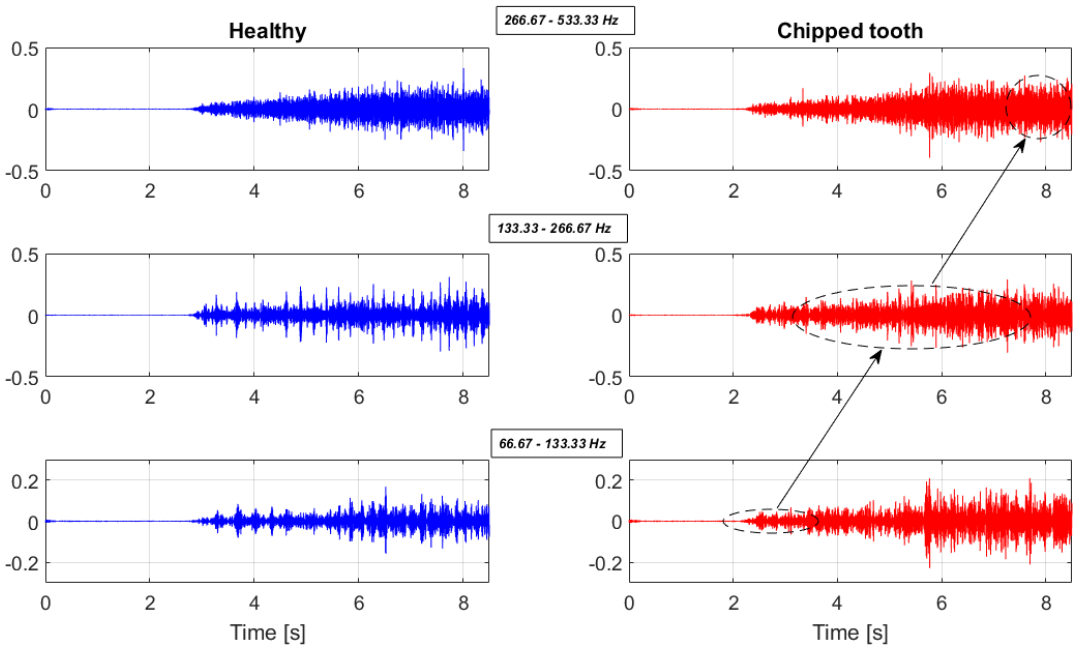

Figure 7-19 DWT of the Healthy gearbox vs Chipped tooth gearbox (66.67 Hz to 533.33 Hz) [1] showing the progression of the mesh frequency and the pinion sidebands

There is a significant increase in the energy in the DWT of the gearbox with a pinion with a chipped tooth compared to that of the gearbox with a pinion with a missing tooth. This can be attributed to the propagation of the mesh frequency and its sidebands during start-up.

The pinion frequency was observed at 19.6 Hz under steady-state conditions. The DWT of the motor current showing the progression of the pinion frequency is plotted in Figure 7-20 below. The Hilbert transform was applied to the signal to remove the fundamental.

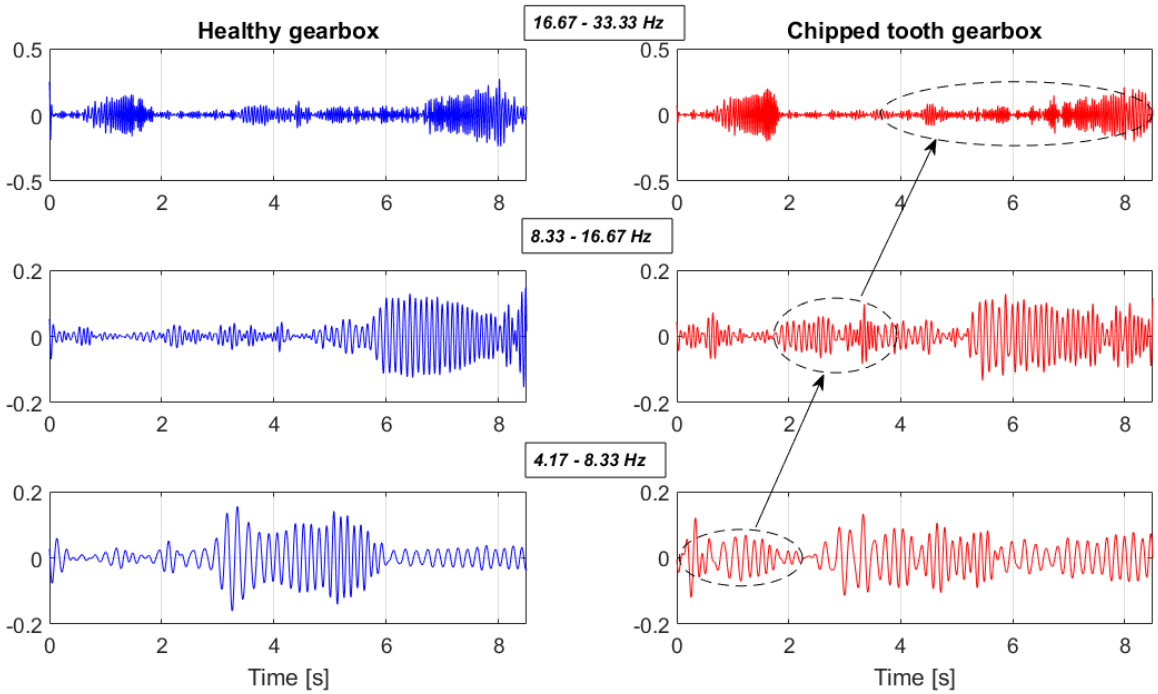

Figure 7-20 Hilbert DWT of motor current showing the evolution of the pinion frequency

There is a significant increase in the energy bands through which the pinion frequency traverses for the scenario with the gearbox with the chipped tooth compared to that of the healthy gearbox.

The progression of the pinion frequency in the Hilbert DWT of the motor current is more evident than the progression of the mesh frequency and the related sidebands in the vibration spectrum. The better performance of the DWT of the motor current can be attributed to the isolation of the frequency of interest (pinion frequency).

7.3.3 Missing Tooth Gearbox

The pinion of the gearbox was replaced with a pinion with a missing tooth. Vibration data was also captured from the casing of the gearbox during a start-up over a period of 10 seconds. The results are discussed below. The vibration signal from the gearbox casing and the motor current, in the time domain, are presented in Figure 7-21 and Figure 7-22 below.

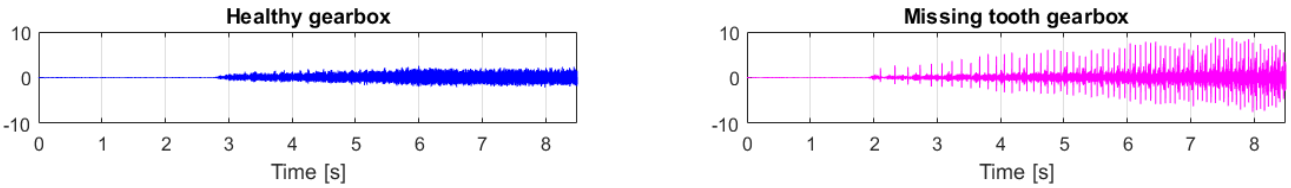

Figure 7-21 Raw vibration data of the healthy gearbox and the missing tooth gearbox

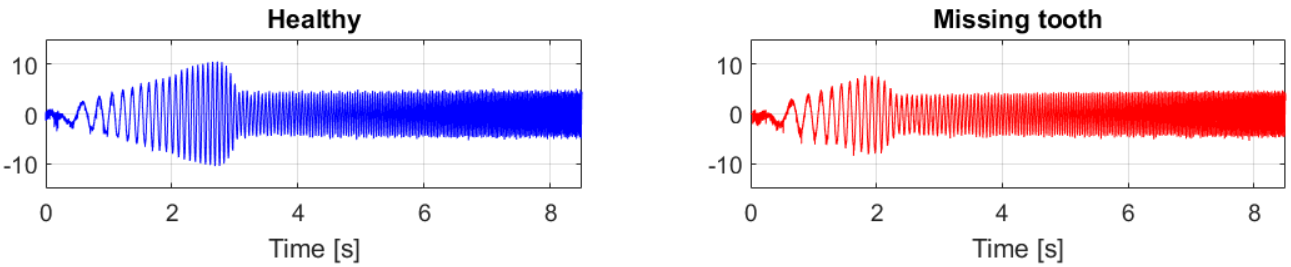

Figure 7-22 Raw motor current data of with the motor loaded with a healthy gearbox and the missing tooth gearbox

The pinion frequency, and the left and right pinion sidebands were observed at 354.2 Hz, 334.5 Hz and 373.8 Hz respectively. The progression of these frequencies in the DWT of the vibration data is shown in Figure 7-23 below.

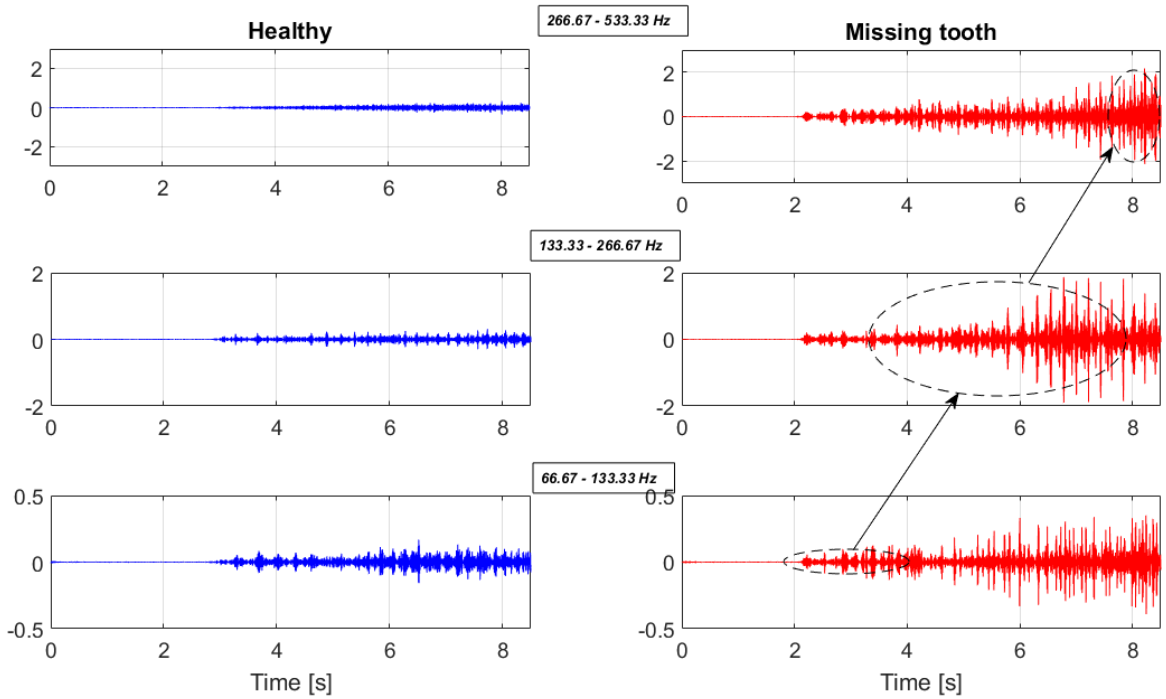

Figure 7-23 DWT of the vibration data of the healthy gearbox vs the missing tooth gearbox [1]

The energy in the DWT of the gearbox with a pinion with a missing tooth is much more than that of the healthy gearbox and that of the gearbox with a pinion with a chipped tooth. This is due to the increased amplitudes of the mesh frequency and its sidebands as was observed in section 6.3.3.

The DWT of the motor current showing the progression of the pinion frequency is plotted in Figure 7-24 below. The pinion frequency was observed at 19.7 Hz under steady-state conditions. Similar to the previous section 7.3.2, the Hilbert transform was applied to the signal to remove the fundamental.

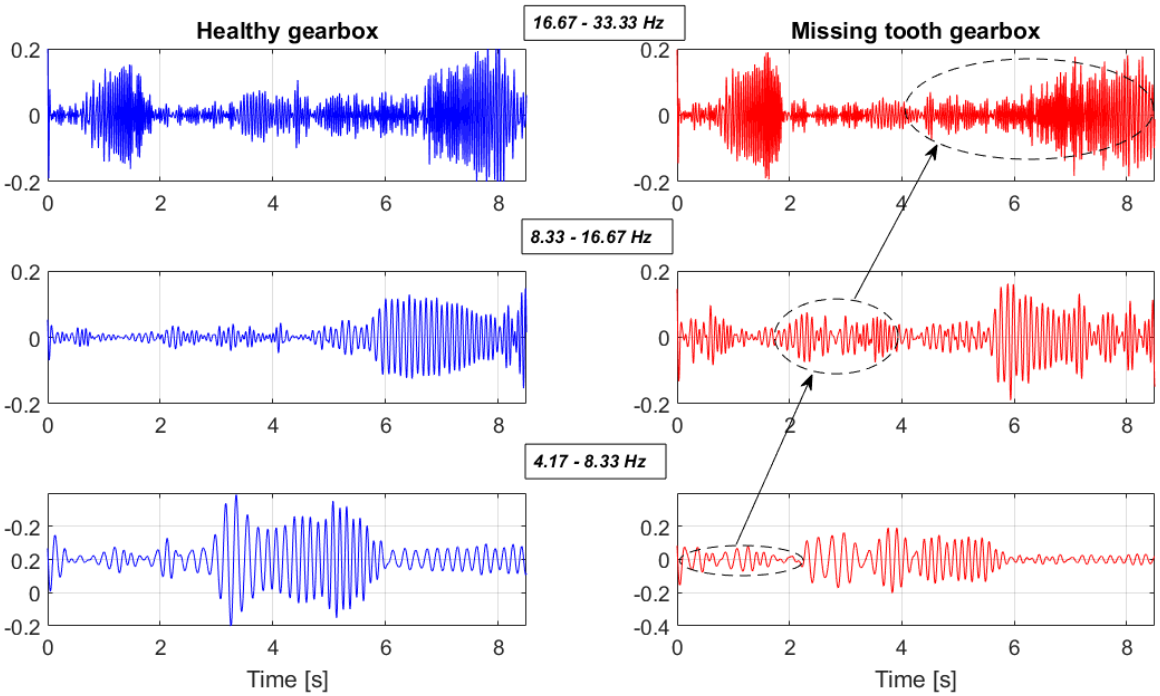

Figure 7-24 Hilbert DWT of the motor current showing the evolution of the pinion frequency

Similar to the observations of the chipped tooth gearbox, the progression of pinion frequency is more significant in the DWT of the gearbox with the missing tooth compared to that of the healthy gearbox. The DWT of the motor current also performed better than the DWT of the gearbox vibration data.

7.3.4 Worn-out Gearbox

The gearbox with the worn-out teeth was fitted as the test gearbox and the motor was ramped up to rated voltage over a period of 10 seconds. The vertical vibrations from the casing of the gearbox were captured, analysed and are discussed in the section below. The vibration signals of the healthy and faulty gearboxes, in the time domain, are shown in Figure 7-25 below.

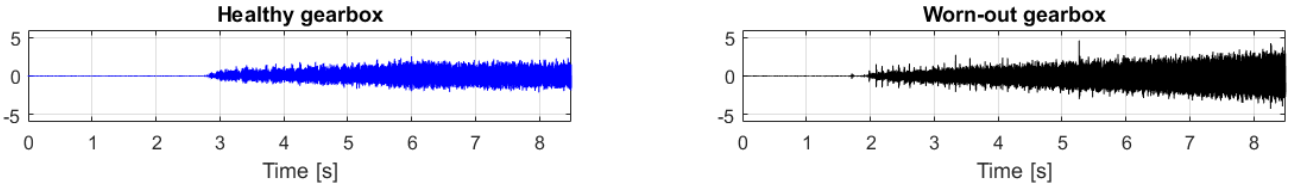

Figure 7-25 Raw vibration data of the healthy gearbox and the gearbox with a worn-out pinion

The DWT's of the vibrations from the healthy and worn-out gearboxes are presented below. The mesh frequency, and the left and right pinion frequencies were observed at 352 Hz, 332.3 Hz, and 371.3 Hz respectively. The progression of these frequencies is highlighted in Figure 7-26 below.

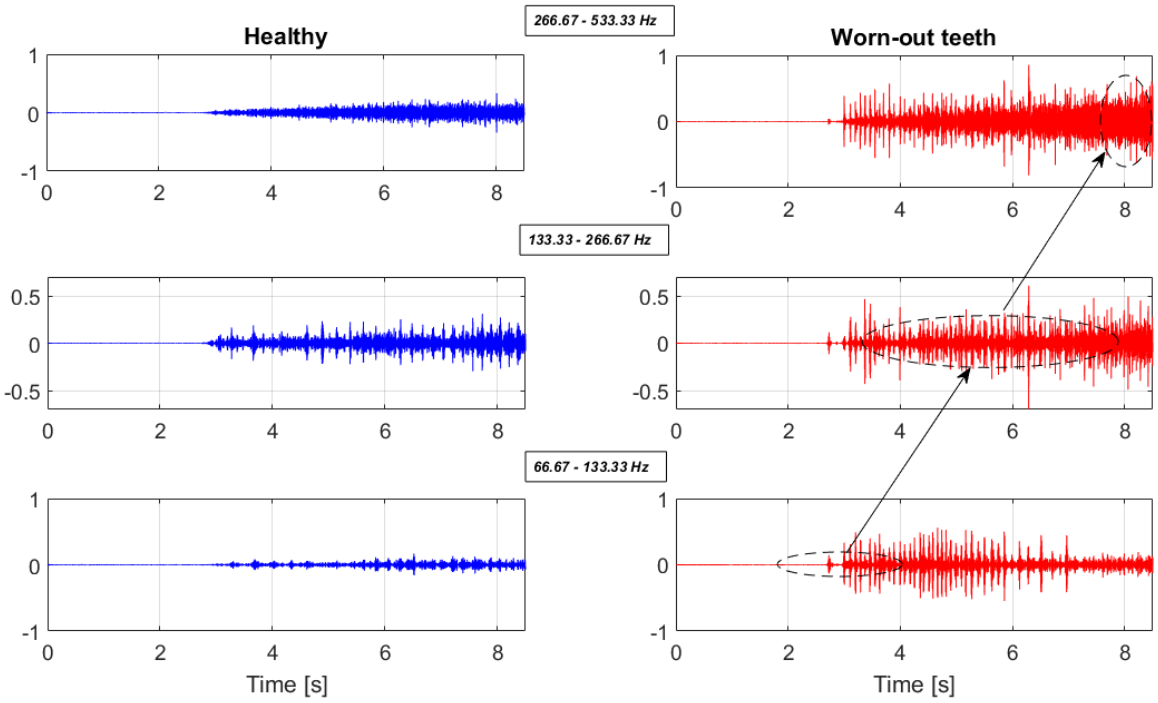

Figure 7-26 DWT of the vibration data of the healthy gearbox vs the gearbox with a worn-out pinion [1]

Similar to the observations in section 6.3.4, the gearbox with the worn-out pinion has more energy than the healthy gearbox in all the frequency bands due to the increased activity in the meshing frequencies and its associated sidebands.

7.3.5 Concluding Remarks

The amplitudes of the vibrations of the faulty gearbox were always higher than those of the healthy gearbox especially as the gearbox reached steady state. The gearbox with a chipped tooth pinion had more energy in the frequency bands through which the mesh frequency and its sidebands propagated. The gearbox with a missing tooth showed even clearer propagation, compared to that with a chipped tooth, of the mesh frequency and the sidebands during the start-up for both the current and vibration DWT's. The current and vibration DWT both performed well in the identification of the discrete gearbox faults.

The worn-out gearbox also had more energy in the frequency bands of the vibration DWT through which the mesh frequency and its sidebands propagated. The current DWT, however, performed very poorly and could not be used to identify the worn-out gearbox fault during start-up.

[1] The dotted eclipse denotes the regions during which the mesh frequencies and its sidebands are estimated to propagate through the frequency band based on Figure 7-16.

8. Detection of Individual Faults within Multiple Faulty Equipment

8.1 Introduction

The purpose of this chapter is to investigate the detection of faults under conditions with multiple faulty equipment using the fault frequencies discussed in previous chapters. More importantly, the use of MCSA as a single tool to identify all faults in the system is investigated. Vibration was not considered as a single tool to identify faults in the system because the use of a single source of vibration could not be used to identify the gearbox and motor faults under isolated conditions[2]. The scenarios comprise:

- A healthy motor, a healthy gearbox, and a healthy compressor which is used for the baseline data.
- A motor with 3 broken rotor bars, a gearbox with a missing tooth, and a compressor with a blocked suction.
- A motor with 4 shorted stator turns, a gearbox with a missing tooth and a compressor with a partially blocked discharge valve.

In all scenarios, the motor was ramped up to 60 Hz, 190 Volts over a 10 second period and data was captured for the transient conditions. For the steady state conditions, 30 seconds of data was also captured with the test rig operating at rated conditions. The signals captured comprise the motor current, motor vibration, gearbox vibration and the reciprocating compressor vibration, while also monitoring the motor voltage, speed and torque.

8.2 Healthy Motor, Healthy Gearbox, and Healthy Compressor

The healthy motor, gearbox and compressor were set-up as shown in Figure 5-12. This is done to serve as the baseline with which the results from the faulty equipment will be compared.

8.2.1 Motor in Steady-state

The raw motor current data is presented in Figure 8-1 below. The FFT of the motor current was plotted in Figure 8-2 and used for comparison with that of the faulty motors.

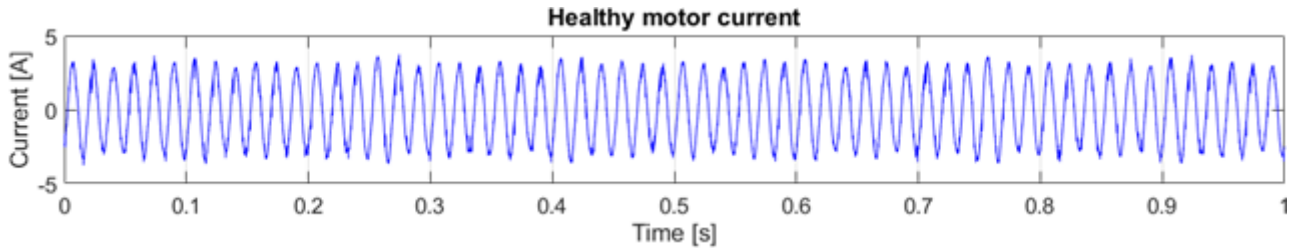

Figure 8-1 Raw data of the healthy motor current under steady state conditions

[2] See Chapter 6, Chapter 7

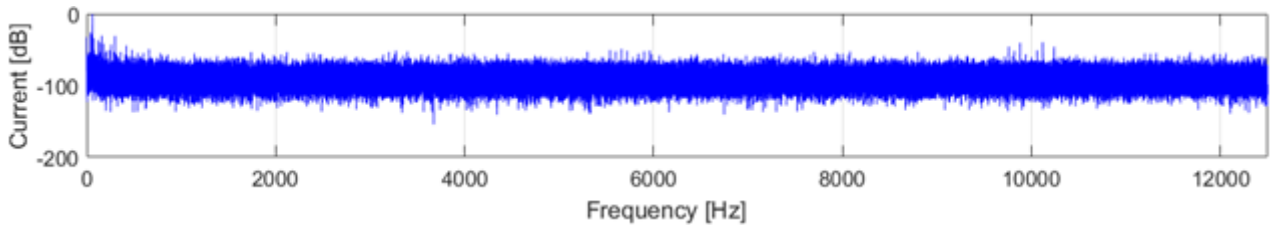

Figure 8-2 Current spectrum of the healthy motor

8.2.2 Motor during Start-up

During start-up, the inverter-fed motor was ramped up to a voltage of 190 Volts and a frequency of 60 Hz over a period of 10 seconds. The time domain of the captured motor current is presented in Figure 8-3 below.

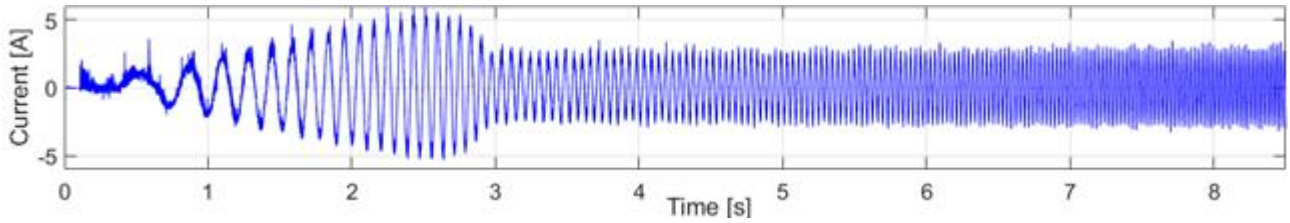

Figure 8-3 Raw data of the healthy motor current under transient conditions

The progression of the $(1 \pm 2s)f$ and the $f_s\left(\frac{n}{p}(1-s) \pm k\right)$ $for\ n = 1, k = 3$ frequencies are plotted in Figure 8-4 and are used to estimate the traversal of these frequencies during start-up. This is in turn used to estimate the progression of the plotted frequencies in the DWT of the motor current

.

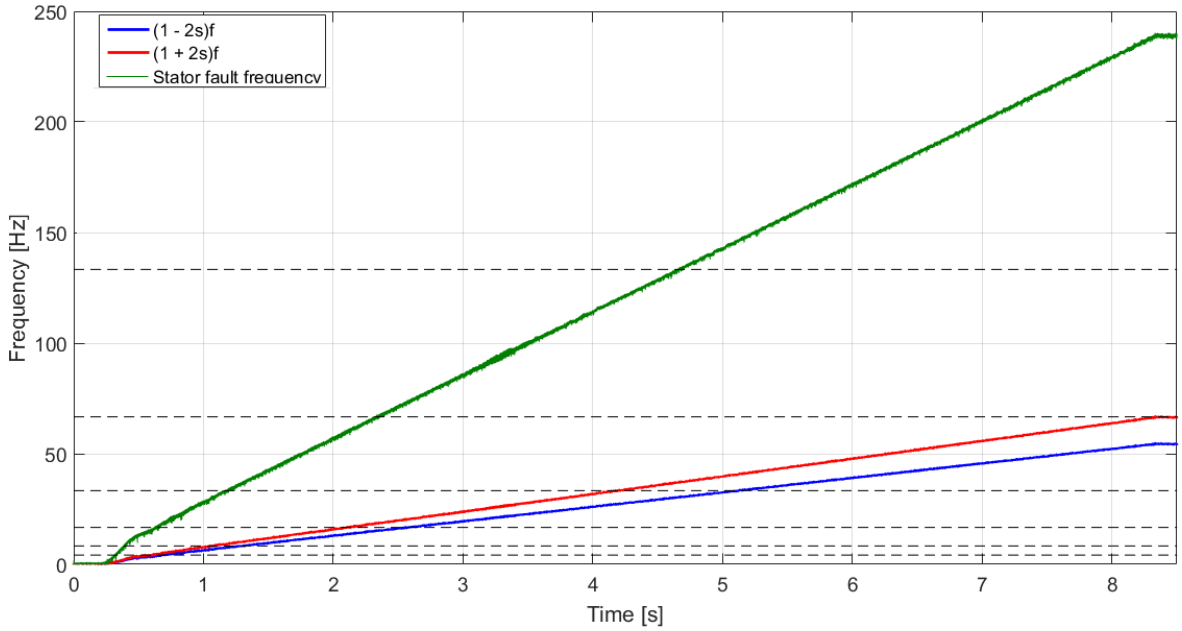

Figure 8-4 Progression of the fault frequencies during start-up

8.2.3 Gearbox in Steady-state

The motor was operated at 60 Hz and the rotational frequency of the healthy motor was measured at 58.25 Hz, the mesh and pinion frequencies were measured at 358.2 Hz and 19.9 Hz respectively. The mesh frequency and the corresponding sidebands are presented in Table 8-1 below.

Table 8-1 Mesh frequencies and corresponding pinion sidebands of the healthy gearbox and gearbox with a missing tooth

Frequency	Frequency [Hz]
Mesh frequency	358.20
Left pinion sideband	338.30
Right pinion sideband	378.10

The $f_s + f_m$ and $f_s \pm f_p$ frequencies in the motor current spectrum were also plotted in Figure 8-5 and observed. The observed fault frequencies are presented in Table 8-2 below.

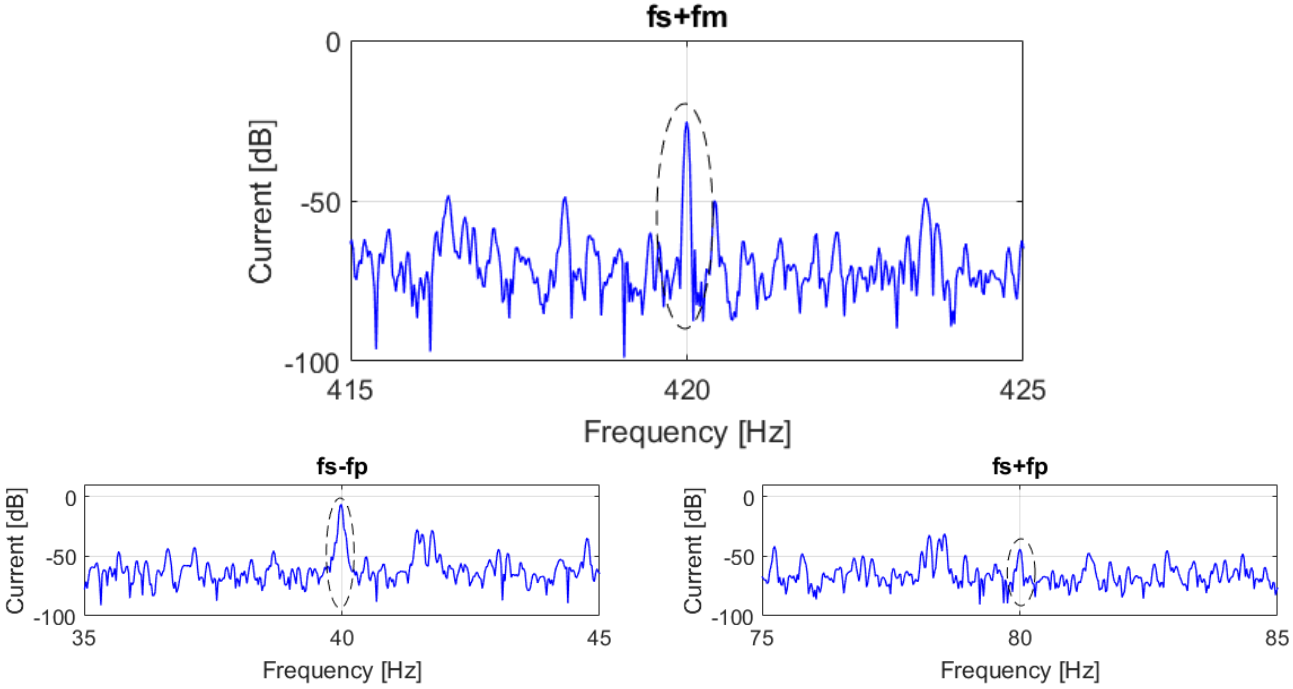

Figure 8-5 Motor current spectrum showing the $fs + f_m$ and $f_s \pm f_p$ frequencies

Table 8-2 Amplitudes and frequencies of the $fs + f_m$ and $f_s \pm f_p$ frequencies of the motor current spectrum for the healthy gearbox

Fault component	Frequency [Hz]	Amplitude [dB]
$f_s + f_m$	420.00	-25.34
$f_s + f_p$	80.00	-44.17
$f_s - f_p$	39.99	-6.82

8.2.4 *Reciprocating Compressor in Steady-state*

The working frequency, f_r, of the piston was measured at 6.08Hz and used to identify the $f_s \pm f_r$ frequencies for in the current spectrum (where f_s is the supply frequency).

The motor current spectra showing the piston frequency sidebands, $f_s \pm f_r$ are presented in Figure 8-6 and Table 8-3 below.

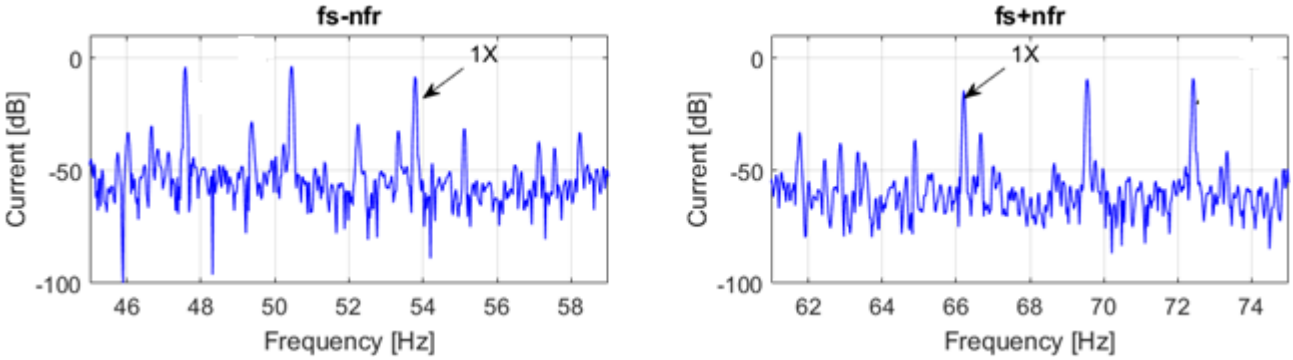

Figure 8-6 Motor current spectrum showing the $f_s \pm f_r$ frequencies with the healthy motor loaded with the healthy compressor

Table 8-3 Amplitudes and frequencies of the $f_s \pm f_r$ frequencies of the healthy motor current spectrum

Fault component	Healthy compressor	
	Frequency [Hz]	Amplitude [dB]
$f_s + f_r$	66.09	-15.36
$f_s - f_r$	53.93	-10.83

8.3 Motor with Broken Rotor Bars, Gearbox with Missing Tooth Pinion and Compressor with Blocked Suction

In this section, the motor, gearbox and reciprocating compressor are set-up in a similar manner to that of the previous section. However, the motor with the broken rotor bar, the gearbox with a missing tooth pinion and the compressor with a blocked suction are used instead of the healthy apparatus and attempts are made to identify the faults.

8.3.1 *Motor in Steady-state*

The motor current spectra of the healthy motor and the motor with broken rotor bars is presented in Figure 8-7 below.

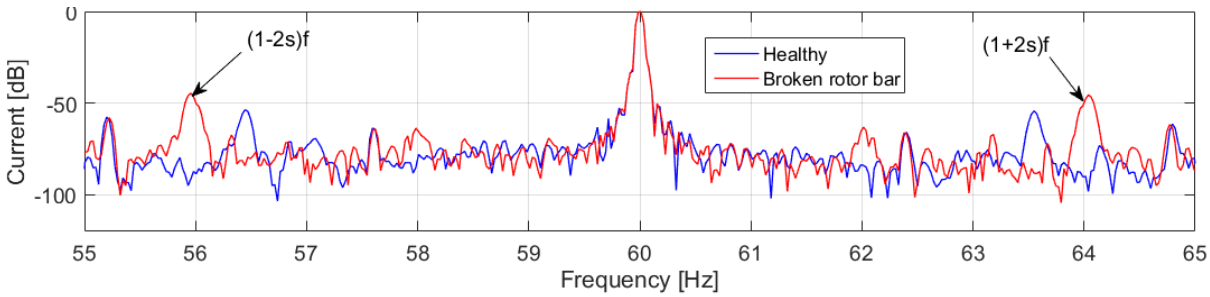

Figure 8-7 Spectra of the motor current under steady state conditions for the healthy motor and the motor with broken rotor bars

The current spectrum was also analysed to detect the broken rotor bar fault in the motor using the $(1 \pm 2s)f$ frequencies. The results were similar to those obtained with broken rotor bar fault under isolated conditions, in section 6.2.2, in which there was an increase in the amplitudes of the $(1 \pm 2s) \cdot f_s$ components in the current spectrum[3].

8.3.2 Motor during Start-up

This section presents a comparison between the motor current of the healthy motor and that of the motor with the broken rotor bars as the motors are ramped up to 190 Volts and 60 Hz. The DWT of the motor current during start-up is presented in Figure 8-8 below.

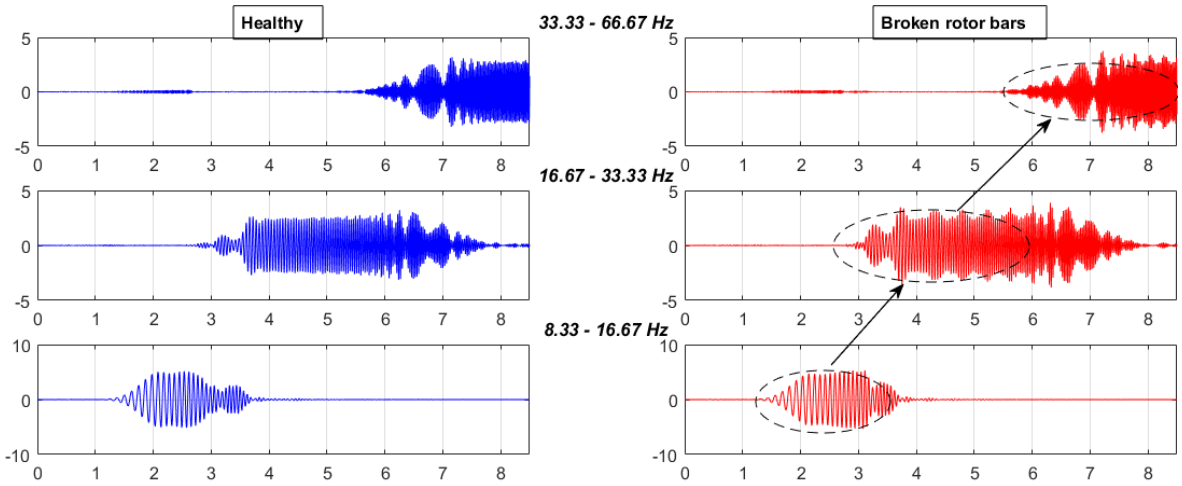

Figure 8-8 DWT of the motor current during start-up

The DWT and Hilbert transform was applied to the motor current during start-up. The results obtained were similar to those obtained under isolated conditions in section 7.2.2 in that there was a significant increase in energy in the frequency bands through which the $(1 \pm 2s)f$ frequency components traversed[4].

8.3.3 Gearbox in Steady-state

This section presents the comparison of the results between the faulty gearbox and the healthy gearbox. The motor was operated at 60 Hz and the rotational frequencies of the healthy motor and the faulty motor are 58.25 Hz and 57.95 Hz respectively. The mesh frequencies are measured at 358.2 Hz and 359.64 Hz for the healthy and faulty gearboxes respectively, and pinion frequencies are 23.3 Hz and 19.98 Hz.

The $f_s + f_m$ and $f_s \pm f_p$ frequencies in the motor current spectrum were also plotted in Figure 8-9 and observed. The results were compared to those obtained in the isolated scenario discussed in 6.3.3 in Table 8-4.

[3] See Figure 6-4
[4] See Figure 7-7

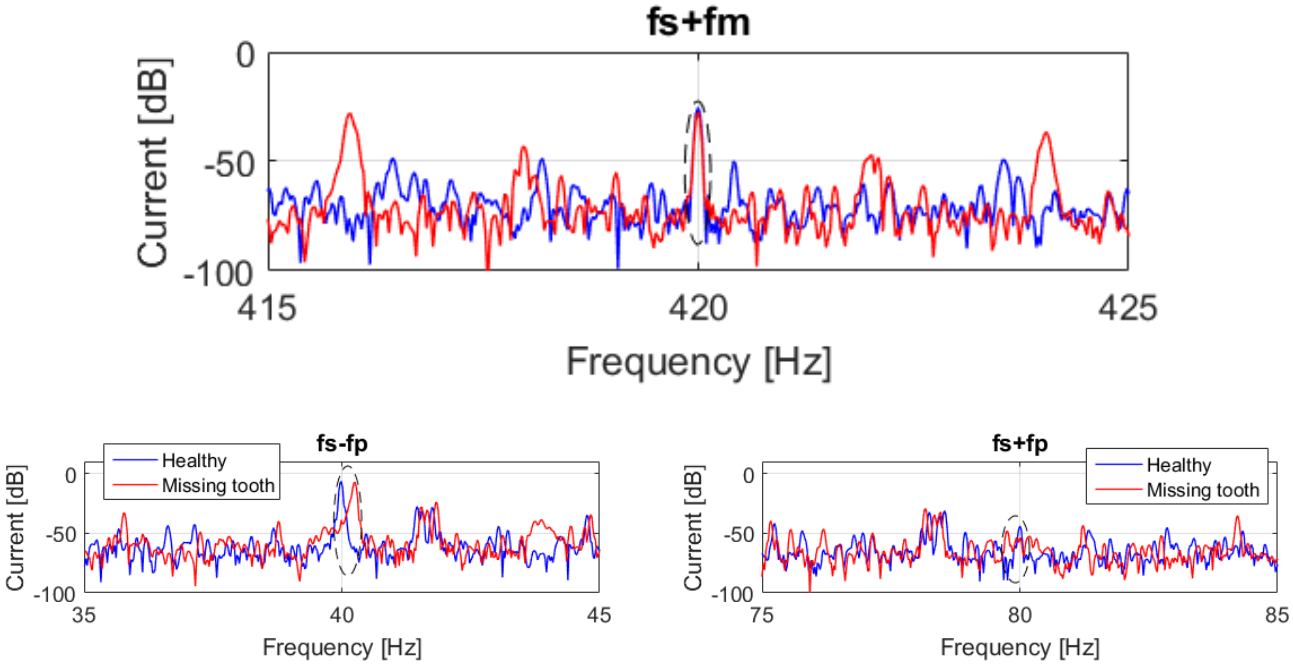

Figure 8-9 Motor current spectrum showing the $fs + f_m$ and $f_s \pm f_p$ frequencies

Table 8-4 Amplitudes and frequencies of the $fs + f_m$ and $f_s \pm f_p$ frequencies of the motor current spectrum with the healthy gearbox and missing tooth gearbox connected

Fault component	Healthy gearbox		Missing tooth gearbox	
	Frequency [Hz]	Amplitude [dB]	Frequency [Hz]	Amplitude [dB]
$f_s + f_m$	420.00	-25.34	420.00	-27.65
$f_s + f_p$	80.00	-44.17	79.76	-48.19
$f_s - f_p$	39.99	-6.82	40.23	-7.83

The amplitude of the $f_s + f_m$, $f_s + f_p$ and the $f_s - f_p$ frequencies for the faulty gearbox reduce by 2.31 dB, 4.02 dB and 1.01 dB respectively, compared to that of the healthy one. The amplitudes of the fault frequency components reduced unlike the observations in the isolated scenario in section 6.3.3 where they increased.

The motor current spectrum did not yield the results obtained under isolated conditions. This can be attributed to the dampened speed oscillations from the gearbox which reduced the amplitude of the fault frequencies [132].

8.3.4 Reciprocating Compressor in Steady-state

The motor current spectrum showing the $f_s + f_r$ and $f_s - f_r$ frequencies was plotted in Figure 8-10 below.

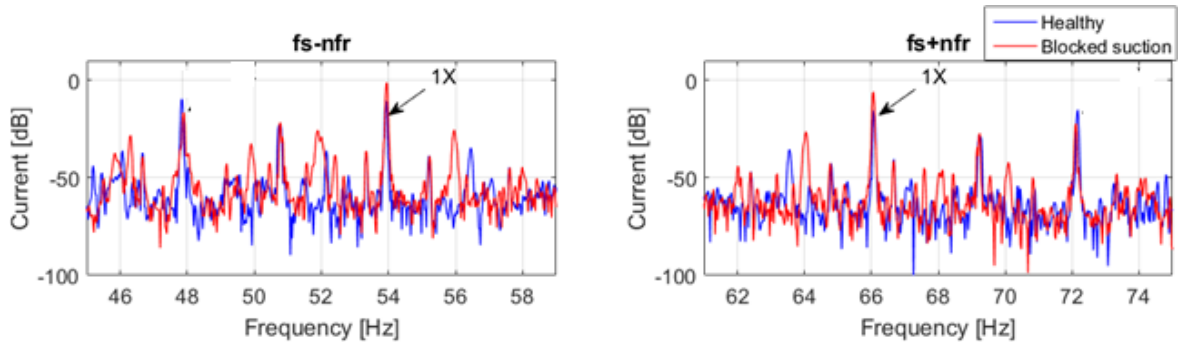

Figure 8-10 Motor current spectrum showing the $f_s \pm f_r$ frequencies for the healthy compressor and the compressor with a blocked suction

The results obtained here were similar to those obtained under isolated conditions in section 6.4.3[5]. The amplitudes of the $f_s + f_r$ and $f_s - f_r$ frequencies increased.

8.3.5 Concluding Remarks

The $(1 \pm 2s)f$ frequencies were clearly observed in the current spectrum of the motor with the broken rotor bars in steady state and also during start-up.

For the gearbox, the mesh frequency and the corresponding pinion sidebands did not perform well in both the current spectrum, both under steady-state and transient conditions. This can be attributed to the mesh frequency of the gearboxes occurring very close the harmonic of the fundamental, and the loading of the gearbox which acts as a damper for the vibrations [85].

For the reciprocating compressor, the observations from the motor current spectrum are also similar to those observed in section 6.4.3 in which the amplitudes of the $f_s \pm f_r$ frequencies increase.

Ultimately, MCSA was able to identify all the faults in the system. It was, however, able to identify both the broken rotor bar fault and the reciprocating compressor faults. It only performed poorly for the gearbox faults.

8.4 Motor with Shorted Stator Inter-turns, Gearbox with a Missing Tooth Pinion and Compressor with a Partially Blocked Discharge

In this section, the motor, gearbox and reciprocating compressor are set-up a similar manner to that of the previous section. However, the motor with the shorted stator turns, the gearbox with a missing tooth pinion and the compressor with a partially blocked discharge valve are used instead of the healthy apparatus.

8.4.1 Motor in Steady-state

The motor current spectra of the healthy motor and the motor with 4 shorted stator turns is presented in Figure 8-11 below.

[5] See Figure 6-36

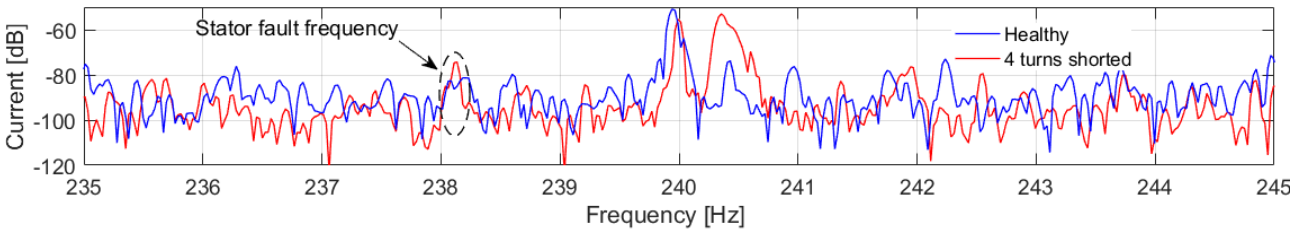

Figure 8-11 Spectra of the motor current under steady state conditions for the healthy motor and the motor with shorted stator turns

The current spectrum was plotted and the $f_s\left(\frac{n}{2}(1-s)\pm k\right)$ frequency for $n = 1$ and $k = 3$ was analysed. The results obtained were similar to those under isolated conditions; the fault frequencies were not easily identifiable due to the noise from the inverter harmonics.

8.4.2 Motor during Start-up

This section analyses the motor currents during start-up. The motors were ramped up to 190 volts and a frequency of 60 Hz. The DWT of the motor current is plotted in Figure 8-12 below and analysed.

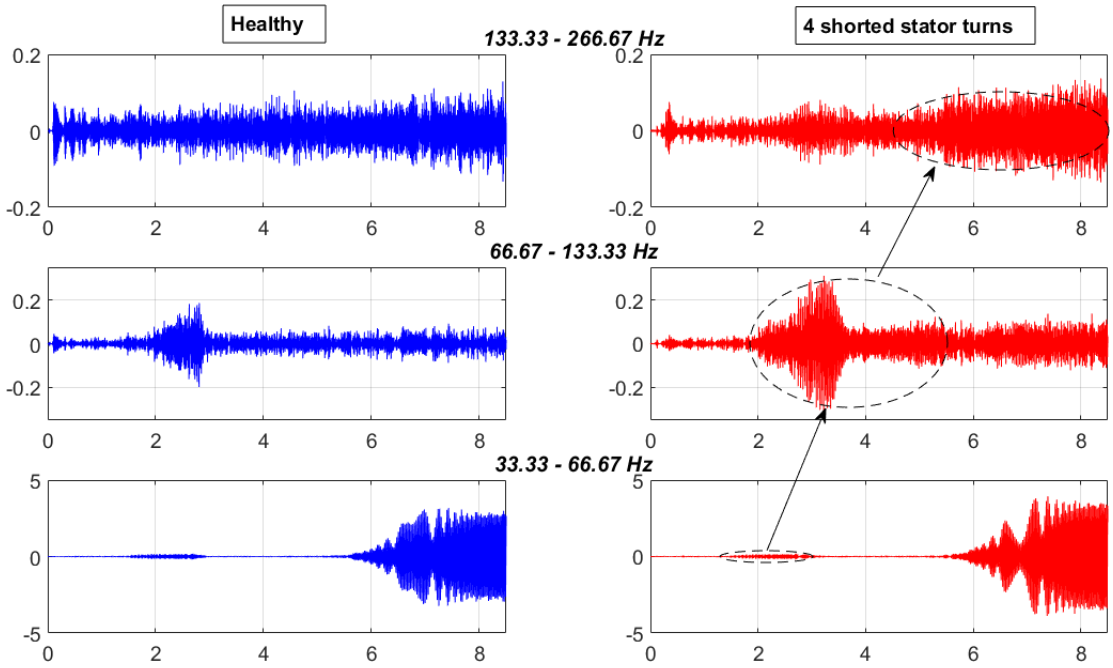

Figure 8-12 DWT of the current of the healthy motor and the motor with shorted stator turns showing the progression of the fault frequency

The DWT of the faulty motor was calculated and plotted and the progression of the fault components was traced out. The fault frequency in the current spectrum was calculated and identified at 238.1 Hz in the previous section. Using the estimates plotted in Figure 8-4, the progression of the fault frequency to 238.1 Hz was identified. The results obtained were similar to those under isolated conditions, in section 7.2.1[6], in that there was a small increase in energy in the frequency bands through which the fault traversed.

[6] See Figure 7-4

8.4.3 Gearbox in Steady-state

This section presents the comparison of the results between the faulty gearbox and the healthy gearbox. The mesh frequency and pinion frequency were measured at 359.2 Hz and 19.8 Hz respectively.

The results from the analysis of the motor current spectrum are presented in Figure 8-13 and Table 8-5 below and analysed.

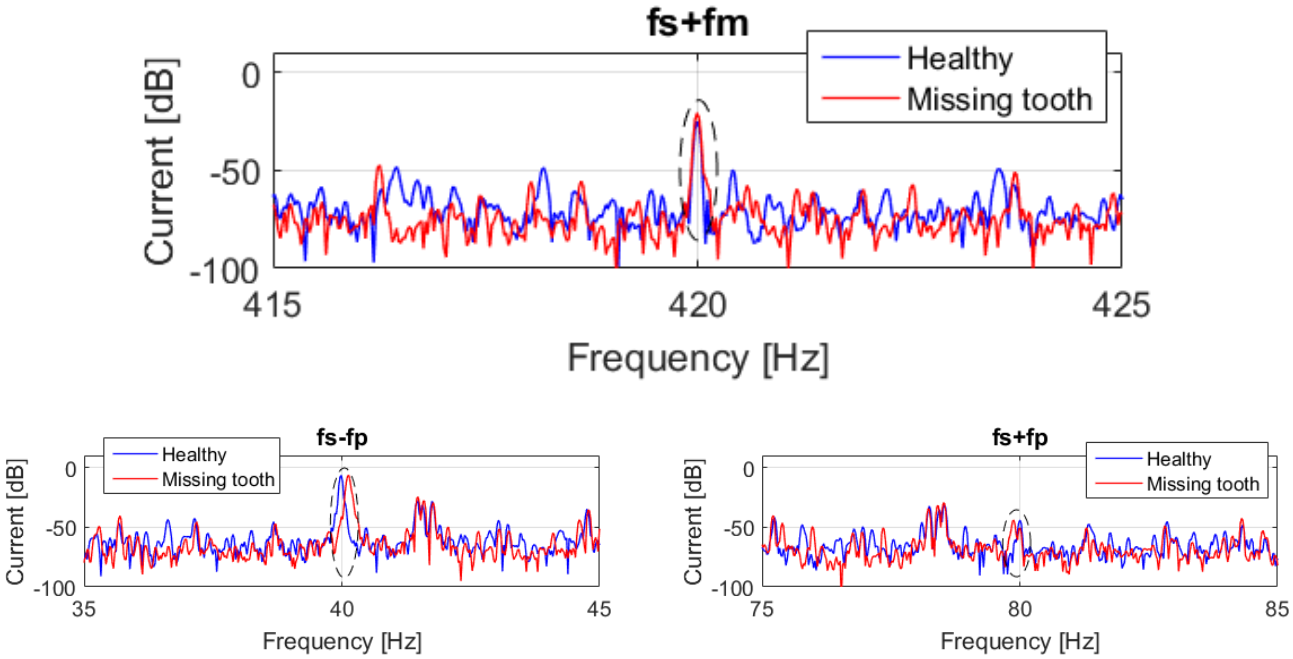

Figure 8-13 Motor current spectrum showing the $fs + f_m$ and $f_s \pm f_p$ frequencies

Table 8-5 Amplitudes and frequencies of the $fs + f_m$ and $f_s \pm f_p$ frequencies of the motor current spectrum with the healthy gearbox and missing tooth gearbox connected

Fault component	Healthy gearbox		Missing tooth gearbox	
	Frequency [Hz]	Amplitude [dB]	Frequency [Hz]	Amplitude [dB]
$f_s + f_m$	420.00	-25.34	420.00	-20.85
$f_s + f_p$	80.00	-44.17	79.88	-44.18
$f_s - f_p$	39.99	-6.82	40.16	-11.92

The amplitude of the $f_s + f_m$ for the faulty scenario increased by 4.49 dB while that of the $f_s + f_p$ and the $f_s - f_p$ frequencies decreased by 0.01 dB and -5.1 dB respectively. The increase in the amplitude of mesh frequency increased; similar to the observations in the isolated scenario. The amplitudes of the pinion sidebands, however, reduced contrary to the observations in the isolated scenario in 6.3.3.

8.4.4 Reciprocating Compressor in Steady-state

The motor current spectrum showing the $f_s + f_r$ and $f_s - f_r$ frequencies is plotted in Figure 8-14 below.

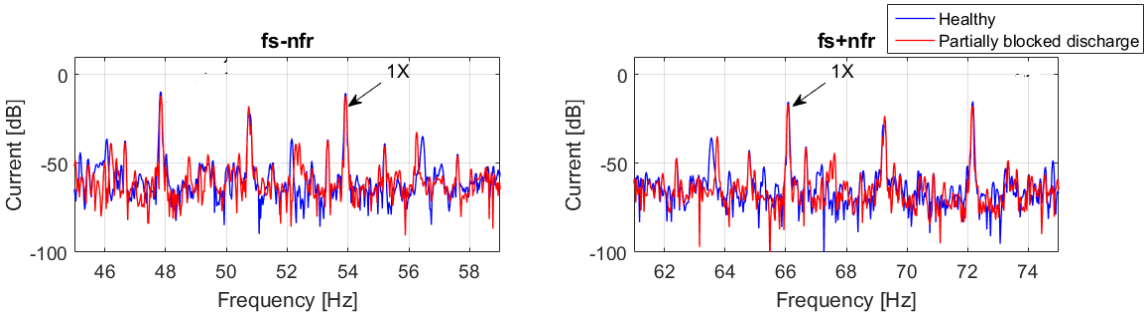

Figure 8-14 Motor current spectrum showing the $f_s \pm f_r$ frequencies for the healthy compressor and the compressor with a partially blocked discharge valve

The working frequency of the compressor with the partially blocked discharge valve was measured at 6.08. The amplitudes of the $f_s \pm f_r$ frequenices in the current specturm were similar to those observed in section 6.4.2[7] in that they both decreased.

8.4.5 Concluding Remarks

The stator fault frequency was not easily identifiable under steady-state conditions in the current spectrum of the motor. Under transient conditions, there was a small change in energy in the frequency bands through which the stator fault frequency traversed.

For the gearbox, only the $f_s + f_m$ frequency increased in amplitude in the motor current spectrum while the $f_s \pm f_p$ frequencies reduced in amplitude. The results here were inconsistent with the observations under isolated/unloaded conditions.

For the reciprocating compressor with the partially blocked discharge valve, the amplitudes of the $f_s \pm f_r$ frequencies, in the current spectrum were also similar to the observations in 6.4.2. in which the amplitudes of the frequencies reduced.

Ultimately, the use of MCSA to identify all the faults in the system did not perform well as it was unable to identify the inter-turn fault in the motor, and the missing tooth fault in the gearbox. However, it performed well for the identification of the partially blocked discharge valve in the reciprocating compressor.

[7] See Figure 6-32

9. Conclusions and Recommendations

This section presents conclusions from the results obtained from the experiments in the previous chapters.

9.1 Conclusions

9.1.1 Time Domain Analysis

Time domain analysis was investigated as a plausible technique for the detection of the chipped tooth, missing tooth and worn-out tooth faults in the gearbox under steady-state conditions. The peak value and RMS always increased when any of the faults was implemented on the gearbox. Although the increased peak value and RMS could be used as an indicator of the presence of a fault, it cannot identify the fault that is present on the gearbox. The crest factor can be used to identify the presence of discrete faults such as a chipped or missing tooth in the gearbox, but is also prone to false positives especially if it is calculated over long time periods. Kurtosis was validated as a credible indicator in the presence of a discrete fault in the gearbox [28].

Time domain analysis of the reciprocating compressor under steady state conditions was also investigated as a technique for the detection of the blocked suction fault and the partially blocked discharge faults. The blocked suction fault resulted in reduced peak and RMS values, while the partially blocked discharge fault resulted in increased peak and RMS values. The kurtosis, however, increased for both faults especially for the blocked suction fault. Time domain analysis performs better when multiple indicators are used to identify faults in equipment. Careful choice of thresholding parameters is also important when using time domain analysis techniques. Time domain analysis did not prove to be a credible tool for the identification of faults in the reciprocating compressor.

9.1.2 Frequency Domain Analysis

Frequency domain analysis was investigated as a technique for the detection of faults in induction motors, gearboxes and reciprocating compressors in steady state. MCSA performed well in the identification of the broken rotor bar fault, and the bearing fault under both isolated conditions and in the scenarios with multiple faults introduced to the system. It, however, performed very poorly for the inter-turn fault. The vibration spectrum, on the other hand, performed better than the current spectrum for the identification of the inter-turn fault, broken rotor bar fault, and the bearing fault. The poor performance of MCSA in the identification of the inter-turn fault can be attributed to the noise from the inverter harmonics.

Analysis of the vibration spectrum of the gearboxes in steady-state was also successful in identifying the presence of the chipped tooth, missing tooth and worn-out teeth faults on the gearbox under isolated conditions. The mesh frequency and the corresponding sidebands were proven as good indicators for the presence of a fault on the gearbox. Furthermore, the amplitudes of the pinion/gear sidebands were able to provide better information regarding the location of the discrete faults. MCSA also performed very well for the gearbox when the fault was isolated and the gearbox was unloaded, and pinion frequency was observed. This was likely due to the larger amplitudes of the vibrations under the no-load conditions.
Frequency domain analysis, however, performed very poorly when multiple faults were introduced to the system. The poor performance of the vibration spectrum was attributed to the dampening of the vibrations of the gearbox under load, and that of the current spectrum can be attributed to the dampening of the vibrations of the gearbox and the noise from the inverter harmonics.

Frequency domain analysis was also investigated for detection of the blocked suction and partially blocked discharge valves of the compressor under steady-state conditions. The changes in the amplitudes of the piston frequencies and their harmonics were more significant in the vibration spectrum from the compressor's accelerometer than they were in the current spectrum and from the vibration spectrum from the motor's accelerometer. The changes in the amplitudes in the vibration spectrum from the motor were within a similar range to those of the current spectrum. Although both the current and vibration spectra performed well in the detection of the faults in the compressor under both isolated and multiple fault conditions, the vibration spectrum performed better than the current spectrum. The current spectrum, however, can still be used to identify faults in the compressor.

MCSA was identified as the single non-invasive tool to be used to identify faults in the equipment under both isolated conditions and also with multiple faults in the system concurrently. MCSA, however, performed poorly for the shorted stator turn fault both under isolated conditions and with multiple faults applied to the system, and also with the gearbox loaded with the reciprocating compressor. It, however, did perform well when the gearbox fault was isolated.

9.1.3 Time-frequency Domain Analysis

The DWT of the motor currents did not perform as well as that of the motor vibrations. The DWT of the motor current for the inter-turn fault did not provide a sufficient change in energy for identification of the fault, while the energy in the DWT of the motor current of the broken rotor bar, bearing and bowed rotor faults did not change as much as that of motor vibrations. The results obtained with multiple faults simulated in the system were similar to those obtained under isolated conditions. The DWT of the motor current, therefore, proved to be a plausible indicator for the bearing, broken rotor and bowed rotor faults but not for the inter-turn fault.

The DWT of the current, with the Hilbert Transform applied to it, performed better than the DWT of the vibration data for the identification of the chipped tooth and missing tooth faults under isolated conditions. The DWT of the vibration data performed better than that of the motor current for the detection of the worn-out teeth under isolated conditions.

However, for the scenarios where the motor, gearbox and compressor all had faults implemented, the gearbox faults could not be identified using DWT. This can be attributed to the subversion of the vibrations of the gearbox by the loading which in turn reduced the impact on the air-gap flux of the motor and thus the performance of MCSA.

The results from the time-frequency domain analysis and corresponded to the findings in the frequency domain which also identified MCSA as a single tool that could be used to identify faults in the equipment. However, it also performed poorly for the inter-turn fault, and for the gearbox faults both under isolated conditions and also with multiple faults applied to the system.

9.2 Recommendations

Although faults in the induction motors were successfully identified using vibrations, the placement of the accelerometers could be improved by moving them closer to the bearings to allow for early detection of the faults.

The use of the statistical indicators for the detection of faults can be improved by calculation over shorter time periods to reduce the possibility of false positives, and by use of additional tools and techniques to confirm the existence of a fault such as analysis of oil debris to confirm wear in a gearbox [58].

For more accurate determination of the causes of the vibrations in the reciprocating compressor, the position of the piston should also be tracked. The pressure in the reciprocating compressor can also be investigated as a parameter for the detection of faults in the reciprocating compressor. The accelerometers should also be placed as close the valves as possible. The sampling frequency should also be increased so that the FFT and DWT of the compressors at higher frequency bands can be observed.

10. List of References

[1] H. Cui *et al*, "Research on fault diagnosis for reciprocating compressor valve using information entropy and SVM method," *J Loss Prev Process Ind,* vol. 22, pp. 864-867, 11, 2009.

[2] G. Singh, "Induction machine drive condition monitoring and diagnostic research—a survey," *Electr. Power Syst. Res.,* vol. 64, pp. 145-158, 2003.

[3] C. Heising, "IEEE recommended practice for the design of reliable industrial and commercial power systems," *IEEE Inc., New York,* 1991.

[4] X. Fan and M. J. Zuo, "Gearbox fault detection using Hilbert and wavelet packet transform," *Mechanical Systems and Signal Processing,* vol. 20, pp. 966-982, 2006.

[5] J. Ma and C. Li, "On localized gear defect detection by demodulation of vibrations–A comparative study," in *Proceedings of the ASME International Mechanical Engineering Congress and Exposition, Part 1, San Francisco, CA,* 1995, pp. 565-576.

[6] S. Schultheis, "Vibration analysis of reciprocating compressors," *Orbit,* vol. 6, pp. 1-9, 1996.

[7] D. Goebel, "Reciprocating Compressor Suction And Discharge-Valve Monitoring," *COMPRESSORtech2,* 2014.

[8] S. Thompson, "Tribology Solutions: Section 1," 2000.

[9] M. Serridge, "Ten crucial concepts behind trustworthy fault detection in machine condition monitoring," in *Vibration and Wear in High Speed Rotating Machinery*Anonymous Springer, 1990, pp. 729-740.

[10] R. Krishnan, *Electric Motor Drives: Modeling, Analysis, and Control.* Prentice Hall, 2001.

[11] S. Bindu and V. V. Thomas, "Diagnoses of internal faults of three phase squirrel cage induction motor — A review," in *Advances in Energy Conversion Technologies (ICAECT), 2014 International Conference On,* 2014, pp. 48-54.

[12] W. Theodore, *Electrical Machines, Drives and Power Systems, 6/E.* Pearson Education India, 2007.

[13] A. Siddique, G. S. Yadava and B. Singh, "A review of stator fault monitoring techniques of induction motors," *Energy Conversion, IEEE Transactions On,* vol. 20, pp. 106-114, 2005.

[14] P. Tavner, L. Ran and J. Penman, *Condition Monitoring of Rotating Electrical Machines.* IET, 2008.

[15] Sang Bin Lee, K. Younsi and G. B. Kliman, "An online technique for monitoring the insulation condition of AC machine stator windings," *Energy Conversion, IEEE Transactions On,* vol. 20, pp. 737-745, 2005.

[16] M. Riera-Guasp, J. A. Antonino-Daviu and G. Capolino, "Advances in Electrical Machine, Power Electronic, and Drive Condition Monitoring and Fault Detection: State of the Art," *IEEE Trans. Ind. Electron.,* vol. 62, pp. 1746-1759, MAR, 2015.

[17] Pinjia Zhang *et al*, "A Survey of Condition Monitoring and Protection Methods for Medium-Voltage Induction Motors," *Industry Applications, IEEE Transactions On,* vol. 47, pp. 34-46, 2011.

[18] R. M. Tallam, T. G. Habetler and R. G. Harley, "Experimental testing of a neural-network-based turn-fault detection scheme for induction machines under accelerated insulation failure conditions," in *Diagnostics for Electric Machines, Power Electronics and Drives, 2003. SDEMPED 2003. 4th IEEE International Symposium On,* 2003, pp. 58-62.

[19] M. Eftekhari *et al*, "Online Detection of Induction Motor's Stator Winding Short-Circuit Faults," *Systems Journal, IEEE,* vol. 8, pp. 1272-1282, 2014.

[20] Jiancheng Song *et al*, "Slot discharge pattern of 10 kV induction motor stator coils under condition of insulation degradation," *Dielectrics and Electrical Insulation, IEEE Transactions On,* vol. 20, pp. 2091-2098, 2013.

[21] A. Bellini *et al*, "Advances in Diagnostic Techniques for Induction Machines," *Industrial Electronics, IEEE Transactions On,* vol. 55, pp. 4109-4126, 2008.

[22] C. Kral, T. G. Habetler and R. G. Harley, "Detection of mechanical imbalances of induction machines without spectral analysis of time-domain signals," *Industry Applications, IEEE Transactions On,* vol. 40, pp. 1101-1106, 2004.

[23] W. Thomson, D. Rankin and D. Dorrell, "On-line current monitoring to diagnose airgap eccentricity in large three-phase induction motors-industrial case histories verify the predictions," *Energy Conversion, IEEE Transactions On,* vol. 14, pp. 1372-1378, 1999.

[24] S. Nandi, H. Toliyat and X. Li, "Condition monitoring and fault diagnosis of electrical motors-a review," *Energy Conversion, IEEE Transactions On,* vol. 20, pp. 719-729, 2005.

[25] S. Nandi, R. M. Bharadwaj and H. Toliyat, "Performance analysis of a three-phase induction motor under mixed eccentricity condition," *Energy Conversion, IEEE Transactions On,* vol. 17, pp. 392-399, 2002.

[26] R. R. Schoen *et al*, "Motor bearing damage detection using stator current monitoring," *Industry Applications, IEEE Transactions On,* vol. 31, pp. 1274-1279, 1995.

[27] I. SpectraQuest, *Applied Vibration Analysis Training Manual & Laboratory Exercises.* Richmond, Virginia: .

[28] S. Al-Arbi, "Condition Monitoring of Gear Systems using Vibration Analysis." , University of Huddersfield, 2012.

[29] (). *Parts of the Reciprocating Compressor*.

[30] M. Ahmed, "The use of Advanced Soft Computing for Machinery Condition Monitoring." , University of Huddersfield, 2014.

[31] R. Motriuk, "Reciprocating compressor valve failure: Digital modelling and analysis," in *1996 1st International Pipeline Conference,* 1996, pp. 993-1002.

[32] Q. Miao and V. Makis, "Condition monitoring and classification of rotating machinery using wavelets and hidden Markov models," *Mechanical Systems and Signal Processing,* vol. 21, pp. 840-855, 2, 2007.

[33] M. N. Rgeai, "Helical Gearbox Fault Detection using Motor Current Signature Analysis." , University of Manchester, 2007.

[34] R. Moore *et al*, "The Reliability-based maintenance strategy: a vision for improving industrial productivity," 1993.

[35] E. CSN, "13306 (2002) Maintenance Terminology," *Cesky Normalizacní Institute, Praha,* .

[36] J. Liu, "An intelligent system for bearing condition monitoring," 2008.

[37] P. Vas, *Parameter Estimation, Condition Monitoring, and Diagnosis of Electrical Machines.* Oxford University Press, USA, 1993.

[38] G. Singh and Ahmed, Saleh Al Kazzaz Sa'ad, "Vibration signal analysis using wavelet transform for isolation and identification of electrical faults in induction machine," *Electr. Power Syst. Res.,* vol. 68, pp. 119-136, 2004.

[39] V. P. Raj, K. Natarajan and T. Girikumar, "Induction motor fault detection and diagnosis by vibration analysis using MEMS accelerometer," in *Emerging Trends in Communication, Control, Signal Processing & Computing Applications (C2SPCA), 2013 International Conference On,* 2013, pp. 1-6.

[40] Z. Feng, M. Liang and F. Chu, "Recent advances in time–frequency analysis methods for machinery fault diagnosis: a review with application examples," *Mechanical Systems and Signal Processing,* vol. 38, pp. 165-205, 2013.

[41] M. El Hachemi Benbouzid, "A review of induction motors signature analysis as a medium for faults detection," *Industrial Electronics, IEEE Transactions On,* vol. 47, pp. 984-993, 2000.

[42] W. R. Finley, M. M. Hodowanec and W. G. Holter, "An analytical approach to solving motor vibration problems," in *Petroleum and Chemical Industry Conference, 1999. Industry Applications Society 46th Annual,* 1999, pp. 217-232.

[43] R. Stewart, *Application of Signal Processing Techniques to Machinery Health Monitoring.* Institute of Sound and Vibration Research, 1980.

[44] M. P. Norton and D. G. Karczub, *Fundamentals of Noise and Vibration Analysis for Engineers.* Cambridge university press, 2003.

[45] Y. Gritli *et al*, "Investigation of motor current signature and vibration analysis for diagnosing rotor broken bars in double cage induction motors," in *Power Electronics, Electrical Drives, Automation and Motion (SPEEDAM), 2012 International Symposium On,* 2012, pp. 1360-1365.

[46] D. Miljković, "Review of machine condition monitoring based on vibration data," in *Mipro 2008,* 2008, .

[47] R. Singal, K. Williams and S. Verma, "Vibration behaviour of stators of electrical machines, part II: experimental study," *J. Sound Vibrat.,* vol. 115, pp. 13-23, 1987.

[48] J. Cameron, W. Thomson and A. Dow, "Vibration and current monitoring for detecting airgap eccentricity in large induction motors," in *IEE Proceedings B (Electric Power Applications),* 1986, pp. 155-163.

[49] F. Immovilli *et al*, "Diagnosis of bearing faults in induction machines by vibration or current signals: A critical comparison," *IEEE Trans. Ind. Appl.,* vol. 46, pp. 1350-1359, 2010.

[50] H. Zheng, Z. Li and X. Chen, "Gear fault diagnosis based on continuous wavelet transform," *Mechanical Systems and Signal Processing,* vol. 16, pp. 447-457, 2002.

[51] P. D. Samuel, D. J. Pines and D. G. Lewicki, "A Comparison of Stationary and Non-Stationary Metrics for Detecting Faults in Helicopter Gearboxes," *Journal of the American Helicopter Society,* vol. 45, pp. 125-136, 2000.

[52] A. Andersson and L. Vedmar, "A dynamic model to determine vibrations in involute helical gears," *J. Sound Vibrat.,* vol. 260, pp. 195-212, 2003.

[53] P. D. Samuel and D. J. Pines, "A review of vibration-based techniques for helicopter transmission diagnostics," *J. Sound Vibrat.,* vol. 282, pp. 475-508, 2005.

[54] B. D. Forrester, *Advanced Vibration Analysis Techniques for Fault Detection and Diagnosis in Geared Transmission Systems.* Swinburne University of Technology, 1996.

[55] J. J. Zakrajsek, D. P. Townsend and H. J. Decker, "An analysis of gear fault detection methods as applied to pitting fatigue failure data," 1993.

[56] A. Aherwar, "An investigation on gearbox fault detection using vibration analysis techniques: A review," *Australian Journal of Mechanical Engineering,* vol. 10, pp. 169-183, 2012.

[57] S. Al-Arbi *et al*, "Characterization of vibration transmission paths for gearbox condition monitoring," 2010.

[58] P. Večeř, M. Kreidl and R. Šmíd, "Condition indicators for gearbox condition monitoring systems," *Acta Polytechnica,* vol. 45, 2005.

[59] Y. Lei *et al*, "Condition monitoring and fault diagnosis of planetary gearboxes: A review," *Measurement,* vol. 48, pp. 292-305, 2, 2014.

[60] M. Lebold *et al*, "Review of vibration analysis methods for gearbox diagnostics and prognostics," in *Proceedings of the 54th Meeting of the Society for Machinery Failure Prevention Technology,* 2000, pp. 16.

[61] F. Choy *et al*, "Vibration signature analysis of a faulted gear transmission system," *J. Propul. Power,* vol. 12, pp. 289-295, 1996.

[62] H. Cui *et al*, "Research on fault diagnosis for reciprocating compressor valve using information entropy and SVM method," *J Loss Prev Process Ind,* vol. 22, pp. 864-867, 2009.

[63] Z. Li and S. Ganeriwala, "Vibration Signatures of Reciprocating Compressors," 2007.

[64] D. J. McCarthy, "Vibration-Based Diagnostics of Reciprocating Machinery." , Massachusetts Institute of Technology, 1994.

[65] W. T. Thomson and M. Fenger, "Current signature analysis to detect induction motor faults," *IEEE Ind. Appl. Mag.,* vol. 7, pp. 26-34, 2001.

[66] A. M. da Silva, R. J. Povinelli and N. A. O. Demerdash, "Induction Machine Broken Bar and Stator Short-Circuit Fault Diagnostics Based on Three-Phase Stator Current Envelopes," *Industrial Electronics, IEEE Transactions On,* vol. 55, pp. 1310-1318, 2008.

[67] N. Mehala and R. Dahiya, "Motor current signature analysis and its applications in induction motor fault diagnosis," *International Journal of Systems Applications, Engineering & Development,* vol. 2, pp. 29-35, 2007.

[68] W. T. Thomson and R. J. Gilmore, "Motor current signature analysis to detect faults in induction motor drives–fundamentals, data interpretation, and industrial case histories," in *Proceedings of 32nd Turbo Machinery Symposium, A&M University, Texas, USA,* 2003, .

[69] W. Thomson, "On-line current monitoring to detect electrical and mechanical faults in three-phase induction motor drives," in *Life Management of Power Plants, 1994., International Conference On,* 1994, pp. 66-73.

[70] C. S. Kalaskar, "Motor Current Signature Analysis to Detect the Fault in Induction Motor," *International Journal of Engineering Research and Applications,* vol. 1, pp. 58-61, 2014.

[71] F. Briz *et al*, "Online diagnostics in inverter-fed induction machines using high-frequency signal injection," *Industry Applications, IEEE Transactions On,* vol. 40, pp. 1153-1161, 2004.

[72] G. M. Joksimovic and J. Penman, "The detection of inter-turn short circuits in the stator windings of operating motors," *Industrial Electronics, IEEE Transactions On,* vol. 47, pp. 1078-1084, 2000.

[73] J. A. Antonino-Daviu *et al*, "A Critical Comparison Between DWT and Hilbert–Huang-Based Methods for the Diagnosis of Rotor Bar Failures in Induction Machines," *Industry Applications, IEEE Transactions On,* vol. 45, pp. 1794-1803, 2009.

[74] M. Riera-Guasp *et al*, "A General Approach for the Transient Detection of Slip-Dependent Fault Components Based on the Discrete Wavelet Transform," *Industrial Electronics, IEEE Transactions On,* vol. 55, pp. 4167-4180, 2008.

[75] G. H. Müller and C. F. Landy, "A novel method to detect broken rotor bars in squirrel cage induction motors when interbar currents are present," *Energy Conversion, IEEE Transactions On,* vol. 18, pp. 71-79, 2003.

[76] J. Pons-Llinares *et al*, "Advanced Induction Motor Rotor Fault Diagnosis Via Continuous and Discrete Time–Frequency Tools," *IEEE Transactions on Industrial Electronics,* vol. 62, pp. 1791-1802, 2015.

[77] J. Antonino-Daviu *et al*, "Application and optimization of the discrete wavelet transform for the detection of broken rotor bars in induction machines," *Applied and Computational Harmonic Analysis,* vol. 21, pp. 268-279, 9, 2006.

[78] S. H. Kia, H. Henao and G. -. Capolino, "Diagnosis of Broken-Bar Fault in Induction Machines Using Discrete Wavelet Transform Without Slip Estimation," *Industry Applications, IEEE Transactions On,* vol. 45, pp. 1395-1404, 2009.

[79] R. R. Schoen and T. G. Habetler, "Effects of Time-Varying Loads on Rotor Fault Detection in Induction Machines," *IEEE Trans. Ind. Appl.,* vol. 31, 1995.

[80] R. Puche-Panadero *et al*, "Improved Resolution of the MCSA Method Via Hilbert Transform, Enabling the Diagnosis of Rotor Asymmetries at Very Low Slip," *Energy Conversion, IEEE Transactions On,* vol. 24, pp. 52-59, 2009.

[81] R. R. Schoen *et al*, "Motor bearing damage detection using stator current monitoring," *IEEE Transactions on Industry Applications,* vol. 31, pp. 1274-1279, 1995.

[82] J. Pons-Llinares *et al*, "Eccentricity diagnosis in inverter-fed induction motors via the analytic wavelet transform of transient currents," in *Electrical Machines (ICEM), 2010 XIX International Conference On,* 2010, pp. 1-6.

[83] M. N. Rgeai, "Helical Gearbox Fault Detection using Motor Current Signature Analysis." , University of Manchester, 2007.

[84] B. R. Rajendra and S. V. Bhaskar, "Condition Monitoring of Gear Box by Using Motor Current Signature Analysis," *International Journal of Scientific and Research Publications,* pp. 563, 2013.

[85] A. R. Mohanty and C. Kar, "Fault Detection in a Multistage Gearbox by Demodulation of Motor Current Waveform," *IEEE Transactions on Industrial Electronics,* vol. 53, pp. 1285-1297, 2006.

[86] S. H. Kia, H. Henao and G. A. Capolino, "Gearbox monitoring using induction machine stator current analysis," in *Diagnostics for Electric Machines, Power Electronics and Drives, 2007. SDEMPED 2007. IEEE International Symposium On,* 2007, pp. 149-154.

[87] C. Kar and A. R. Mohanty, "Monitoring gear vibrations through motor current signature analysis and wavelet transform," *Mechanical Systems and Signal Processing,* vol. 20, pp. 158-187, 1, 2006.

[88] C. Kar and A. R. Mohanty, "Vibration and current transient monitoring for gearbox fault detection using multiresolution Fourier transform," *J. Sound Vibrat.,* vol. 311, pp. 109-132, 3/18, 2008.

[89] Y. Lin, H. Wu and C. Wu, "Automated condition classification of a reciprocating compressor using time–frequency analysis and an artificial neural network," *Smart Mater. Struct.,* vol. 15, pp. 1576, 2006.

[90] A. Naid *et al*, "Bispectrum analysis of motor current signals for fault diagnosis of reciprocating compressors," in *Key Engineering Materials,* 2009, pp. 505-511.

[91] U. Haba *et al*, "Detection and Diagnosis of Compound Faults in a Reciprocating Compressor based on Motor Current Signatures," 2016.

[92] F. Gu *et al*, "Electrical motor current signal analysis using a modified bispectrum for fault diagnosis of downstream mechanical equipment," *Mechanical Systems and Signal Processing,* vol. 25, pp. 360-372, 2011.

[93] J. F. Moreno, F. P. Hidalgo and M. Martinez, "Realisation of tests to determine the parameters of the thermal model of an induction machine," in *Electric Power Applications, IEE Proceedings-,* 2001, pp. 393-397.

[94] O. Okoro, "Steady and transient states thermal analysis of a 7.5-kW squirrel-cage induction machine at rated-load operation," *Energy Conversion, IEEE Transactions On,* vol. 20, pp. 730-736, 2005.

[95] J. Milimonfared *et al*, "A novel approach for broken-rotor-bar detection in cage induction motors," *Industry Applications, IEEE Transactions On,* vol. 35, pp. 1000-1006, 1999.

[96] M. C. Garcia, M. A. Sanz-Bobi and J. del Pico, "SIMAP: Intelligent System for Predictive Maintenance: Application to the health condition monitoring of a windturbine gearbox," *Comput. Ind.,* vol. 57, pp. 552-568, 2006.

[97] T. A. Lipo and K. C. Chang, "A new approach to flux and torque-sensing in induction machines," *IEEE Trans. Ind. Appl.,* pp. 731-737, 1986.

[98] H. Henao *et al*, "Trends in Fault Diagnosis for Electrical Machines: A Review of Diagnostic Techniques," *Industrial Electronics Magazine, IEEE,* vol. 8, pp. 31-42, 2014.

[99] R. Romary *et al*, "Electrical machines fault diagnosis by stray flux analysis," in *Electrical Machines Design Control and Diagnosis (WEMDCD), 2013 IEEE Workshop On,* 2013, pp. 247-256.

[100] A. Bellini *et al*, "Quantitative evaluation of induction motor broken bars by means of electrical signature analysis," *Industry Applications, IEEE Transactions On,* vol. 37, pp. 1248-1255, 2001.

[101] F. Filippetti *et al*, "Current pattern analysis to detect induction machine non rotational anomalies," in *Proceedings of the 1998 International Conference on Electrical Machines,* 1998, pp. 448-453.

[102] S. B. Lee, R. M. Tallam and T. G. Habetler, "A robust, on-line turn-fault detection technique for induction machines based on monitoring the sequence component impedance matrix," *Power Electronics, IEEE Transactions On,* vol. 18, pp. 865-872, 2003.

[103] I. Albizu *et al*, "Techniques for online diagnosis of stator shorted turns in induction motors," *Electric Power Components and Systems,* vol. 34, pp. 97-114, 2006.

[104] Z. Gao, C. Cecati and S. X. Ding, "A survey of fault diagnosis and fault-tolerant techniques-Part I: fault diagnosis With model-based and signal-based approaches," *IEEE Trans. Ind. Electron.,* vol. 62, pp. 3757-3767, 2015.

[105] G. C. Stone, H. G. Sedding and M. J. Costello, "Application of partial discharge testing to motor and generator stator winding maintenance," *Industry Applications, IEEE Transactions On,* vol. 32, pp. 459-464, 1996.

[106] S. M. Tetrault, G. C. Stone and H. G. Sedding, "Monitoring partial discharges on 4-kV motor windings," *Industry Applications, IEEE Transactions On,* vol. 35, pp. 682-688, 1999.

[107] I. LUDECA, "A basic guide to understanding vibration analysis for machinery diagnosis," 2011.

[108] J. S. Hsu, "Monitoring of defects in induction motors through air-gap torque observation," *Industry Applications, IEEE Transactions On,* vol. 31, pp. 1016-1021, 1995.

[109] Y. Lee *et al*, "An acoustic diagnostic technique for use with electric machine insulation," *Dielectrics and Electrical Insulation, IEEE Transactions On,* vol. 1, pp. 1186-1193, 1994.

[110] M. A. Hamel, "Condition Monitoring of Helical Gears Using Acoustic Emission (AE) Technology," 2013.

[111] M. Ojaghi, M. Sabouri and J. Faiz, "Diagnosis methods for stator winding faults in three-phase squirrel-cage induction motors," *International Transactions on Electrical Energy Systems,* vol. 24, pp. 891-912, 2014.

[112] P. Vas, *Artificial-Intelligence-Based Electrical Machines and Drives: Application of Fuzzy, Neural, Fuzzy-Neural, and Genetic-Algorithm-Based Techniques.* Oxford University Press, 1999.

[113] F. Filippetti, G. Franceschini and C. Tassoni, "Neural networks aided on-line diagnostics of induction motor rotor faults," *Industry Applications, IEEE Transactions On,* vol. 31, pp. 892-899, 1995.

[114] A. K. Mahamad, S. Saon and T. Hiyama, "Predicting remaining useful life of rotating machinery based artificial neural network," *Comput. Math. Appl.,* vol. 60, pp. 1078-1087, 2010.

[115] J. F. Martins, V. F. Pires and A. J. Pires, "Unsupervised Neural-Network-Based Algorithm for an On-Line Diagnosis of Three-Phase Induction Motor Stator Fault," *Industrial Electronics, IEEE Transactions On,* vol. 54, pp. 259-264, 2007.

[116] W. J. Staszewski, K. Worden and G. R. Tomlinson. Time–frequency analysis in gearbox fault detection using the wigner–ville distribution and pattern recognition. *Mechanical Systems and Signal*

Processing 11(5), pp. 673-692. 1997. . DOI: http://dx.doi.org.ezproxy.uct.ac.za/10.1006/mssp.1997.0102.

[117] P. W. Stevens, D. Hall and E. Smith, "A multidisciplinary research approach to rotorcraft health and usage monitoring," in *Proc. Annual Forum, American Helicopter Society,* 1996, pp. 1732-1751.

[118] H. Martin, "Detection of gear damage by statistical vibration analysis," in *Institution of Mechanical Engineers Conference Publications,* 1992, pp. 395-395.

[119] De Almeida, Rui Gomes Teixeira, da Silva Vicente, Silmara Alexandra and L. R. Padovese, "New technique for evaluation of global vibration levels in rolling bearings," *Shock Vibrat.,* vol. 9, pp. 225-234, 2002.

[120] G. J. S. Hahn and S. Samuel, *Statistical Models in Engineering.* 1967.

[121] (). *Daubechies Wavelet*.

[122] M. A. S. K. Khan and M. A. Rahman, *Wavelet Based Diagnosis and Protection of Electric Motors.* INTECH Open Access Publisher, 2010.

[123] V. Čižek, "Discrete hilbert transform," *Audio and Electroacoustics, IEEE Transactions On,* vol. 18, pp. 340-343, 1970.

[124] D. Miljković, "Brief Review of Motor Current Signature Analysis," *HDKBR INFO Magazin,* vol. 5, pp. 14-26, 2015.

[125] (). *Clustering of the Self-Organizing Map based Approach in Induction Machine Rotor Faults Diagnostics*.

[126] J. Rangel-Magdaleno *et al*, "Novel methodology for online half-broken-bar detection on induction motors," *Instrumentation and Measurement, IEEE Transactions On,* vol. 58, pp. 1690-1698, 2009.

[127] C. Concari, G. Franceschini and C. Tassoni, "Differential diagnosis based on multivariable monitoring to assess induction machine rotor conditions," *Industrial Electronics, IEEE Transactions On,* vol. 55, pp. 4156-4166, 2008.

[128] A. Korde, "On-line condition monitoring of motors using electrical signature analysis," in *Recent Advances in Condition-Based Plant Maintenance. in Seminar Organized by Indian Institute of Plant Engineers, Mumbai, India,* 2002, .

[129] J. Jung, J. Lee and B. Kwon, "Online diagnosis of induction motors using MCSA," *IEEE Trans. Ind. Electron.,* vol. 53, pp. 1842-1852, 2006.

[130] C. Scheffer and P. Girdhar, *Practical Machinery Vibration Analysis and Predictive Maintenance.* Elsevier, 2004.

[131] H. P. Bloch and J. J. Hoefner, *Reciprocating Compressors:: Operation and Maintenance.* Gulf Professional Publishing, 1996.

[132] M. Blodt *et al*, "Mechanical load fault detection in induction motors by stator current time-frequency analysis," *IEEE Trans. Ind. Appl.,* vol. 42, pp. 1454-1463, 2006.

[133] B. Y. Lee, H. S. Liu and Y. S. Tarng. Monitoring of tool fracture in end milling using induction motor current. *J. Mater. Process. Technol. 70(1),* pp. 279-284. 1997. . DOI: http://dx.doi.org.ezproxy.uct.ac.za/10.1016/S0924-0136(97)00082-4.

[134] C. Kar and A. R. Mohanty, "Monitoring gear vibrations through motor current signature analysis and wavelet transform," *Mechanical Systems and Signal Processing,* vol. 20, pp. 158-187, 1, 2006.

[135] B. R. Rajendra and S. V. Bhaskar, "Condition Monitoring of Gear Box by Using Motor Current Signature Analysis," *International Journal of Scientific and Research Publications,* pp. 563, .

[136] (). *Machine Fault Simulator Magnum - The Best Tool Available for Learning Machine Diagnosis*.

[137] M. Dlamini. Development of and induction motor condition monitoring test rigg and fault detection strategies. 2014.

[138] M. Dlamini, P. S. Barendse and A. M. Khan, "Detecting faults in inverter-fed induction motors during startup transient conditions," in *Energy Conversion Congress and Exposition (ECCE), 2014 IEEE,* 2014, pp. 3131-3138.

[139] (). *NI 9215 datasheet*.

[140] (). *NI 9215 User Manual*.

[141] (). *NI 9234 Datasheet*.

[142] (). *NI 9234 User Manual*.

[143] I. SpectraQuest, *User Operating Manual for Machinery Fault Simulator.*

[144] A. Siddique, G. Yadava and B. Singh, "A review of stator fault monitoring techniques of induction motors," *Energy Conversion, Ieee Transactions On,* vol. 20, pp. 106-114, 2005.

11. Appendices

11.1 Appendix A – Gearbox

11.1.1 Piston Frequencies

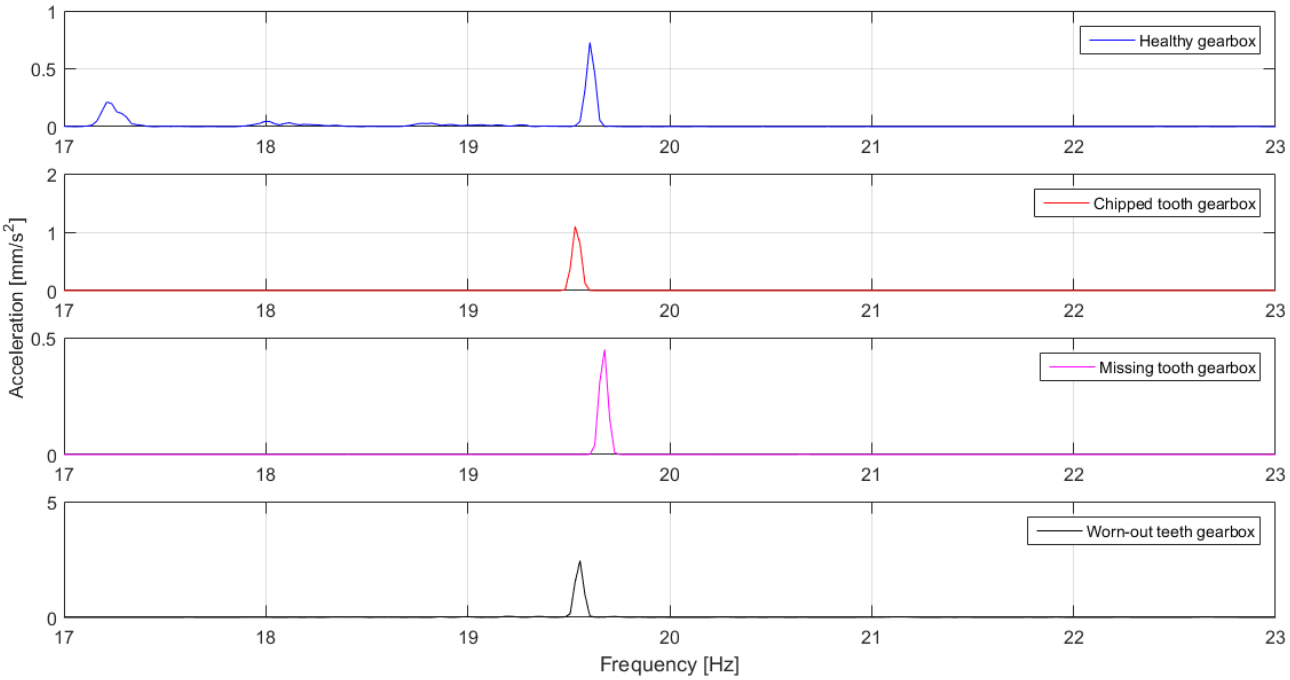

Figure 11-1 Piston frequencies of the various gearboxes at no load

Table 11-1 Piston frequencies of the gearboxes at no load

Gearbox	Frequency [Hz]	Amplitude [mm/s²]
Healthy	19.60	0.73
Chipped tooth	19.53	1.10
Missing tooth	19.58	0.45
Worn-out teeth	19.56	2.45

Table 11-2 Energy in the various frequency bands of the test gearboxes

Frequency band	Healthy	Chipped tooth	Missing tooth	Worn-out
533.33 - 1066.67	1.30e-03	2.21e-03	1.39e-02	3.80e-03
266.67 - 533.33	2.91e-04	4.65e-04	1.44e-02	2.61e-03
133.33 - 266.67	3.29e-04	4.63e-04	5.91e-03	8.72e-04
66.67 - 133.33	1.23e-04	2.61e-04	6.23e-04	9.93e-04
33.33 - 66.67	4.45e-05	1.25e-04	4.21e-04	7.81e-05
16.67 - 33.33	1.69e-05	7.77e-05	2.34e-04	2.08e-05
8.33 - 16.67	8.31e-06	3.33e-05	1.01e-04	6.05e-06
4.17 - 8.33	4.06e-06	1.62e-05	4.40e-05	5.03e-06
0 - 4.17	4.77e-06	1.86e-05	6.05e-05	8.86e-06

11.1.2 MCSA of the Worn-out Gearbox

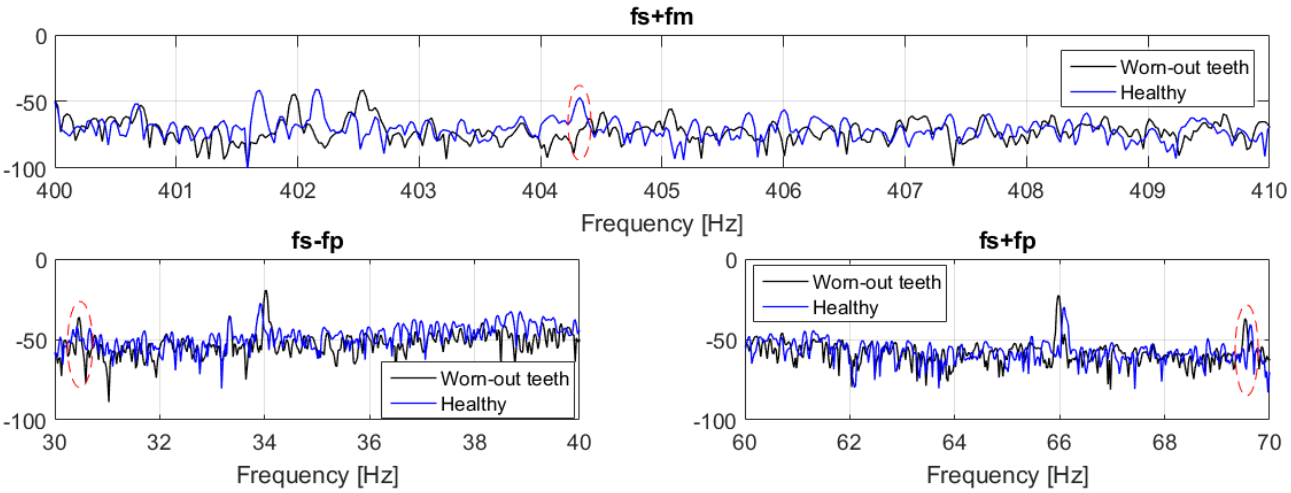

Figure 11-2 Motor current spectrum showing $f_s + f_m$, $f_s + f_p$ and $f_s - f_p$ of the healthy gearbox and the gearbox with the worn-out teeth

Table 11-3 Frequencies and amplitudes of the $f_s + f_m$, $f_s + f_p$ and $f_s - f_p$ frequency components in the motor current spectrum for the gearbox with the worn-out teeth

Fault component	Healthy gearbox		Worn-out teeth gearbox	
	Frequency [Hz]	Amplitude [dB]	Frequency [Hz]	Amplitude [dB]
$f_s + f_m$	404.3	-47.11	-	-
$f_s + f_p$	69.63	-40.75	69.53	-37.04
$f_s - f_p$	30.42	-41.65	30.47	-36.29

11.2 Appendix B – Reciprocating Compressor

11.2.1 Partially Blocked Discharge Valve Fault

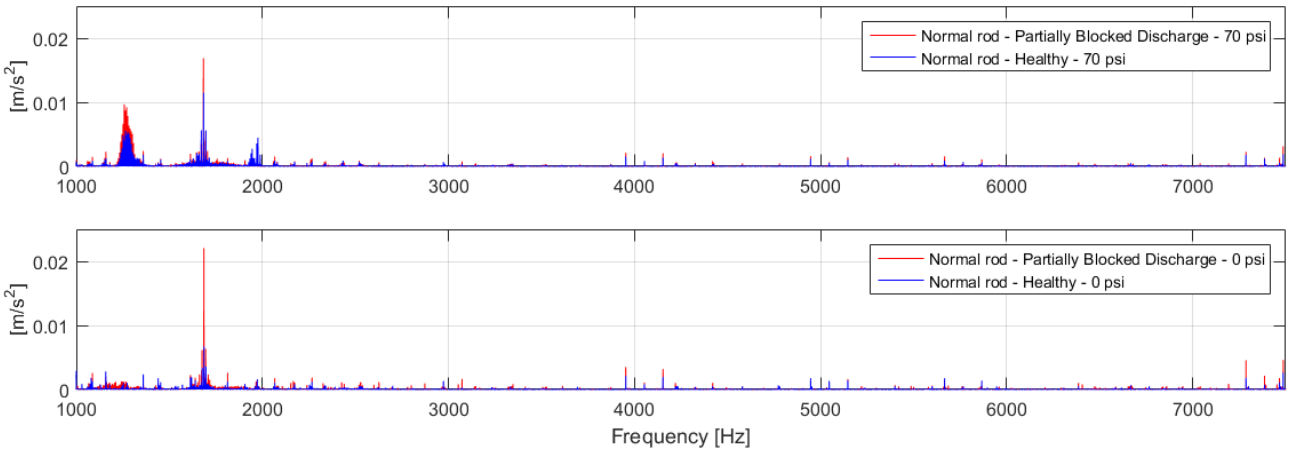

Figure 11-3 FFT of the healthy compressor and the compressor with a partially blocked discharge at 70 psi and 0 psi air tank pressure

Table 11-4 Energy in the various frequency bands of the DWT's of the healthy compressor and the compressor with a partially blocked discharge valve at 0 psi

Frequency band	Healthy	Partially blocked discharge
2133.33 Hz to 4266.67 Hz	0.0208	0.0425
1066.67 Hz to 2133.33 Hz	0.0220	0.0312
533.33 Hz to 1066.67 Hz	0.0087	0.0103
266.67 Hz to 533.33 Hz	0.0142	0.0126
133.33 Hz to 266.67 Hz	0.0126	0.0110
66.67 Hz to 133.33 Hz	0.0035	0.0077
33.33 Hz to 66.67 Hz	0.0013	0.0027
16.67 Hz to 33.33 Hz	0.0004	0.0009
8.3 Hz to 16.67 Hz	0.0002	0.0004
4.17 Hz to 8.3 Hz	0.0001	0.0002

11.2.2 Blocked Suction Fault

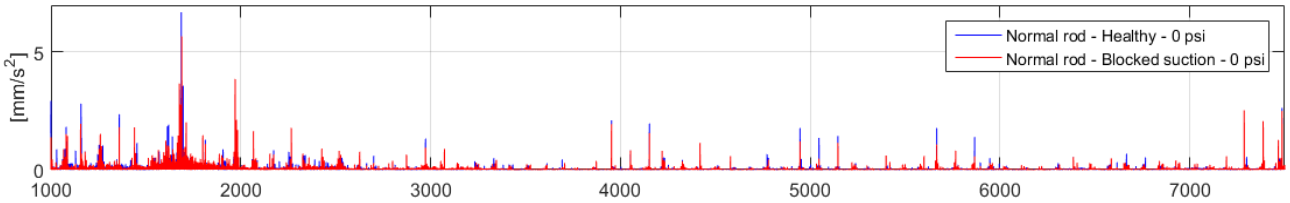

Figure 11-4 FFT of the healthy compressor and the compressor with a blocked suction at 0 psi air tank pressure

11.3 Appendix C - Code

```
%Code to display the FFT of a signal
% clear;
Fs =25600; % Sampling frequency

% Sum of a 50 Hz sinusoid and a 120 Hz sinusoid
T = 1./Fs; % time step

% fs = 50;

% SM_Grid_Healthy_0_768kSample_25_6kHz_ss
% SM_Grid_2turns_100_768kSample_25_6kHz_ss
% SM_Grid_4turns_100_768kSample_25_6kHz_ss
% SM_100_grid_bf_768kS_25_6kHz_ss
% SM_100_grid_bow_768kS_25_6kHz_ss
% SM_100_Inv50_healthy_768kS_25_6kHz_ss
% SM_100_Inv60_2turns_768kS_25_6kHz_ss
% SM_100_Inv50_brb_768kS_25_6kHz_ss_2
% SM_100_Inv50_bf_768kS_25_6kHz_ss
% SM_100_Inv50_bow_768kS_25_6kHz_ss
% SM_Grid_Healthy_100_768kSample_25_6kHz_ss
% data = load('SM_0_grid_brb_768kS_25_6kHz_ss_2.txt');

%----------- Motors -----------------
% data_name = 'SM_0_Inv50_healthy_768kS_25_6kHz_ss.txt'; col = 'b';
% data_name = 'SM_50_Inv50_healthy_768kS_25_6kHz_ss.txt'; col = 'b';
% data_name = 'SM_100_Inv50_healthy_768kS_25_6kHz_ss'; col = 'b';
% data_name = 'SM_0_Inv60_healthy_768kS_25_6kHz_ss.txt'; col = 'k';
% data_name = 'SM_100_Inv60_healthy_768kS_25_6kHz_ss.txt'; col = 'k';

% data_name = 'SM_0_Inv50_bow_768kS_25_6kHz_ss'; col = 'r';
% data_name = 'SM_50_Inv50_bow_768kS_25_6kHz_ss'; col = 'r';
% data_name = 'SM_100_Inv50_bow_768kS_25_6kHz_ss2.txt'; col = 'r';

% data_name = 'SM_0_Inv50_2turns_768kS_25_6kHz_ss'; col = 'r';
% data_name = 'SM_50_Inv50_2turns_768kS_25_6kHz_ss'; col = 'r';
% data_name = 'SM_100_Inv50_2turns_768kS_25_6kHz_ss'; col = 'r';

% data_name = 'SM_0_Inv50_4turns_768kS_25_6kHz_ss.txt'; col = 'r';
% data_name = 'SM_50_Inv50_4turns_768kS_25_6kHz_ss.txt'; col = 'r';
% data_name = 'SM_100_Inv50_4turns_768kS_25_6kHz_ss'; col = 'r';

% data_name = 'SM_0_Inv50_brb_768kS_25_6kHz_ss.txt'; col = 'r';
% data_name = 'SM_50_Inv50_brb_768kS_25_6kHz_ss.txt'; col = 'r';
% data_name = 'SM_100_Inv50_brb_768kS_25_6kHz_ss_2.txt'; col = 'r';

% data_name = 'SM_0_Inv50_bf_768kS_25_6kHz_ss'; col = 'r';
% data_name = 'SM_50_Inv50_bf_768kS_25_6kHz_ss'; col = 'r';
% data_name = 'SM_100_Inv50_bf_768kS_25_6kHz_ss'; col = 'r';

% -------- Gearboxes ------------
% data_name = 'GB_healthy_50_Hz_0_load_inv_ss'; col = 'b';
% data_name = 'chipped_tooth_gearbox_inv_ss'; col = 'r';
% data_name = 'GB_missing_tooth_50_Hz_0_load_inv_ss'; col = 'm';
% data_name = 'worn_gearbox_inv_ss'; col = 'k';

% ------- Compressor ------------
% data_name = 'big_rod_leaking_valve_healthy_discharge_60Hz_ss_0_psi'; col =
'b';
```

```
% data_name =
'big_rod_leaking_valve_partially_blocked_discharge_60Hz_ss_70_psi'; col = 'r';
% data_name = 'big_rod_leaking_valve_partially_blocked_discharge_60Hz_ss_0_psi';
col = 'r';
% data_name =
'big_rod_leaking_valve_partially_blocked_discharge_60Hz_ss_70_psi'; col = 'r';
% data_name = 'big_rod_leaking_valve_healthy_discharge_60Hz_ss_45_psi_3'; col =
'b';
% data_name =
'big_rod_leaking_valve_partially_blocked_discharge_60Hz_ss_45_psi_3'; col = 'r';
% data_name = 'big_rod_leaking_valve_blocked_suction_60Hz_ss_0_psi'; col = 'r';

% data_name = 'normal_rod_healthy_valve_healthy_suction_60Hz_ss_0_psi_2'; col =
'b';
% data_name = 'normal_rod_healthy_valve_blocked_suction_60Hz_ss'; col = 'r';
% data_name =
'normal_rod_healthy_valve_partially_blocked_discharge_60Hz_ss_45_psi_3'; col =
'r';
% data_name = 'normal_rod_healthy_valve_healthy_suction_60Hz_ss_45_psi_3'; col =
'b';
% data_name = 'normal_rod_healthy_valve_blocked_suction_60Hz_ss'; col = 'r';
% data_name =
'normal_rod_healthy_valve_partially_blocked_discharge_60Hz_ss_0_psi'; col = 'r';
data_name = 'normal_rod_healthy_valve_healthy_suction_60Hz_ss_70_psi'; col =
'b';
% data_name =
'normal_rod_healthy_valve_partially_blocked_discharge_60Hz_ss_70_psi'; col =
'r';

%

% --------- Combinations ----------
% data_name = 'Healthy_motor_+_Healthy_Gearbox_Healthy_compressor'; col = 'b';
% data_name = 'Healthy_motor_+_Healthy_Gearbox_2'; col = 'b';
% data_name = '2_turns_+_Healthy_Gearbox'; col = 'r';
% data_name = '4_turns_+_Healthy_Gearbox'; col = 'm';
% data_name = '2_turns_+_Healthy_Gearbox_start_up'; col = 'r';
% data_name = '2_turns_motor_+_missing_Gearbox_bs_compressor'; col = 'r';
% data_name = '4_turns_motor_+_missing_Gearbox_bs_compressor'; col = 'm';
% data_name = 'brb_+_missing_Gearbox_bs_compressor'; col = 'r';
% data_name = '4_turns_+_missing_Gearbox_pbd_compressor'; col = 'm';

%
data = load(data_name);
% y = data(:,5);
y = data(:,12);

% load(data_name);

% y = Y; col = 'b';
y = y(1:768000);
% y = GB_Y;
N = length(y); % number of samples
% y = iomega(y,(1/25600),3,2); col = 'k';
t = (0:N-1)*T; % Time vector
% fr = 0:0.5:200;
NFFT = 2^nextpow2(N);% extend the number of samples for zero padding
% x = rms(data(:,4));
% y = GB_Y;
% Sp = data(:,8); % reads the voltage
% Sp = (Sp.*-2934)./4.73388; % scales the voltage to get speed
% nr = mean(Sp); % calculates the mean speed

% to perform the hibert apply
```

```
%Iahil = abs(hilbert(Ia))-mean(abs(hilbert(Ia)));
%
w2 = window(@hann,N);
% perform the PSD
[Pxx,F] = pwelch(y,w2,[],NFFT,Fs);
% Pxx = fftshift(Pxx);
% t=fpeak(F,Pxx,30,[23,40,700,inf]);

f_loc = find(Pxx == max(Pxx(2000:2100))); fs = F(f_loc);
Pxxn = Pxx./max(Pxx);% normalises the PSD

% figure; plot(F,10*log10(Pxxn),col); ylabel(' (dB/Hz) ');
figure; plot(F,10*log10(Pxx),col); ylabel(' (dB/Hz) ');
% figure; plot(F,Pxx/max(Pxx),col); ylabel(' [mm/s^{2}] ');
% figure; plot(F,Pxx,col); ylabel(' [mm/s^{2}] ');

% displayname = input('Display name?\n');
% figure; plot(F,Pxx, col,'DisplayName',displayname);
% ylabel('Acceleration (ms^{-2})');

% figure; psd(spectrum.periodogram,y,'NFFT',length(y),'Fs',25600);
% figure; plot(F,10*log10(Pxx) - mean(10*log10(Pxx)), col);
xlabel('Frequency (Hz)')
set(gca, 'FontSize', 12);
% set(gcf, 'Position', get(0,'Screensize')); % Maximize figure.
legend('show'); grid on;


% xlim([140 160]); ylim([-100,-20]);
% fprintf('Rotational frequency = %4.4f\n', fs);
% % fprintf('Rotational frequency = %4.4f\n', frm);
% fprintf('Slip = %4.4f\n', s);




% This code performs a discrete wavelet transform and wavelet packets
% decompositions
clear;
fs = 25600; % sampling frequency
f = 50; % fundamental frequency
ds = 3; % downsample value, if set to 1 no downsample takes place
fds = fs/ds; % new sampling frequency
wlt = 'db44'; % choice of wavelet
Nf = 10; % number of decomposition levels, set to 0 for default

% Load transient signal here

% ********************Gearbox*********************************
% data = load('GB_healthy_50_Hz_0_load_inv_startup'); col = 'b'; % start = 10;
% data = load('GB_chipped_tooth_50_Hz_0_load_inv_startup'); col = 'r'; % start =
10.08
% data = load('GB_missing_tooth_50_Hz_0_load_inv_startup'); col = 'm'; % start =
9.8
% data = load('worn_gearbox_inv_startup'); col = 'k'; % start = 12.25

%***************************** Motor ******************************%
% data = load('SM_100_Inv50_healthy_768kS_25_6kHz_startup'); col = 'b';
% data = load('SM_100_Inv50_brb_768kS_25_6kHz_startup_2'); col = 'r';
% data = load('SM_100_Inv50_bf_768kS_25_6kHz_startup'); col = 'r';
% data = load('SM_100_Inv50_bow_768kS_25_6kHz_startup'); col = 'r';
% data = load('SM_100_Inv50_bow_768kS_25_6kHz_startup'); col = 'r';
```

```
%****************************** Compressor ******************************%
% data = load('big_rod_leaking_valve_healthy_discharge_60Hz_ss_0_psi'); col =
'b';
% data = load('big_rod_leaking_valve_healthy_discharge_60Hz_ss_70_psi'); col =
'b';
% data =
load('big_rod_leaking_valve_partially_blocked_discharge_60Hz_ss_70_psi'); col =
'r';
% data = load('big_rod_leaking_valve_blocked_suction_60Hz_ss_0_psi'); col = 'r';
% data =
load('normal_rod_leaking_valve_partially_blocked_discharge_60Hz_start_up_0_psi_3
'); col = 'b';
% data = load('normal_rod_healthy_valve_healthy_suction_60Hz_ss_70_psi'); col =
'b';
% data = load('normal_rod_healthy_valve_healthy_suction_60Hz_ss_0_psi_2'); col =
'b';
% data =
load('normal_rod_healthy_valve_partially_blocked_discharge_60Hz_ss_0_psi'); col
= 'r';
% data =
load('normal_rod_healthy_valve_partially_blocked_discharge_60Hz_ss_70_psi'); col
= 'r';
% data = load('normal_rod_healthy_valve_blocked_suction_60Hz_ss'); col = 'r';
% data = load('big_rod_leaking_valve_healthy_discharge_60Hz_startup_0_psi_3');
col = 'b';
% data =
load('big_rod_leaking_valve_partially_blocked_discharge_60Hz_startup_0_psi_3');
col = 'r';
% data = load('big_rod_leaking_valve_blocked_suction_60Hz_start_up'); col = 'm';
% data = load('normal_rod_healthy_valve_healthy_suction_60Hz_start_up_0_psi_3');
col = 'b';
% data =
load('normal_rod_leaking_valve_partially_blocked_discharge_60Hz_start_up_0_psi_3
'); col = 'r';
% data = load('normal_rod_healthy_valve_blocked_suction_60Hz_start_up'); col =
'm';

%%%%%%%%%%%%% Combinations %%%%%%%%%%%%%%%%%%%%%%%%%%%%
% data = load('Healthy_motor_+_Healthy_Gearbox_Healthy_compressor'); col = 'b';
% data = load('brb_+_missing_Gearbox_bs_compressor'); col = 'r';
% data = load('4_turns_+_missing_Gearbox_pbd_compressor'); col = 'r';

% data = load('Healthy_motor_+_Healthy_Gearbox_Healthy_compressor_startup'); col
= 'b';
% data = load('brb_+_missing_Gearbox_bs_compressor_startup'); col = 'r';
% data = load('4_turns_+_missing_Gearbox_pbd_compressor_startup'); col = 'r';

% s1 = Ia; % set signal equal to measurand

s1 = data(:,10);

% % to perform the hibert apply
% s1 = abs(hilbert(s1))-mean(abs(hilbert(s1)));

% Possibility of downsampling
if ds~=1
    ds;
    s1 = downsample(s1,ds);
end

s1_len = length(s1);
t = (0:1:s1_len-1)/fds; % generate time vector
% Calculate the frequency bands for the wavelet decomposition-------------
if Nf == 0
```

```
    Nf = log(fds/f)/log(2); % number of decomposition levels
    Nf = double(uint32(Nf)); % need an integer value
end

D = freq_bands( f, fds, Nf ); % calculate frequency bands ad display
% Wavelet decomposition
[s1_App, s1_Det] = wav_analysis(s1, Nf, wlt);

% Display wavelet decomposition here
% Max of four subplots per figure and show the detail levels and last
% approximation level only
for k = 0:4:Nf-1
    figure
    for k2 = 1:min(4,Nf-k)
        hold on
        ha(k2) = subplot(4,1,k2); plot(t,s1_Det(k+k2,:),col); grid on;
        enrgy(k+k2) = sum(s1_Det(k+k2,:)'.^2)/(62.5*10000);
%         set(gca,'FontSize',10,'XLim',[0 t(end)]);
        set(gca,'FontSize',10,'XLim',[0 10]);
%         set(gca,'FontSize',10,'XLim',[4.3, 4.5]);
        title([num2str(D(1+k+k2)) '-' num2str(D(k+k2)) ' Hz']);
        k2;
    end
    linkaxes(ha,'x');
end
hold on
ha(k2+1) = subplot(4,1,k2+1); plot(t,s1_App(10,:),'m'); grid on;
enrgy(11) = sum(s1_App(10,:)'.^2)/(62.5*10000);
linkaxes(ha,'x');
% set(gca,'Fontsize',10,'XLim',[0 t(end)]); grid on;
set(gca,'FontSize',10,'XLim',[0,10]); grid on;
% set(gca,'FontSize',10,'XLim',[4.3,4.5]); grid on;
title([ '0 -' num2str(D(end)) ' Hz']);
xlabel('Time(s)');
```

11. EBE Faculty: Assessment of Ethics in Research Projects

Any person planning to undertake research in the Faculty of Engineering and the Built Environment at the University of Cape Town is required to complete this form before collecting or analysing data. When completed it should be submitted to the supervisor (where applicable) and from there to the Head of Department. If any of the questions below have been answered YES, and the applicant is NOT a fourth year student, the Head should forward this form for approval by the Faculty EIR committee. submit to Ms Zulpha Geyer (zulpha.geyer@uct.ac.za; Chem Eng Building, Ph 021 650 4791) Students must include a copy of the completed form with the final year project report it is submitted for examination.

Name of Principal Researcher/Student: Andrew Matthew Ipurale Department: ELECTRICAL ENGINEERING

If a Student: YES Degree: MSc Electrical Engineering Supervisor: A/Prof Paul Barendse

If a Research Contract indicate source of funding/sponsorship:

Research Project Title: Condition Monitoring and Fault Detection in Inverter-fed Rotating Machinery

Overview of ethics issues in your research project:

Question 1: Is there a possibility that your research could cause harm to a third party (i.e. a person not involved in your project)?	YES	NO✓
Question 2: Is your research making use of human subjects as sources of data? If your answer is YES, please complete Addendum 2.	YES	NO✓
Question 3: Does your research involve the participation of or provision of services to communities? If your answer is YES, please complete Addendum 3.	YES	NO✓
Question 4: If your research is sponsored, is there any potential for conflicts of interest? If your answer is YES, please complete Addendum 4.	YES	NO✓

If you have answered YES to any of the above questions, please append a copy of your research proposal, as well as any interview schedules or questionnaires (Addendum 1) and please complete further addenda as appropriate.

I hereby undertake to carry out my research in such a way that

- there is no apparent legal objection to the nature or the method of research; and
- the research will not compromise staff or students or the other responsibilities of the University;
- the stated objective will be achieved, and the findings will have a high degree of validity;
- limitations and alternative interpretations will be considered;
- the findings could be subject to peer review and publicly available; and
- I will comply with the conventions of copyright and avoid any practice that would constitute plagiarism.

Signed by:

	Full name and signature	Date
Principal Researcher/Student:	Andrew Matthew Ipurale	17 February 2017

This application is approved by:

Supervisor (if applicable):	A/Prof Paul Barendse	17 February 2017
HOD (or delegated nominee): Final authority for all assessments with NO to all questions and for all undergraduate research.	Janine Bixley	17 February 2017
Chair : Faculty EIR Committee: For applicants other than undergraduate students who have answered YES to any of the above		